DEVELOPMENT OF FRAMEWORK FOR THERMAL PATTERNS ANALYSIS FOR DIAGNOSIS OF DISEASES

Thesis Submitted
In Partial Fulfillment of the Requirements
for the Degree of

DOCTOR OF PHILOSOPHY

by

Trasha Gupta
(Roll No. 2K18/PHDCO/508)

Under the Supervision of

Prof. Rajni Jindal
Department of Computer Science and Engineering

Prof. S. Indu
Department of Electronics and Communications Engineering

Department of Computer Science & Engineering
DELHI TECHNOLOGICAL UNIVERSITY
(Formerly Delhi College of Engineering)
Shahabad Daulatpur, Main Bawana Road, Delhi-110042, INDIA

August, 2025

DELHI TECHNOLOGICAL UNIVERSITY
(Formerly Delhi College of Engineering)
Shahabad Daulatpur, Main Bawana Road, Delhi-110042, INDIA

CANDIDATE'S DECLARATION

I, **Trasha Gupta, (2K18/PHDCO/508)** hereby declare that the work which is being presented in the thesis entitled **"Development of Framework for Thermal Patterns Analysis for Diagnosis of Diseases"** in partial fulfillment of the requirements for the award of the Degree of Doctor of Philosophy, submitted in the Department of Computer Science & Engineering, Delhi Technological University is an authentic record of my own work carried out during the period from 2019 to 2025 under the supervision of Prof. Rajni Jindal and Prof. S. Indu.

The matter presented in the thesis has not been submitted by me for the award of any other degree of this or any other Institute.

Trasha Gupta
(2K18/PHDCO/508)

This is to certify that the student has incorporated all the corrections suggested by the examiners in the thesis and the statement made by the candidate is correct to the best of our knowledge.

Prof. Rajni Jindal	**Prof. S. Indu**	**Prof. Sumantra Dutta Roy**
Department of Computer Science and Engineering	Department of Electronics and Communications Engineering	Department of Electrical Engineering, IIT Delhi
Supervisor	**Co-Supervisor**	**External Examiner**

DELHI TECHNOLOGICAL UNIVERSITY
(Formerly Delhi College of Engineering)
Shahabad Daulatpur, Main Bawana Road, Delhi-110042, INDIA

CERTIFICATE

Certified that **Trasha Gupta (2K18/PHDCO/508)** has carried out her research work presented in this thesis entitled **"Development of Framework for Thermal Patterns Analysis for Diagnosis of Diseases"** for the award of **Doctor of Philosophy** from Department of Computer Science & Engineering, Delhi Technological University, Delhi, under our supervision. The thesis embodies results of original work, and studies are carried out by the student herself and the contents of the thesis do not form the basis of the award of any other degree to the candidate or to anybody else from this or any other institution.

Prof. Rajni Jindal	**Prof. S. Indu**
(Supervisor)	(Co-Supervisor)
Department of Computer Science and Engineering	Department of Electronics and Communications Engineering
Delhi Technological University	Delhi Technological University
Delhi	Delhi

Date: 05/08/2025
Place: New Delhi

ACKNOWLEDGMENTS

This section of my thesis holds immense significance as I reflect on the many people who, directly or indirectly, have made this PhD journey worthwhile. While the thesis itself has a page limit, my gratitude does not. Therefore, I will try to be concise and mention just a few names here.

I sincerely extend my deepest gratitude to the esteemed Honorable Vice-Chancellor, DTU, Prof. Prateek Sharma Sir, for his unwavering support. I am also profoundly thankful to the respected Registrar sir, Prof. Madhusudan Sir, for graciously granting me the opportunity to pursue this research. Additionally, I am immensely grateful to Prof. Ramesh Srivastava for his invaluable encouragement and for allowing me to advance in this academic endeavor.

A special note of appreciation goes to my advisors, Prof. Rajni Jindal and Prof. S. Indu, whose guidance, and constant encouragement have been instrumental in shaping my PhD journey. Their belief in my potential and their insights have played a crucial role in this research, and I cannot thank them enough. Their feedback have given a different and more meaningful perspective which helped in shaping this thesis.

I am sincerely grateful to Prof. Ramesh Agrawal Sir, JNU, my mentor, for his unwavering support and guidance throughout my Ph.D. journey. His patience, encouragement, and insightful advice have been truly invaluable. Sir, your belief in me, even during the most challenging times, has been a constant source of motivation. Your wisdom and mentorship have not only helped me complete this research but have also shaped me both academically and personally. I am incredibly fortunate to have had you as my mentor, and I will always cherish the lessons and values you have imparted. Thank you, Sir, for everything!

This journey would not have been possible without the immense support of my family, friends, and colleagues, who stood by me during the highs and lows. Maa, Papa, Mumma, and Papa, no words can truly express my gratitude for the countless prayers, sacrifices, and endless encouragement you have given me to help me grow in my career. Your love has been my greatest strength. My sister Shakshi and my brother Avi have been my constant sources of motivation, joy and strength. They both with their optimism and constant support, has been someone I could always rely on, no matter the situation. I looked up to them for so many things, and they were always there for me, ALWAYS!.

To my dear husband, Sunil, you have been my pillar through this journey, playing so many roles—my counselor, my patient listener, my guiding light, and my constant support in both Ph.D. and non-Ph.D. challenges. Your steadfast belief in me, through both successes and setbacks, has kept me going, and I am forever grateful for your love and companionship.

The true strength behind my PhD journey has been my beloved daughter, Harsha, whose innocent yet persistent question, "Mumma, when will your PhD be over?" echoed throughout this endeavor. Her longing to sleep beside me each night remained unfulfilled, as those quiet hours were the only time I could devote to my studies. Though I could never fully satisfy her yearning for my presence, her patience, love, and unspoken sacrifices became the silent motivation that carried me through. Beta, "This achievement is as much yours as it is mine".

I am deeply grateful to my dear friends Sumedha, Payal, Vidisha, Kavinder, Dhirendra, Anshul, Pooja, Parul, Shilpa mam, Anjana Mam, Dinesh Chautani sir, Heena for their endless love, support, encouragement, and for making this adventurous Ph.D. journey so special and full of cherished memories.

To everyone who has contributed and blessed me grow — academically, professionally, and personally, THANK YOU. This thesis is not just a culmination of my research but a reflection of the collective support and inspiration I have received along the way.

Date: 05/08/2025 **(Trasha Gupta)**
Place: Delhi

ABSTRACT

Attitude towards quality of life in the current century is unhealthy, resulting in several diseases. Consequently, life expectancy has significantly declined since 2000. Various medical imaging procedures like X-rays, Magnetic Resonance Imaging, Ultra-Sonography, etc., in combination with pathological tests form the basis for all medical conclusions. However, these imaging procedures are invasive in nature, require specialized radiologists, and not accessible to the populace. Hence, Thermography-based technology is proposed in this thesis for screening and diagnosing abnormality/inflammation in human body. Medical thermal imaging is unique in its potential to demonstrate the physiological change and metabolic processes in a human body through thermal patterns radiated by it. Thermal imaging technology accompanied with robust and automated computational-aided diagnostic systems can be deployed at public gathering locations (like malls, hospitals, etc.) and on smartphones to timely detect and warn about potential health issues of their body caused by inflammation.

Thermography-based cameras have shown their efficacy during the recently seen pandemic time in screening the physical behavior of the human body and reporting unhealthy individuals instantly. Furthermore, improper use of Thermography-based technology may result in wrong temperature readings due to their low resolution. This thesis have examined its potential in conjunction with Machine and Deep Learning techniques for identifying inflammation in the human body as a classification problem. We have proposed two statistical models aimed at differentiating normal and abnormal thermal patterns in medical thermal imaging. The first model utilizes a novel of asymmetry-based features extracted from three publicly available datasets, focusing on detecting abnormalities related to breast cancer, diabetes, and thyroid disorders. The second model systematically evaluates the performance of this proposed feature set in comparison with eight state-of-the-art feature extraction techniques, establishing a standardized methodology for analyzing medical thermal images. To ensure unbiased evaluation, a two-level sampling strategy was employed to address dataset imbalance, and cross-validation techniques. A lightweight deep learning-based classification model designed for mobile deployment is presented to detect and characterize abnormalities caused by inflammation in human thermal images.

In the context of medical thermal image segmentation, we present two novel density-based modified P_CFS techniques, - DSIFC-P_cFS and DSIMFC-P_cFS, for segmenting inflamed regions in abnormal thermal images. The limitations of existing segmentation models include reliance on private datasets with limited samples, subjectivity in ground truth generation, and sensitivity to parameter selection, thereby the proposed methods aim to improve robustness, accuracy, and reliability in medical thermal image analysis. The first model (DSIFC-P_CFS) uses a density-based heuristic to automatically determine cluster centers and membership values. Furthermore, spatial information is integrated into the model to reduce sensitivity to noise and preserve fine image structures without requiring prior smoothing. The second model (DSIMFC-P_CFS) further refines clustering by incorporating modified Renyi's entropy to improve segmentation accuracy and optimize cluster partitions. The models are optimized using Lagrangian methods and validated on thermal imaging datasets covering diabetic foot, breast cancer, and thyroid disorders, with and without artificial noise (Gaussian, Salt & Pepper, and Mixed Noise).

We evaluated the performance of all developed methods using publicly available medical thermal imaging datasets through both visual and quantitative assessments. Additionally, we compared their performance with well-established and state-of-the-art algorithms. Statistical analysis was conducted using paired T-Test and Friedman Test, demonstrating the superiority of the proposed methods over existing state-of-the-art algorithms in classification and segmentation tasks. Overall the findings establish a strong foundation for future research in automated thermography-based diagnostic systems, particularly for early disease detection in real-world clinical settings.

Table of Contents

List of Tables

List of Figures

Chapter 1

Introduction

The lifestyle led by today's generation and its negligence towards health is highly susceptible to various diseases like Cancer, Cardiovascular Disease, Diabetes, Thyroid, etc. Additionally, late-stage presentation and limited access to diagnosis and treatment contribute equally to increase in mortality rates, especially in developing nations, where access to advanced diagnostic healthcare infrastructure, is challenging[1]. For instance, a 2018 report of Breast Cancer statistics recorded 1,62,468 new registered cases and 87,090 reported deaths[2]. The survival rates of breast cancer in India are low as the detection takes place late. More than 50% of breast cancer patients in India suffering from stages 3 and 4, where the chances of survival are incredibly low[3].

Medical imaging procedures like X-rays, Magnetic Resonance Imaging (MRI), Ultra-Sonography (USG), Endoscopy, Tactile Imaging (TI), and Computerized Tomography Scan (CT Scan) are available for the diagnosis of diseases. In fact, these procedures in combination with pathological tests form the basis for all medical conclusions. However, these imaging procedures are invasive in nature, require specialized radiologists, and not accessible to the populace[1, 2]. Also, these devices require unique installation and follow a complicated process, limiting the number of possible tests per equipment. Therefore, an adjunct modality for screening human body[4], Digital Infrared Thermal Imaging technology (DITI) (also called as Thermography-based technology), is proposed in this thesis for screening and

---

[1] https://www.who.int/news/item/13-12-2019-world-bank-and-who-half-the-world-lacks-access-to-essential-health-services-100-million-still-pushed-into-extreme-poverty-because-of-health-expenses

[2] https://cytecare.com/blog/breast-cancer/statistics-of-breast-cancer/

[3] https://www.oncostem.com/blog/alarming-facts-about-breast-cancer-in-india/

[4] https://www.fda.gov/consumers/consumer-updates/breast-cancer-screening-thermogram-no-substitute-mammogram

diagnosing abnormality/inflammation in human body. Recently, Thermography based cameras have been deployed around the world[5] at various organizations and public gathering points as a first measure of screening COVID-19 patients and reporting unhealthy individuals instantly [3, 4, 5, 6]. But due to low resolution of thermal cameras and human intervention in the procedure, they resulted in poor performance.

This chapter introduces DITI as potential modality for screening abnormality in human body and describes the related datasets and its pre-processing steps used for the study. Further, this chapter discusses the challenges, significance, and contribution of this research. The organization of thesis is elaborated in section 1.4.

1.1 Thermography Based Imaging

Fundamentally, any black body continuously emits infrared radiation, with the emitted energy directly related to its temperature, as described by the Stefan–Boltzmann law[7, 8]. The thermographic sensitive camera accurately captures this information and then directly transforms into corresponding temperature values through this law, enabling precise thermal analysis. The Figure 1.1 illustrates a representation of a breast thermal image as a gray-scale image along with its temperature file.

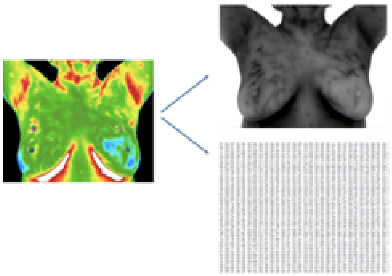

Fig. 1.1: Thermal Image representation as gray-scale image along with its temperature file.

Thermography-based imaging for human body provides its biological and functional assessment. It captures physical indicators of abnormal activity within the vascular system, sensory system, or sympathetic nervous system [9]. The research work [9] explored the correlation between thermographic findings and breast cancer diagnosis.

---

[5] https://www.fda.gov/medical-devices/general-hospital-devices-and-supplies/thermal-imaging-systems-infrared-thermographic-systems-thermal-imaging-cameras

Any disease in the human body leads to inflammatory activities (indicated by Erythrocyte Sedimentation Rate (ESR) pathological test[10, 11, 12]). These activities cause intense thermal patterns radiated by the corresponding body part[13, 14]. Thermography-based cameras capture these thermal patterns and use them as markers for identifying the abnormal regions [15, 13, 16, 17].

Thermography-based technology is an human and environment-friendly approach of screening abnormality in human bodies. It is simple, non-invasive, cost-wise appropriate, painless, contact-less, and portable modality[18, 19]. This technology is instant, human-friendly, and straightforward to use for individuals of all age groups. Thermography-based imaging systems requires very little equipment for deployment and use, especially in rural areas with limited power facilities. The figure 1.2[6] illustrates the ease in setup and capturing thermal images.

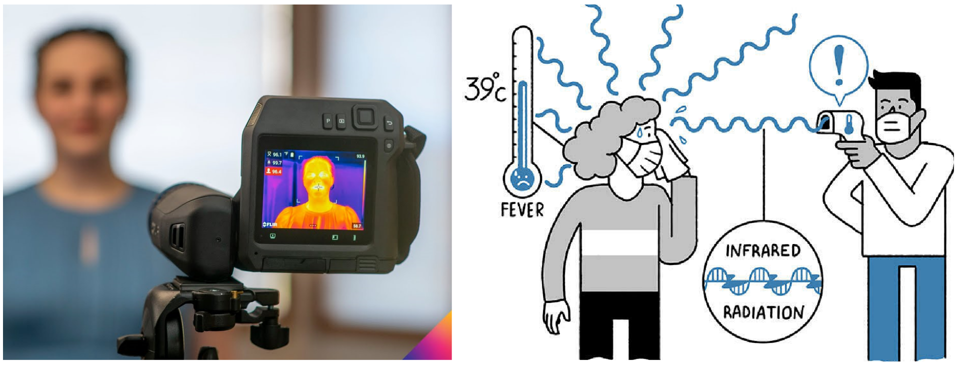

Fig. 1.2: Illustration of setup and capturing thermal images.

Considering the Sustainable Development Goals (SDGs), thermography-based screening contributes both directly and indirectly to multiple SDGs, particularly those related to health. The SDG-3 emphasizes the goal of *"Ensuring healthy lives and promoting well-being for all at all ages."*. The integration of thermal cameras with automated Computational Intelligence-Aided Diagnostic Systems can be implemented in public gathering spaces to detect potential diseases caused by inflammation. This approach shall strengthen healthcare systems while offering a solution that is both human- and environmentally-friendly.

---

[6] https://www.fda.gov/medical-devices/general-hospital-devices-and-supplies/thermal-imaging-systems-infrared-thermographic-systems-thermal-imaging-cameras

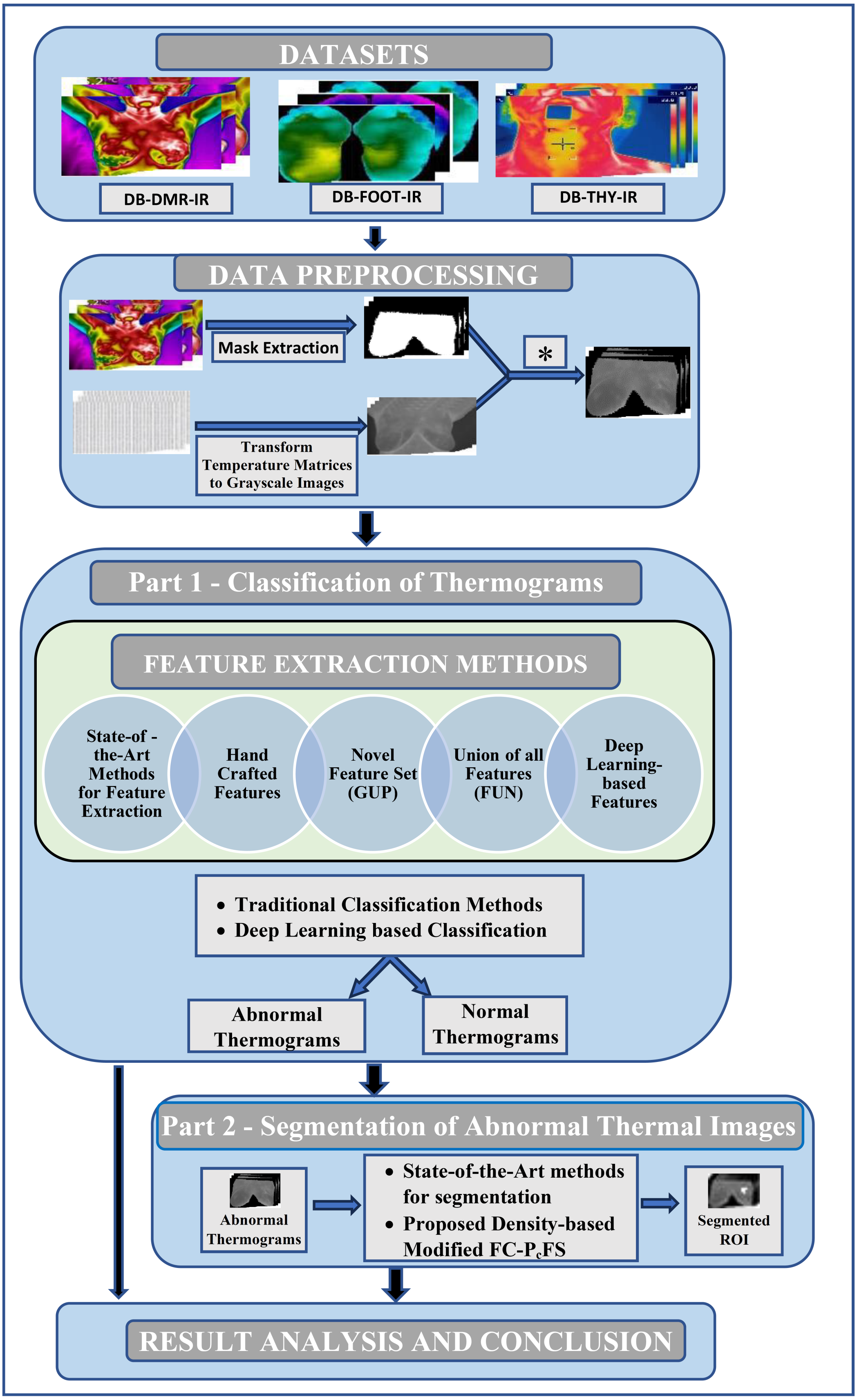

Fig. 1.3: The graphical abstract of the methodology followed in the thesis.

1.2 Problem Statement

Thermal imaging technology offers several advantages over other medical modalities, as it effectively captures inflammation and abnormalities in the human body. However, thermal images generally have lower resolution and are highly susceptible to inevitable environmental noise during capture. To address these challenges, thermal cameras integrated with robust and automated Computational Intelligence-Aided Diagnostic Systems can be developed for deploying in public spaces to detect and alert individuals to potential diseases caused by inflammation, thereby enhancing healthcare systems.

In view of this objective, we evaluated existing feature extraction methods for analyzing thermal patterns on a uniform platform using publicly available datasets. We then proposed a refined feature set comprising relevant and non-redundant features for distinguishing thermal patterns. Additionally, we developed lightweight deep learning-based features capable of differentiating abnormal thermal patterns from normal ones, making them suitable for deployment on mobile devices.

Furthermore, we designed a pre-processing framework for thermal images and introduced two robust picture fuzzy clustering-based methods for segmenting inflamed regions. Figure 1.3 presents the graphical abstract of the methodology adopted in this thesis. All results were statistically analyzed and validated. Our proposed algorithms demonstrated improved performance compared to existing methods for screening and diagnosing inflammation in the human body.

1.2.1 Dataset Description and its Pre-Processing

The experiments are conducted using three publicly available thermography based datasets- **DB-DMR-IR**[7] dataset [20], **DB-FOOT-IR**[21] and **DB-THY-IR**[8] [22]. Figure 1.4 exemplifies the normal and abnormal subjects (in RGB and normalized gray-scale format) for breast cancer, diabetes and thyroid cancer.

Following describes the pre-processing steps of the three datasets used:

- **DB-DMR-IR and DB-THY-IR** - The authors [20, 22] used both static and dynamic acquisition protocol. They used an environment with a temperature range of 20 – 24°C to cool the patient's relevant region, followed by image capturing using a FLIR thermal camera (model SC620). The patients were directed to relax for 15-20 minutes before capturing images to minimize

---

[7] http://visual.ic.uff.br/dmi/

[8] http://visual.ic.uff.br/thyroid/pt/

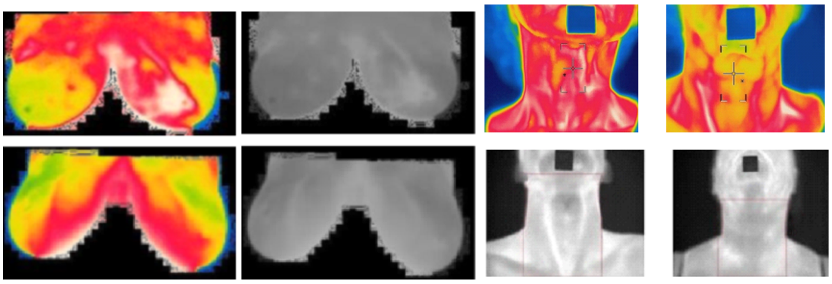

(a) Breast Cancer gray-scale and Thermal Images

(b) Thyroid Cancer gray-scale and Thermal Images

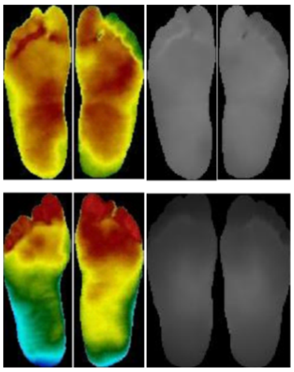

(c) Diabetic Feet Ulcer gray-scale and Thermal Images

Fig. 1.4: Example of abnormal and normal Thermograms for various diseases.

the possible displacements of glands and attain thermal equilibrium. They acquired 20 Infrared images of dimensions 640 X 480 for a duration of five minutes for each patient. The thermal images taken last in the sequence are used in the experiments. The corresponding temperature matrices were available in both datasets. The medical and demo graphical history of the patients is also available[78]. BIRADS-related information is not present for the DB-DMR-IR database.

- **DB-FOOT-IR** - The authors [21] acquired images using a FLIR Thermal camera (model FLIR E60). During the acquisition, the camera's position was placed at a distance of one meter from the feet. The participants were directed to clean their feet with a damp towel and then relax in a room with a temperature of 20 - 22°C for 15 minutes before capturing images to reach a state of thermal equilibrium. The corresponding temperature matrices were also available with the images.

Relaxing for 15-30 minutes before capturing images helps achieve a state of thermal equilibrium in the body. This helps in developing a robust application and eliminates any temperature variation. The experiments considered images acquired after achieving the body's thermal equilibrium. The acquired thermal images are pseudo-colored/false-colored and can not be used directly. Also, thermography-based applications use thermal images transformed to corresponding temperature matrices. In all the datasets, the temperature matrices are available along with the images. The temperature matrices are normalized, assuming the human body's minimum and maximum temperature to be 20° C and 45°C, respectively, and transformed into corresponding gray-scale images in the range [0-255] for experiments and visualization purposes using the equation -

$$I = (T - 20)\frac{255}{45 - 20} \tag{1.1}$$

where T denotes the temperature matrix, and I is the corresponding transformed gray-scale image. The Region of Interest (ROI) was cropped from the transformed gray-scale images, removing the background and other irrelevant body parts using MATLAB's utility *impoly*. All the images in a dataset were resized to a uniform size to eliminate any non-uniformity in images due to variations in human body sizes.

1.3 Main Contributions of the Thesis

The main contributions of this research are the models development for classifying medical thermal images as Normal/Abnormal and segmenting the inflamed regions from abnormal thermal images.

1.3.1 Statistical Indicators for Thermal Pattern Differentiation

There does not exist an experimental comparison of the state-of-the-art feature extraction methods on a platform using a common dataset, classifier, or cross validation/ sampling strategy. Hence, it is not appropriate to comment on the suitability of a feature extraction method for diagnosing abnormality/inflammation in the human body using Thermography.

- A novel set of hand-crafted features are developed and extracted for temperature's asymmetry analysis in publicly available medical thermal imaging datasets.

- Then, eight state-of-the-art feature extraction methods[23, 2, 24, 25, 26, 27, 15, 28] alongside the proposed feature extraction method is statistically compared and analyzed the performance to distinguish an abnormal thermal image from a normal one on a uniform platform.
- We developed a unified model, comprising of relevant and non-redundant features (UnionFeature_Set), capable of identifying abnormal thermal patterns due to inflammation caused by diseases and captured by a thermal cameras.
- The above objectives are investigated using four well-known feature selection methods to select relevant features from the ten features-sets. Also, the four well-known classifiers are used for a fair performance comparison of the selected set of relevant features. We used three publicly available datasets of Medical Thermal Imaging for the entire investigation, having different diseases. The publicly available datasets are skewed (i.e. difference in classes frequency in the dataset is high), so a 2-level sampling strategy is developed and used to conduct the experiments.

1.3.2 Deep Learning-based Thermal Biomarker Analysis

A lightweight deep learning-based model for classifying thermal images as Normal/Abnormal is developed making it appropriate for deploying on mobile devices for ease of human use.

- UnionFeature_Set and various hand-crafted and Deep Learning-based feature-sets are extracted from two thermal imaging based datasets and their performance is compared using four state-of-the-art classifiers and 10-fold cross validation sampling strategy.
- Light weight pre-trained Deep Learning models are proposed to characterize and classify abnormal patterns in medical thermal images.

1.3.3 Framework for Inflamed Region Segmentation

Limited work is done towards segmentation of affected regions in the diseased human body's thermal images ([15, 29, 30, 31, 32, 33, 34, 35, 36]). Also, most of the segmentation models proposed are evaluated on private datasets having fewer samples which is not available for further consideration and analysis by the research community. Hence, the performances obtained are not reputable. In this regard, following contributions are made in the thesis:

1. Two robust Density-based Picture Fuzzy clustering models with spatial information, are proposed, to segment the affected regions/hotspots from abnormal thermal images. Hyper-parameters are automatically initialized using a density-based heuristic, requiring minimum hyper-parameter tuning. Incorporating Spatial information in the model has eliminated the requisite of smoothing the thermal image and retained fine image structures.
2. The optimization problem is formulated by combining Density-based P_cFS method with regularized and modified Renyi's Entropy to obtain a good partition matrix and appropriate number of clusters. The complete optimization problem is solved using Lagrangian method of multiplier [37] and obtained their cluster prototypes.
3. The robustness of the proposed segmentation methods is validated statistically over other methods using the Friedman Test. Also, the time complexity is investigated in comparison to other related methods.
4. Research has yet to give a course to develop a robust segmentation method for analyzing and segmenting noisy and low-resolution human thermal images. To address this research gap, a separate dataset - DB-NOISE-IR, is created, wherein three types of artificial noise - Salt and Pepper Noise, Gaussian Noise, and Mixed Noise are introduced. We thoroughly performed the comparative performance analysis of our method with that of other methods. We found that the our methods have performed significantly better particularly for the noisy dataset.

1.4 Organization of the Thesis

The content of this thesis is systematically organized as follows. The **chapter 2** discusses the existing approaches related to classification of the medical thermal images using traditional Machine Learning and Deep Learning methods. Also, it compares the existing techniques for segmentation of inflamed regions from thermal images. It also finds the research objectives.

Rest of the thesis is divided in two parts (Figure 1.3)- Part 1 covers the Classification of thermal images as Normal/Abnormal in **chapter 3** and **chapter 4** and

Part 2 covers the segmentation framework of abnormal thermal images using Picture Fuzzy clustering approach in **Chapter 5**. Further, the **chapter 6** presents important conclusions drawn from the proposed work and it also gives the details of future works/applications for thermal images in medical domain.

Chapter 2

Literature Review

This chapter conducts a thorough and systematic review of state-of-the-art methods for feature extraction, classification, and hot-spot segmentation in medical thermal imaging for various diseases using traditional Machine and Deep Learning approaches, while also highlighting their limitations. The chapter includes discussion of merits and demerits of existing methods and finally proposes the research objectives for the thesis.

2.1 Background on Medical Thermal Imaging

Researchers have thoroughly investigated the capability of Thermal Imaging complemented with Computer-Aided Diagnosis (CAD) for detecting/screening various diseases like breast cancer, skin cancer, arthritis, cardiovascular diseases, ulcers, and diabetes [38, 39, 40, 41, 42, 43] as a classification problem. Digital Infrared technology evolved during 1900-1920. It was first used and documented in medical research for examining breast cancer in 1956 [44]. He discovered that cancerous tissues lay higher temperature on the skin surface than non-cancerous ones. In the early '70s, a mass-ranging study, breast cancer Detection and Demonstration Project (BCDDP), was conducted in the United States to evaluate thermography's diagnostic ability for breast cancer. However, poor study design, lack of trained technicians, and unsuitable environmental controls and protocols led to the failure of the project [16, 45].

The research work [46] presented a study on 85,000 subjects with 90% sensitivity and 88% specificity. In their investigation, to attain thermal equilibrium, they included two cooling mechanisms- fan and ice water. This methodology decreased the false-positive rate by 3.5%, leading to 96.5% sensitivity. The potential of thermography has also been studied concerning inflammatory pain[47, 48]. The works [49, 50] employed an Otsu thresholding technique to segment the thyroid-based ROI from its thermal images.

Research studies have established a direct correlation between increasing temperature and foot complications in individuals with diabetes [51, 52]. Notably, temperature elevation can occur up to a week before the development of a foot ulcer [53]. Additionally, [54] explored the potential of thermography for home monitoring and the early detection of warning signs of abnormalities. Researchers claimed that being a contactless and user-friendly technology, thermography offers a convenient solution for at-home monitoring.

2.2 Traditional Machine Learning Methods for Thermal Pattern Analysis

This section reviews the related work for classifying inflammation in medical thermal images using traditional Machine Learning approaches. The method proposed in the research work [23] extracted 37 asymmetry-based descriptors from a skewed and private dataset of 146 breast thermal images (29 malignant and 117 benign) and classified them using a fuzzy classifier. A classification accuracy of 79.53% was obtained with 14 fuzzy partitions per attribute on the test dataset.

The research work [55] used Hough transform to automatically segment left and right breasts and performed an asymmetry-based analysis using first-order statistics on a small dataset of 6 normal and 18 cancerous thermal images. They concluded that higher-order statistics detect asymmetry effectively. Texture-based features [2], were extracted from Gray Level Co-occurrence Matrix (GLCM) and Gray Level Run Length Matrix (GLRLM) of breast thermal images. These features were extracted from 50 samples and fed to the Support Vector Machine (SVM) classifier with a 3-fold cross validation sampling approach. The proposed system produced an accuracy of 88.10%, sensitivity, and specificity of 85.71% and 90.48%, respectively, on their private dataset.

The research work [24] proposed 11 energy-based features for asymmetry analysis. They computed features from modified Local Binary Pattern (LBP) Colour and Edge matrices. These matrices were computed from gray-scale images of left and right breasts. They used a heterogeneous dataset of 65 breast thermography images and classified the extracted features using Hidden Markov Model (HMM) Classifier. They achieved an accuracy of 93.75%. The research work [25] extracted 144 features from Wavelet Transform of normalized and segmented temperature matrices of breast thermal images. Then asymmetry-based features were computed from the local energy matrices for 24 sub-bands. They used a publicly available DB-DMR-IR dataset [20] with 100 frontal views of static breast thermal images. Then they used Random Subspace Feature selection (RSFS) for selecting relevant features, followed by 5-fold cross validation with SVM using Gaussian Kernel. They achieved an accuracy of 91%.

The research work [56] extracted asymmetry based 24 discriminating features - 7 statistical and 17 texture features from two datasets (DBT-TU-JU, a private dataset and DB-DMR-IR dataset [20]). Then, Mann-Whitney-Wilcoxon statistical test was used to select significant features (with $p \leq 0.05$). The authors used six classifiers to detect thermography-based breast irregularity for efficient diagnosis. The results showed that Artificial Neural Network and SVM classifiers provided the best accuracy of 87.50$\%$ for the DB-DMR-IR database and 84.29$\%$ for the DBT-TU-JU dataset. The research works [57, 28] applied Curvelet Transform to segment a breast thermal image and extract GLCM-based features. [57] obtained an accuracy rate of 90.91$\%$ with SVM classifier and Gaussian kernel with Leave-one-Out Cross Validation (LOOCV). An accuracy of 93.33$\%$ using SVM with 20-fold cross validation was obtained[28].

The authors [58] used thermography complemented with other imaging modalities to diagnose thyroid-related problems. The authors in the research work [15] analyzed Rheumatoid Arthritis disease. They extracted texture-based features from the knee thermograms and inflamed ROIs. They obtained an accuracy of 73$\%$ using SVM with 3-fold cross validation.

The research work [59] performed experiments on average temperatures values for neuropathy patients Vs. diabetic patients without neuropathy. They concluded that the former has a higher average temperature than the latter. A study [41, 60] also confirmed the above remark that diabetic neuropathy patients' foot temperatures were significantly higher than that of subjects without neuropathy. Infrared thermography has been successfully used to detect complications like foot ulcers related to diabetic feet.

The authors [27] extracted asymmetric 12 texture and 2 temperature-based features from 11 ROIs, which are prone to ulceration in both left and right foot, thermal images, and temperature profiles of 60 subjects. They performed an asymmetry-based analysis between the ipsi-lateral and contra-lateral regions of the foot. The features are classified into normal and ulcerated using SVM classifier with an ac-

Table 2.1: The State-Of-The-Art research work for classifying abnormality in thermal images using traditional Machine Learning Approaches.

Reference	Number of features	Features Description	Dataset and Disease Considered	Feature Selection	Classifier	Metrics and Result on Test data
[23] **(SCH)**	37	Features were computed from polar coordinate representation of left and bright gray-scale images - Mean, Standard Deviation, Median, 90-Percentile, Moments m01 and m10, Centre of Gravity (CoG), Distance between CoG and Geometrical Centre, Cross-Correlation, Difference Histogram, Absolute Value of its Maximum, Number of Bins Exceeding 0.01, number of zero crossings, energy, difference of positive and negative (from Normalised Histograms) Homogeneity, Energy, Contrast, Symmetry (from Gray Level Cross Co-occurrence Matrix), Difference of absolute values, Distance of difference maximum from the centre (from Fourier Spectrum of left and right breast), Mutual Information, Cross Co-occurrence Features, Mutual Information, Fourier Descriptors from the Laplace filter applied images	Breast Cancer analysis - Private Dataset - 146 cases (29 Malignant, 117 Benign)	-	10-fold cross validation with Fuzzy Classifier (14 fuzzy partitions) using KEEL software	Acc - 79.53, Sens - 79.86, Spec- 79.49
[2] **(ACH)**	16	Texture-based analysis - Features from Normalized GLCM and GLRLM (in directions $\theta = 0°$, 45°, 90° and 135°) were computed - Homogeneity, Energy, Entropy, Moment 1, Moment 2, Moment 3, Moment 4, Entropy, Angular Second Moment, Contrast, Mean, Short Runs Emphasis, Long Runs Emphasis, Run Percentage, Gray Level Non-Uniformity, and Run Length Non-Uniformity	Breast Cancer analysis - Private Dataset - 50 cases (25 Normal , 25 Malignant (15 patients had stage III cancer and rest had stage II cancer)	selected with p-Values (≤ 0.05)	3-fold stratified cross validation using SVM	Acc - 85.71, AUC-88.10, Sens - 85.71, Spec - 90.48
[24] **(RAS)**	11	Asymmetry-based analysis - Modified LBP Colour and Edge matrices were computed using Clique Matrices from gray-scale images of left and right breast - Tsallis-Entropy, GLCM-based Energy, Difference between Co-occurrence levels-based energy, Euclidean distance of histograms, sum (from Modified LBP Colour and Edge matrices), Difference of GLCM Matrices(4 different directions 0°, 45°, 90° and 135°)	Breast Cancer analysis - Private Dataset - 65 breast thermography images collected heterogeneously (40 Malignant and 25 Normal)	-	HMM Classifier with LOO cross validation	Acc - 93.75, Sens - 95.00, Spec - 92.00
[25] **(SAT)**	144	Asymmetry-based analysis - Temperature matrices of the corresponding breast thermogram were normalized and segmented automatically into left and right breast. The Discrete Wavelet Transform was applied using different digital filters (Daubechies-1, Daubechies-10, Coiflet-1, Coiflet-5, Symlet-2, and Symlet-8) at different scales. Asymmetry based Features were computed from the Local energy matrices, calculated for 24 sub-bands - Energy, Mean, Variance, Skewness, Kurtosis, Entropy (from Local energy matrices, calculated for 24 sub-bands)	Breast Cancer analysis - DB-DMR-IR Dataset -100 frontal view static breast thermogram (47 abnormal, 53 normal)	RSFS Method - 33 features were selected	5-fold cross validation with SVM using Gaussian Kernel	Acc - 91, Sens - 87.23, Spec - 94.34
[26] **(CRZ)**	5	Texture based analysis - 5 features - number of pixels, mean value, variance, maximum entropy and index value - are extracted from automatically segmented ROI using threshold values (up to 4) optimized by the Differential Evolutionary method (by maximizing the total fuzzy entropy measure)	Diabetic Foot Plantar analysis - DB-Foot-Plantar Database - 167 samples (122- Abnormal and 45 Normal)	-	10-fold cross validation with SVM using Linear Kernel	Acc - 99.2857
[27] **(SAM)**	14	Asymmetry Based analysis- 2 Statistical features were extracted from segmented temperature profiles - Mean temperature and Standard Deviation of temperature. 12 Haralick's Texture based features were extracted from normalized GLCM (in direction 0) of the same segmented grayscale images - Auto Correlation, Contrast, Correlation, Dissimilarity, Energy, Entropy, Homogeneity, Maximum Probability, Sum of Squares- Variance, Sum Average, Sum Variance, Sum Entropy	Diabetic Foot analysis - Private dataset - 660 samples (60 subjects * 11 ROI samples from each subject) (264 Normal and 396 Abnormal samples)	-	SVM with (140 samples for training and 520 samples for Testing)	Acc-95.61, Sens-96.5, Spec-92.41
[15] **(BAR)**	119	Texture Based analysis - Various Texture based Features were extracted from Knee thermogram and inflamed ROI automatically segmented from Knee Thermogram - First order statistical features (Mean, variance, median, mode, skewness, kurtosis, energy, entropy, standard deviation), 13 Haralick features from each of Mean and difference based (energy, contrast, correlation, variance, homogeneity, sum average, sum of variance, sum entropy, entropy, difference variance, difference entropy, information measures of correlation (from x axis and y axis individually), Gray level difference statistics based features (Homogeneity, contrast, energy, entropy, mean), Neighbourhood Gray-tone Difference matrix based features (Coarseness, contrast, busyness, complexity, texture strength), Statistical feature matrix based features (Coarseness, contrast, periodicity, regularity/roughness), Texture energy measure (Texture energy using LL, EE,SS, LE,ES, LS kernel), Frequency level features from Fourier power spectrum(Radial sum, angular sum) and shape based features (Area, Euler number, perimeter, convexity, eccentricity, orientation, solidity	Rheumatoid Arthritis - Private Dataset - 110 samples of Knee thermograms (60 samples with Arthritis and 50 samples from Control group)	Accuracy based selection of Feature groups - 6 feature groups (50 features)	3-fold cross validation with SVM	Acc - 73
[28] **(KAR)**	20	Texture based analysis - Images are semi-automatically segmented and enhanced using morphological operators. Then three sets of features (GLCM-based, regional-based, and Statistics based) are extracted from curvelet Transformed images - Contrast, Correlation, Energy, Homogeneity, Area, Major Axis Length, Minor Axis Length, Eccentricity, Orientation, EquivDiameter, Perimeter, Min Value, Max Value, Skewness, Kurtosis Norm Value Mean, Variance, Median, Entropy	Breast Cancer analysis - Private Dataset - 60 samples (30 positive and 30 negative samples)	P-Test with 5% level of significance - 16 Features	20-fold cross validation with SVM (cubic kernel)	Acc- 93.33

curacy of 95.61%, sensitivity of 96.5%, and specificity of 92.41%. In most diabetic patients, symptoms of ulcers are not observed until the ulcer is infected [61, 62].

Table 2.1 summarizes the research work done to diagnose abnormality/inflammation due to various diseases using thermography. The table lists the datasets used, the classification model, and the best results obtained in the respective papers.

2.3 Deep Learning-based Thermal Image Analysis

This section reviews the related research work concerning the classification and segmentation of inflammation in medical thermal images using Deep Learning approaches. The authors [63] addressed the problem of sinusitis detection using thermal images with the help of an enhanced Deep Learning-based approach. They used 1080 face thermal images. They used the InceptionV3 model to classify the data into four classes - normal, unilateral left and right maxillary sinusitis and bilateral maxillary sinusitis. They obtained an accuracy of 99.5% with 99% as sensitivity.

The research work [64] classified abnormal breast cancer thermal images using deep learning in two phases. In the first phase, they automatically segmented the breast region using U-Net architecture. They designed their network for breast cancer thermal image classification in the second phase. They employed 1000 images of DB-DMR-IR dataset and obtained an accuracy of 99.33% using Adaptive Moment Estimation Optimizer.

The authors [65] used enhanced deep convolutional neural networks for the prognosis of breast cancer. They used 1000 samples from DB-DMR-IR dataset and achieved an accuracy of 96.8%. In the research work [66], the authors diagnosed the fatty liver problem using machine learning and deep learning techniques. They investigated 123 Normal and 44 Abnormal thermal images from 32 volunteers and obtained an accuracy of 94% using features extracted from Inception-ResNet-v2 architecture and a fully connected layer classifier.

The authors [67] explored Vision transformer-based models to detect inflammation in the joints using thermal imaging. They used 600 thermal images of hands. The proposed method classified the healthy and arthritis patients with an accuracy of 90%. The research work [68] collected RGB and thermal images from 270 participants and identified 225 as abnormal and the rest as normal. They employed EfficientNetb3-UNet model to classify active diabetic foot ulcers and obtained an F1 score of 0.79.

The research work [69] investigated deep learning approaches for classifying breast tumors using thermal images. They proposed Mask Region Based Convolution Neural Network (MR-CNN) architecture along with transfer learning models for breast tumour diagnosis. For transfer learning, they used ResNet-50 and ResNet-101. In their work, they used breast images of 56 women (19 normal and 37 abnormal) and obtained %97.1 as the accuracy on the test dataset with ResNet-50. However, the model used could be lighter and appropriate for mobile devices.

The authors [70] used a thermal imaging dataset of 41 cancerous and 155 healthy participants for classification using autoencoders. They obtained a performance of 94.87% as accuracy, 87.5% as sensitivity and 96.77% as specificity. The authors[43] employed deep learning approaches to precisely locate and segment the region for massage during physiotherapy, enhancing musculoskeletal healthcare.

The authors[71] proposed to combine multiple views of the breast from different angles for a given subject. They use transfer learning using architectures - DenseNet121, EfficientNetB0 and VGG19 to classify the subject as normal/ abnormal. They obtained an accuracy of 93% using VGG16 model. The research work [72] proposed a two-stage approach for breast cancer detection. They used VGG16 architecture to extract the features and then selected the subset of features using the Grunwald–Letnikov Dragonfly Algorithm. They finally used the SVM classifier on the DB-DMR-IR dataset, having 900 thermal images, 596 abnormal and 304 normal. They achieved an ideal performance.

2.4 Related Work on Image Segmentation

Image segmentation forms an integral part of precise medical image analysis. Image segmentation techniques/methods can be broadly classified/categorized as Threshold-based techniques[73, 74], Region-based [75, 76], Clustering-Based [77, 78, 79], Deformable models [80], Semantic Segmentation techniques [81, 82]. Table 2.2 briefly compares the various methods for image segmentation.

Further, clustering-based techniques for image segmentation can be categorized as Partition-based, Density-based, and Hierarchical-based Clustering methods. Centroid-based techniques are one of the most explored Partition-based clustering techniques for medical image segmentation and analysis[83]. K-Means is one of the simplest Centroid-based hard clustering method[84]. The crisp nature of K-Means allows a data point to belong to only one cluster. On the other hand, Fuzzy C-Means (FCM) is a soft clustering method based on fuzzy sets. It allows data points to represent their affinity with all the clusters in the form of membership/belongingness[85, 86]. The concept of Intuitionistic Fuzzy C- Means (IFCM) Clustering Method [87] was introduced, wherein the hesitance degree was merged with FCM. Also, the clustering using Picture Fuzzy Sets (PFS)[88] was introduced in the research works [89, 90], which integrated the refusal degree with Intuitionistic Fuzzy Sets. Picture Fuzzy C- Means (PFCM) is based on PFS. However, these methods require initializing the number of clusters and membership matrices. It is susceptible to this initialization and affected by the noise/outliers present in the data.

Table 2.2: Comparison of various image segmentation techniques

S. No	**Image Segmentation Technique**	**References**	**Advantages**	**Disadvantages**
1.	Thresholding method	[73, 74]	Simple and fast method; Effective for images with uniform and distinct intensity values in a contrasting background; Reduces the impact of noise	Sensitive to threshold values, noise and other artifacts like low resolution, low contrast, shading; Inefficient for multimodal images.
2.	Region-Growing method	[75, 76]	Segmentation performance is better for images with precise edges	Manual interaction to choose the seed points, similarity criterion between pixels; Performance is poor in the presence of noise and other artifacts like low resolution, shading, in-homogeneous lighting, etc.
3.	Deformable model	[80]	Can represent a broad range of shapes and incorporate their constraints; Robust to noise and spurious edges;	Requires manual interaction to choose a tailored model with appropriate specifications, which is computationally intensive.
4.	Semantic Segmentation techniques	[81, 82]	Detailed information like objects labels and associations among them in an image can be extracted; Generates suitable feature representations.	Computationally expensive for high-resolution images; Sensitive to quality and quantity of labeled training data; Model generated may be over-fitted due to tuning of parameters.
5.	Clustering-Based method	[77, 78, 79]	Fast and simple to implement; Labelled data is not required for training	Sensitive to initialization of number of clusters, Vulnerable to outliers and other imaging artifacts

Though the variants of FCM, IFCM, and PFCM ([83, 91, 92, 93, 94, 95, 96]) exist that perform better than FCM, IFCM and PFCM, respectively, but they also fail to produce optimal segmentation in the presence of noise, outliers, and other non-linear structures present in the image[83]. Initializing the membership matrix as the distance between the data points and a cluster centroid may lead to inaccurate results due to the imprecision in capturing the images and defining the initial cluster center points. This poor adaptability is because the algorithms still depend on fuzzy membership degrees.

Table 2.3: The State-Of-The-Art research works for Medical Thermal Image Segmentation.

S. No	Reference	Approach used	Dataset and Disease Considered	Result obtained	Limitation
1.	[30]	Adaptive Thresholding method followed by Level set method	DBT[1](100 Samples) and DMR (240 healthy samples and 47 unhealthy samples)	DBT - [DSC - 0.78 ± 0.004], DMR - [DSC - 0.802 ± 0.004]	Initial placement of contour, embedding of the object and gaps in the boundaries
2.	[31]	Ensemble of various segmentations from a clustering method followed by minimization of information-theoretic measure for consensus Segmentation in the ensemble	Knee-joint Dataset (50 samples)	JI - 0.98	Sensitive to the size of ensemble used
3.	[32]	Modified Region Growing Method along with Entropy parameter	DBT (40 samples), DMR (44 samples), and Knee-joint Dataset (50 samples)	DBT - [JI - 0.68], DMR - [JI - 0.62], Knee-joint Dataset - [JI - 0.80]	Improper selection of threshold may increase over-segmentation and under-segmentation, Manual selection of seed points, Selection of stopping criteria, Noise and intensity in-homogeneity results in holes or over-segmentation
4.	[33]	Thresholding method with Modified Region Shrinking	DMR (44 samples), Knee-joint Dataset (50 samples)	DMR - [DSC - 0.576], Knee-joint Dataset - [DSC - 0.805]	Selection of threshold value and stopping criteria, Not considered the spatial details, Improper selection of threshold may increase over-segmentation and under-segmentation, Manual selection of seed points, Noise and variation of intensity results in holes or over-segmentation
5.	[36]	Lazy Snapping method	Different human body parts thermal images (39 samples)	Overall Sensitivity - 0.7	Highly sensitive to the initial seed points
6.	[98]	Modified Region Growing Method	DBT (40 samples), DMR (44 samples), and Knee-joint Dataset (50 samples)	DBT - [JI - 0.54, DSC - 0.66], DMR - [JI - 0.56, DSC - 0.69], Knee-joint Dataset - [JI - 0.68, DSC - 0.79]	Improper selection of threshold may increase over-segmentation and under-segmentation, Manual selection of seed points and stopping criteria, Noise and variation of intensity results in holes or over-segmentation
7.	[97]	Thresholding method followed by Morphological analysis	DBT (100 Samples) and DMR (240 healthy samples and 47 unhealthy samples)	DBT - [DSC - 0.84 ± 0.11, JI - 0.86 ± 0.13] DMR - [DSC - 0.70 ± 0.17, JI - 0.56 ± 0.18]	Performance may differ if different palettes of pseudo-colours are used to represent breast thermograms.
8.	[99]	Snakes algorithm followed by FCM	Human plantar surface thermal Images (59 samples)	This approach performed well for all the current images.	Sensitive to initialization of number of clusters, membership matrix, and cluster centers, Selection of parameters (e.g. bandwidth), and Computationally expensive.
9.	[100]	*K*-Means and FCM	Medical thermal Images (6 samples)	FCM performed better and can find the first and the second hottest regions.	Sensitive to initialization of number of clusters and membership matrix and is affected by the noise/outliers present in the data.
10.	[101]	*K*-Means	20 Subjects - 10 subjects suffering from Orofacial Pain and 10 normal subjects	Left and right face profiles gave 3.78 and 3.97% as percentage temperature differences	Sensitive to initialization of number of clusters and membership matrix Selection of parameters (e.g. bandwidth in MS) and is affected by the noise/outliers present in the data.
11.	[102]	Colour-based *K*-Means clustering followed by Statistical features extraction and classification using Quantum-based classifiers like QSVM	Hand thermal images (240 samples - Dorsal and ventral view for both right and left hand of 30 healthy and 30 unhealthy subjects)	QSVM Classification Accuracy - 92.7%	Sensitive to initialization of number of clusters and is affected by the noise/outliers present in the data.

[2]Datasets - DBT - DBT-TU-JU, DMR - DB-DMR-IR[20], Performance Metrics - DSC- Dice Similarity score, JI - Jaccard Index

2.4.1 Segmentation of Medical Thermal Images

The State-of-the-art work done for segmentation of affected regions in diseased human body's thermal images is limited [15, 30, 31, 32, 33, 34, 36]. Table 2.3 briefly states and compares the various state-of-the-art research for segmenting thermal images.

The research work [36] proposed using lazy snapping for segmenting the abnormality from the medical thermal images. The overall sensitivity of the system was 70%. The proposed algorithm is sensitive to the initialization of seed points.

The authors [30] characterized the suspicious regions in the thermal breast images and developed an adaptive thresholding method. For evaluating segmentation of suspicious regions, they obtained the Dice Similarity scores on two datasets - one private dataset (DBT-TU-JU) and one public dataset (DB-DMR-IR [20]) as 0.78 ± 0.004 and 0.80 ± 0.004, respectively.

The authors [97] proposed a novel model to grade the severity of Suspicious Hyperthermic Regions (SHR)in breasts thermal images as mild or severely abnormal. They segmented SHRs from the Intensity Contrast Map (ICM) of the normalized blue channel of the breast's thermal RGB image. Basically, the SHRs contrast with their surrounding regions in color and intensity. The SHRs were partitioned into five levels, each level having intensity values $[(i-1) \times L, (i \times L)-1]$, $L = 50$. Further, the morphology of partitioned SHRs was analyzed using Relative Suspicious Area, Fractal dimension, Convex Area, Area, and Equivalent diameter to grade its severity. They obtained an accuracy of 91% with a sensitivity of 91.30% and specificity of 90.32% for grading the severity of thermograms in the DBT-TU-JU dataset. The method's performance will differ if different pseudo-color palettes are used to represent breast thermograms.

The authors [31] applied a clustering method by varying the number of clusters and generated m segmented thermal images having i segments, $i \in [1, m]$. Then, minimization of the information-theoretic measure was used to fuse information from these segments for consensus segmentation, and finally, the inflamed region from 50 knee thermograms was extracted. They obtained an accuracy of 96.06%. Also, they graded their severity of arthritis using this ensemble method. This method is highly sensitive to the size of the ensemble and clustering methods used. Finally, using its average intensity value, they categorized the extracted inflamed region as mild or moderate.

The research work [32] modified the Region Growing method to extract the inflamed region. They used entropy parameters to overcome the problem of over and under-segmentation. The Region Growing algorithm is applied to the original image and entropy-applied image. Then, the intersection of the two outputs is taken as the actual result. They experimented with their approach on three datasets. They obtained the over-segmentation (O_{seg}) and under-segmentation (U_{seg}) values less than 0.1. They obtained the Jaccard Index of 0.68, 0.62, and 0.80 for DBT-TU-JU, DB-DMR-IR, and Knee-joint Datasets, respectively.

The research work [103] performed a comparative study of the state-of-the-art methods for image segmentation on DB-DMR-IR[20]. They concluded that Particle Swarm Optimization (PSO) algorithm and Multi-Seed Region-Growing technique provided the optimal segmentation results. The authors [34] used Anisotropic Diffusion Filter to remove noise and increase the sharpness of tissue boundaries from the segmented 18 neck thermograms (10 healthy and 8 cancerous cases) for Thyroid cancer assessment. Then, they divided the temperature profile, in the ROI, into five equal intervals between the Maximum and average temperature of the ROI and represented them with a specific color. They found that a rise in local temperature($1°C - 1.5°C$) could be observed as a hot spot, and it interferes with the symmetry of the gland's thermal balance. They concluded that dynamic thermal imaging aided with computer vision techniques stipulate thyroid gland disorders.

The research work [98] also used a similar approach wherein the modified RG method was applied on log-transformed image in place of entropy-applied image. Also, they extended the RG method and defined their Automatic multi-seed selection method wherein the pixels with the highest gray value are selected as the seed points for the first epoch. After i^{th} epoch, pixels with the highest gray values, not included in the first epoch and satisfying the given conditions, are selected. They obtained an accuracy of 98.07% and 96.40% on their private datasets - DBT-TU-JU and Knee-joint datasets, respectively, and 98.25% on the publicly available dataset - DB-DMR-IR[20]. The research work [33] proposed a Region Shrinking-based method using Electrostatic Force Image (EFI) for extracting inflamed regions from medical thermal images. After computing the values of EFI, the intensity values are adjusted. After that, the weighted threshold is generated automatically. Finally, the inflamed region is extracted based on computed thresholds. They experimented with the methodology on their private dataset - Knee-joint dataset, and publicly available dataset - DB-DMR-IR[20]. The average accuracy obtained by the proposed method for both datasets are 98.2% and 96.98%, respectively.

The research work [35] performed segmentation of 4 breast thermograms using various unsupervised methods (Expectation Maximization, FCM, and *K*-Means) and analyzed the result qualitatively. They observed that segmentation output from K-Means resulted in empty clusters, and FCM gave a better indication of the disease. The research work [102] segments the thermal images and then classifies the segmented thermal images as normal or abnormal.

Table 2.3 briefly states and compares the various state-of-the-art research works for segmenting medical thermal images.

2.5 Multi-Modal fusion with Thermal Imaging

This section reviews the related work on the fusion of thermal imaging with other medical imaging modalities. Each imaging technique offers distinct types of diagnostic information for instance MRI reports displays the pathological changes in soft tissues, CT scans reveal dense structures such as bones, and X-rays detects fractures and bone mis-alignments, etc[104]. The authors [105] proposes an innovative Multi-Mode Fused Recursive Neural Network (MMF-RvNN) framework designed to significantly improve early breast cancer detection. The core of this method involves fusing thermal imaging with MRI, enabling the capture of both metabolic and anatomical details of potential tumors. They obtained a high rate of peak signal-to-noise ratio (45.9 dB), structural similarity index measure (0.98), and entropy(8.7) on their private data set of 1522 thermal images and 700 MRI scans[105].

The research work [106] introduces an adaptive multi-modal hybrid model that combines ultrasound and infrared thermal images to classify thyroid nodules. The model extracts features from both image types, fuses them, and achieves high accuracy in distinguishing between benign and malignant nodules. This approach offers a non-invasive, radiation-free, and cost-effective screening tool. On their private data set, their AmmH model achieved an F1 and F2 scores of 97.17% and 97.38%, respectively. The proposed multi-modal model extracts features from various modal images, thereby enhancing the comprehensiveness of thyroid nodules descriptions. The research work[107] integrated infrared thermal imaging with various other modalities of medical imaging intelligent sensing agents such as terahertz imaging. They employed fractional Fourier transform to filter imaging data followed by Laplacian pyramid for image fusion. The authors [108] introduced a method to fuse thermal and visible images. Their objective is to create a single image that benefits from the thermal radiation information of the infrared image and the rich texture details of the visible image. This function ensures the fused image maintains pixel intensity similar to the infrared image and gradient information similar to the visible image.

2.6 Research Gaps

From the discussion in Section 2.2, we found that numerous feature extraction methods have been proposed but not compared with the existing work in the literature. Researchers have claimed the results on their private datasets. To the best of our knowledge, no experimental comparison of the state-of-the-art methods exists on a platform using a common data set, classifier, or cross validation strategy. Also, datasets used for analysis are very small or skewed in most research works. Hence, it is not appropriate to comment on the suitability of a feature extraction method for detecting abnormal thermal patterns due to various diseases.

The deep learning models used to detect abnormality are very heavy, having millions of parameters and are incompatible with mobile devices, requiring less memory- and computation-based models.

In the context of medical thermal image segmentation, the majority of existing models have been evaluated using private datasets with limited sample sizes, which are not accessible to the research community for further validation and analysis. As a result, the reported performance metrics lack reliability and reproducibility. Furthermore, only a limited number of studies have assessed their methodologies on publicly available datasets; however, the corresponding in-house generated ground truth data is often not made available, rendering the results highly subjective. Also, the performance obtained is not satisfactory, suggesting a potential for improvement. To the best of our knowledge, research has yet to give a course to develop a robust segmentation method for analyzing and segmenting noisy and low-resolution human thermal images.

2.7 Proposed Research Objectives

Based on the analysis and discussion of the existing algorithms for feature extraction, classification, and hot-spot segmentation from thermal images, we have formulated the following objectives for the thesis:

- Review and empirical comparison of feature extraction methods proposed in significant literature for analyzing thermal patterns on a uniform platform using publicly available datasets, feature selection mechanism, and classifiers.

- Build novel indicators for differentiating abnormal thermal patterns from normal ones.
- Develop a Deep Learning model that understands thermal biomarkers and differentiates the abnormal thermal patterns from normal ones.
- Build a framework for pre-processing the thermal images and segment the inflamed regions

Chapter 3

Statistical Indicators for Thermal Pattern Differentiation

This chapter introduces two statistical models designed to differentiate between normal and abnormal medical thermal images. The first model employs a set of hand-crafted features extracted from three publicly available medical thermal imaging datasets. The second model systematically evaluates the performance of first model in comparison with state-of-the-art feature extraction methods for analyzing human body thermal patterns. It assesses these approaches individually and in combination on a defined uniform platform, identifying a set of relevant and non-redundant features for distinguishing thermal patterns. The chapter includes experimental results and analysis for both the methods followed by the chapter summary at the end.

3.1 Introduction

The researchers have explored Thermal Imaging based CAD extensively for diagnosing various diseases in the last two decades [16, 40, 36]. Different research works have proposed their features extraction methods for identifying abnormal thermal patterns [109, 25, 24, 15, 27, 26, 28, 23, 2]. Also, researchers have used different classifiers and cross validation strategies to evaluate the proposed model. A few research work [109, 26, 25] have evaluated their method on a publicly available dataset. However, most of them [24, 15, 27, 28, 23, 2] evaluated their proposed features on the respective/private datasets, which is very small in size and not available for further evaluation by the research community.

To the best of our knowledge, no experimental comparison of the state-of-the-art methods exists on a platform using a common dataset, classifier, or cross validation/ sampling strategy. Hence, it is not appropriate to comment on the suitability of a feature extraction method for diagnosing abnormality/inflammation in the human body using Thermography. Also, the guidelines of the U.S. Food and Drug Administration[1] states that there does not exist any valid scientific statement/data that shows thermography to be an effective screening tool for any medical condition, including the early detection of breast cancer or other diseases and health conditions. Driven by this motivation, thermography's effectiveness and feasibility for diagnosing various diseases is assessed. This work proposes a novel set of hand-crafted features extracted from publicly available medical thermal imaging datasets targeted for breast cancer, diabetes, and thyroid cancer detection. In addition, this work systematically compares eight state-of-the-art feature extraction methods alongside the proposed feature-set on a platform using publicly available Datasets, Feature Selection mechanisms, Classifiers, and a 2-level sampling strategy. Thereafter, the union of feature sets proposed in the nine research works is proposed and evaluated on the same platform.

However, the features extracted from the image by a given feature extraction method may contain irrelevant and redundant features. Also, it has been observed that feature selection methods are recommended when the dataset size (i.e. the number of instances) is smaller than the number of features. Evaluation of a small dataset with a large number of features can lead to degradation in the model's performance. To our knowledge, limited work is done towards exploring relevant features using feature selection techniques [25, 15, 2]. Most of the research works [24, 27, 109, 23, 26, 58, 41, 61, 62] have not utilized feature selection methods to find a subset of relevant features from thermography images. Therefore, there is a need to investigate feature selection methods to overcome the problem of a small sample size dataset. With this, we will compare whether the model's performance improves. Also, a reduced set of relevant features will enhance the visualization, reduce the over-fitting problem, and improve generalization accuracy.

The key contributions of the chapter are listed below as:

- In this study, a novel set of hand-crafted features are developed and extracted from publicly available medical thermal imaging datasets for temperature's asymmetry analysis, specifically aimed at detecting breast cancer, diabetes,

---

[1] https://www.fda.gov/medical-devices/safety-communications/fda-warns-thermography-should-not-be-used-place-mammography-detect-diagnose-or-screen-breast-cancer#:~:text=There%20is%20no%20valid%20scientific, other%20diseases%20and%20health%20conditions.

and thyroid cancer. This work aims to evaluate the effectiveness and feasibility of thermography as a diagnostic tool for various diseases.

- Then, eight state-of-the-art feature extraction methods[23, 2, 24, 25, 26, 27, 15, 28] alongside the proposed feature extraction method is statistically compared and analyzed the performance to distinguish an abnormal thermal image from a normal one on a uniform platform.
- We also aim to develop a unified model capable of identifying abnormal thermal patterns due to inflammation caused by diseases and detected by a thermal cameras. The model is evaluated on the same platform.
- The above objectives are investigated using four well-known feature selection methods to select relevant features from the ten features-sets. Also, the four well-known classifiers are used for a fair performance comparison of the selected set of relevant features. We used three publicly available datasets of Medical Thermal Imaging for the entire investigation, having different diseases. The publicly available datasets are skewed (i.e. difference in classes frequency in the dataset is high), so a 2-level sampling strategy is developed and used to conduct the experiments.

This chapter is structured as follows: Section 3.2 details the methodology, covering feature extraction approaches in section 3.2.1, feature selection methods, classification techniques, and sampling strategies in section 3.2.2. The experimental framework is described in section 3.3. The exhaustive analysis of the proposed approach with state-of-the-art approaches on various datasets using quantitative and visual analysis done in section 3.4. The chapter is concluded with its summary in section 3.5.

3.2 Methodology

This section describes the novel set of hand-crafted features, developed and extracted to detect abnormality in the form of inflammation from medical thermal images of human body. This work aims to assess the effectiveness and feasibility of thermography as a diagnostic tool for various diseases. Also, this section describes the methodology for systematic and empirical review of the feature-sets proposed in the research works[23, 2, 24, 25, 26, 27, 15, 28], both individually and in combination. Finally, a unified set of features from these nine research works is compiled and evaluated on the same platform.

3.2.1 Features Extraction

The human body typically exhibits symmetrical temperature distribution. A temperature asymmetry between the left and right sides of the body may indicate an abnormality. Leveraging this principle, along with insights into inflammatory activities provided by temperature matrices, the abnormalities in human body can be detected. The pre-processed images are divided into two equal parts of same size for thermal asymmetry analysis (Figure 3.1). Then, following three sets of features - Local Binary Pattern (LBP)-based statistical features, GLCM-based, and LBP-Otsu threshold are extracted, from both the parts.

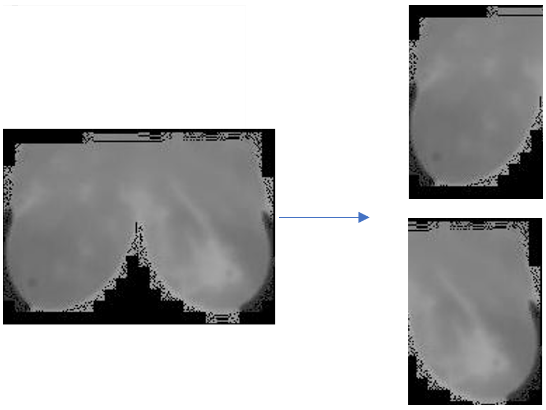

Fig. 3.1: Division of Breast Thermal image in two equal parts for asymmetry analysis.

- **Gray-Level Co-Occurrence Matrix (GLCM)-based Features** - 10 Haralick features[110] (Entropy, contrast, Correlation, Energy, Sum variance, Sum entropy, Difference variance, Information measure of correlation, Homogeneity, Sum average) are computed from the normalized GLCM sub-matrix.The matrix is obtained for the image in four directions (0°, 45°, 90°and 135°) with an offset of 1. The sub-matrix range is chosen empirically, for each dataset, using the histogram that depicts the significant range where the probability of having sick region/intensities is higher than that of a healthy region, (figure 3.2) ([121, 157] for DB-DMR-IR, [127, 154] for DB-FOOT-IR, and [124, 165] for DB-THY-IR,). Particularly, this range discriminates healthy regions/sample from an abnormal region/sample. Thereafter, an average of four feature-sets (along 4 directions - 0°, 45°, 90° and 135°) was calculated.

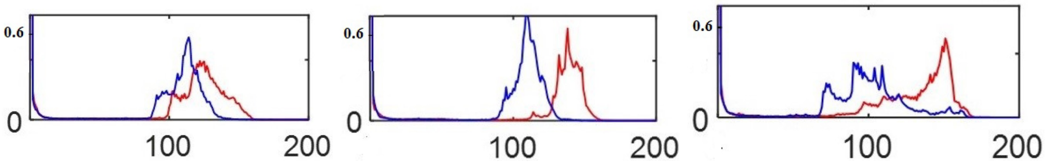

(a) (b) (c)

Fig. 3.2: Probability distribution of intensities in normal and abnormal subjects for DB-DMR-IR (a), DB-FOOT-IR (b), and DB-THY-IR (c) datasets.

- **Local Binary Patterns (LBP)-based Statistical Features** - The Rotation Invariant LBP were computed for both the parts in the image. The image was sub-divided into 18 grids, of equal dimensions. Then five statistical features- mean, variance, Skewness, Kurtosis, and entropy were computed from each grid for both parts of the image.
- **LBP-Otsu Threshold** - The Otsu-threshold value was computed from the Rotation Invariant LBPs of the complete image. The optimum threshold value th^* was obtained, which maximizes the variance of intensities between classes $var^2(th)$, from the LBP of the original image using the expression -

$$th^* = \underset{0<th<L-1}{\operatorname{argmax}} \; var^2(th) \tag{3.1}$$

To analyze temperature based asymmetry in the body, the absolute difference of the extracted features from both parts of the image is determined. Finally, a set of 101 features are attained and the feature set is renamed as GUP. The obtained features are normalized in the range [0,1]

Additionally, eight state-of-the-art feature extraction methods, detailed in Table 2.1, are extracted with the exact line of detail from three datasets, described in Chapter 1. The extracted features were normalized to a range of [0,1]. A combined feature set, named UnionFeature_Set, was created by taking union of all eight feature sets with the previously extracted feature-set. The duplicate features were removed. The resulting UnionFeature_Set comprises 467 features, arranged as outlined in Table 2.1.

The UnionFeature_Set is prepared to analyze the behavior and performance of the features with each other and on the proposed platform. Also, this is done to investigate that whether combining features complements each other to give better results and find the most relevant feature set for characterizing inflammation in human body captured using a thermal sensitive camera. All the 10 feature-sets, obtained, are investigated on a common platform using a combination of four feature selection, four classification approaches, and 2-level sampling strategies for comparing their performance.

3.2.2 Machine Learning Platform

This work defines the uniform platform as a Machine Learning (ML) pipeline of all possible combinations of four well-known feature selection strategies (Pearson Correlation (PC), Minimum Redundancy Maximum Relevance (mRMR), ReliefF (ReF), and Chi-Squared (ChiSq)), four classifiers (k-Nearest Neighbor (k-NN), SVM, Decision Trees Classifier (DTC) and Random Forest Classifier(RFC)) on three publicly available Thermal imaging based medical datasets (DB-DMR-IR, DB-FOOT-IR, and DB-THY-IR). Also, each pipeline is assessed using a 2-level sampling strategy. With this, the strength of feature selection methods, classifiers, and 2-level sampling strategy will be evaluated for the various state-of-the-art approaches for detecting abnormality characterized by inflammation in human body. This subsection describes and contrasts the components of the uniform platform used for comparing various feature extraction approaches.

3.2.2.1 Feature Selection (FS) Methods

The feature sets proposed/extracted in the literature may contain redundant or irrelevant features for the study. In either scenario, it may degrade the predictability of the decision system. Using more/redundant features may consume a considerable amount of memory and training time. A limited number of studies [15, 25, 2] have used the feature selection method to assess the relevance of features for identifying abnormality/inflammation in human body.

This study applies four well-known FS methods to rank the extracted and normalized features. A feature is included (based on its rank) incrementally to the set until the best performance is achieved. The following FS methods are used to evaluate the relevance.

- **Pearson Correlation Score (PC) -** PC Score[111], is a uni-variate approach that selects a subset of features highly correlated with the classification. The Pearson correlation coefficient is calculated as

$$PC\_Score(f_i) = \frac{cov(f_i, Y)}{\sqrt{var(f_i)}\sqrt{var(Y)}} \tag{3.2}$$

where f_i is the feature whose PC score is evaluated with respect to the class label Y (output), cov is the covariance, and var defines the variance. The absolute value of correlation value closer to 1 indicates a stronger correlation among the prescribed variables, while zero value implies no correlation between the variables.

- **Chi-Squared Score (ChiSq) -** ChiSq Score [112] is another uni-variate FS method that evaluates the association of a feature with the class label. The ChiSq score for a feature f_i, with r different values and binary classification problem, is calculated as-

$$ChiSq\_Score(f_i) = \sum_{j=1}^{r}\sum_{c=1}^{2}\frac{(n_{jc} - u_{jc})^2}{u_{jc}} \tag{3.3}$$

$$u_{jc} = \frac{n_{*c} \times n_j}{n} \tag{3.4}$$

  where n_{jc} defines the number of samples with j^{th} feature of class c, n_j defines the number of samples with the j^{th} feature value, and n_{*c} denotes the number of samples in class c. A higher ChiSq score indicates high relevance of a feature and its high ability to distinguish the class.

- **ReliefF Score (ReF) -** ReF Score [113] is an instance-based and sixth variation of Relief FS family [114]. It computes the discriminating strength of a sample's feature value with its K nearest neighbors. This approach awards high weight-age to the features that give diverging values to their neighbors of different classes and penalizes the ones that give different values to neighbors of the same class. It basically searches for k near misses from each class and averages their contributions for updating weights, weighted with the prior probability of each class. ReF score for a feature f_i is computed as

$$\begin{aligned} ReF\_Score(f_i) = \sum_{j=1}^{l}(-\frac{1}{l \times K}\sum_{x_r \in NH(j)} dist(x_j(i), x_r(i)) \\ + \sum_{y \neq y_j}\frac{h(y)}{l \times K \times (1 - h(y))}\sum_{x_r \in NM(j,y)} dist(x_j(i), x_r(i))) \end{aligned} \tag{3.5}$$

  where l is the number of samples randomly selected from n samples, $NH(j)$ and $NM(j, y)$ define the set of nearest samples of x_j in the same class and in other class y, respectively, both of size K. The function $h(y)$ defines the instances ratio in class y. Higher the score, more relevant the feature is.

- **Minimum Redundancy Maximum Relevance Score (mRMR) -** mRMR Score, is multivariate FS method [115], based on Mutual Information (MI). The relevance of features with the class and the redundancy of features with each other is considered simultaneously. The mRMR algorithm measures the redundancy by taking the MI of features pairwise. Simultaneously, it quantifies relevance using the MI of attribute A with class variable Y. It selects and ranks the feature according to the Mutual Information Quotient (MIQ) value in the forward selection scheme. The MIQ value is computed as follows:

  $$MIQ_A = \frac{V_A}{W_A} \tag{3.6}$$

  where V_A and W_A are the relevance and redundancy of feature A, respectively, and is computed as:

  $$V_A = MI(A, Y) \tag{3.7}$$

  and

  $$W_A = \frac{1}{|S|} \sum_{Z \in S} MI(A, Z). \tag{3.8}$$

  where $|S|$ is the number of features in the dataset and $MI(\cdot)$, between two variables X and Z, defines the non-linear correlation between two variables and is computed as

  $$MI(X, Z) = \sum_{i,j} P(X = x_i, Z = z_j) \log \frac{P(X = x_i, Z = z_j)}{P(X = x_i)P(Z = z_j)} \tag{3.9}$$

Three uni-variate and one multivariate state-of-the-art FS methods are implemented for the study. Uni-variate feature selection methods evaluate and rank a single feature concerning the class variable. PC is a low-cost and straightforward method. It does not consider the mean values and is invariant to linear transformations of the given feature but assumes linear dependencies between the variable and response variable, which may not always be accurate. Perfectly correlated features are genuinely redundant as no additional information is gained by adding them to the feature set. Chi-Sq is another statistical FS method that is unbiased but not discriminating to an informative level of features. The Chi-Sq FS method evaluates the continuous features after their discretization. The number of bins needs to be specified. The ReF FS method is not dependent on any heuristics. Though ReF is not considered a multivariate FS method but it is noise-tolerant and robust to feature interactions. It depends on the number of nearest neighbors K.

Since the uni-variate FS method evaluates features individually, it may contain highly correlated features during the selection phase. mRMR provides a feature-set with maximal dependency on the target value and minimal dependency among each other. As mRMR considers the MI among features, better behavior is obtained even when noise is present in data. Continuous variables require discretization pre-processing before applying mRMR.

3.2.2.2 Classifiers

The problem under consideration is a binary classification problem. The features were fed iteratively to four classifiers: k-NN, SVM, DTC, and RFC, in an incremental manner, in the order of ranks provided by the respective feature selection methods. Following oulines the classifiers used:

- **k-Nearest Neighbor (k-NN) -** k-NN [116] is a famous instance-based method for classification and regression. It is a non-parametric classifier, simple to implement and interpret. In k-NN, an unlabeled instance is assigned a class belonging to most of its k neighbors. This algorithm is sensitive to the choice of k.

- **Support Vector Machine (SVM) -** SVM [117] is, originally, a binary classification approach that finds an optimal hyperplane to discriminate the instances belonging to two classes. The optimal hyperplane maximizes the margin around itself. A kernel function ($\Phi : \mathbb{R}^D \rightarrow \mathbb{R}^{HS}$) may be used to project the data into a higher space so that the resulting data can be separated by a linear classifier (hyperplane). The optimal hyperplane $f(x) = \langle w, \Phi(x) \rangle + b$ can be obtained by solving the quadratic optimization problem

$$\text{minimize} \frac{1}{2} \parallel w \parallel_2^2 + Co(\sum_{i=1}^{N} \Delta_i) \tag{3.10}$$

$$\text{with respect to } \mathbf{w} \in \mathbb{R}^{HS}, \Delta \in \mathbb{R}_+^N, b \in \mathbb{R} \tag{3.11}$$

$$\text{subject to } y_i(\langle w, \Phi(x_i) \rangle + b) \geq 1 - \Delta_i, \forall i \tag{3.12}$$

where ***w*** is the weight coefficients vector, *Co* is a positive trade-off parameter between model simplicity and classification error, Δ is the slack variable vector, and *b* corresponds to the bias in the hyperplane equation.

- **Decision Trees Classifier (DTC) -** DTC [118] summarize the data in form of a decision tree. Nodes in the tree represent features selected for branching further on its values, and the tree's leaves indicate the class label. The DTC employs a greedy approach to choose an attribute for the split at every node. If the purity of the class labels in the resulting sub-nodes is less than the parent node's purity, it implies that information has been gained, and the split must be maintained. The algorithm is applied recursively to form subtrees, terminating when a given subset contains instances of only one class.
- **Random Forest Classifier (RFC) -** The general framework of the RFC[119] uses an ensemble of more than one DTC. An unlabeled instance is classified to the mode of the classes (classification) or average prediction (regression) of the individual trees.

This study considers four above-stated state-of-the-art classifiers for the experiments. k-NN[116] is a straightforward algorithm but has a high cost (computation and storage) of classifying new instances [119, 120]. Also, it is biased by the value of k. The smaller values of k may miss-classify due to noise in the data. The larger value of k reduces the effect of noise on the classification but makes the experiments computationally expensive. It is also sensitive to the choice of similarity function due to many or irrelevant features. If the dataset is skewed, then k-NN must not be chosen [119, 120]. It may be a choice if the dataset is small and the relationship between the dependent and independent variables is unknown. SVM [117, 119, 120] is based on a robust theory and avoids estimating probabilities on the given dataset. It is highly effective in applications with dimensions more than the number of samples. Generally, it is not sensitive to over-fitting and is not biased by outliers. A non-linearly separable data can be transformed to a higher dimension that is linearly separable by applying the kernel trick. Selecting the appropriate kernel function and its hyper-parameters is a tricky task. SVM performs better when dealing with multi-dimensions and continuous features[117, 119, 120]. The major drawback of SVM is the lack of transparency and interpret-ability of results[119, 120].

The DTC[118] is another powerful classifier that handles datasets with qualitative features[119, 120]. Numeric data has to be discretized beforehand. The learning speed concerning a high number of attributes and instances is fair. It is relatively tolerant of irrelevant attributes and missing values. It provides transparency in the model but may result in an over-fitted model for small datasets. One approach to tackle over-fitting is to pre-prune the decision tree. Also, a minor change in the dataset can change the tree entirely.

In contrast, RFC is robust and accurate for many problems with skewed datasets or datasets with high dimensionality and instances[119, 120]. If the data is changed a little (or noise is added), the individual trees may change, but the forest is relatively stable as it is an ensemble of many trees and gives stable results. The model generated is less over-fitted comparatively. A grid search of different parameters and random seeds is required to obtain the best results, but it is computationally expensive[119, 120]. Individual trees need to be uncorrelated/independent to get an unbiased result. RFC can easily tackle the problem of highly correlated features.

3.2.2.3 Sampling Strategies and Performance Metrics

This work considers Accuracy and F-Measure as primary criteria for evaluating the performance. Accuracy defines the probability of correctly classifying an instance in the test sample. It is an optimal metric when the dataset is balanced regarding the class's instances frequency. F-Measure is calculated as the harmonic mean of sensitivity and specificity. The corresponding classifier parameters were optimal if they yielded the most considerable accuracy and F- measure.

A 2-level sampling method for performing the experiments is developed. In the first level, given a dataset D, if D is a skewed dataset (i.e. difference of class frequency in the dataset is high), two datasets - D1 and D2 are formed randomly such that the frequency of samples in both the classes in D1 and D2 is the same. In dataset D, the class with higher frequency is divided into two parts (P1 and P2) randomly such that the intersection of P1 and P2 is NULL. Finally, two subsets D1 and D2 are generated by appending minority class data to both P1 and P2, respectively.

In the second level, for each dataset (D1 and D2) formed, a standard re-sampling method that is k-fold cross validation for k=5, 10, and Leave-One-Out Cross Validation (LOOCV) is performed, independently, to obtain a more reliable estimate of the factual accuracy. The Accuracy and F-Measure values of K-fold cross validation (K = 5, 10 and LOOCV) of a model are obtained by averaging them across each fold of k-fold cross validation and then over subsets (D1 and D2) of dataset D. For instance, the average of D1's and D2's 5-fold cross validation results (for instance) was taken as the final result of D's 5-fold cross validation results for a given classifier and parameter values. This sampling strategy is illustrated in figure 3.3. Finally, the optimal model parameters are selected based on their best

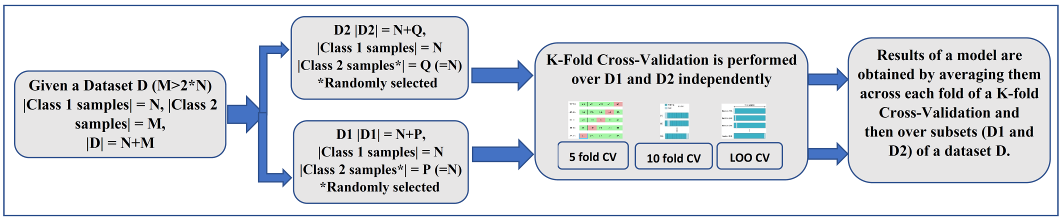

Fig. 3.3: 2-level sampling strategy used.

performance.

3.3 Experimental Design

The experiments were conducted on a computer using Windows 10 operating system with 16GB RAM and i7 (9^{th} generation) Processor. MATLAB 2020 (64-bit) was used for conducting the entire experiment. Figure 3.4 illustrates the ML framework followed for conducting the experiments. Statistics of the datasets used in the chapter are mentioned in Table 3.1. The pre-processing steps for the three datasets are described in Chapter 1, section 1.2.1.

Table 3.1: Size of the datasets used in the study

DataSets	Subsets formed	Abnormal Samples	Normal Samples	Total Cases
DB-DMR-IR Database	D1	40	40	80
	D2	40	40	80
	Total samples	40	80	120
DB-FOOT-IR Database	D1	45	45	90
	D2	45	45	90
	Total samples	90	45	135
DB-THY-IR Database	-	18	16	34

Table 3.2: Description of Feature Selection Method's parameters and their settings in the experiment.

Algorithm	Parameters	Parameters Values	Description of these parameters
ReF	K	$[5-15]$	The number of nearest neighbors from each class to be used.
ChiSq Score	Number of bins	$[10-20]$	The number of bins for discretization of numerical features.

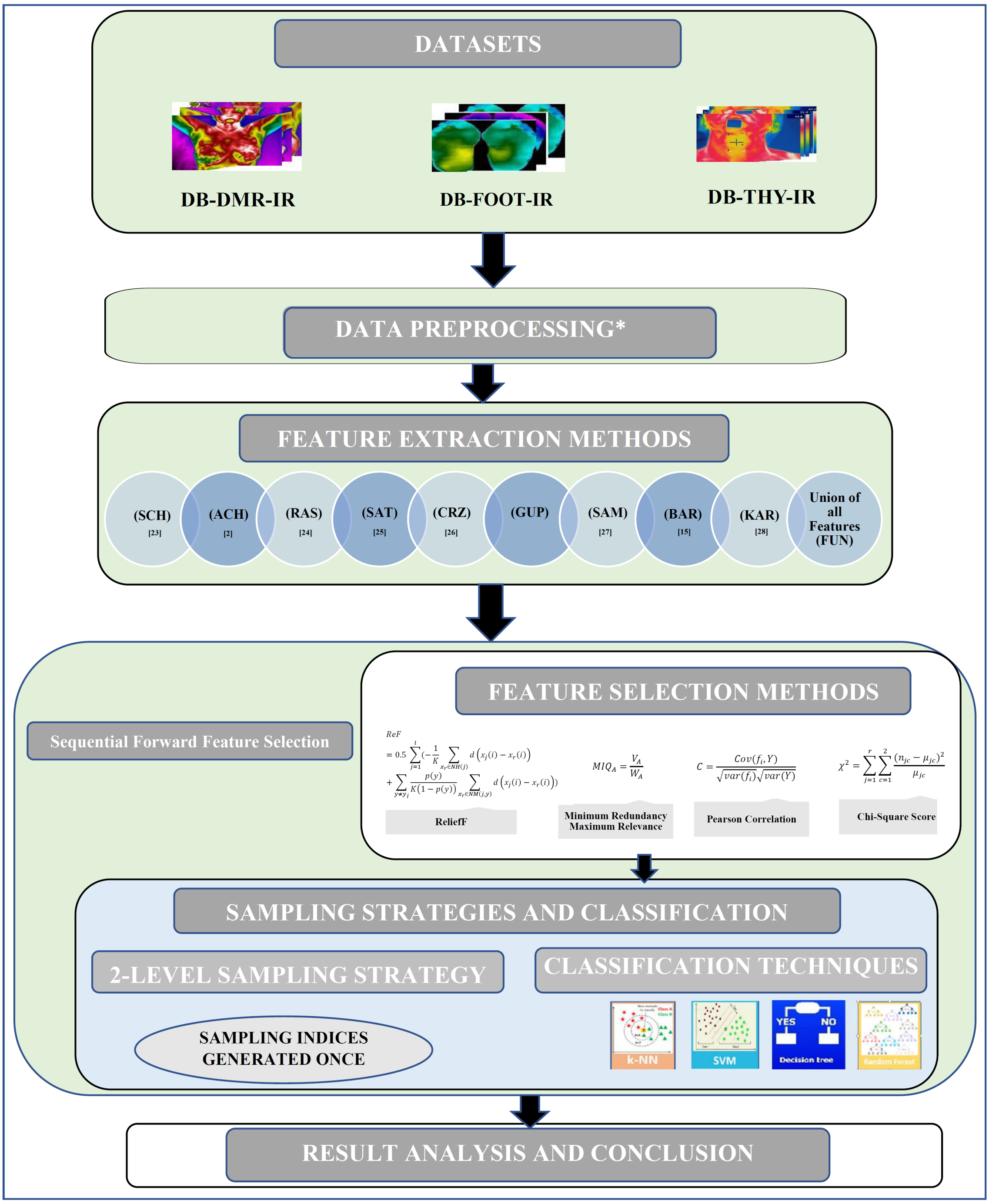

Fig. 3.4: The Machine Learning Framework/Uniform Platform for the Experiments conducted.

With the exact line of detail, the features extractions methods mentioned in Table 2.1 are implemented and extracted features from transformed and segmented gray-scale images. Alongside a novel feature-set is created to perform temperature's asymmetry analysis in medical thermal images. Also, a feature-set is prepared by taking a union of all the feature-sets - UnionFeature_Set, for further analysis and obtained a total of 467 distinct features (UnionFeature_Set). All the feature-sets generated were normalized.

Table 3.3: Description of classifier's parameters and their settings in the experiment.

Algorithm	Parameters	Parameters Values	Description of these parameters
k-NN	k	$[1 - 20]$	The number of neighbors to be used.
	Distance Metric	Euclidean Distance	The distance function for finding proximity with neighbors.
SVM	Cost	$[1 - 1024]$	The cost parameter C.
	Kernel Type	Linear, RBF	The type of kernel functions, used.
	Gamma	$[2^{-4} - 2^{4}]$	The parameter of kernels functions (RBF, Polynomial, and Sigmoid).
DTC	Splitting criteria	Gini's Diversity Index, Cross Entropy	Criteria used for selecting an attribute for further splitting
	Pruning criteria	Enabled, Disabled	Pruning the tree limits over-fitting of training data.
	Minimum leaf size	[4, 8, 12, 16, 20]	The minimum number of instances per leaf.
RFC	Ensemble size	[3-50]	The number of weak classifiers/trees used in the ensemble.

We applied four well-known feature selection approaches to evaluate the relevance of all the features in feature sets, independently of the classifier. Table 3.2 summarizes the parameters and their values used for grid search for feature selection methods. K is a crucial tuning parameter of ReF. It is ranged in [5 - 15] with a step size of 4 and used Manhattan distance as the similarity measure. In the Chi-Sq method, the number of bins for discretization of the numeric attributes ranged over [10- 20]. The T-Test is applied to the proposed GUP and UnionFeature_Set feature-sets to select the features and evaluate their effectiveness incrementally. The features were fed iteratively to the classifier in the order of ranks provided by the respective feature selection methods (section 3.2.2.1) for each classifier parameter stated in table 4 and all the datasets. Also, the features are fed incrementally as per their rank to the classifier and best performance is recorded in terms of accuracy and F-Measure.

This work uses four commonly used classifiers (k-NN, SVM, DTC, and RFC). Also grid search is performed with the respective parameters of the classifiers to achieve the best results. The classifier parameters for grid search are summarized in Table 3.3. k is a crucial tuning parameter of k-NN and is ranged in [1 - 20] with a step size of 2. Euclidean distance is used as the similarity measure.

The LIBSVM[2] implementation of SVM is used with two kernel functions -

---

[2] https://www.csie.ntu.edu.tw/cjlin/libsvm/

Linear and Radial Basis function (RBF). The RBF is used to handle the non-linearity between the features and class labels. Grid search is performed to optimize the hyper-parameters - Cost Parameter, C, for linear and RBF kernel functions, γ parameter for RBF kernel. To determine optimal hyper-parameters, the study considered the values of C as $[1 - 1024]$ and the smoothing parameter value, γ, for RBF kernel was considered in the range $[2^{-4} - 2^{4}]$ in multiples of 2.

The parameters considered for DTC to achieve the best results are Splitting Criteria, Pruning Criteria, and Minimum Leaf Size. Gini's Diversity Index and Cross-Entropy are used as the splitting criteria. The experiments are performed with pruning enabled and disabled, and the minimum leaf size is ranged over [4, 8, 12, 16, 20]. In the Random Forest Classifier (RFC) framework, the number of weak classifiers (DTCs) is varied over the range [3 - 50], with a step size of 4. A Random Forest is constructed with a template of a DTC with the exact parameter specifications as stated for DTC.

The dataset used in most of the literature is skewed [23, 24, 26, 27]. This study has performed 2-level sampling to get the datasets having a balanced number of samples from each class. The 2-level Sampling for all the datasets was done only once for all the pipelines; that is, each of DB-DMR-IR and DB-FOOT-IR datasets is divided into two subsets, D1 and D2, and further generated 5 and 10 random stratified partitions from each subset, respectively, only once. It was done to eliminate any randomness in the experiments. That is, the partitions were kept the same for all the pipelines. Along with 5-fold and 10-fold cross validation, LOOCV was also done to contrast the behavior of data. All the results are recorded along with the parameters for which the best accuracy and F-Measure are achieved.

3.4 Results and Discussion

The performance of experimental results is compared based on classification Accuracy and F-Measure. Also, Accuracy and F-Measure values of a model are obtained by averaging them across each fold of k-fold cross validation and all subsets (D1 and D2) of dataset D(= DB-DMR-IR and DB-FOOT-IR). The experiments conducted on three datasets are independent and not related to each other in any respect. Figures 3.5, 3.6 and 3.7 illustrate the visual comparison of classification accuracy values for a given combination of feature extraction method, FS methods, classifiers, and cross validation approaches.

We can observe from Figures 3.5, 3.6 and 3.7 that among the three re-sampling

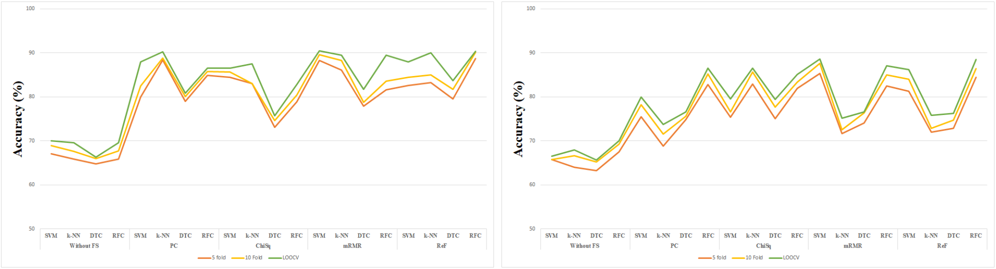

(a) RAS [24]

(b) SCH[23]

(c) SAM[27]

(d) ACH[2]

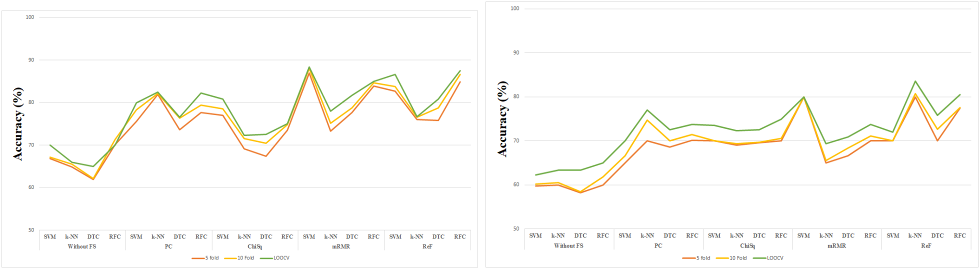

(e) SAT[25]

(f) KAR[28]

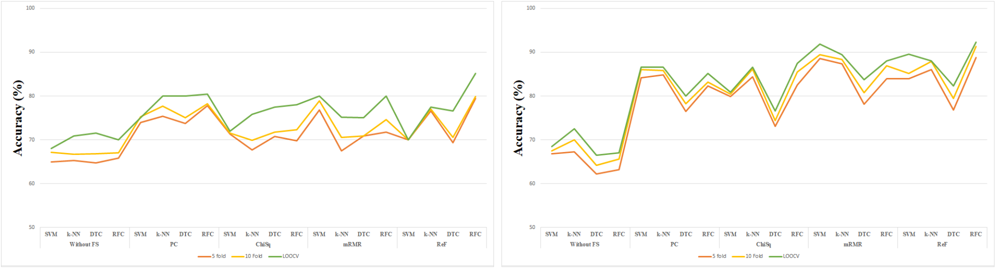

(g) CRZ[26]

(h) BAR[15]

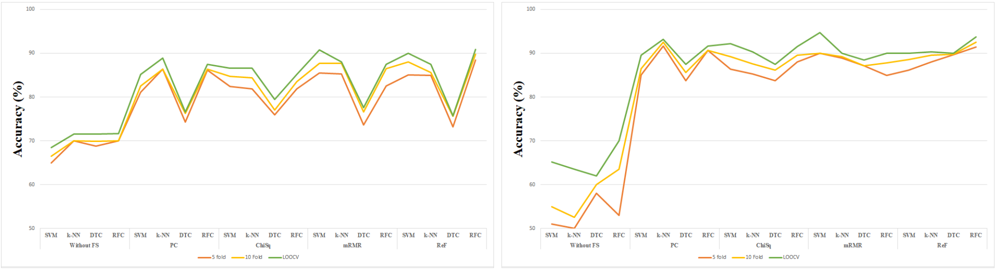

(i) GUP

(j) UnionFeature_Set

Fig. 3.5: Comparison of classification accuracy values for a given combination of feature extraction, feature selection methods, and cross validation strategies on DB-DMR-IR dataset.

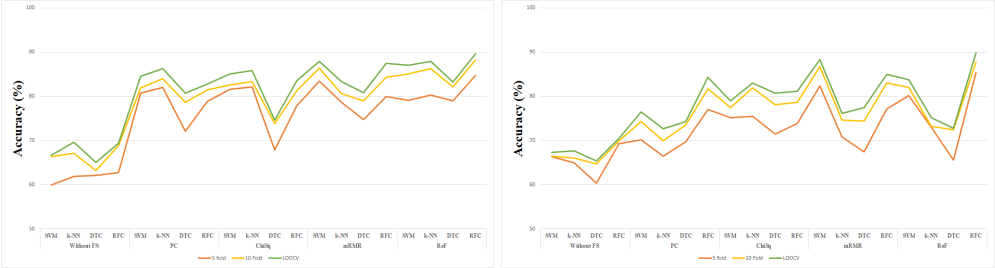

(a) RAS [24] (b) SCH[23]

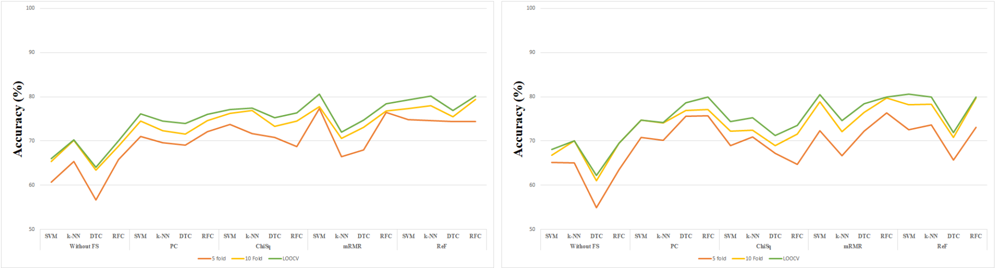

(c) SAM[27] (d) ACH[2]

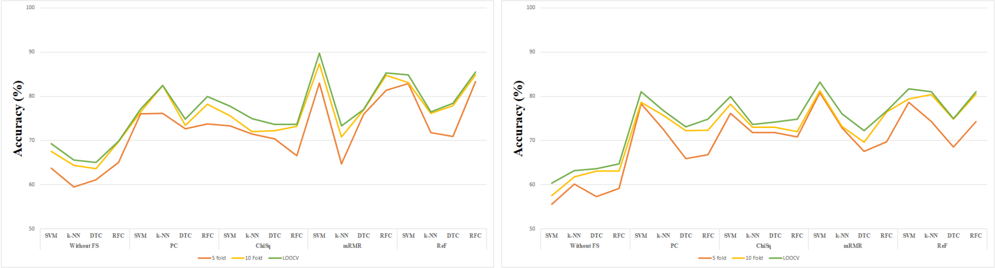

(e) SAT[25] (f) KAR[28]

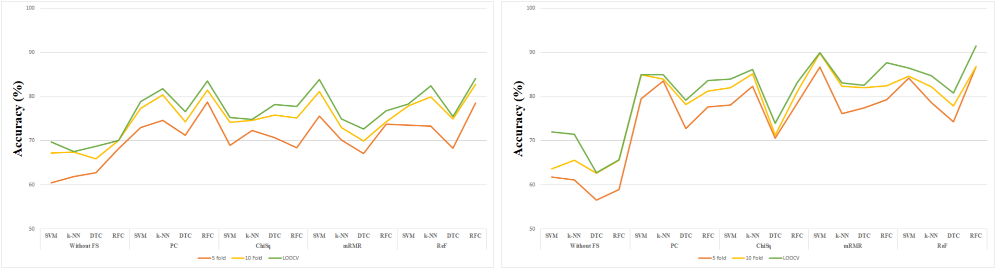

(g) CRZ[26] (h) BAR[15]

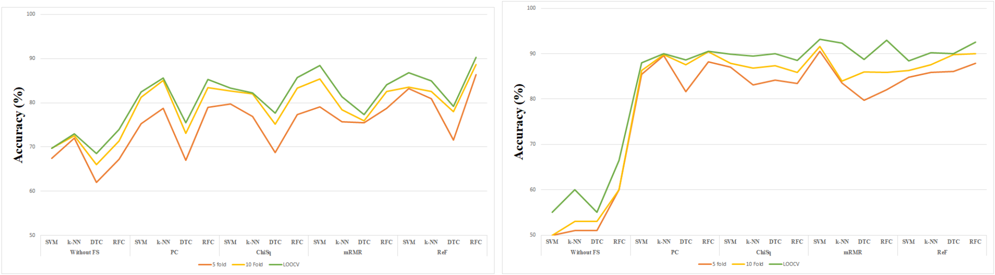

(i) GUP (j) UnionFeature_Set

Fig. 3.6: Comparison of classification accuracy values for a given combination of feature extraction, feature selection methods, and cross validation strategies on DB-FOOT-IR dataset.

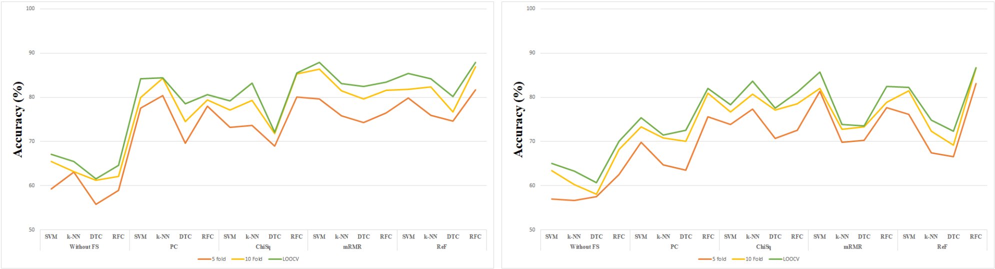

(a) RAS [24]   (b) SCH[23]

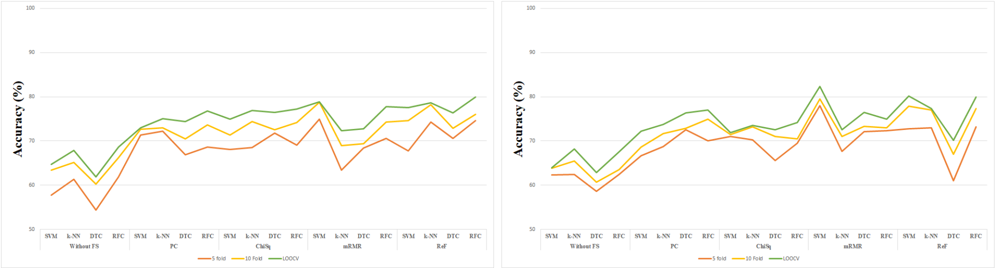

(c) SAM[27]   (d) ACH[2]

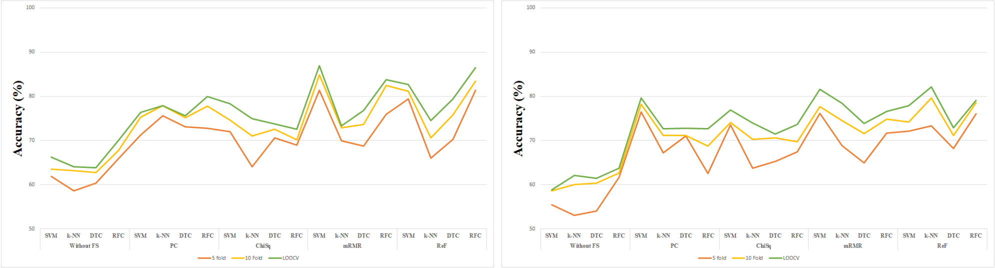

(e) SAT[25]   (f) KAR[28]

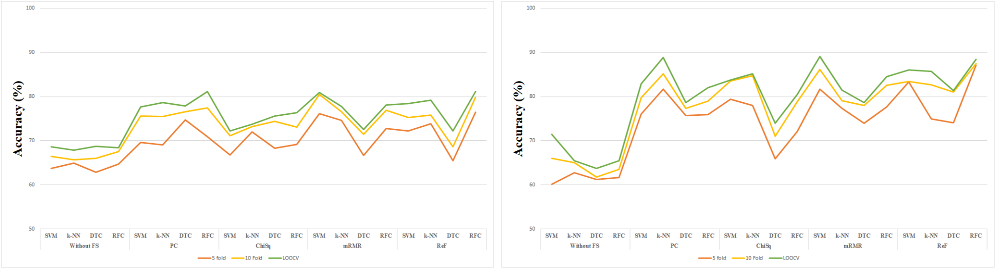

(g) CRZ[26]   (h) BAR[15]

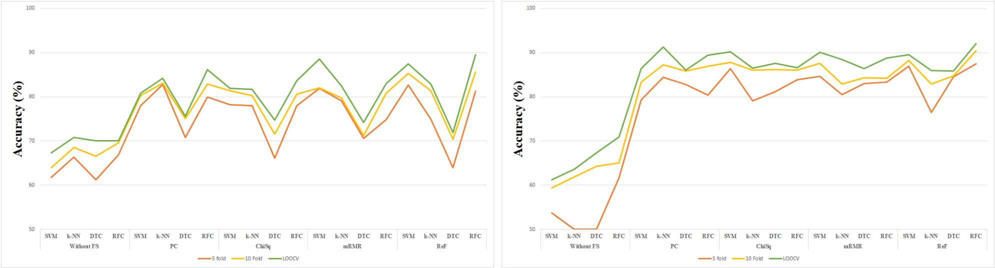

(i) GUP   (j) UnionFeature_Set

Fig. 3.7: Comparison of classification accuracy values for a given combination of feature extraction, feature selection methods, and cross validation strategies on DB-THY-IR dataset.

strategies (5-fold, 10-fold, and LOOCV), LOOCV strategy (green line) gave the best results for all the nine feature extraction methods, individually and on their union. The best performance is achieved using LOOCV as the maximum number of samples for training is available. Henceforth, all the analysis is done on results obtained with LOOCV, shown in Table 3.5 for DB-DMR-IR, DB-FOOT-IR, and DB-THY-IR datasets, respectively.

Broadly, following are observed from Table 3.5 corresponding to DB-DMR-IR, DB-FOOT-IR and DB-THY-IR datasets:

- The union of features, (UnionFeature_Set), from the existing eight research works alongside a proposed GUP feature-set, provided better results in comparison to each of the research work individually for all the combinations of 4 FS methods and 4 classifiers across all the datasets. Table 3.4 states the best-performing models along with their accuracy and F-Measure for all the datasets considered.

Table 3.4: The classification accuracy(%) and F-measure values (%) obtained from the best performing model using LOOCV strategy on DB-DMR-IR, DB-FOOT-IR, and DB-THY-IR datasets.

DataSets	FE Method	Classification Model	Feature-subset	Accuracy (%)	F-Measure (%)
DB-DMR-IR	UnionFeature_Set	SVM+mRMR	45	94.75	93.80
DB-FOOT-IR	UnionFeature_Set	SVM+mRMR	57	93.14	92.55
DB-THY-IR	UnionFeature_Set	RF+ReF	39	92.06	91.42

- The classification accuracy for all the nine feature extraction methods, individually and in their union, improves with the use of all four FS methods (PC, ChiSq, mRMR, and ReF). In some cases, a reduced feature set gave the same performance as that with all features of a given feature extraction method. Hence, better visualization may be achieved with a reduced subset of features without losing performance.

Sections 3.4.1 and 3.4.3 introspect the performance of nine feature extraction methods, considered individually and in combination, respectively. Also, the performance comparison of all the 40 combinations of feature extraction (FE) and FS methods is done in section 3.4.2.

3.4.1 Comparison of Feature Extraction (FE) Methods

This subsection introspects the performance of state-of-the-art feature extraction methods based on the results in Table 3.5. The following can be observed:

Table 3.5: The accuracy (%) and F-Measure values (%) obtained from various combinations of feature extraction methods, feature selection methods, classifiers, and LOOCV strategy on three datasets.

S.No.	Reference	Evaluation of Reference on the Dataset	Feature Selection (FS) method	DB-DMR-IR								DB-FOOT-IR								DB-THY-IR							
				Accuracy				F-Measure				Accuracy				F-Measure				Accuracy				F-Measure			
				SVM	k-NN	DTC	RFC	SVM	k-NN	DTC	RFC	SVM	k-NN	DTC	RFC	SVM	k-NN	DTC	RFC	SVM	k-NN	DTC	RFC	SVM	k-NN	DTC	RFC
1	**RAS[24]**	**DB-DMR-IR- Acc-72.5%, F-Meas-70%, DB-FOOT-IR-Acc-61.5%, F-Meas-60%, DB-THY-IR- Acc-57.5%, F-Meas-55%**	**WFS**	70	69.6	66.3	69.6	70	67.5	66.23	68.50	66.64	69.66	65	69.37	65.74	70	65	68.50	67.1	65.5	61.6	64.6	66.72	64.07	63.6	62.50
			PC	88	90.29	80.86	86.57	85	90.35	80.59	85.04	84.53	86.31	80.73	82.76	83.87	85.71	80	82.31	84.17	84.37	78.5	80.64	83.24	83.44	78.78	80.00
			ChiSq	86.5	87.5	75.71	82.86	85.89	87.97	75.8	81.78	85.05	85.84	74.66	83.52	86.19	84.61	73.71	84.00	79.16	83.17	72.07	85.53	80	83.18	73.1	84.61
			mRMR	**90.5**	89.43	81.67	89.43	**87.5**	90.62	80.27	89.81	87.91	83.28	80.78	87.49	86.8	84.58	79.14	87.12	**87.9**	83.1	82.41	83.4	**87.05**	81.61	82.32	83.54
			ReF	88	90	83.71	90.35	92.07	90	85.51	91.92	87.07	87.93	83.21	**89.67**	86.09	87.43	81.92	**91.54**	85.4	84.2	80.19	**87.9**	84.38	85.97	81.73	**88.49**
2	**SCH[23]**	**DB-DMR-IR- Acc-65.5%, F-Meas-65.0%, DB-FOOT-IR-Acc-60%, F-Meas-60%, DB-THY-IR- Acc-60%, F-Meas-60%**	**WFS**	66.57	68	65.6	70	67.99	66.74	64.18	69.96	67.29	67.65	65.37	70.49	66.14	66.99	64.76	69.01	65	63.3	60.7	70	65	62.87	59.57	68.27
			PC	80	73.71	76.57	86.57	80	72.39	76.5	88.31	76.43	72.64	74.31	84.29	78.1	72.23	72.74	82.32	75.4	71.51	72.57	81.97	73.86	69.88	72.43	83.33
			ChiSq	79.5	86.57	79.43	85.14	77.5	88.33	79.16	85.93	78.94	83.04	80.72	81.16	80	82.43	80.14	79.88	78.3	83.67	77.53	81.14	77.08	82.02	76.27	80.00
			mRMR	**88.57**	75.14	76.57	87.12	**83.6**	76.62	75.96	87.59	88.38	76.13	77.4	84.96	87.06	74.56	76.51	85.46	85.77	73.84	73.57	82.42	83.85	74.58	73.77	81.32
			ReF	86.17	75.83	76.29	88.5	84.6	76.3	75	89.69	83.74	75.15	72.82	**89.82**	82.66	73.25	71.52	**89.3**	82.27	74.83	72.29	**86.7**	82.26	74.94	70.3	**87.37**
3	**SAM[27]**	**DB-DMR-IR- Acc-60%, F-Meas-60%, DB-FOOT-IR-Acc-58.75%, F-Meas-55%, DB-THY-IR- Acc-55%, F-Meas-55%**	**WFS**	66.57	69.43	66.6	70	65.13	67.66	68.38	69.56	66.04	70.28	64.08	70	64.71	69.65	63.3	72.09	64.77	67.93	61.9	68.6	63.24	66.61	62.87	69.45
			PC	78	77.5	76.57	80	77.9	76.24	75	80.00	76.14	74.56	73.99	76.04	76.49	73.53	72.31	77.15	73	75.1	74.37	76.83	74.4	75.31	74.5	74.91
			ChiSq	77.5	78.57	79.43	79.43	77.5	77.93	80	79.05	77.16	77.4	75.27	76.34	75.46	76.28	76.16	75.54	74.9	76.87	76.5	77.23	73.32	78.02	76.5	79.12
			mRMR	80.86	72.29	76.57	79.43	80	70	74.83	78.91	**80.58**	72.02	74.68	78.39	**81.88**	71.61	73.91	79.85	78.86	72.39	72.77	77.73	77.19	70.4	72.51	76.52
			ReF	79.5	**82.71**	80.14	80	78.18	**82.64**	81.16	80.00	79.28	80.19	76.88	80.19	80.33	81.76	74.94	78.68	77.6	78.61	76.34	**80**	79.28	78.5	76.23	**80**
4	**ACH[2]**	**DB-DMR-IR- Acc-58.55%, F-Meas-56.76%, DB-FOOT-IR-Acc-58.5%, F-Meas-56.6%, DB-THY-IR- Acc-56.5%, F-Meas-55%**	**WFS**	68	70	65.5	70	69.76	70	65.5	69.56	68.11	70	62.17	69.5	69.58	72.01	61.13	69.53	64	68.19	62.9	67.5	62.07	67.4	64.31	66.64
			PC	75	75.14	78.57	81.67	75	76.16	80	83.05	74.74	74.17	78.64	80	73.96	73.06	79.97	80.00	72.24	73.74	76.37	77.07	73.26	72.62	75.57	76.55
			ChiSq	73.71	75.83	72.29	76.57	74.18	75.61	70.65	74.63	74.41	75.32	71.29	73.55	72.63	76.97	70.47	73.11	71.91	73.53	72.59	74.17	70.34	74.47	71.28	74.25
			mRMR	78	76.57	79.43	77.5	78	76.69	77.55	77.50	**80.53**	74.62	78.46	80	**81.42**	75.62	77	80.00	**82.3**	72.57	76.43	75	**81.41**	72.19	75.03	75.00
			ReF	80	**84.5**	75	80	80	**85.76**	75	80.00	80.58	80	71.94	80	80	80	71.58	80.00	80.2	77.34	70.14	80	80	77.17	69.94	80.00
5	**SAT[25]**	**DB-DMR-IR- Acc-77.5%, F-Meas-76.53%, DB-FOOT-IR-Acc-75%, F-Meas-73.75%, DB-THY-IR- Acc-74.5%, F-Meas-73.5%**	**WFS**	70	66	65	70	66.6	65	65	70.00	69.34	65.61	65.03	69.84	67.36	64.67	63.48	68.14	66.2	64.1	63.9	70.1	64.42	63.64	61.91	68.65
			PC	80	82.5	76.57	82.29	81.58	82.5	75.99	83.88	77.09	82.5	74.88	79.93	75.5	82.5	75.02	80.05	76.4	77.9	75.57	79.99	75.46	78.64	75.4	81.55
			ChiSq	80.86	72.29	72.5	75	80.43	72.91	72.5	75.00	77.75	75	73.68	73.67	79.25	75	73.1	72.25	78.36	75	73.8	72.54	76.61	75	73.34	74.37
			mRMR	**88.35**	78	81.67	85	**87.55**	76.59	80.59	85.00	**89.77**	73.34	76.99	85.29	**91.53**	73.79	75.98	86.93	**86.9**	73.3	76.77	83.8	**88.33**	74.46	74.93	83.82
			ReF	86.67	76.67	80.86	87.5	86.72	75	80.99	87.50	84.87	76.51	78.46	85.5	84.14	76.51	76.74	84.10	82.67	74.47	79.36	86.5	81.5	74.34	78.68	85.00
6	**KAR[28]**	**DB-DMR-IR- Acc-63.5%, F-Meas-60%, DB-FOOT-IR-Acc-54.5%, F-Meas-52%, DB-THY-IR- Acc-50%, F-Meas-50%**	**WFS**	62.29	63.33	63.33	65	61.65	62.47	64.54	65.00	60.41	63.24	63.67	64.74	61.63	63.89	61.82	64.61	58.79	62.13	61.43	63.7	57.68	63.47	62.18	63.42
			PC	70	77	72.5	73.71	70	78.53	72.5	72.14	81.05	76.79	73.09	74.86	80.31	75.76	74.4	73.94	79.66	72.7	72.8	72.71	81.56	71.45	72.49	73.88
			ChiSq	73.55	72.29	72.5	75	71.66	70.65	72.5	75.00	79.97	73.64	74.22	74.87	79.03	72.5	74.12	76.57	76.86	73.99	71.5	73.64	76.83	73.44	71.5	73.06
			mRMR	80	69.4	70.86	73.71	80	68.63	71.81	72.46	**83.19**	76.02	72.25	76.68	**82.17**	77.56	72.34	75.35	81.6	78.4	73.86	76.61	80.49	77.4	73.53	77.67
			ReF	72	**83.58**	75.83	80.5	70	**84.05**	75.79	80.60	81.72	81.05	75	81.05	79.84	80	75	82.29	77.86	**82.081**	72.93	79.1	78.7	**82.621**	74.92	78.47
7	**CRZ[26]**	**DB-DMR-IR- Acc-70.13%, F-Meas-70%, DB-FOOT-IR-Acc-67.6%, F-Meas-66.6%, DB-THY-IR- Acc-63.75%, F-Meas-62.5%**	**WFS**	68	70.83	71.57	70	65	68.5	66	70.00	69.68	67.55	68.71	70	70.71	67.02	66.94	70.00	68.6	67.93	68.77	68.4	69.26	68.88	70.62	67.13
			PC	75	80	80	80.48	73.54	80	80	82.80	78.83	81.77	76.59	83.58	77.7	81.36	76.02	83.91	77.7	78.7	77.9	**81.14**	78.13	76.83	77.32	**80.69**
			ChiSq	72	75.83	77.5	78	70	75.75	77.5	77.19	75.27	74.89	78.16	77.83	76.32	74.28	79.26	77.66	72.24	73.73	75.6	76.4	71.91	73.17	74.76	76.29
			mRMR	80	75.2	75	80	80	76.98	75	80.00	83.82	75	72.7	76.81	84.97	75	71.21	75.24	80.9	77.8	72.54	78.1	79.67	76.95	72.01	77.56
			ReF	70	77.5	76.57	**85.14**	80.51	77.65	76.35	**83.50**	78.28	82.45	75.52	**84.08**	76.79	81.91	75.33	**83.698**	78.4	79.14	72.27	**81.14**	77.33	80.77	70.95	**80.62**
8	**BAR[15]**	**DB-DMR-IR- Acc-69.5%, F-Meas-66.66%, DB-FOOT-IR-Acc-53.5%, F-Meas-52%, DB-THY-IR-Acc-51%, F-Meas-50%**	**WFS**	68.5	**72.5**	66.5	67	69.34	70	65	67.00	72	71.5	62.81	65.74	70	66.36	61.48	66.03	71.5	65.5	63.7	65.5	70	65.5	64.09	64.16
			PC	86.57	86.57	80	85.14	85.65	85.91	80	85.49	84.94	85	79.2	83.65	83.61	87.87	78.13	84.22	82.9	88.89	78.66	81.97	83.69	87.98	78.22	83.04
			ChiSq	80.86	86.57	76.57	87.43	80.54	84.95	75.43	88.45	83.97	86.18	74.01	83.2	83.75	84.27	73.82	83.80	83.8	85.2	74.01	80.46	84.16	83.4	74.19	78.75
			mRMR	91.86	89.43	83.71	88	91.71	87.79	83.3	87.78	90	83.09	82.58	87.7	90	82.11	81.82	86.15	**89.1**	81.43	78.67	84.53	**87.2**	81.55	77.65	83.04
			ReF	89.5	88	82.29	**92.28**	89.3	88	81.68	**91.72**	86.5	84.74	80.8	**91.5**	86.14	82.79	81.17	**90.07**	86.09	85.7	81.41	88.45	84.18	87.69	80	86.47
9	**GUP**	**DB-DMR-IR- Acc-80%, FMeas-80%, DB-FOOT-IR-Acc-75%, FMeas-72.8%, DB-THY-IR- Acc-88.57%, F-Meas-88.46%**	**WFS**	68.5	71.5	71.5	71.66	68.5	72.06	70	70.00	69.68	73.04	68.57	73.95	68.78	71.17	66.62	75.29	67.3	70.77	70	70.1	67.76	70.42	70	68.52
			PC	85.14	88.86	76.57	87.5	84.67	87.29	75.99	89.09	82.5	85.6	75.49	85.28	82.79	83.69	73.62	84.88	80.84	84.16	75.57	86.2	80	82.63	76.47	85.76
			ChiSq	86.57	86.57	79.43	85.14	85.51	86	80	85.94	83.29	82.27	77.65	85.7	81.76	82.56	75.74	86.63	81.87	81.67	74.73	83.64	81.55	80	75.13	82.81
			mRMR	90.71	88	77.6	87.5	92.5	88	77.18	87.50	88.41	81.38	77.36	84.08	86.5	82.66	79.08	83.87	88.51	82.5	74.2	83	87.96	82.5	74.58	83.76
			ReF	90	87.5	75.71	**90.86**	90	88	74.98	**90.53**	86.83	84.93	79.15	**90.30**	86.18	85.53	79	**88.835**	87.5	82.9	71.91	**89.56**	87.5	83.72	72.9	**87.87**
10	**UnionFeature_Set**		**WFS**	65.14	63.5	62	70	66.06	68	67.59	67.00	55	60	55	66.5	55	55	50	60.00	61.24	63.6	67.33	70.9	59.58	63.39	66.08	72.32
			PC	89.6	93.16	87.5	91.66	92.5	92.65	87.5	92.28	88	90	88.58	90.5	86.18	90.51	86.87	91.67	86.37	91.23	86.1	89.46	84.46	90.24	85.94	90.78
			ChiSq	92.17	90.29	87.5	91.5	93.88	91.51	87.5	92.36	89.85	89.48	90	88.48	91.07	89.07	87.54	86.74	90.15	86.5	87.57	86.6	88.28	88.18	86.08	87.70
			mRMR	**94.75**	90	88.5	90	**93.8**	90	85	90.00	**93.14**	92.38	88.68	92.95	**92.55**	90	89.03	90.21	90.07	88.39	86.4	88.8	89.85	86.3	87.55	88.32
			ReF	90	90.29	90	93.67	90.98	91.92	90.85	95.69	88.37	90.23	90	92.5	86.55	88.66	90	91.16	89.5	85.99	85.8	**92.06**	88.84	86.39	84.17	**91.42**

- Without feature selection and among nine individual research works, the feature-set suggested in the work BAR[15] gave the best result for DB-DMR-IR with k-NN and DB-THY-IR with SVM. The features set suggested in the feature-set GUP gave the best performance for DB-FOOT-IR with k-NN and RFC. With feature selection also and all the datasets, the feature-set suggested in work BAR[15] gave better performance than the other eight research works.

- Finally, the combination of features (UnionFeature_Set) provides maximum classification accuracy of 94.75% for DB-DMR-IR and 93.14% for DB-FOOT-IR datasets with the combination of mRMR and SVM. The dataset DB-THY-IR gave an accuracy of 92.06% with the combination of RFC and ReF. The F-Measure obtained are 93.80%, 92.55%, and 91.42% for DB-DMR-IR, DB-FOOT-IR, and DB-THY-IR datasets, respectively. Similar results on DB-DMR-IR and DB-FOOT-IR are obtained with the combination of ReF and RFC.

- Majority of the FE methods (RAS[24], SCH[23], SAT[25], GUP and CRZ[26]) performed better with the combination of [mRMR and SVM] and [Ref and RFC] for DB-DMR-IR dataset. All the feature extraction methods gave the best results with the same combinations ([mRMR and SVM] and [Ref and RFC]) for DB-FOOT-IR and DB-THY-IR datasets.

- GLCM and GLRM-based features suggested in research works ACH[2], CRZ[26], and KAR[28], have not yielded satisfactory results for all the datasets with and Without FS (WFS) methods. Amongst the nine FE methods, the worst performance is shown by the feature-set suggested in KAR[28] for all the datasets, without using any FS method. With feature selection, the average performance of the feature extraction methods KAR[28] and CRZ[26] is minimum for all the datasets.

- Amongst four classifiers, the best performance is achieved with SVM or RFC for most of the feature-sets on all the datasets.

- The combinations of [mRMR and SVM] and [Ref and RFC] performed better in the majority of the ten feature-sets for all the datasets.

- DTC did not perform effectively for most of the research works and datasets.

3.4.2 Comparison of Combinations of FE and FS Methods

This subsection investigates the performance of four FS methods in conjunction with the nine feature extraction methods suggested in the literature individually and their combination (UnionFeature_Set). The results are validated statistically also.

Figure 3.8 illustrates the comparison of average classification accuracy (over 4 different classifiers) for a combination of feature extraction and selection method on three datasets, respectively. The following can be observed from Figure 3.8, about the various combinations:

- For each FS method, the average performance improved significantly compared to Without FS, in terms of accuracy and F-Measure, for each feature extraction method.
- The average performance achieved with all the four FS methods on UnionFeature_Set is better than feature selection on all of the individual nine feature-sets suggested in the literature.
- On average, the performance of ReF and mRMR is similar and better than PC and ChiSq for the majority of the feature extraction methods and all the datasets.

The relative performance of 40 combinations of 10 feature extraction and 4 FS methods for all the datasets separately is investigated with the help of a robust ranking mechanism[121]. This method ranks the combinations based on their net improvement in performance with reference to the worst performance (m_c^{WFS}) obtained among 10 FE methods and without any feature selection and best performance (M_c). Let N and n_c denote the number of combinations (= 40) of feature extraction and selection methods and the number of classifiers (= 4). The average percentage improvement in accuracy, ($g_i, i = \{1, 2, ..., N\}$), of a combination i, is calculated as follows:

$$g_i = \frac{1}{n_c} \sum_{c=1}^{n_c} \frac{a_{ic} - m_c^{WFS}}{M_c - m_c^{WFS}} \times 100 \tag{3.13}$$

where a_{ic} is the accuracy achieved for the model with combination i and classifier c. The rank of a combination i, r_i , is assigned as $r_a \leq r_b$ if $g_a \geq g_b$.

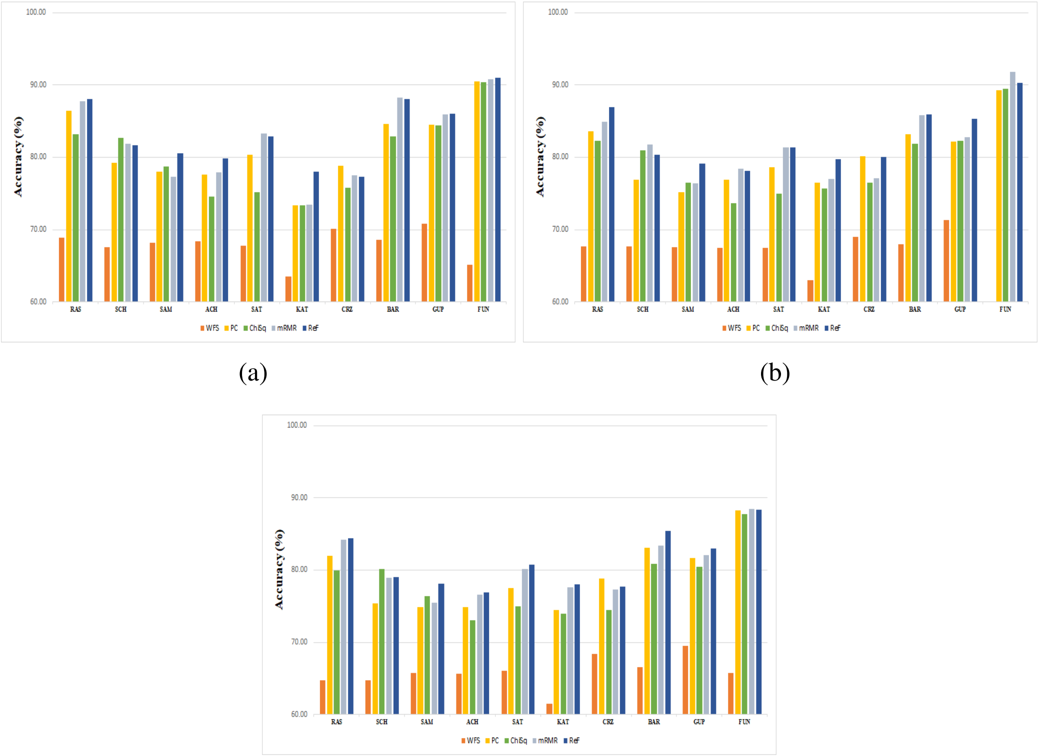

(a) (b)

(c)

Fig. 3.8: Comparison of the average classification accuracy values for a given combination of feature extraction and selection method for DB-DMR-IR (a), DB-FOOT-IR (b), and DB-THY-IR (c) datasets.

Table 3.6 shows net percentage improvement in accuracy for all combinations of feature extraction and selection methods for all the datasets. Figure 3.9 illustrate ranking of the combinations obtained by sorting the improvement in accuracy values in descending order for all the datasets, respectively. Following is observed from Table 3.6 and Figure 3.9:

- The improvement in relative accuracy (%) with the combination of Union-Feature_Set and any feature selection is higher than any other combination for all the datasets. The maximum improvement in accuracy is achieved with the ReF and mRMR for all the datasets, respectively.
- The improvement in performance with feature-set used in the research work KAR[28], SAM[27] and ACH[2] is worse for all the datasets.
- ReF and mRMR FS methods achieved higher net profit/improvement in accuracy compared to PC and ChiSq, for most of the research works, in individual and in combination, and all the datasets. ReF and mRMR both take

care of the correlation between the features and minimize the redundancy in the feature set.

Table 3.6: Performance Improvement (%) in Accuracy for all the combinations of feature extraction and selection methods.

S. No	Combinations of FE and FS Methods	DMR-IR	DB-FOOT-IR	DB-THY-IR	S. No	Combinations of FE and FS Methods	DMR-IR	DB-FOOT-IR	DB-THY-IR
1	UnionFeature_Set+ReF(FUN+ReF)	**93.93**	94.82	93.33	21	[23]+ReF(SCH+ReF)	62.12	65.49	60.69
2	UnionFeature_Set+mRMR(FUN+mRMR)	92.81	**99.05**	**93.53**	22	[27]+ReF(SAM+ReF)	58.78	60.82	58.08
3	UnionFeature_Set+PC(FUN+PC)	92.05	91.61	93.32	23	[25]+PC(SAT+PC)	57.79	59.51	55.78
4	UnionFeature_Set+C2Sq(FUN+C2Sq)	91.48	91.64	91.12	24	[2]+ReF(ACH+ReF)	56.07	57.84	53.29
5	[15]+mRMR(BAR+mRMR)	84.09	80.82	75.82	25	[23]+PC(SCH+PC)	54.16	54.92	48.45
6	[24]+ReF(RAS+ReF)	83.65	84.83	79.64	26	[26]+PC(CRZ+PC)	53.33	64.54	60.69
7	[15]+ReF(BAR+ReF)	83.54	81.89	83.10	27	[27]+C2Sq(SAM+C2Sq)	52.63	52.71	52.13
8	[24]+mRMR(RAS+mRMR)	82.46	78.12	78.79	28	[28]+ReF(KAR+ReF)	50.32	62.50	57.30
9	[24]+PC(RAS+PC)	78.04	74.01	70.84	29	[27] +PC(SAM+PC)	50.07	48.67	46.76
10	GUP + ReF	76.39	80.01	73.96	30	[2]+mRMR(ACH+mRMR)	49.66	58.31	52.31
11	GUP+mRMR	76.12	71.51	70.77	31	[2]+PC(ACH+PC)	49.02	54.29	47.06
12	[15]+PC(BAR+PC)	71.81	72.97	75.02	32	[26]+ReF(CRZ+ReF)	48.39	64.35	56.39
13	GUP+PC	71.63	70.62	70.18	33	[26]+mRMR(CRZ+mRMR)	48.27	53.81	54.80
14	GUP+C2Sq(GUP+C2Sq)	71.30	70.49	65.82	34	[27] +mRMR(SAM+mRMR)	47.40	52.20	48.41
15	[25]+mRMR(SAT+mRMR)	67.36	67.00	64.67	35	[26]+C2Sq(CRZ+C2Sq)	43.13	52.92	45.75
16	[24]+C2Sq(RAS+C2Sq)	66.72	70.32	64.14	36	[25]+C2Sq(SAT+C2Sq)	39.90	47.74	46.64
17	[25]+ReF(SAT+ReF)	66.41	67.48	67.09	37	[2]+C2Sq(ACH+C2Sq)	38.55	43.99	40.55
18	[15]+C2Sq(BAR+C2Sq)	66.35	69.13	66.92	38	[28]+PC(KAR+PC)	34.37	51.93	44.92
19	[23]+C2Sq(SCH+C2Sq)	65.86	66.40	65.09	39	[28]+C2Sq(KAR+C2Sq)	34.27	49.60	43.40
20	[23]+mRMR(SCH+mRMR)	62.44	68.25	60.05	40	[28]+mRMR(KAR+mRMR)	34.23	53.75	55.79

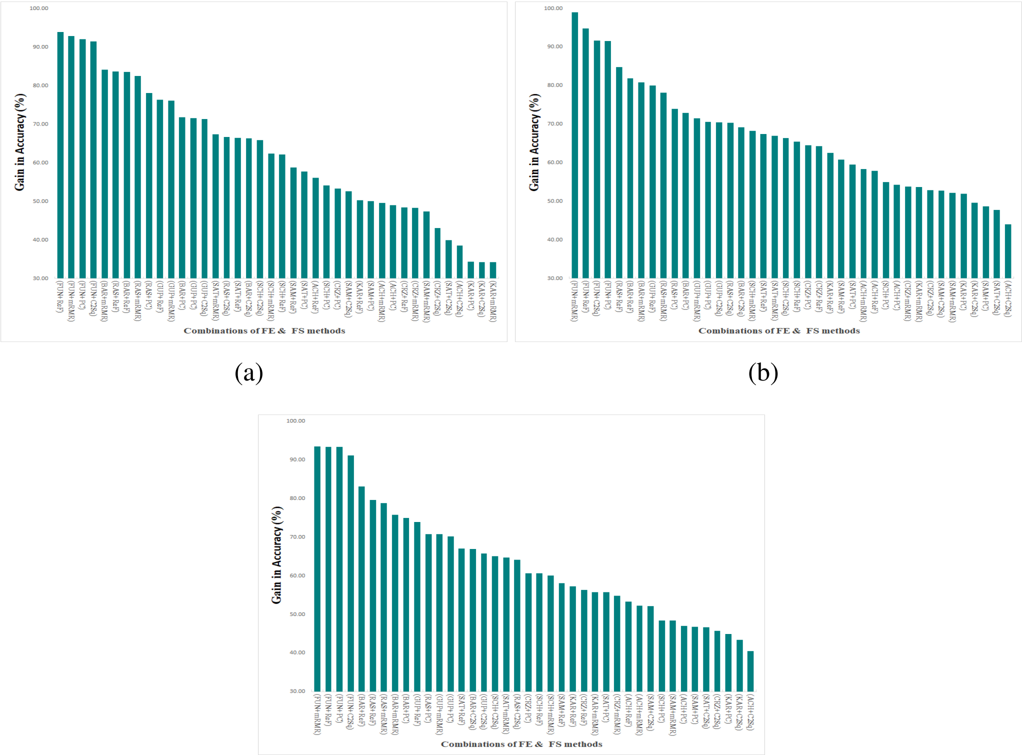

(a) (b)

(c)

Fig. 3.9: Ranking of combinations of feature extraction and selection methods based on Performance Improvement (%) for DB-DMR-IR (a), DB-FOOT-IR (b) and DB-THY-IR (c) datasets.

3.4.3 Comparison of Features (GUP and UnionFeature_Set)

This section introspects the performance of proposed feature sets - UnionFeature_Set and GUP, having a total of 467 and 101, respectively, distinct features, quantitatively and qualitatively. The accuracy and F-Measure values of the experiments with UnionFeature_Set and GUP on the proposed framework are stated in the last two rows of Table 3.5.

Table 3.7: The Features (GUP feature-set) and their p-Values with which the best result is obtained for all the datasets.

Feature Name	**DB-DMR-IR**	**DB-FOOT-IR**	**DB-THY-IR**
Mean	0.051	0.0611	0.0217
Variance	0.059	0.0756	0.0267
Skewness	0.046	0.0593	0.0185
Kurtosis	0.041	0.0588	0.0122
Entropy$_{LBP}$	0.024	0.0365	0.0763
Otsu Threshold	0.023	0.0294	0.0222
Entropy$_{GLCM}$	0.071	0.0337	0.0291
contrast	0.042	0.0471	0.0522
Correlation	**0.0034**	**0.0058**	**0.0002**
Energy	0.014	**0.0089**	0.5771
Sum variance	0.027	0.0310	0.0246
Sum entropy	0.0241	0.0304	0.0234
Difference variance	**0.0044**	**0.0087**	**0.0020**
Homogeneity	0.0151	0.0686	0.0760
Sum average	0.0625	0.0555	0.0527
Information measure of correlation	0.022	**0.0010**	0.0151

Table 3.7 presents the features in the GUP feature set along with their corresponding p-values across all datasets. The reported p-values for DB-DMR-IR and DB-FOOT-IR are obtained by averaging them over both subsets (D1 and D2). Additionally, the statistical features derived from LBP are averaged across all 18 grids to compute the p-values. The table indicates that Energy and Correlation are statistically significant for analyzing thermal patterns at a 1% significance level across all health conditions. Meanwhile, the Otsu-Threshold exhibits a marginally significant difference between normal and abnormal thermal images across all datasets.

The Table 3.8 displays the subset of features for which the best result is obtained for all the datasets, along with their p-values using the T-Test. Tables 3.9, 3.10, and 3.11 present the color map of correlation matrices of the features with which the best performance is achieved for the three datasets, respectively. The absolute value of the correlation between a feature pair is considered. Following observations are made from Tables 3.8, 3.9, 3.10, and 3.11 for the experiments conducted on UnionFeature_Set:

- UnionFeature_Set performed best with a reduced set of 45 and 57 features for DB-DMR-IR, DB-FOOT-IR selected with mRMR and 39 features for DB-THY-IR selected using ReF, wherein the features are from the research works, SCH[23], RAS[24], SAT[25], BAR[15], GUP, and ACH[2].
- Majority of the features in feature subset (Table 3.8) that gave the best results are found to be relevant at the significance level, $\alpha = 0.01$, for all the datasets. Also, most of them (RAS[24], BAR[15], GUP, and ACH[2]) are common for the datasets considered.
- Most of the best-performing features (Table 3.8) are minimally correlated to each other for all the datasets (cell colors are lighter red in shade(orange), Tables 3.9, 3.10 and 3.11).
- Features proposed by BAR[15] are found to be the most prominent features for discriminating against abnormal thermal patterns.
- The thermal patterns for abnormality due to inflammation are best distinguished when the features (Histogram-based features, First Order Statistical features, Texture-based features, and LBP-based features) are computed from the segmented region of interest (BAR[15] and CRZ[26]).

Also, the qualitative analysis of the best-performing models (stated in table 3.4) is performed using Explainable AI with SHapley Additive exPlanation (SHAP) [122, 123, 124]. SHAP explains the prediction given by a classification model using a game theory-based approach. It uses Shapley values to measure the contribution of features in predicting the outcome of the model. The Python SHAP library is used to understand the feature's importance in predicting abnormality in the human body, captured in thermal images. To analyze the importance of the features in UnionFeature_Set, all the 467 features with the model (with tuned parameters) are passed to SHAP Explainer to analyze their importance.

Table 3.9: The colour map of the correlation matrix for the features with which the best result is obtained for DB-DMR-IR dataset.

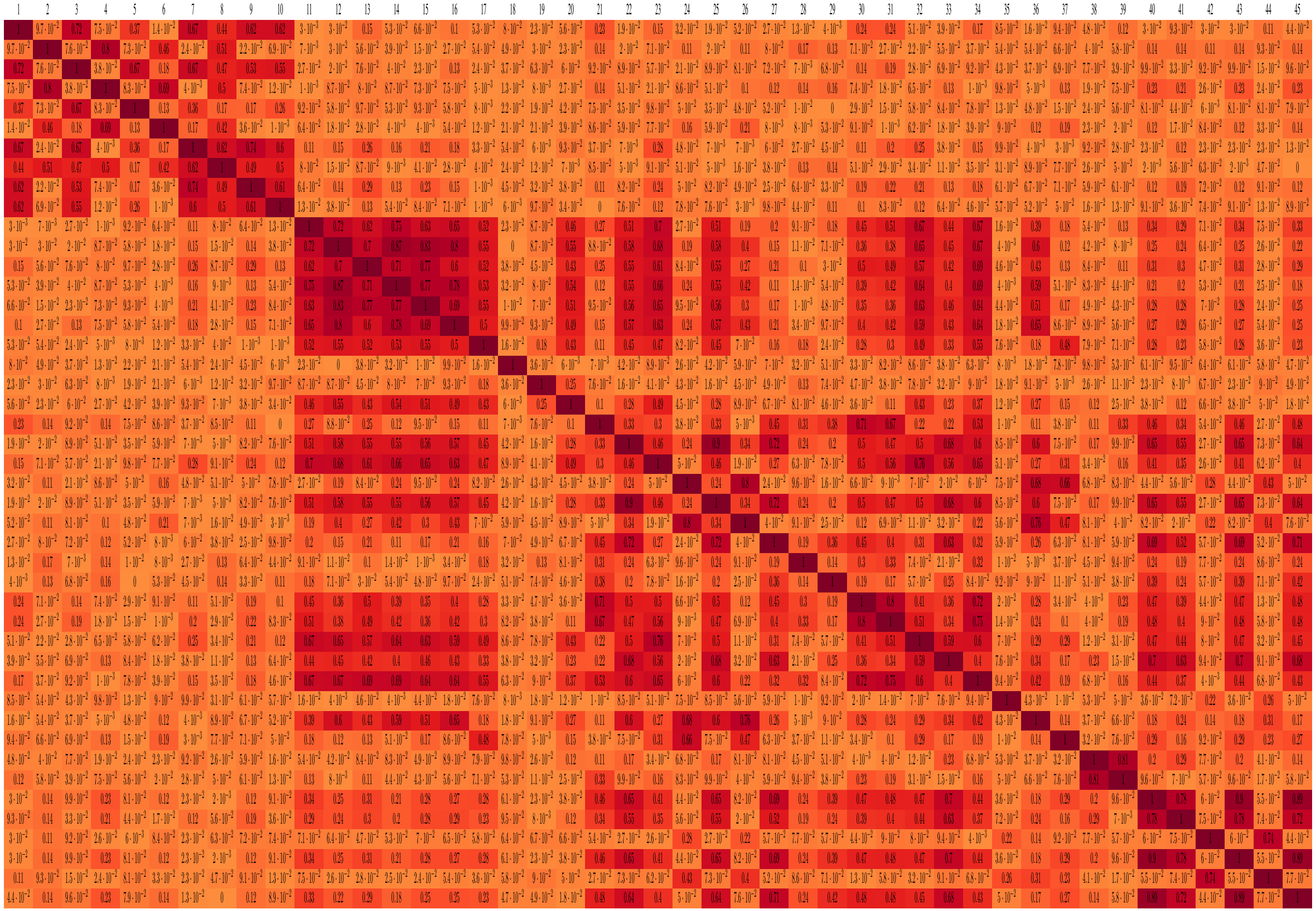

1	2	3	4	5	6	7	8	9	10	11	12	13	14	15	16	17	18	19	20	21	22	23	24	25	26	27	28	29	30	31	32	33	34	35	36	37	38	39	40	41	42	43	44	45
1	$9.7\cdot10^{-2}$	0.72	$7.5\cdot10^{-2}$	0.37	$1.4\cdot10^{-2}$	0.67	0.44	0.62	0.62	$3\cdot10^{-3}$	$3\cdot10^{-2}$	0.15	$5.3\cdot10^{-2}$	$6.6\cdot10^{-2}$	0.1	$5.3\cdot10^{-2}$	$8\cdot10^{-2}$	$2.3\cdot10^{-2}$	$5.6\cdot10^{-2}$	0.23	$1.9\cdot10^{-2}$	0.15	$3.2\cdot10^{-2}$	$1.9\cdot10^{-2}$	$5.2\cdot10^{-2}$	$2.7\cdot10^{-2}$	$1.3\cdot10^{-2}$	$4\cdot10^{-3}$	0.24	0.24	$5.1\cdot10^{-2}$	$3.9\cdot10^{-2}$	0.17	$8.5\cdot10^{-2}$	$1.6\cdot10^{-2}$	$9.4\cdot10^{-2}$	$4.8\cdot10^{-2}$	0.12	$3\cdot10^{-2}$	$9.3\cdot10^{-2}$	$3\cdot10^{-2}$	$3\cdot10^{-2}$	0.11	$4.4\cdot10^{-2}$
$9.7\cdot10^{-2}$	1	$7.6\cdot10^{-2}$	0.8	$7.3\cdot10^{-2}$	0.46	$2.4\cdot10^{-2}$	0.51	$2.2\cdot10^{-2}$	$6.9\cdot10^{-2}$	$7\cdot10^{-3}$	$3\cdot10^{-2}$	$5.6\cdot10^{-2}$	$3.9\cdot10^{-2}$	$1.5\cdot10^{-2}$	$2.7\cdot10^{-2}$	$5.4\cdot10^{-2}$	$4.9\cdot10^{-2}$	$3\cdot10^{-2}$	$2.3\cdot10^{-2}$	0.14	$2\cdot10^{-2}$	$7.1\cdot10^{-2}$	0.11	$2\cdot10^{-2}$	0.11	$8\cdot10^{-2}$	0.17	0.13	$7.1\cdot10^{-2}$	$2.7\cdot10^{-2}$	$2.2\cdot10^{-2}$	$5.5\cdot10^{-2}$	$3.7\cdot10^{-2}$	$5.4\cdot10^{-2}$	$5.4\cdot10^{-2}$	$6.6\cdot10^{-2}$	$4\cdot10^{-2}$	$5.8\cdot10^{-2}$	0.14	0.14	0.11	0.14	$9.3\cdot10^{-2}$	0.14
0.72	$7.6\cdot10^{-2}$	1	$3.8\cdot10^{-2}$	0.67	0.18	0.67	0.47	0.53	0.55	$2.7\cdot10^{-2}$	$2\cdot10^{-2}$	$7.6\cdot10^{-2}$	$4\cdot10^{-2}$	$2.3\cdot10^{-2}$	0.13	$2.4\cdot10^{-2}$	$3.7\cdot10^{-2}$	$6.3\cdot10^{-2}$	$6\cdot10^{-2}$	$9.2\cdot10^{-2}$	$8.9\cdot10^{-2}$	$5.7\cdot10^{-2}$	$2.1\cdot10^{-2}$	$8.9\cdot10^{-2}$	$8.1\cdot10^{-2}$	$7.2\cdot10^{-2}$	$7\cdot10^{-3}$	$6.8\cdot10^{-2}$	0.14	0.19	$2.8\cdot10^{-2}$	$6.9\cdot10^{-2}$	$9.2\cdot10^{-2}$	$4.3\cdot10^{-2}$	$3.7\cdot10^{-2}$	$6.9\cdot10^{-2}$	$7.7\cdot10^{-2}$	$3.9\cdot10^{-2}$	$9.9\cdot10^{-2}$	$3.3\cdot10^{-2}$	$9.2\cdot10^{-2}$	$9.9\cdot10^{-2}$	$1.5\cdot10^{-2}$	$9.6\cdot10^{-2}$
$7.5\cdot10^{-2}$	0.8	$3.8\cdot10^{-2}$	1	$8.3\cdot10^{-2}$	0.69	$4\cdot10^{-3}$	0.5	$7.4\cdot10^{-2}$	$1.2\cdot10^{-2}$	$1\cdot10^{-3}$	$8.7\cdot10^{-2}$	$8\cdot10^{-2}$	$8.7\cdot10^{-2}$	$7.3\cdot10^{-2}$	$7.5\cdot10^{-2}$	$5\cdot10^{-3}$	$1.3\cdot10^{-2}$	$8\cdot10^{-3}$	$2.7\cdot10^{-2}$	0.14	$5.1\cdot10^{-2}$	$2.1\cdot10^{-2}$	$8.6\cdot10^{-2}$	$5.1\cdot10^{-2}$	0.1	0.12	0.14	0.16	$7.4\cdot10^{-2}$	$1.8\cdot10^{-2}$	$6.5\cdot10^{-2}$	0.13	$1\cdot10^{-3}$	$9.8\cdot10^{-2}$	$5\cdot10^{-3}$	0.13	$1.9\cdot10^{-2}$	$7.5\cdot10^{-2}$	0.23	0.21	$2.6\cdot10^{-2}$	0.23	$2.4\cdot10^{-2}$	0.23
0.37	$7.3\cdot10^{-2}$	0.67	$8.3\cdot10^{-2}$	1	0.13	0.36	0.17	0.17	0.26	$9.2\cdot10^{-2}$	$5.8\cdot10^{-2}$	$9.7\cdot10^{-2}$	$5.3\cdot10^{-2}$	$9.3\cdot10^{-2}$	$5.8\cdot10^{-2}$	$8\cdot10^{-3}$	$2.2\cdot10^{-2}$	$1.9\cdot10^{-2}$	$4.2\cdot10^{-2}$	$7.5\cdot10^{-2}$	$3.5\cdot10^{-2}$	$9.8\cdot10^{-2}$	$5\cdot10^{-2}$	$3.5\cdot10^{-2}$	$4.8\cdot10^{-2}$	$5.2\cdot10^{-2}$	$1\cdot10^{-2}$	0	$2.9\cdot10^{-2}$	$1.5\cdot10^{-2}$	$5.8\cdot10^{-2}$	$8.4\cdot10^{-2}$	$7.8\cdot10^{-2}$	$1.3\cdot10^{-2}$	$4.8\cdot10^{-2}$	$1.5\cdot10^{-2}$	$2.4\cdot10^{-2}$	$5.6\cdot10^{-2}$	$8.1\cdot10^{-2}$	$4.4\cdot10^{-2}$	$6\cdot10^{-3}$	$8.1\cdot10^{-2}$	$8.1\cdot10^{-2}$	$7.9\cdot10^{-2}$
$1.4\cdot10^{-2}$	0.46	0.18	0.69	0.13	1	0.17	0.42	$3.6\cdot10^{-2}$	$1\cdot10^{-3}$	$6.4\cdot10^{-2}$	$1.8\cdot10^{-2}$	$2.8\cdot10^{-2}$	$4\cdot10^{-3}$	$4\cdot10^{-3}$	$5.4\cdot10^{-2}$	$1.2\cdot10^{-2}$	$2.1\cdot10^{-2}$	$2.1\cdot10^{-2}$	$3.9\cdot10^{-2}$	$8.6\cdot10^{-2}$	$5.9\cdot10^{-2}$	$7.7\cdot10^{-2}$	0.16	$5.9\cdot10^{-2}$	0.21	$8\cdot10^{-3}$	$8\cdot10^{-3}$	$5.3\cdot10^{-2}$	$9.1\cdot10^{-2}$	$1\cdot10^{-3}$	$6.2\cdot10^{-2}$	$1.8\cdot10^{-2}$	$3.9\cdot10^{-2}$	$9\cdot10^{-2}$	0.12	0.19	$2.3\cdot10^{-2}$	$2\cdot10^{-2}$	0.12	$1.7\cdot10^{-2}$	$8.4\cdot10^{-2}$	0.12	$3.3\cdot10^{-2}$	0.14
0.67	$2.4\cdot10^{-2}$	0.67	$4\cdot10^{-3}$	0.36	0.17	1	0.62	0.74	0.6	0.11	0.15	0.26	0.16	0.21	0.18	$3.3\cdot10^{-2}$	$5.4\cdot10^{-2}$	$6\cdot10^{-3}$	$9.3\cdot10^{-2}$	$3.7\cdot10^{-2}$	$7\cdot10^{-3}$	0.28	$4.8\cdot10^{-2}$	$7\cdot10^{-3}$	$7\cdot10^{-3}$	$6\cdot10^{-2}$	$2.7\cdot10^{-2}$	$4.5\cdot10^{-2}$	0.11	0.2	0.25	$3.8\cdot10^{-2}$	0.15	$9.9\cdot10^{-2}$	$4\cdot10^{-3}$	$3\cdot10^{-3}$	$9.2\cdot10^{-2}$	$2.8\cdot10^{-2}$	$2.3\cdot10^{-2}$	0.12	$2.3\cdot10^{-2}$	$2.3\cdot10^{-2}$	$2.3\cdot10^{-2}$	$1.3\cdot10^{-2}$
0.44	0.51	0.47	0.5	0.17	0.42	0.62	1	0.49	0.5	$8\cdot10^{-2}$	$1.5\cdot10^{-2}$	$8.7\cdot10^{-2}$	$9\cdot10^{-3}$	$4.1\cdot10^{-2}$	$2.8\cdot10^{-2}$	$4\cdot10^{-2}$	$2.4\cdot10^{-2}$	$1.2\cdot10^{-2}$	$7\cdot10^{-3}$	$8.5\cdot10^{-2}$	$5\cdot10^{-3}$	$9.1\cdot10^{-2}$	$5.1\cdot10^{-2}$	$5\cdot10^{-3}$	$1.6\cdot10^{-2}$	$3.8\cdot10^{-2}$	0.13	0.14	$5.1\cdot10^{-2}$	$2.9\cdot10^{-2}$	$3.4\cdot10^{-2}$	$1.1\cdot10^{-2}$	$3.5\cdot10^{-2}$	$3.1\cdot10^{-2}$	$8.9\cdot10^{-2}$	$7.7\cdot10^{-2}$	$2.6\cdot10^{-2}$	$5\cdot10^{-2}$	$2\cdot10^{-3}$	$5.6\cdot10^{-2}$	$6.3\cdot10^{-2}$	$2\cdot10^{-3}$	$4.7\cdot10^{-2}$	0
0.62	$2.2\cdot10^{-2}$	0.53	$7.4\cdot10^{-2}$	0.17	$3.6\cdot10^{-2}$	0.74	0.49	1	0.61	$6.4\cdot10^{-2}$	0.14	0.29	0.13	0.23	0.15	$1\cdot10^{-3}$	$4.5\cdot10^{-2}$	$3.2\cdot10^{-2}$	$3.8\cdot10^{-2}$	0.11	$8.2\cdot10^{-2}$	0.24	$5\cdot10^{-2}$	$8.2\cdot10^{-2}$	$4.9\cdot10^{-2}$	$2.5\cdot10^{-2}$	$6.4\cdot10^{-2}$	$3.3\cdot10^{-2}$	0.19	0.22	0.21	0.13	0.18	$6.1\cdot10^{-2}$	$6.7\cdot10^{-2}$	$7.1\cdot10^{-2}$	$5.9\cdot10^{-2}$	$6.1\cdot10^{-2}$	0.12	0.19	$7.2\cdot10^{-2}$	0.12	$9.1\cdot10^{-2}$	0.12
0.62	$6.9\cdot10^{-2}$	0.55	$1.2\cdot10^{-2}$	0.26	$1\cdot10^{-3}$	0.6	0.5	0.61	1	$1.3\cdot10^{-2}$	$3.8\cdot10^{-2}$	0.13	$5.4\cdot10^{-2}$	$8.4\cdot10^{-2}$	$7.1\cdot10^{-2}$	$1\cdot10^{-3}$	$6\cdot10^{-3}$	$9.7\cdot10^{-2}$	$3.4\cdot10^{-2}$	0	$7.6\cdot10^{-2}$	0.12	$7.8\cdot10^{-2}$	$7.6\cdot10^{-2}$	$3\cdot10^{-3}$	$9.8\cdot10^{-2}$	$4.4\cdot10^{-2}$	0.11	0.1	$8.3\cdot10^{-2}$	0.12	$6.4\cdot10^{-2}$	$4.6\cdot10^{-2}$	$5.7\cdot10^{-2}$	$5.2\cdot10^{-2}$	$5\cdot10^{-2}$	$1.6\cdot10^{-2}$	$1.3\cdot10^{-2}$	$9.1\cdot10^{-2}$	$3.6\cdot10^{-2}$	$7.4\cdot10^{-2}$	$9.1\cdot10^{-2}$	$1.3\cdot10^{-2}$	$8.9\cdot10^{-2}$
$3\cdot10^{-3}$	$7\cdot10^{-3}$	$2.7\cdot10^{-2}$	$1\cdot10^{-3}$	$9.2\cdot10^{-2}$	$6.4\cdot10^{-2}$	0.11	$8\cdot10^{-2}$	$6.4\cdot10^{-2}$	$1.3\cdot10^{-2}$	1	0.72	0.62	0.75	0.63	0.65	0.52	$2.3\cdot10^{-2}$	$8.7\cdot10^{-2}$	0.46	0.27	0.51	0.7	$2.7\cdot10^{-2}$	0.51	0.19	0.2	$9.1\cdot10^{-2}$	0.18	0.45	0.51	0.67	0.44	0.67	$1.6\cdot10^{-2}$	0.39	0.18	$5.4\cdot10^{-2}$	0.13	0.34	0.29	$7.1\cdot10^{-2}$	0.34	$7.5\cdot10^{-2}$	0.33
$3\cdot10^{-2}$	$3\cdot10^{-2}$	$2\cdot10^{-2}$	$8.7\cdot10^{-2}$	$5.8\cdot10^{-2}$	$1.8\cdot10^{-2}$	0.15	$1.5\cdot10^{-2}$	0.14	$3.8\cdot10^{-2}$	0.72	1	0.7	0.87	0.83	0.8	0.55	0	$8.7\cdot10^{-2}$	0.55	$8.8\cdot10^{-2}$	0.58	0.68	0.19	0.58	0.4	0.15	$1.1\cdot10^{-2}$	$7.1\cdot10^{-2}$	0.36	0.38	0.65	0.45	0.67	$4\cdot10^{-3}$	0.6	0.12	$4.2\cdot10^{-2}$	$8\cdot10^{-3}$	0.25	0.24	$6.4\cdot10^{-2}$	0.25	$2.6\cdot10^{-2}$	0.22
0.15	$5.6\cdot10^{-2}$	$7.6\cdot10^{-2}$	$8\cdot10^{-2}$	$9.7\cdot10^{-2}$	$2.8\cdot10^{-2}$	0.26	$8.7\cdot10^{-2}$	0.29	0.13	0.62	0.7	1	0.71	0.77	0.6	0.52	$3.8\cdot10^{-2}$	$4.5\cdot10^{-2}$	0.43	0.25	0.55	0.61	$8.4\cdot10^{-2}$	0.55	0.27	0.21	0.1	$3\cdot10^{-2}$	0.5	0.49	0.57	0.42	0.69	$4.6\cdot10^{-2}$	0.43	0.13	$8.4\cdot10^{-2}$	0.11	0.31	0.3	$4.7\cdot10^{-2}$	0.31	$2.8\cdot10^{-2}$	0.29
$5.3\cdot10^{-2}$	$3.9\cdot10^{-2}$	$4\cdot10^{-2}$	$8.7\cdot10^{-2}$	$5.3\cdot10^{-2}$	$4\cdot10^{-3}$	0.16	$9\cdot10^{-3}$	0.13	$5.4\cdot10^{-2}$	0.75	0.87	0.71	1	0.77	0.78	0.53	$3.2\cdot10^{-2}$	$8\cdot10^{-2}$	0.54	0.12	0.55	0.66	0.24	0.55	0.42	0.11	$1.4\cdot10^{-2}$	$5.4\cdot10^{-2}$	0.39	0.42	0.64	0.4	0.69	$4\cdot10^{-3}$	0.59	$5.1\cdot10^{-2}$	$8.3\cdot10^{-2}$	$4.4\cdot10^{-2}$	0.21	0.2	$5.3\cdot10^{-2}$	0.21	$2.5\cdot10^{-2}$	0.18
$6.6\cdot10^{-2}$	$1.5\cdot10^{-2}$	$2.3\cdot10^{-2}$	$7.3\cdot10^{-2}$	$9.3\cdot10^{-2}$	$4\cdot10^{-3}$	0.21	$4.1\cdot10^{-2}$	0.23	$8.4\cdot10^{-2}$	0.63	0.83	0.77	0.77	1	0.69	0.55	$1\cdot10^{-2}$	$7\cdot10^{-2}$	0.51	$9.5\cdot10^{-2}$	0.56	0.65	$9.5\cdot10^{-2}$	0.56	0.3	0.17	$1\cdot10^{-3}$	$4.8\cdot10^{-2}$	0.35	0.36	0.63	0.46	0.64	$4.4\cdot10^{-2}$	0.51	0.17	$4.9\cdot10^{-2}$	$4.3\cdot10^{-2}$	0.28	0.28	$7\cdot10^{-2}$	0.28	$2.4\cdot10^{-2}$	0.25
0.1	$2.7\cdot10^{-2}$	0.13	$7.5\cdot10^{-2}$	$5.8\cdot10^{-2}$	$5.4\cdot10^{-2}$	0.18	$2.8\cdot10^{-2}$	0.15	$7.1\cdot10^{-2}$	0.65	0.8	0.6	0.78	0.69	1	0.5	$9.9\cdot10^{-2}$	$9.3\cdot10^{-2}$	0.49	0.15	0.57	0.63	0.24	0.57	0.43	0.21	$3.4\cdot10^{-2}$	$9.7\cdot10^{-2}$	0.4	0.42	0.59	0.43	0.64	$1.8\cdot10^{-2}$	0.65	$8.6\cdot10^{-2}$	$8.9\cdot10^{-2}$	$5.6\cdot10^{-2}$	0.27	0.29	$6.5\cdot10^{-2}$	0.27	$5.4\cdot10^{-2}$	0.25
$5.3\cdot10^{-2}$	$5.4\cdot10^{-2}$	$2.4\cdot10^{-2}$	$5\cdot10^{-3}$	$8\cdot10^{-3}$	$1.2\cdot10^{-2}$	$3.3\cdot10^{-2}$	$4\cdot10^{-2}$	$1\cdot10^{-3}$	$1\cdot10^{-3}$	0.52	0.55	0.52	0.53	0.55	0.5	1	$1.6\cdot10^{-2}$	0.18	0.43	0.11	0.45	0.47	$8.2\cdot10^{-2}$	0.45	$7\cdot10^{-2}$	0.16	0.18	$2.4\cdot10^{-2}$	0.28	0.3	0.49	0.33	0.55	$7.6\cdot10^{-2}$	0.18	0.48	$7.9\cdot10^{-2}$	$7.1\cdot10^{-2}$	0.28	0.23	$5.8\cdot10^{-2}$	0.28	$3.6\cdot10^{-2}$	0.23
$8\cdot10^{-2}$	$4.9\cdot10^{-2}$	$3.7\cdot10^{-2}$	$1.3\cdot10^{-2}$	$2.2\cdot10^{-2}$	$2.1\cdot10^{-2}$	$5.4\cdot10^{-2}$	$2.4\cdot10^{-2}$	$4.5\cdot10^{-2}$	$6\cdot10^{-3}$	$2.3\cdot10^{-2}$	0	$3.8\cdot10^{-2}$	$3.2\cdot10^{-2}$	$1\cdot10^{-2}$	$9.9\cdot10^{-2}$	$1.6\cdot10^{-2}$	1	$3.6\cdot10^{-2}$	$6\cdot10^{-3}$	$7\cdot10^{-3}$	$4.2\cdot10^{-2}$	$8.9\cdot10^{-2}$	$2.6\cdot10^{-2}$	$4.2\cdot10^{-2}$	$5.9\cdot10^{-2}$	$7\cdot10^{-2}$	$3.2\cdot10^{-2}$	$5.1\cdot10^{-2}$	$3.3\cdot10^{-2}$	$8.2\cdot10^{-2}$	$8.6\cdot10^{-2}$	$3.8\cdot10^{-2}$	$6.3\cdot10^{-2}$	$8\cdot10^{-3}$	$1.8\cdot10^{-2}$	$7.8\cdot10^{-2}$	$9.8\cdot10^{-2}$	$5.3\cdot10^{-2}$	$6.1\cdot10^{-2}$	$9.5\cdot10^{-2}$	$6.4\cdot10^{-2}$	$6.1\cdot10^{-2}$	$5.8\cdot10^{-2}$	$4.7\cdot10^{-2}$
$2.3\cdot10^{-2}$	$3\cdot10^{-2}$	$6.3\cdot10^{-2}$	$8\cdot10^{-3}$	$1.9\cdot10^{-2}$	$2.1\cdot10^{-2}$	$6\cdot10^{-3}$	$1.2\cdot10^{-2}$	$3.2\cdot10^{-2}$	$9.7\cdot10^{-2}$	$8.7\cdot10^{-2}$	$8.7\cdot10^{-2}$	$4.5\cdot10^{-2}$	$8\cdot10^{-2}$	$7\cdot10^{-2}$	$9.3\cdot10^{-2}$	0.18	$3.6\cdot10^{-2}$	1	0.25	$7.6\cdot10^{-2}$	$1.6\cdot10^{-2}$	$4.1\cdot10^{-2}$	$4.3\cdot10^{-2}$	$1.6\cdot10^{-2}$	$4.5\cdot10^{-2}$	$4.9\cdot10^{-2}$	0.13	$7.4\cdot10^{-2}$	$4.7\cdot10^{-2}$	$3.8\cdot10^{-2}$	$7.8\cdot10^{-2}$	$3.2\cdot10^{-2}$	$9\cdot10^{-2}$	$1.8\cdot10^{-2}$	$9.1\cdot10^{-2}$	$5\cdot10^{-3}$	$2.6\cdot10^{-2}$	$1.1\cdot10^{-2}$	$2.3\cdot10^{-2}$	$8\cdot10^{-3}$	$6.7\cdot10^{-2}$	$2.3\cdot10^{-2}$	$9\cdot10^{-2}$	$4.9\cdot10^{-2}$
$5.6\cdot10^{-2}$	$2.3\cdot10^{-2}$	$6\cdot10^{-2}$	$2.7\cdot10^{-2}$	$4.2\cdot10^{-2}$	$3.9\cdot10^{-2}$	$9.3\cdot10^{-2}$	$7\cdot10^{-3}$	$3.8\cdot10^{-2}$	$3.4\cdot10^{-2}$	0.46	0.55	0.43	0.54	0.51	0.49	0.43	$6\cdot10^{-3}$	0.25	1	0.1	0.28	0.49	$4.5\cdot10^{-2}$	0.28	$8.9\cdot10^{-2}$	$6.7\cdot10^{-2}$	$8.1\cdot10^{-2}$	$4.6\cdot10^{-2}$	$3.6\cdot10^{-2}$	0.11	0.43	0.23	0.37	$1.2\cdot10^{-2}$	0.27	0.15	0.12	$2.5\cdot10^{-2}$	$3.8\cdot10^{-2}$	0.12	$6.6\cdot10^{-2}$	$3.8\cdot10^{-2}$	$5\cdot10^{-2}$	$1.8\cdot10^{-2}$
0.23	0.14	$9.2\cdot10^{-2}$	0.14	$7.5\cdot10^{-2}$	$8.6\cdot10^{-2}$	$3.7\cdot10^{-2}$	$8.5\cdot10^{-2}$	0.11	0	0.27	$8.8\cdot10^{-2}$	0.25	0.12	$9.5\cdot10^{-2}$	0.15	0.11	$7\cdot10^{-3}$	$7.6\cdot10^{-2}$	0.1	1	0.33	0.3	$3.8\cdot10^{-2}$	0.33	$5\cdot10^{-3}$	0.45	0.31	0.38	0.71	0.67	0.22	0.22	0.53	$1\cdot10^{-2}$	0.11	$3.8\cdot10^{-2}$	0.11	0.33	0.46	0.34	$5.4\cdot10^{-2}$	0.46	$2.7\cdot10^{-2}$	0.48
$1.9\cdot10^{-2}$	$2\cdot10^{-2}$	$8.9\cdot10^{-2}$	$5.1\cdot10^{-2}$	$3.5\cdot10^{-2}$	$5.9\cdot10^{-2}$	$7\cdot10^{-3}$	$5\cdot10^{-3}$	$8.2\cdot10^{-2}$	$7.6\cdot10^{-2}$	0.51	0.58	0.55	0.55	0.56	0.57	0.45	$4.2\cdot10^{-2}$	$1.6\cdot10^{-2}$	0.28	0.33	1	0.46	0.24	0.9	0.34	0.72	0.24	0.2	0.5	0.47	0.5	0.68	0.6	$8.5\cdot10^{-2}$	0.6	$7.5\cdot10^{-2}$	0.17	$9.9\cdot10^{-2}$	0.65	0.55	$2.7\cdot10^{-2}$	0.65	$7.3\cdot10^{-2}$	0.64
0.15	$7.1\cdot10^{-2}$	$5.7\cdot10^{-2}$	$2.1\cdot10^{-2}$	$9.8\cdot10^{-2}$	$7.7\cdot10^{-2}$	0.28	$9.1\cdot10^{-2}$	0.24	0.12	0.7	0.68	0.61	0.66	0.65	0.63	0.47	$8.9\cdot10^{-2}$	$4.1\cdot10^{-2}$	0.49	0.3	0.46	1	$5\cdot10^{-2}$	0.46	$1.9\cdot10^{-2}$	0.27	$6.3\cdot10^{-2}$	$7.8\cdot10^{-2}$	0.5	0.56	0.76	0.56	0.65	$5.1\cdot10^{-2}$	0.27	0.31	$3.4\cdot10^{-2}$	0.16	0.41	0.35	$2.6\cdot10^{-2}$	0.41	$6.2\cdot10^{-2}$	0.4
$3.2\cdot10^{-2}$	0.11	$2.1\cdot10^{-2}$	$8.6\cdot10^{-2}$	$5\cdot10^{-2}$	0.16	$4.8\cdot10^{-2}$	$5.1\cdot10^{-2}$	$5\cdot10^{-2}$	$7.8\cdot10^{-2}$	$2.7\cdot10^{-2}$	0.19	$8.4\cdot10^{-2}$	0.24	$9.5\cdot10^{-2}$	0.24	$8.2\cdot10^{-2}$	$2.6\cdot10^{-2}$	$4.3\cdot10^{-2}$	$4.5\cdot10^{-2}$	$3.8\cdot10^{-2}$	0.24	$5\cdot10^{-2}$	1	0.24	0.8	$2.4\cdot10^{-2}$	$9.6\cdot10^{-2}$	$1.6\cdot10^{-2}$	$6.6\cdot10^{-2}$	$9\cdot10^{-3}$	$7\cdot10^{-2}$	$2\cdot10^{-2}$	$6\cdot10^{-2}$	$7.5\cdot10^{-2}$	0.68	0.66	$6.8\cdot10^{-2}$	$8.3\cdot10^{-2}$	$4.4\cdot10^{-2}$	$5.6\cdot10^{-2}$	0.28	$4.4\cdot10^{-2}$	0.43	$5\cdot10^{-2}$
$1.9\cdot10^{-2}$	$2\cdot10^{-2}$	$8.9\cdot10^{-2}$	$5.1\cdot10^{-2}$	$3.5\cdot10^{-2}$	$5.9\cdot10^{-2}$	$7\cdot10^{-3}$	$5\cdot10^{-3}$	$8.2\cdot10^{-2}$	$7.6\cdot10^{-2}$	0.51	0.58	0.55	0.55	0.56	0.57	0.45	$4.2\cdot10^{-2}$	$1.6\cdot10^{-2}$	0.28	0.33	0.9	0.46	0.24	1	0.34	0.72	0.24	0.2	0.5	0.47	0.5	0.68	0.6	$8.5\cdot10^{-2}$	0.6	$7.5\cdot10^{-2}$	0.17	$9.9\cdot10^{-2}$	0.65	0.55	$2.7\cdot10^{-2}$	0.65	$7.3\cdot10^{-2}$	0.64
$5.2\cdot10^{-2}$	0.11	$8.1\cdot10^{-2}$	0.1	$4.8\cdot10^{-2}$	0.21	$7\cdot10^{-3}$	$1.6\cdot10^{-2}$	$4.9\cdot10^{-2}$	$3\cdot10^{-3}$	0.19	0.4	0.27	0.42	0.3	0.43	$7\cdot10^{-2}$	$5.9\cdot10^{-2}$	$4.5\cdot10^{-2}$	$8.9\cdot10^{-2}$	$5\cdot10^{-3}$	0.34	$1.9\cdot10^{-2}$	0.8	0.34	1	$4\cdot10^{-2}$	$9.1\cdot10^{-2}$	$2.5\cdot10^{-2}$	0.12	$6.9\cdot10^{-2}$	$1.1\cdot10^{-2}$	$3.2\cdot10^{-2}$	0.22	$5.6\cdot10^{-2}$	0.76	0.47	$8.1\cdot10^{-2}$	$4\cdot10^{-2}$	$8.2\cdot10^{-2}$	$2\cdot10^{-2}$	0.22	$8.2\cdot10^{-2}$	0.4	$7.6\cdot10^{-2}$
$2.7\cdot10^{-2}$	$8\cdot10^{-2}$	$7.2\cdot10^{-2}$	0.12	$5.2\cdot10^{-2}$	$8\cdot10^{-3}$	$6\cdot10^{-2}$	$3.8\cdot10^{-2}$	$2.5\cdot10^{-2}$	$9.8\cdot10^{-2}$	0.2	0.15	0.21	0.11	0.17	0.21	0.16	$7\cdot10^{-2}$	$4.9\cdot10^{-2}$	$6.7\cdot10^{-2}$	0.45	0.72	0.27	$2.4\cdot10^{-2}$	0.72	$4\cdot10^{-2}$	1	0.19	0.36	0.45	0.4	0.31	0.63	0.32	$5.9\cdot10^{-2}$	0.26	$6.3\cdot10^{-2}$	$8.1\cdot10^{-2}$	$5.9\cdot10^{-2}$	0.69	0.52	$5.7\cdot10^{-2}$	0.69	$5.2\cdot10^{-2}$	0.71
$1.3\cdot10^{-2}$	0.17	$7\cdot10^{-3}$	0.14	$1\cdot10^{-2}$	$8\cdot10^{-3}$	$2.7\cdot10^{-2}$	0.13	$6.4\cdot10^{-2}$	$4.4\cdot10^{-2}$	$9.1\cdot10^{-2}$	$1.1\cdot10^{-2}$	0.1	$1.4\cdot10^{-2}$	$1\cdot10^{-3}$	$3.4\cdot10^{-2}$	0.18	$3.2\cdot10^{-2}$	0.13	$8.1\cdot10^{-2}$	0.31	0.24	$6.3\cdot10^{-2}$	$9.6\cdot10^{-2}$	0.24	$9.1\cdot10^{-2}$	0.19	1	0.14	0.3	0.33	$7.4\cdot10^{-2}$	$2.1\cdot10^{-2}$	0.32	$1\cdot10^{-2}$	$5\cdot10^{-3}$	$3.7\cdot10^{-2}$	$4.5\cdot10^{-2}$	$9.4\cdot10^{-2}$	0.24	0.19	$7.7\cdot10^{-2}$	0.24	$8.6\cdot10^{-2}$	0.24
$4\cdot10^{-3}$	0.13	$6.8\cdot10^{-2}$	0.16	0	$5.3\cdot10^{-2}$	$4.5\cdot10^{-2}$	0.14	$3.3\cdot10^{-2}$	0.11	0.18	$7.1\cdot10^{-2}$	$3\cdot10^{-2}$	$5.4\cdot10^{-2}$	$4.8\cdot10^{-2}$	$9.7\cdot10^{-2}$	$2.4\cdot10^{-2}$	$5.1\cdot10^{-2}$	$7.4\cdot10^{-2}$	$4.6\cdot10^{-2}$	0.38	0.2	$7.8\cdot10^{-2}$	$1.6\cdot10^{-2}$	0.2	$2.5\cdot10^{-2}$	0.36	0.14	1	0.19	0.17	$5.7\cdot10^{-2}$	0.25	$8.4\cdot10^{-2}$	$9.2\cdot10^{-2}$	$9\cdot10^{-2}$	$1.1\cdot10^{-2}$	$5.1\cdot10^{-2}$	$3.8\cdot10^{-2}$	0.39	0.24	$5.7\cdot10^{-2}$	0.39	$7.1\cdot10^{-2}$	0.42
0.24	$7.1\cdot10^{-2}$	0.14	$7.4\cdot10^{-2}$	$2.9\cdot10^{-2}$	$9.1\cdot10^{-2}$	0.11	$5.1\cdot10^{-2}$	0.19	0.1	0.45	0.36	0.5	0.39	0.35	0.4	0.28	$3.3\cdot10^{-2}$	$4.7\cdot10^{-2}$	$3.6\cdot10^{-2}$	0.71	0.5	0.5	$6.6\cdot10^{-2}$	0.5	0.12	0.45	0.3	0.19	1	0.8	0.41	0.36	0.72	$2\cdot10^{-2}$	0.28	$3.4\cdot10^{-2}$	$4\cdot10^{-3}$	0.23	0.47	0.39	$4.4\cdot10^{-2}$	0.47	$1.3\cdot10^{-2}$	0.48
0.24	$2.7\cdot10^{-2}$	0.19	$1.8\cdot10^{-2}$	$1.5\cdot10^{-2}$	$1\cdot10^{-3}$	0.2	$2.9\cdot10^{-2}$	0.22	$8.3\cdot10^{-2}$	0.51	0.38	0.49	0.42	0.36	0.42	0.3	$8.2\cdot10^{-2}$	$3.8\cdot10^{-2}$	0.11	0.67	0.47	0.56	$9\cdot10^{-3}$	0.47	$6.9\cdot10^{-2}$	0.4	0.33	0.17	0.8	1	0.51	0.34	0.75	$1.4\cdot10^{-2}$	0.24	0.1	$4\cdot10^{-2}$	0.19	0.48	0.4	$9\cdot10^{-2}$	0.48	$5.8\cdot10^{-2}$	0.48
$5.1\cdot10^{-2}$	$2.2\cdot10^{-2}$	$2.8\cdot10^{-2}$	$6.5\cdot10^{-2}$	$5.8\cdot10^{-2}$	$6.2\cdot10^{-2}$	0.25	$3.4\cdot10^{-2}$	0.21	0.12	0.67	0.65	0.57	0.64	0.63	0.59	0.49	$8.6\cdot10^{-2}$	$7.8\cdot10^{-2}$	0.43	0.22	0.5	0.76	$7\cdot10^{-2}$	0.5	$1.1\cdot10^{-2}$	0.31	$7.4\cdot10^{-2}$	$5.7\cdot10^{-2}$	0.41	0.51	1	0.59	0.6	$7\cdot10^{-2}$	0.29	0.29	$1.2\cdot10^{-2}$	$3.1\cdot10^{-2}$	0.47	0.44	$8\cdot10^{-2}$	0.47	$3.2\cdot10^{-2}$	0.45
$3.9\cdot10^{-2}$	$5.5\cdot10^{-2}$	$6.9\cdot10^{-2}$	0.13	$8.4\cdot10^{-2}$	$1.8\cdot10^{-2}$	$3.8\cdot10^{-2}$	$1.1\cdot10^{-2}$	0.13	$6.4\cdot10^{-2}$	0.44	0.45	0.42	0.4	0.46	0.43	0.33	$3.8\cdot10^{-2}$	$3.2\cdot10^{-2}$	0.23	0.22	0.68	0.56	$2\cdot10^{-2}$	0.68	$3.2\cdot10^{-2}$	0.63	$2.1\cdot10^{-2}$	0.25	0.36	0.34	0.59	1	0.4	$7.6\cdot10^{-2}$	0.34	0.17	0.23	$1.5\cdot10^{-2}$	0.7	0.63	$9.4\cdot10^{-2}$	0.7	$9.1\cdot10^{-2}$	0.68
0.17	$3.7\cdot10^{-2}$	$9.2\cdot10^{-2}$	$1\cdot10^{-3}$	$7.8\cdot10^{-2}$	$3.9\cdot10^{-2}$	0.15	$3.5\cdot10^{-2}$	0.18	$4.6\cdot10^{-2}$	0.67	0.67	0.69	0.69	0.64	0.64	0.55	$6.3\cdot10^{-2}$	$9\cdot10^{-2}$	0.37	0.53	0.6	0.65	$6\cdot10^{-2}$	0.6	0.22	0.32	0.32	$8.4\cdot10^{-2}$	0.72	0.75	0.6	0.4	1	$9.4\cdot10^{-2}$	0.42	0.19	$6.8\cdot10^{-2}$	0.16	0.44	0.37	$4\cdot10^{-3}$	0.44	$6.8\cdot10^{-2}$	0.43
$8.5\cdot10^{-2}$	$5.4\cdot10^{-2}$	$4.3\cdot10^{-2}$	$9.8\cdot10^{-2}$	$1.3\cdot10^{-2}$	$9\cdot10^{-2}$	$9.9\cdot10^{-2}$	$3.1\cdot10^{-2}$	$6.1\cdot10^{-2}$	$5.7\cdot10^{-2}$	$1.6\cdot10^{-2}$	$4\cdot10^{-3}$	$4.6\cdot10^{-2}$	$4\cdot10^{-3}$	$4.4\cdot10^{-2}$	$1.8\cdot10^{-2}$	$7.6\cdot10^{-2}$	$8\cdot10^{-3}$	$1.8\cdot10^{-2}$	$1.2\cdot10^{-2}$	$1\cdot10^{-2}$	$8.5\cdot10^{-2}$	$5.1\cdot10^{-2}$	$7.5\cdot10^{-2}$	$8.5\cdot10^{-2}$	$5.6\cdot10^{-2}$	$5.9\cdot10^{-2}$	$1\cdot10^{-2}$	$9.2\cdot10^{-2}$	$2\cdot10^{-2}$	$1.4\cdot10^{-2}$	$7\cdot10^{-2}$	$7.6\cdot10^{-2}$	$9.4\cdot10^{-2}$	1	$4.3\cdot10^{-2}$	$1\cdot10^{-2}$	$5.3\cdot10^{-2}$	$5\cdot10^{-2}$	$3.6\cdot10^{-2}$	$7.2\cdot10^{-2}$	0.22	$3.6\cdot10^{-2}$	0.26	$5\cdot10^{-2}$
$1.6\cdot10^{-2}$	$5.4\cdot10^{-2}$	$3.7\cdot10^{-2}$	$5\cdot10^{-3}$	$4.8\cdot10^{-2}$	0.12	$4\cdot10^{-3}$	$8.9\cdot10^{-2}$	$6.7\cdot10^{-2}$	$5.2\cdot10^{-2}$	0.39	0.6	0.43	0.59	0.51	0.65	0.18	$1.8\cdot10^{-2}$	$9.1\cdot10^{-2}$	0.27	0.11	0.6	0.27	0.68	0.6	0.76	0.26	$5\cdot10^{-3}$	$9\cdot10^{-2}$	0.28	0.24	0.29	0.34	0.42	$4.3\cdot10^{-2}$	1	0.14	$3.7\cdot10^{-2}$	$6.6\cdot10^{-2}$	0.18	0.24	0.14	0.18	0.31	0.17
$9.4\cdot10^{-2}$	$6.6\cdot10^{-2}$	$6.9\cdot10^{-2}$	0.13	$1.5\cdot10^{-2}$	0.19	$3\cdot10^{-3}$	$7.7\cdot10^{-2}$	$7.1\cdot10^{-2}$	$5\cdot10^{-2}$	0.18	0.12	0.13	$5.1\cdot10^{-2}$	0.17	$8.6\cdot10^{-2}$	0.48	$7.8\cdot10^{-2}$	$5\cdot10^{-3}$	0.15	$3.8\cdot10^{-2}$	$7.5\cdot10^{-2}$	0.31	0.66	$7.5\cdot10^{-2}$	0.47	$6.3\cdot10^{-2}$	$3.7\cdot10^{-2}$	$1.1\cdot10^{-2}$	$3.4\cdot10^{-2}$	0.1	0.29	0.17	0.19	$1\cdot10^{-2}$	0.14	1	$3.2\cdot10^{-2}$	$7.6\cdot10^{-2}$	0.29	0.16	$9.2\cdot10^{-2}$	0.29	0.23	0.27
$4.8\cdot10^{-2}$	$4\cdot10^{-2}$	$7.7\cdot10^{-2}$	$1.9\cdot10^{-2}$	$2.4\cdot10^{-2}$	$2.3\cdot10^{-2}$	$9.2\cdot10^{-2}$	$2.6\cdot10^{-2}$	$5.9\cdot10^{-2}$	$1.6\cdot10^{-2}$	$5.4\cdot10^{-2}$	$4.2\cdot10^{-2}$	$8.4\cdot10^{-2}$	$8.3\cdot10^{-2}$	$4.9\cdot10^{-2}$	$8.9\cdot10^{-2}$	$7.9\cdot10^{-2}$	$9.8\cdot10^{-2}$	$2.6\cdot10^{-2}$	0.12	0.11	0.17	$3.4\cdot10^{-2}$	$6.8\cdot10^{-2}$	0.17	$8.1\cdot10^{-2}$	$8.1\cdot10^{-2}$	$4.5\cdot10^{-2}$	$5.1\cdot10^{-2}$	$4\cdot10^{-3}$	$4\cdot10^{-2}$	$1.2\cdot10^{-2}$	0.23	$6.8\cdot10^{-2}$	$5.3\cdot10^{-2}$	$3.7\cdot10^{-2}$	$3.2\cdot10^{-2}$	1	0.81	0.2	0.29	$7.7\cdot10^{-2}$	0.2	$4.1\cdot10^{-2}$	0.14
0.12	$5.8\cdot10^{-2}$	$3.9\cdot10^{-2}$	$7.5\cdot10^{-2}$	$5.6\cdot10^{-2}$	$2\cdot10^{-2}$	$2.8\cdot10^{-2}$	$5\cdot10^{-2}$	$6.1\cdot10^{-2}$	$1.3\cdot10^{-2}$	0.13	$8\cdot10^{-3}$	0.11	$4.4\cdot10^{-2}$	$4.3\cdot10^{-2}$	$5.6\cdot10^{-2}$	$7.1\cdot10^{-2}$	$5.3\cdot10^{-2}$	$1.1\cdot10^{-2}$	$2.5\cdot10^{-2}$	0.33	$9.9\cdot10^{-2}$	0.16	$8.3\cdot10^{-2}$	$9.9\cdot10^{-2}$	$4\cdot10^{-2}$	$5.9\cdot10^{-2}$	$9.4\cdot10^{-2}$	$3.8\cdot10^{-2}$	0.23	0.19	$3.1\cdot10^{-2}$	$1.5\cdot10^{-2}$	0.16	$5\cdot10^{-2}$	$6.6\cdot10^{-2}$	$7.6\cdot10^{-2}$	0.81	1	$9.6\cdot10^{-2}$	$7\cdot10^{-3}$	$5.7\cdot10^{-2}$	$9.6\cdot10^{-2}$	$1.7\cdot10^{-2}$	$5.8\cdot10^{-2}$
$3\cdot10^{-2}$	0.14	$9.9\cdot10^{-2}$	0.23	$8.1\cdot10^{-2}$	0.12	$2.3\cdot10^{-2}$	$2\cdot10^{-3}$	0.12	$9.1\cdot10^{-2}$	0.34	0.25	0.31	0.21	0.28	0.27	0.28	$6.1\cdot10^{-2}$	$2.3\cdot10^{-2}$	$3.8\cdot10^{-2}$	0.46	0.65	0.41	$4.4\cdot10^{-2}$	0.65	$8.2\cdot10^{-2}$	0.69	0.24	0.39	0.47	0.48	0.47	0.7	0.44	$3.6\cdot10^{-2}$	0.18	0.29	0.2	$9.6\cdot10^{-2}$	1	0.78	$6\cdot10^{-2}$	0.9	$5.5\cdot10^{-2}$	0.89
$9.3\cdot10^{-2}$	0.14	$3.3\cdot10^{-2}$	0.21	$4.4\cdot10^{-2}$	$1.7\cdot10^{-2}$	0.12	$5.6\cdot10^{-2}$	0.19	$3.6\cdot10^{-2}$	0.29	0.24	0.3	0.2	0.28	0.29	0.23	$9.5\cdot10^{-2}$	$8\cdot10^{-3}$	0.12	0.34	0.55	0.35	$5.6\cdot10^{-2}$	0.55	$2\cdot10^{-2}$	0.52	0.19	0.24	0.39	0.4	0.44	0.63	0.37	$7.2\cdot10^{-2}$	0.24	0.16	0.29	$7\cdot10^{-3}$	0.78	1	$7.5\cdot10^{-2}$	0.78	$7.4\cdot10^{-2}$	0.72
$3\cdot10^{-2}$	0.11	$9.2\cdot10^{-2}$	$2.6\cdot10^{-2}$	$6\cdot10^{-3}$	$8.4\cdot10^{-2}$	$2.3\cdot10^{-2}$	$6.3\cdot10^{-2}$	$7.2\cdot10^{-2}$	$7.4\cdot10^{-2}$	$7.1\cdot10^{-2}$	$6.4\cdot10^{-2}$	$4.7\cdot10^{-2}$	$5.3\cdot10^{-2}$	$7\cdot10^{-2}$	$6.5\cdot10^{-2}$	$5.8\cdot10^{-2}$	$6.4\cdot10^{-2}$	$6.7\cdot10^{-2}$	$6.6\cdot10^{-2}$	$5.4\cdot10^{-2}$	$2.7\cdot10^{-2}$	$2.6\cdot10^{-2}$	0.28	$2.7\cdot10^{-2}$	0.22	$5.7\cdot10^{-2}$	$7.7\cdot10^{-2}$	$5.7\cdot10^{-2}$	$4.4\cdot10^{-2}$	$9\cdot10^{-2}$	$8\cdot10^{-2}$	$9.4\cdot10^{-2}$	$4\cdot10^{-3}$	0.22	0.14	$9.2\cdot10^{-2}$	$7.7\cdot10^{-2}$	$5.7\cdot10^{-2}$	$6\cdot10^{-2}$	$7.5\cdot10^{-2}$	1	$6\cdot10^{-2}$	0.74	$4.4\cdot10^{-2}$
$3\cdot10^{-2}$	0.14	$9.9\cdot10^{-2}$	0.23	$8.1\cdot10^{-2}$	0.12	$2.3\cdot10^{-2}$	$2\cdot10^{-3}$	0.12	$9.1\cdot10^{-2}$	0.34	0.25	0.31	0.21	0.28	0.27	0.28	$6.1\cdot10^{-2}$	$2.3\cdot10^{-2}$	$3.8\cdot10^{-2}$	0.46	0.65	0.41	$4.4\cdot10^{-2}$	0.65	$8.2\cdot10^{-2}$	0.69	0.24	0.39	0.47	0.48	0.47	0.7	0.44	$3.6\cdot10^{-2}$	0.18	0.29	0.2	$9.6\cdot10^{-2}$	0.9	0.78	$6\cdot10^{-2}$	1	$5.5\cdot10^{-2}$	0.89
0.11	$9.3\cdot10^{-2}$	$1.5\cdot10^{-2}$	$2.4\cdot10^{-2}$	$8.1\cdot10^{-2}$	$3.3\cdot10^{-2}$	$2.3\cdot10^{-2}$	$4.7\cdot10^{-2}$	$9.1\cdot10^{-2}$	$1.3\cdot10^{-2}$	$7.5\cdot10^{-2}$	$2.6\cdot10^{-2}$	$2.8\cdot10^{-2}$	$2.5\cdot10^{-2}$	$2.4\cdot10^{-2}$	$5.4\cdot10^{-2}$	$3.6\cdot10^{-2}$	$5.8\cdot10^{-2}$	$9\cdot10^{-2}$	$5\cdot10^{-2}$	$2.7\cdot10^{-2}$	$7.3\cdot10^{-2}$	$6.2\cdot10^{-2}$	0.43	$7.3\cdot10^{-2}$	0.4	$5.2\cdot10^{-2}$	$8.6\cdot10^{-2}$	$7.1\cdot10^{-2}$	$1.3\cdot10^{-2}$	$5.8\cdot10^{-2}$	$3.2\cdot10^{-2}$	$9.1\cdot10^{-2}$	$6.8\cdot10^{-2}$	0.26	0.31	0.23	$4.1\cdot10^{-2}$	$1.7\cdot10^{-2}$	$5.5\cdot10^{-2}$	$7.4\cdot10^{-2}$	0.74	$5.5\cdot10^{-2}$	1	$7.7\cdot10^{-2}$
$4.4\cdot10^{-2}$	0.14	$9.6\cdot10^{-2}$	0.23	$7.9\cdot10^{-2}$	0.14	$1.3\cdot10^{-2}$	0	0.12	$8.9\cdot10^{-2}$	0.33	0.22	0.29	0.18	0.25	0.25	0.23	$4.7\cdot10^{-2}$	$4.9\cdot10^{-2}$	$1.8\cdot10^{-2}$	0.48	0.64	0.4	$5\cdot10^{-2}$	0.64	$7.6\cdot10^{-2}$	0.71	0.24	0.42	0.48	0.48	0.45	0.68	0.43	$5\cdot10^{-2}$	0.17	0.27	0.14	$5.8\cdot10^{-2}$	0.89	0.72	$4.4\cdot10^{-2}$	0.89	$7.7\cdot10^{-2}$	1

Table 3.8: The Features (UnionFeature_Set) and their p-Values with which the best result is obtained for all the datasets.

S. No.	Reference	Feature Name	p-Value for DB-DMR-IR Dataset	p-Value for DB-FOOT-IR Dataset	p-Value for DB-THY-IR Dataset
F1	**BAR[15]**	Texture energy using LS kernel	**9.54E-06**	**0.000736465**	-
F2	**BAR[15]**	Contrast(Neighborhood gray-tone difference matrix based)	**3.46088E-05**	**0.000232748**	**2.15761E-05**
F3	**BAR[15]**	Contrast(Gray level difference statistics based)	**5.19114E-05**	**0.000261966**	**3.89146E-05**
F4	**BAR[15]**	Coarseness(Neighborhood gray-tone difference matrix based)	**6.09136E-05**	**7.73816E-05**	**0.000301748**
F5	**BAR[15]**	Busyness (Neighborhood gray-tone difference matrix based)	**6.86098E-05**	**6.47659E-05**	**0.000231966**
F6	**BAR[15]**	Texture energy using LE kernel	**0.000276149**	**0.00526576**	**0.008670024**
F7	**BAR[15]**	Eccentricity	**0.000321131**	**0.000414763**	-
F8	**BAR[15]**	Regularity/roughness(Statistical feature matrix based)	**0.000352973**	-	-
F9	**BAR[15]**	Euler number	**0.000471395**	**0.001101846**	-
F10	**BAR[15]**	Convexity	**0.000502856**	**0.000353501**	**1.9523E-05**
F11	**BAR[15]**	Texture energy using ES kernel	**0.001455341**	**0.001712522**	**0.001762114**
F12	**ACH[2]**	Moment 3	**0.001557873**	**0.003381957**	**0.006502389**
F13	**CRZ[26]**	Number of pixels (segmented using Differential Evolution)	**0.001719172**	**0.000356737**	**0.008154521**
F14	**KAR[28]**	Kurtosis(from Curvelet transformed)	**0.001733792**	**0.000955772**	**0.000222863**
F15	**ACH[2]**	Moment 4	**0.002101889**	**0.004432993**	**0.001562873**
F16	**ACH[2]**	Angular Second Moment	**0.003475957**	**0.000263501**	-
F17	**GUP**	Correlation from GLCM Sub-Matrix	**0.003475957**	**0.005187852**	-
F18	**GUP**	Difference variance from GLCM Sub-Matrix	**0.004481993**	**0.008749024**	**0.002048889**
F19	**ACH[2]**	Entropy	**0.006473389**	**0.004462993**	-
F20	**BAR[15]**	Texture energy using LL kernel	**0.006486389**	**0.000616753**	**0.00902678**
F21	**GUP**	Energy from GLCM Sub-Matrix	0.014647123	**0.00899278**	-
F22	**GUP**	Homogeneity from GLCM Sub-Matrix	0.015107258	-	-
F23	**GUP**	Information measure of correlation from GLCM Sub-Matrix	0.022027663	**0.001099846**	0.015121258
F24	**GUP**	Otsu Threshold	0.023440631	0.029550677	0.022001663
F25	**GUP**	Sum entropy from GLCM Sub-Matrix	0.024172069	0.030451145	0.023452631
F26	**GUP**	Sum variance from GLCM Sub-Matrix	0.027386128	0.031046951	0.024097069
F27	**RAS[24]**	Difference between Co-occurrence levels based energy (from Modified LBP Colour matrix)	0.027408579	0.032323166	0.027390128
F28	**SAT[25]**	Skewness (from Local energy matrices, calculated for sub band 12)	0.027454128	-	-
F29	**RAS[24]**	Difference between Co-occurrence levels based energy (from Modified LBP Edge matrix)	0.030428145	0.0352833	**5.89856E-05**
F30	**RAS[24]**	Difference of GLCM Matrices	0.030987951	0.036041195	0.021953663
F31	**SAT[25]**	Kurtosis (from Local energy matrices, calculated for sub band 12)	0.032310166	0.131642063	0.014568123
F32	**RAS[24]**	Euclidean distance of histograms (from Modified LBP Color matrix)	0.032340166	0.040762057	0.027479579
F33	**RAS[24]**	Euclidean distance of histograms (from Modified LBP Edge matrix)	0.0353093	0.044455997	-
F34	**SAT[25]**	Mean (from Local energy matrices, calculated for sub-band 6)	0.036016195	-	-
F35	**RAS[24]**	GLCM based Energy (from Modified LBP Colour matrix)	0.036059195	0.046864998	0.024161069
F36	**RAS[24]**	GLCM based Energy (from Modified LBP Edge matrix)	0.036136696	0.047042847	**0.000972879**
F37	**RAS[24]**	Sum from Modified LBP Colour matrix	0.036277198	0.051967651	-
F38	**RAS[24]**	Sum from Modified LBP Edge matrix	0.03639456	0.053655003	-
F39	**SCH[23]**	Contrast (Gray Level Cross co-occurrence matrix from Laplace filter applied images)	0.036920254	0.030455145	0.031042951
F40	**SCH[23]**	Contrast (Gray Level Cross co-occurrence matrix)	0.038373094	-	-
F41	**SAT[25]**	Variance (from Local energy matrices, calculated for sub-band 12)	0.056953143	**0.001364869**	0.075566216
F42	**SCH[23]**	Symmetry (Gray Level Cross co-occurrence matrix from Laplace filter applied images)	0.066294345	0.118365239	-
F43	**SAT[25]**	Entropy (from Local energy matrices, calculated for sub-band 7)	0.069901974	0.122022261	-
F44	**SCH[23]**	Difference Histogram,	0.083531184	0.09977041	0.090448805
F45	**SCH[23]**	Difference of positive and negative (from Normalized Histograms)	0.0852041	0.107557706	**0.000670753**
F46	**BAR[15]**	Angular sum from Fourier power spectrum	-	**4.29E-06**	**0.000114174**
F47	**BAR[15]**	Coarseness(Statistical feature matrix based)	-	**2.80144E-05**	**0.000349501**
F48	**BAR[15]**	Complexity(Neighborhood gray-tone difference matrix based)	-	**8.25699E-05**	**0.000438763**
F49	**BAR[15]**	Energy (Gray level difference statistics based)	-	**0.000957879**	-
F50	**BAR[15]**	Entropy (Gray level difference statistics based)	-	**0.000993772**	-
F51	**BAR[15]**	Homogeneity(Gray level difference statistics based)	-	**0.001426869**	-
F52	**BAR[15]**	Mean (Gray level difference statistics based)	-	**0.001433341**	-
F53	**BAR[15]**	Periodicity(Statistical feature matrix based)	-	**0.000838435**	**0.000529959**
F54	**BAR[15]**	Radial sum from Fourier power spectrum	-	**0.000934663**	-
F55	**BAR[15]**	Solidity	-	**0.001122531**	-
F56	**BAR[15]**	Texture energy using EE kernel	-	**0.00121398**	**0.005243872**
F57	**BAR[15]**	Texture energy using SS kernel	-	**0.00058523**	-
F58	**BAR[15]**	Texture strength(Neighborhood gray-tone difference matrix based)	-	**0.001730656**	-
F59	**ACH[2]**	Long Runs Emphasis	-	-	**0.00522876**
F60	**SCH[23]**	Distance of difference maximum from the centre(from Fourier Spectrum of left and right breast),	-	0.109284161	**0.00167705**
F61	**SCH[23]**	Energy (Gray Level Cross co-occurrence matrix from Laplace filter applied images)	-	0.114465656	**0.001557873**
F62	**SCH[23]**	Mutual Information,	-	0.117180514	**0.008740024**
F63	**SAT[25]**	Kurtosis (from Local energy matrices, calculated for sub band 20)	-	-	**0.000233966**
F64	**SAT[25]**	Skewness (from Local energy matrices, calculated for sub band 2)	-	-	**0.000250748**
F65	**SAT[25]**	Variance (from Local energy matrices, calculated for sub band 9)	-	0.023478631	-

Table 3.10: The colour map of correlation matrix for the features with which the best result is obtained for DB-FOOT-IR dataset.

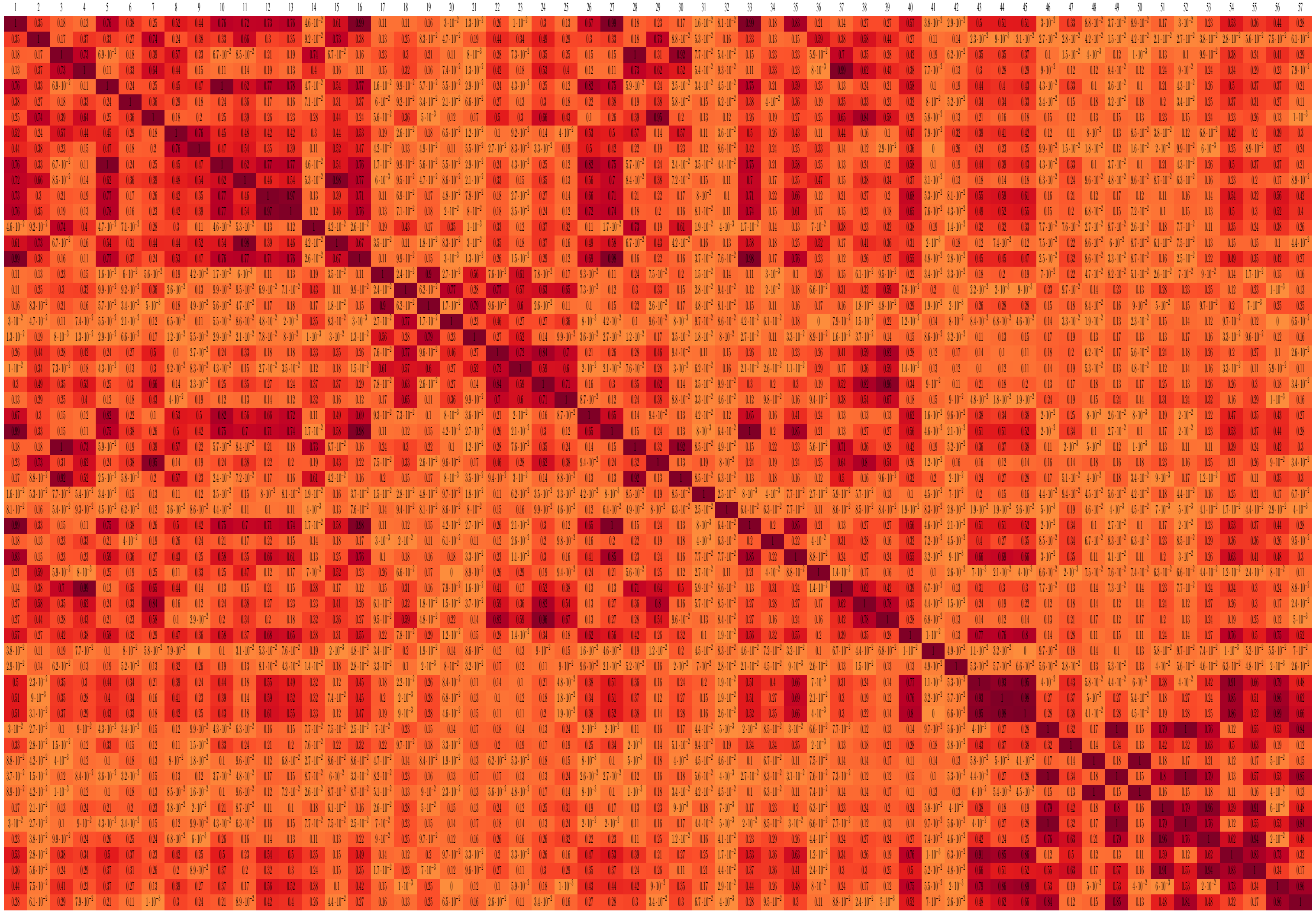

Table 3.11: The colour map of correlation matrix for the features with which the best result is obtained for DB-THY-IR dataset.

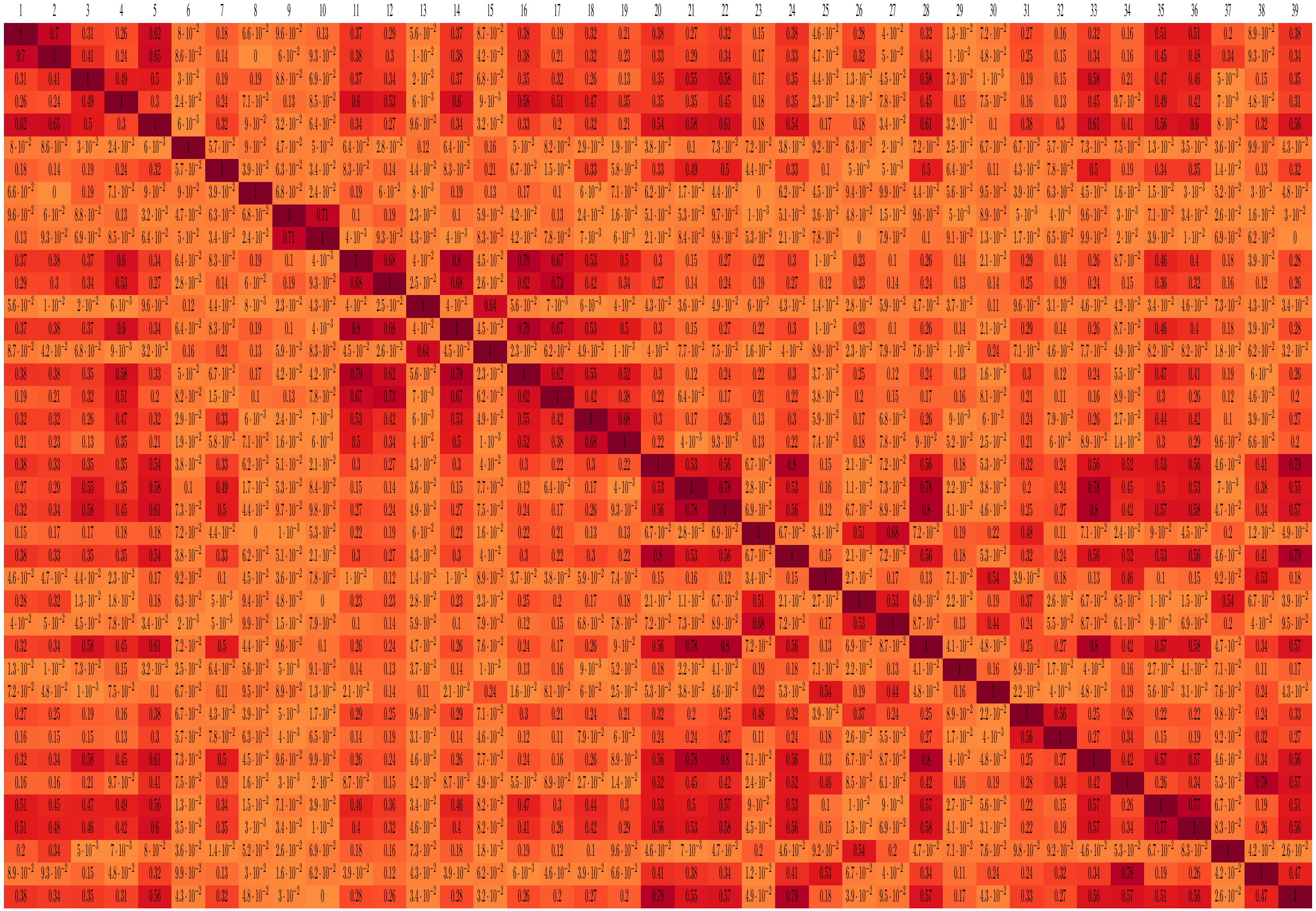

1	2	3	4	5	6	7	8	9	10	11	12	13	14	15	16	17	18	19	20	21	22	23	24	25	26	27	28	29	30	31	32	33	34	35	36	37	38	39
1	0.7	0.31	0.26	0.62	$8\cdot10^{-2}$	0.18	$6.6\cdot10^{-2}$	$9.6\cdot10^{-2}$	0.13	0.37	0.29	$5.6\cdot10^{-2}$	0.37	$8.7\cdot10^{-2}$	0.38	0.19	0.32	0.21	0.38	0.27	0.32	0.15	0.38	$4.6\cdot10^{-2}$	0.28	$4\cdot10^{-2}$	0.32	$1.3\cdot10^{-2}$	$7.2\cdot10^{-2}$	0.27	0.16	0.32	0.16	0.51	0.51	0.2	$8.9\cdot10^{-2}$	0.38
0.7	1	0.41	0.24	0.65	$8.6\cdot10^{-2}$	0.14	0	$6\cdot10^{-2}$	$9.3\cdot10^{-2}$	0.38	0.3	$1\cdot10^{-2}$	0.38	$4.2\cdot10^{-2}$	0.38	0.21	0.32	0.23	0.33	0.29	0.34	0.17	0.33	$4.7\cdot10^{-2}$	0.32	$5\cdot10^{-2}$	0.34	$1\cdot10^{-2}$	$4.8\cdot10^{-2}$	0.25	0.15	0.34	0.16	0.45	0.48	0.34	$9.3\cdot10^{-2}$	0.34
0.31	0.41	1	0.49	0.5	$3\cdot10^{-2}$	0.19	0.19	$8.8\cdot10^{-2}$	$6.9\cdot10^{-2}$	0.37	0.34	$2\cdot10^{-2}$	0.37	$6.8\cdot10^{-2}$	0.35	0.32	0.26	0.13	0.35	0.55	0.58	0.17	0.35	$4.4\cdot10^{-2}$	$1.3\cdot10^{-2}$	$4.5\cdot10^{-2}$	0.58	$7.3\cdot10^{-2}$	$1\cdot10^{-3}$	0.19	0.15	0.58	0.21	0.47	0.46	$5\cdot10^{-3}$	0.15	0.35
0.26	0.24	0.49	1	0.3	$2.4\cdot10^{-2}$	0.24	$7.1\cdot10^{-2}$	0.13	$8.5\cdot10^{-2}$	0.6	0.53	$6\cdot10^{-3}$	0.6	$9\cdot10^{-3}$	0.58	0.51	0.47	0.35	0.35	0.35	0.45	0.18	0.35	$2.3\cdot10^{-2}$	$1.8\cdot10^{-2}$	$7.8\cdot10^{-2}$	0.45	0.15	$7.5\cdot10^{-2}$	0.16	0.13	0.45	$9.7\cdot10^{-2}$	0.49	0.42	$7\cdot10^{-3}$	$4.8\cdot10^{-2}$	0.31
0.62	0.65	0.5	0.3	1	$6\cdot10^{-3}$	0.32	$9\cdot10^{-2}$	$3.2\cdot10^{-2}$	$6.4\cdot10^{-2}$	0.34	0.27	$9.6\cdot10^{-2}$	0.34	$3.2\cdot10^{-2}$	0.33	0.2	0.32	0.21	0.54	0.58	0.61	0.18	0.54	0.17	0.18	$3.4\cdot10^{-2}$	0.61	$3.2\cdot10^{-2}$	0.1	0.38	0.3	0.61	0.41	0.56	0.6	$8\cdot10^{-2}$	0.32	0.56
$8\cdot10^{-2}$	$8.6\cdot10^{-2}$	$3\cdot10^{-2}$	$2.4\cdot10^{-2}$	$6\cdot10^{-3}$	1	$5.7\cdot10^{-2}$	$9\cdot10^{-2}$	$4.7\cdot10^{-2}$	$5\cdot10^{-2}$	$6.4\cdot10^{-2}$	$2.8\cdot10^{-2}$	0.12	$6.4\cdot10^{-2}$	0.16	$5\cdot10^{-2}$	$8.2\cdot10^{-2}$	$2.9\cdot10^{-2}$	$1.9\cdot10^{-2}$	$3.8\cdot10^{-2}$	0.1	$7.3\cdot10^{-2}$	$7.2\cdot10^{-2}$	$3.8\cdot10^{-2}$	$9.2\cdot10^{-2}$	$6.3\cdot10^{-2}$	$2\cdot10^{-3}$	$7.2\cdot10^{-2}$	$2.5\cdot10^{-2}$	$6.7\cdot10^{-2}$	$6.7\cdot10^{-2}$	$5.7\cdot10^{-2}$	$7.3\cdot10^{-2}$	$7.5\cdot10^{-2}$	$1.3\cdot10^{-2}$	$3.5\cdot10^{-2}$	$3.6\cdot10^{-2}$	$9.9\cdot10^{-2}$	$4.3\cdot10^{-2}$
0.18	0.14	0.19	0.24	0.32	$5.7\cdot10^{-2}$	1	$3.9\cdot10^{-2}$	$6.3\cdot10^{-2}$	$3.4\cdot10^{-2}$	$8.3\cdot10^{-2}$	0.14	$4.4\cdot10^{-2}$	$8.3\cdot10^{-2}$	0.21	$6.7\cdot10^{-2}$	$1.5\cdot10^{-2}$	0.33	$5.8\cdot10^{-2}$	0.33	0.49	0.5	$4.4\cdot10^{-2}$	0.33	0.1	$5\cdot10^{-3}$	$5\cdot10^{-3}$	0.5	$6.4\cdot10^{-2}$	0.11	$4.3\cdot10^{-2}$	$7.8\cdot10^{-2}$	0.5	0.19	0.34	0.35	$1.4\cdot10^{-2}$	0.13	0.32
$6.6\cdot10^{-2}$	0	0.19	$7.1\cdot10^{-2}$	$9\cdot10^{-2}$	$9\cdot10^{-2}$	$3.9\cdot10^{-2}$	1	$6.8\cdot10^{-2}$	$2.4\cdot10^{-2}$	0.19	$6\cdot10^{-2}$	$8\cdot10^{-3}$	0.19	0.13	0.17	0.1	$6\cdot10^{-3}$	$7.1\cdot10^{-2}$	$6.2\cdot10^{-2}$	$1.7\cdot10^{-2}$	$4.4\cdot10^{-2}$	0	$6.2\cdot10^{-2}$	$4.5\cdot10^{-2}$	$9.4\cdot10^{-2}$	$9.9\cdot10^{-2}$	$4.4\cdot10^{-2}$	$5.6\cdot10^{-2}$	$9.5\cdot10^{-2}$	$3.9\cdot10^{-2}$	$6.3\cdot10^{-2}$	$4.5\cdot10^{-2}$	$1.6\cdot10^{-2}$	$1.5\cdot10^{-2}$	$3\cdot10^{-3}$	$5.2\cdot10^{-2}$	$3\cdot10^{-2}$	$4.8\cdot10^{-2}$
$9.6\cdot10^{-2}$	$6\cdot10^{-2}$	$8.8\cdot10^{-2}$	0.13	$3.2\cdot10^{-2}$	$4.7\cdot10^{-2}$	$6.3\cdot10^{-2}$	$6.8\cdot10^{-2}$	1	0.71	0.1	0.19	$2.3\cdot10^{-2}$	0.1	$5.9\cdot10^{-2}$	$4.2\cdot10^{-2}$	0.13	$2.4\cdot10^{-2}$	$1.6\cdot10^{-2}$	$5.1\cdot10^{-2}$	$5.3\cdot10^{-2}$	$9.7\cdot10^{-2}$	$1\cdot10^{-3}$	$5.1\cdot10^{-2}$	$3.6\cdot10^{-2}$	$4.8\cdot10^{-2}$	$1.5\cdot10^{-2}$	$9.6\cdot10^{-2}$	$5\cdot10^{-3}$	$8.9\cdot10^{-2}$	$5\cdot10^{-3}$	$4\cdot10^{-3}$	$9.6\cdot10^{-2}$	$3\cdot10^{-3}$	$7.1\cdot10^{-2}$	$3.4\cdot10^{-2}$	$2.6\cdot10^{-2}$	$1.6\cdot10^{-2}$	$3\cdot10^{-2}$
0.13	$9.3\cdot10^{-2}$	$6.9\cdot10^{-2}$	$8.5\cdot10^{-2}$	$6.4\cdot10^{-2}$	$5\cdot10^{-2}$	$3.4\cdot10^{-2}$	$2.4\cdot10^{-2}$	0.71	1	$4\cdot10^{-3}$	$9.3\cdot10^{-2}$	$4.3\cdot10^{-2}$	$4\cdot10^{-3}$	$8.3\cdot10^{-2}$	$4.2\cdot10^{-2}$	$7.8\cdot10^{-2}$	$7\cdot10^{-3}$	$6\cdot10^{-3}$	$2.1\cdot10^{-2}$	$8.4\cdot10^{-2}$	$9.8\cdot10^{-2}$	$5.3\cdot10^{-2}$	$2.1\cdot10^{-2}$	$7.8\cdot10^{-2}$	0	$7.9\cdot10^{-2}$	0.1	$9.1\cdot10^{-2}$	$1.3\cdot10^{-2}$	$1.7\cdot10^{-2}$	$6.5\cdot10^{-2}$	$9.9\cdot10^{-2}$	$2\cdot10^{-2}$	$3.9\cdot10^{-2}$	$1\cdot10^{-2}$	$6.9\cdot10^{-2}$	$6.2\cdot10^{-2}$	0
0.37	0.38	0.37	0.6	0.34	$6.4\cdot10^{-2}$	$8.3\cdot10^{-2}$	0.19	0.1	$4\cdot10^{-3}$	1	0.68	$4\cdot10^{-2}$	0.8	$4.5\cdot10^{-2}$	0.79	0.67	0.53	0.5	0.3	0.15	0.27	0.22	0.3	$1\cdot10^{-2}$	0.23	0.1	0.26	0.14	$2.1\cdot10^{-2}$	0.29	0.14	0.26	$8.7\cdot10^{-2}$	0.46	0.4	0.18	$3.9\cdot10^{-2}$	0.28
0.29	0.3	0.34	0.53	0.27	$2.8\cdot10^{-2}$	0.14	$6\cdot10^{-2}$	0.19	$9.3\cdot10^{-2}$	0.68	1	$2.5\cdot10^{-2}$	0.68	$2.6\cdot10^{-2}$	0.62	0.73	0.42	0.34	0.27	0.14	0.24	0.19	0.27	0.12	0.23	0.14	0.24	0.13	0.14	0.25	0.19	0.24	0.15	0.36	0.32	0.16	0.12	0.26
$5.6\cdot10^{-2}$	$1\cdot10^{-2}$	$2\cdot10^{-2}$	$6\cdot10^{-3}$	$9.6\cdot10^{-2}$	0.12	$4.4\cdot10^{-2}$	$8\cdot10^{-3}$	$2.3\cdot10^{-2}$	$4.3\cdot10^{-2}$	$4\cdot10^{-2}$	$2.5\cdot10^{-2}$	1	$4\cdot10^{-2}$	0.64	$5.6\cdot10^{-2}$	$7\cdot10^{-3}$	$6\cdot10^{-3}$	$4\cdot10^{-2}$	$4.3\cdot10^{-2}$	$3.6\cdot10^{-2}$	$4.9\cdot10^{-2}$	$6\cdot10^{-2}$	$4.3\cdot10^{-2}$	$1.4\cdot10^{-2}$	$2.8\cdot10^{-2}$	$5.9\cdot10^{-2}$	$4.7\cdot10^{-2}$	$3.7\cdot10^{-2}$	0.11	$9.6\cdot10^{-2}$	$3.1\cdot10^{-2}$	$4.6\cdot10^{-2}$	$4.2\cdot10^{-2}$	$3.4\cdot10^{-2}$	$4.6\cdot10^{-2}$	$7.3\cdot10^{-2}$	$4.3\cdot10^{-2}$	$3.4\cdot10^{-2}$
0.37	0.38	0.37	0.6	0.34	$6.4\cdot10^{-2}$	$8.3\cdot10^{-2}$	0.19	0.1	$4\cdot10^{-3}$	0.8	0.68	$4\cdot10^{-2}$	1	$4.5\cdot10^{-2}$	0.79	0.67	0.53	0.5	0.3	0.15	0.27	0.22	0.3	$1\cdot10^{-2}$	0.23	0.1	0.26	0.14	$2.1\cdot10^{-2}$	0.29	0.14	0.26	$8.7\cdot10^{-2}$	0.46	0.4	0.18	$3.9\cdot10^{-2}$	0.28
$8.7\cdot10^{-2}$	$4.2\cdot10^{-2}$	$6.8\cdot10^{-2}$	$9\cdot10^{-3}$	$3.2\cdot10^{-2}$	0.16	0.21	0.13	$5.9\cdot10^{-2}$	$8.3\cdot10^{-2}$	$4.5\cdot10^{-2}$	$2.6\cdot10^{-2}$	0.64	$4.5\cdot10^{-2}$	1	$2.3\cdot10^{-2}$	$6.2\cdot10^{-2}$	$4.9\cdot10^{-2}$	$1\cdot10^{-3}$	$4\cdot10^{-2}$	$7.7\cdot10^{-2}$	$7.5\cdot10^{-2}$	$1.6\cdot10^{-2}$	$4\cdot10^{-2}$	$8.9\cdot10^{-2}$	$2.3\cdot10^{-2}$	$7.9\cdot10^{-2}$	$7.6\cdot10^{-2}$	$1\cdot10^{-2}$	0.24	$7.1\cdot10^{-2}$	$4.6\cdot10^{-2}$	$7.7\cdot10^{-2}$	$4.9\cdot10^{-2}$	$8.2\cdot10^{-2}$	$8.2\cdot10^{-2}$	$1.8\cdot10^{-2}$	$6.2\cdot10^{-2}$	$3.2\cdot10^{-2}$
0.38	0.38	0.35	0.58	0.33	$5\cdot10^{-2}$	$6.7\cdot10^{-2}$	0.17	$4.2\cdot10^{-2}$	$4.2\cdot10^{-2}$	0.79	0.62	$5.6\cdot10^{-2}$	0.79	$2.3\cdot10^{-2}$	1	0.62	0.55	0.52	0.3	0.12	0.24	0.22	0.3	$3.7\cdot10^{-2}$	0.25	0.12	0.24	0.13	$1.6\cdot10^{-2}$	0.3	0.12	0.24	$5.5\cdot10^{-2}$	0.47	0.41	0.19	$6\cdot10^{-3}$	0.26
0.19	0.21	0.32	0.51	0.2	$8.2\cdot10^{-2}$	$1.5\cdot10^{-2}$	0.1	0.13	$7.8\cdot10^{-2}$	0.67	0.73	$7\cdot10^{-3}$	0.67	$6.2\cdot10^{-2}$	0.62	1	0.42	0.38	0.22	$6.4\cdot10^{-2}$	0.17	0.21	0.22	$3.8\cdot10^{-2}$	0.2	0.15	0.17	0.16	$8.1\cdot10^{-2}$	0.21	0.11	0.16	$8.9\cdot10^{-2}$	0.3	0.26	0.12	$4.6\cdot10^{-2}$	0.2
0.32	0.32	0.26	0.47	0.32	$2.9\cdot10^{-2}$	0.33	$6\cdot10^{-3}$	$2.4\cdot10^{-2}$	$7\cdot10^{-3}$	0.53	0.42	$6\cdot10^{-3}$	0.53	$4.9\cdot10^{-2}$	0.55	0.42	1	0.68	0.3	0.17	0.26	0.13	0.3	$5.9\cdot10^{-2}$	0.17	$6.8\cdot10^{-2}$	0.26	$9\cdot10^{-3}$	$6\cdot10^{-2}$	0.24	$7.9\cdot10^{-2}$	0.26	$2.7\cdot10^{-2}$	0.44	0.42	0.1	$3.9\cdot10^{-2}$	0.27
0.21	0.23	0.13	0.35	0.21	$1.9\cdot10^{-2}$	$5.8\cdot10^{-2}$	$7.1\cdot10^{-2}$	$1.6\cdot10^{-2}$	$6\cdot10^{-3}$	0.5	0.34	$4\cdot10^{-2}$	0.5	$1\cdot10^{-3}$	0.52	0.38	0.68	1	0.22	$4\cdot10^{-3}$	$9.3\cdot10^{-2}$	0.13	0.22	$7.4\cdot10^{-2}$	0.18	$7.8\cdot10^{-2}$	$9\cdot10^{-2}$	$5.2\cdot10^{-2}$	$2.5\cdot10^{-2}$	0.21	$6\cdot10^{-2}$	$8.9\cdot10^{-2}$	$1.4\cdot10^{-2}$	0.3	0.29	$9.6\cdot10^{-2}$	$6.6\cdot10^{-2}$	0.2
0.38	0.33	0.35	0.35	0.54	$3.8\cdot10^{-2}$	0.33	$6.2\cdot10^{-2}$	$5.1\cdot10^{-2}$	$2.1\cdot10^{-2}$	0.3	0.27	$4.3\cdot10^{-2}$	0.3	$4\cdot10^{-2}$	0.3	0.22	0.3	0.22	1	0.53	0.56	$6.7\cdot10^{-2}$	0.8	0.15	$2.1\cdot10^{-2}$	$7.2\cdot10^{-2}$	0.56	0.18	$5.3\cdot10^{-2}$	0.32	0.24	0.56	0.52	0.53	0.56	$4.6\cdot10^{-2}$	0.41	0.79
0.27	0.29	0.55	0.35	0.58	0.1	0.49	$1.7\cdot10^{-2}$	$5.3\cdot10^{-2}$	$8.4\cdot10^{-2}$	0.15	0.14	$3.6\cdot10^{-2}$	0.15	$7.7\cdot10^{-2}$	0.12	$6.4\cdot10^{-2}$	0.17	$4\cdot10^{-3}$	0.53	1	0.78	$2.8\cdot10^{-2}$	0.53	0.16	$1.1\cdot10^{-2}$	$7.3\cdot10^{-2}$	0.78	$2.2\cdot10^{-2}$	$3.8\cdot10^{-2}$	0.2	0.24	0.78	0.45	0.5	0.53	$7\cdot10^{-3}$	0.38	0.55
0.32	0.34	0.58	0.45	0.61	$7.3\cdot10^{-2}$	0.5	$4.4\cdot10^{-2}$	$9.7\cdot10^{-2}$	$9.8\cdot10^{-2}$	0.27	0.24	$4.9\cdot10^{-2}$	0.27	$7.5\cdot10^{-2}$	0.24	0.17	0.26	$9.3\cdot10^{-2}$	0.56	0.78	1	$6.9\cdot10^{-2}$	0.56	0.12	$6.7\cdot10^{-2}$	$8.9\cdot10^{-2}$	0.8	$4.1\cdot10^{-2}$	$4.6\cdot10^{-2}$	0.25	0.27	0.8	0.42	0.57	0.58	$4.7\cdot10^{-2}$	0.34	0.57
0.15	0.17	0.17	0.18	0.18	$7.2\cdot10^{-2}$	$4.4\cdot10^{-2}$	0	$1\cdot10^{-3}$	$5.3\cdot10^{-2}$	0.22	0.19	$6\cdot10^{-2}$	0.22	$1.6\cdot10^{-2}$	0.22	0.21	0.13	0.13	$6.7\cdot10^{-2}$	$2.8\cdot10^{-2}$	$6.9\cdot10^{-2}$	1	$6.7\cdot10^{-2}$	$3.4\cdot10^{-2}$	0.51	0.68	$7.2\cdot10^{-2}$	0.19	0.22	0.48	0.11	$7.1\cdot10^{-2}$	$2.4\cdot10^{-2}$	$9\cdot10^{-2}$	$4.5\cdot10^{-2}$	0.2	$1.2\cdot10^{-2}$	$4.9\cdot10^{-2}$
0.38	0.33	0.35	0.35	0.54	$3.8\cdot10^{-2}$	0.33	$6.2\cdot10^{-2}$	$5.1\cdot10^{-2}$	$2.1\cdot10^{-2}$	0.3	0.27	$4.3\cdot10^{-2}$	0.3	$4\cdot10^{-2}$	0.3	0.22	0.3	0.22	0.8	0.53	0.56	$6.7\cdot10^{-2}$	1	0.15	$2.1\cdot10^{-2}$	$7.2\cdot10^{-2}$	0.56	0.18	$5.3\cdot10^{-2}$	0.32	0.24	0.56	0.52	0.53	0.56	$4.6\cdot10^{-2}$	0.41	0.79
$4.6\cdot10^{-2}$	$4.7\cdot10^{-2}$	$4.4\cdot10^{-2}$	$2.3\cdot10^{-2}$	0.17	$9.2\cdot10^{-2}$	0.1	$4.5\cdot10^{-2}$	$3.6\cdot10^{-2}$	$7.8\cdot10^{-2}$	$1\cdot10^{-2}$	0.12	$1.4\cdot10^{-2}$	$1\cdot10^{-2}$	$8.9\cdot10^{-2}$	$3.7\cdot10^{-2}$	$3.8\cdot10^{-2}$	$5.9\cdot10^{-2}$	$7.4\cdot10^{-2}$	0.15	0.16	0.12	$3.4\cdot10^{-2}$	0.15	1	$2.7\cdot10^{-2}$	0.17	0.13	$7.1\cdot10^{-2}$	0.54	$3.9\cdot10^{-2}$	0.18	0.13	0.46	0.1	0.15	$9.2\cdot10^{-2}$	0.53	0.18
0.28	0.32	$1.3\cdot10^{-2}$	$1.8\cdot10^{-2}$	0.18	$6.3\cdot10^{-2}$	$5\cdot10^{-3}$	$9.4\cdot10^{-2}$	$4.8\cdot10^{-2}$	0	0.23	0.23	$2.8\cdot10^{-2}$	0.23	$2.3\cdot10^{-2}$	0.25	0.2	0.17	0.18	$2.1\cdot10^{-2}$	$1.1\cdot10^{-2}$	$6.7\cdot10^{-2}$	0.51	$2.1\cdot10^{-2}$	$2.7\cdot10^{-2}$	1	0.53	$6.9\cdot10^{-2}$	$2.2\cdot10^{-2}$	0.19	0.37	$2.6\cdot10^{-2}$	$6.7\cdot10^{-2}$	$8.5\cdot10^{-2}$	$1\cdot10^{-2}$	$1.5\cdot10^{-2}$	0.54	$6.7\cdot10^{-2}$	$3.9\cdot10^{-2}$
$4\cdot10^{-2}$	$5\cdot10^{-2}$	$4.5\cdot10^{-2}$	$7.8\cdot10^{-2}$	$3.4\cdot10^{-2}$	$2\cdot10^{-3}$	$5\cdot10^{-3}$	$9.9\cdot10^{-2}$	$1.5\cdot10^{-2}$	$7.9\cdot10^{-2}$	0.1	0.14	$5.9\cdot10^{-2}$	0.1	$7.9\cdot10^{-2}$	0.12	0.15	$6.8\cdot10^{-2}$	$7.8\cdot10^{-2}$	$7.2\cdot10^{-2}$	$7.3\cdot10^{-2}$	$8.9\cdot10^{-2}$	0.68	$7.2\cdot10^{-2}$	0.17	0.53	1	$8.7\cdot10^{-2}$	0.13	0.44	0.24	$5.5\cdot10^{-2}$	$8.7\cdot10^{-2}$	$6.1\cdot10^{-2}$	$9\cdot10^{-3}$	$6.9\cdot10^{-2}$	0.2	$4\cdot10^{-2}$	$9.5\cdot10^{-2}$
0.32	0.34	0.58	0.45	0.61	$7.2\cdot10^{-2}$	0.5	$4.4\cdot10^{-2}$	$9.6\cdot10^{-2}$	0.1	0.26	0.24	$4.7\cdot10^{-2}$	0.26	$7.6\cdot10^{-2}$	0.24	0.17	0.26	$9\cdot10^{-2}$	0.56	0.78	0.8	$7.2\cdot10^{-2}$	0.56	0.13	$6.9\cdot10^{-2}$	$8.7\cdot10^{-2}$	1	$4.1\cdot10^{-2}$	$4.8\cdot10^{-2}$	0.25	0.27	0.8	0.42	0.57	0.58	$4.7\cdot10^{-2}$	0.34	0.57
$1.3\cdot10^{-2}$	$1\cdot10^{-2}$	$7.3\cdot10^{-2}$	0.15	$3.2\cdot10^{-2}$	$2.5\cdot10^{-2}$	$6.4\cdot10^{-2}$	$5.6\cdot10^{-2}$	$5\cdot10^{-3}$	$9.1\cdot10^{-2}$	0.14	0.13	$3.7\cdot10^{-2}$	0.14	$1\cdot10^{-2}$	0.13	0.16	$9\cdot10^{-3}$	$5.2\cdot10^{-2}$	0.18	$2.2\cdot10^{-2}$	$4.1\cdot10^{-2}$	0.19	0.18	$7.1\cdot10^{-2}$	$2.2\cdot10^{-2}$	0.13	$4.1\cdot10^{-2}$	1	0.16	$8.9\cdot10^{-2}$	$1.7\cdot10^{-2}$	$4\cdot10^{-2}$	0.16	$2.7\cdot10^{-2}$	$4.1\cdot10^{-2}$	$7.1\cdot10^{-2}$	0.11	0.17
$7.2\cdot10^{-2}$	$4.8\cdot10^{-2}$	$1\cdot10^{-3}$	$7.5\cdot10^{-2}$	0.1	$6.7\cdot10^{-2}$	0.11	$9.5\cdot10^{-2}$	$8.9\cdot10^{-2}$	$1.3\cdot10^{-2}$	$2.1\cdot10^{-2}$	0.14	0.11	$2.1\cdot10^{-2}$	0.24	$1.6\cdot10^{-2}$	$8.1\cdot10^{-2}$	$6\cdot10^{-2}$	$2.5\cdot10^{-2}$	$5.3\cdot10^{-2}$	$3.8\cdot10^{-2}$	$4.6\cdot10^{-2}$	0.22	$5.3\cdot10^{-2}$	0.54	0.19	0.44	$4.8\cdot10^{-2}$	0.16	1	$2.2\cdot10^{-2}$	$4\cdot10^{-3}$	$4.8\cdot10^{-2}$	0.19	$5.6\cdot10^{-2}$	$3.1\cdot10^{-2}$	$7.6\cdot10^{-2}$	0.24	$4.3\cdot10^{-2}$
0.27	0.25	0.19	0.16	0.38	$6.7\cdot10^{-2}$	$4.3\cdot10^{-2}$	$3.9\cdot10^{-2}$	$5\cdot10^{-3}$	$1.7\cdot10^{-2}$	0.29	0.25	$9.6\cdot10^{-2}$	0.29	$7.1\cdot10^{-2}$	0.3	0.21	0.24	0.21	0.32	0.2	0.25	0.48	0.32	$3.9\cdot10^{-2}$	0.37	0.24	0.25	$8.9\cdot10^{-2}$	$2.2\cdot10^{-2}$	1	0.56	0.25	0.28	0.22	0.22	$9.8\cdot10^{-2}$	0.24	0.33
0.16	0.15	0.15	0.13	0.3	$5.7\cdot10^{-2}$	$7.8\cdot10^{-2}$	$6.3\cdot10^{-2}$	$4\cdot10^{-3}$	$6.5\cdot10^{-2}$	0.14	0.19	$3.1\cdot10^{-2}$	0.14	$4.6\cdot10^{-2}$	0.12	0.11	$7.9\cdot10^{-2}$	$6\cdot10^{-2}$	0.24	0.24	0.27	0.11	0.24	0.18	$2.6\cdot10^{-2}$	$5.5\cdot10^{-2}$	0.27	$1.7\cdot10^{-2}$	$4\cdot10^{-3}$	0.56	1	0.27	0.34	0.15	0.19	$9.2\cdot10^{-2}$	0.32	0.27
0.32	0.34	0.58	0.45	0.61	$7.3\cdot10^{-2}$	0.5	$4.5\cdot10^{-2}$	$9.6\cdot10^{-2}$	$9.9\cdot10^{-2}$	0.26	0.24	$4.6\cdot10^{-2}$	0.26	$7.7\cdot10^{-2}$	0.24	0.16	0.26	$8.9\cdot10^{-2}$	0.56	0.78	0.8	$7.1\cdot10^{-2}$	0.56	0.13	$6.7\cdot10^{-2}$	$8.7\cdot10^{-2}$	0.8	$4\cdot10^{-2}$	$4.8\cdot10^{-2}$	0.25	0.27	1	0.42	0.57	0.57	$4.6\cdot10^{-2}$	0.34	0.56
0.16	0.16	0.21	$9.7\cdot10^{-2}$	0.41	$7.5\cdot10^{-2}$	0.19	$1.6\cdot10^{-2}$	$3\cdot10^{-3}$	$2\cdot10^{-2}$	$8.7\cdot10^{-2}$	0.15	$4.2\cdot10^{-2}$	$8.7\cdot10^{-2}$	$4.9\cdot10^{-2}$	$5.5\cdot10^{-2}$	$8.9\cdot10^{-2}$	$2.7\cdot10^{-2}$	$1.4\cdot10^{-2}$	0.52	0.45	0.42	$2.4\cdot10^{-2}$	0.52	0.46	$8.5\cdot10^{-2}$	$6.1\cdot10^{-2}$	0.42	0.16	0.19	0.28	0.34	0.42	1	0.26	0.34	$5.3\cdot10^{-2}$	0.78	0.57
0.51	0.45	0.47	0.49	0.56	$1.3\cdot10^{-2}$	0.34	$1.5\cdot10^{-2}$	$7.1\cdot10^{-2}$	$3.9\cdot10^{-2}$	0.46	0.36	$3.4\cdot10^{-2}$	0.46	$8.2\cdot10^{-2}$	0.47	0.3	0.44	0.3	0.53	0.5	0.57	$9\cdot10^{-2}$	0.53	0.1	$1\cdot10^{-2}$	$9\cdot10^{-3}$	0.57	$2.7\cdot10^{-2}$	$5.6\cdot10^{-2}$	0.22	0.15	0.57	0.26	1	0.77	$6.7\cdot10^{-2}$	0.19	0.51
0.51	0.48	0.46	0.42	0.6	$3.5\cdot10^{-2}$	0.35	$3\cdot10^{-3}$	$3.4\cdot10^{-2}$	$1\cdot10^{-2}$	0.4	0.32	$4.6\cdot10^{-2}$	0.4	$8.2\cdot10^{-2}$	0.41	0.26	0.42	0.29	0.56	0.53	0.58	$4.5\cdot10^{-2}$	0.56	0.15	$1.5\cdot10^{-2}$	$6.9\cdot10^{-2}$	0.58	$4.1\cdot10^{-2}$	$3.1\cdot10^{-2}$	0.22	0.19	0.57	0.34	0.77	1	$8.3\cdot10^{-2}$	0.26	0.56
0.2	0.34	$5\cdot10^{-3}$	$7\cdot10^{-3}$	$8\cdot10^{-2}$	$3.6\cdot10^{-2}$	$1.4\cdot10^{-2}$	$5.2\cdot10^{-2}$	$2.6\cdot10^{-2}$	$6.9\cdot10^{-2}$	0.18	0.16	$7.3\cdot10^{-2}$	0.18	$1.8\cdot10^{-2}$	0.19	0.12	0.1	$9.6\cdot10^{-2}$	$4.6\cdot10^{-2}$	$7\cdot10^{-3}$	$4.7\cdot10^{-2}$	0.2	$4.6\cdot10^{-2}$	$9.2\cdot10^{-2}$	0.54	0.2	$4.7\cdot10^{-2}$	$7.1\cdot10^{-2}$	$7.6\cdot10^{-2}$	$9.8\cdot10^{-2}$	$9.2\cdot10^{-2}$	$4.6\cdot10^{-2}$	$5.3\cdot10^{-2}$	$6.7\cdot10^{-2}$	$8.3\cdot10^{-2}$	1	$4.2\cdot10^{-2}$	$2.6\cdot10^{-2}$
$8.9\cdot10^{-2}$	$9.3\cdot10^{-2}$	0.15	$4.8\cdot10^{-2}$	0.32	$9.9\cdot10^{-2}$	0.13	$3\cdot10^{-2}$	$1.6\cdot10^{-2}$	$6.2\cdot10^{-2}$	$3.9\cdot10^{-2}$	0.12	$4.3\cdot10^{-2}$	$3.9\cdot10^{-2}$	$6.2\cdot10^{-2}$	$6\cdot10^{-3}$	$4.6\cdot10^{-2}$	$3.9\cdot10^{-2}$	$6.6\cdot10^{-2}$	0.41	0.38	0.34	$1.2\cdot10^{-2}$	0.41	0.53	$6.7\cdot10^{-2}$	$4\cdot10^{-2}$	0.34	0.11	0.24	0.24	0.32	0.34	0.78	0.19	0.26	$4.2\cdot10^{-2}$	1	0.47
0.38	0.34	0.35	0.31	0.56	$4.3\cdot10^{-2}$	0.32	$4.8\cdot10^{-2}$	$3\cdot10^{-2}$	0	0.28	0.26	$3.4\cdot10^{-2}$	0.28	$3.2\cdot10^{-2}$	0.26	0.2	0.27	0.2	0.79	0.55	0.57	$4.9\cdot10^{-2}$	0.79	0.18	$3.9\cdot10^{-2}$	$9.5\cdot10^{-2}$	0.57	0.17	$4.3\cdot10^{-2}$	0.33	0.27	0.56	0.57	0.51	0.56	$2.6\cdot10^{-2}$	0.47	1

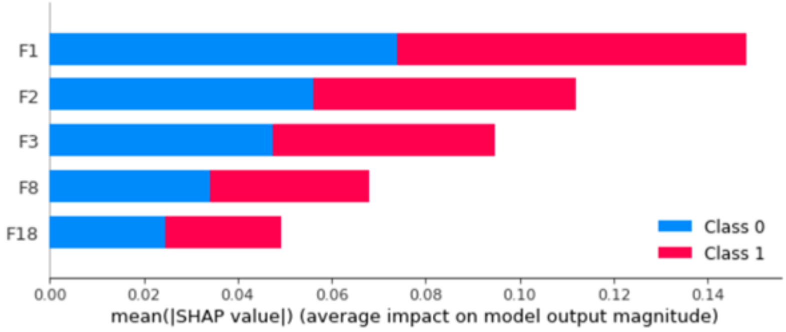

(a) DB-DMR-IR

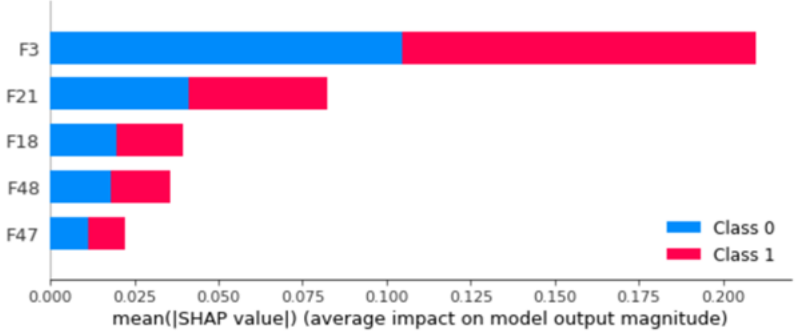

(b) DB-FOOT-IR

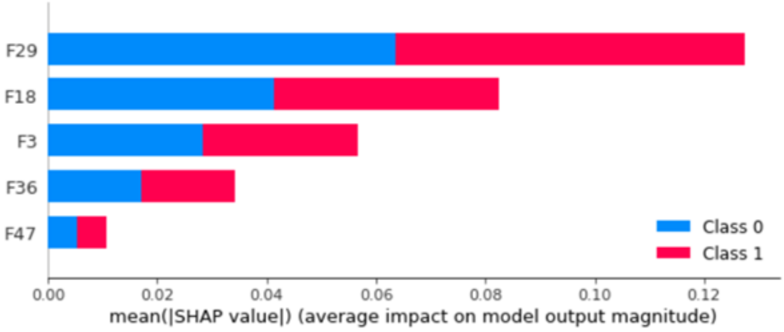

(c) DB-THY-IR

Fig. 3.10: The absolute summary plot of the best performing models using UnionFeature_Set for the three datasets.

Figure 3.10 displays the absolute summary plot of the models(3.4) for the three datasets – DB-DMR-IR, DB-FOOT-IR, and DB-THY-IR. The figure also demonstrates the relative importance of features by class. In this figure, the average absolute value of the SHAP values for each variable is taken in order to obtain a bar chart as a function of the contribution of each variable to the prediction of the model. The features are ordered from being most (top) to least (bottom) influential.The graphs are plotted for the five most significant features (out of 467 features) that contribute to the model's prediction. The following is observed from figure 3.10 and Table 3.8.

- Feature F1 (Texture energy using LS kernel BAR[15]) is the most influential feature for predicting the abnormality in DB-DMR-IR dataset. Features F3 (Contrast of Gray level difference statistics BAR[15]) and F29 (Difference between Co-occurrence levels based energy from Modified LBP Edge matrix RAS[24]) are the most influential for DB-FOOT-IR and DB-THY-IR datasets respectively.
- Features F3 (Contrast of Gray level difference statistics BAR[15]) and F18 (Difference variance from GLCM Sub-Matrix GUP) are significant features in all the models for predicting abnormality in the human body.
- Texture and Energy-based Features extracted from the ROI are observed to be more influential compared to the ones extracted from the entire thermal image for all the datasets.

Thus, a feature subset is obtained from UnionFeature_Set (Table 3.8) that is most relevant and not redundant for diagnosing inflammation using Thermography. Also, the respective feature-sets effectively distinguish normal and abnormal thermal patterns for the datasets.

3.5 Chapter Summary

This chapter introduces two statistical models aimed at differentiating normal and abnormal thermal patterns in medical thermal imaging. The first model utilizes a novel set of hand-crafted features extracted from three publicly available datasets, focusing on detecting abnormalities related to breast cancer, diabetes, and thyroid disorders. The methodology involves asymmetry-based features extraction techniques, including GLCM-based texture features, LBP-based statistical features, and LBP-Otsu threshold features, which are used to detect temperature asymmetry in the human body. The second model systematically evaluates the performance of this proposed feature set in comparison with eight state-of-the-art feature extraction techniques, establishing a standardized methodology for analyzing thermal images. In this model, a total of 467 distinct features were compiled by integrating features from multiple existing studies into a unified feature set (UnionFeature_Set). Feature selection was performed using four widely used methods — PC, mRMR, ReF, and ChiSq, to refine the feature space, while classification was conducted using *k*-NN, SVM, DTC, and RFC. To ensure unbiased evaluation, a two-level sampling strategy was employed to address dataset imbalance, and cross validation techniques, including 5-fold, 10-fold, and LOOCV were used to assess model generalization.

The results of the study demonstrated that without feature selection, the BAR feature set performed best for DB-DMR-IR and DB-THY-IR datasets, while the GUP feature set yielded the highest accuracy for DB-FOOT-IR. However, when feature selection methods were applied, the UnionFeature_Set consistently outperformed individual feature extraction methods, significantly improving classification accuracy. Among the feature selection techniques, ReF and mRMR proved to be the most effective in selecting relevant features while reducing redundancy. In terms of classifier performance, SVM and RFC emerged as the most effective models, particularly when combined with mRMR and ReF feature selection techniques, whereas Decision Trees showed relatively lower performance, especially for datasets with high-dimensional feature spaces. Finally, we obtained a feature-subset of 45, 57, and 39 features (from UnionFeature_Set) filtered by mRMR feature selection method for DB-DMR-IR and DB-FOOT-IR, and ReF FS method for DB-THY-IR, respectively. The feature-subset obtained for all the datasets are relevant, non-redundant, and distinguishes normal and abnormal thermal patterns with an accuracy of 94.75% on the DB-DMR-IR, 93.14% on DB-FOOT-IR, and 92.06% on DB-THY-IR dataset. The findings establish a standardized and statistically validated approach for thermal pattern differentiation using machine learning, highlighting the potential of thermography as a diagnostic tool. The study addresses critical challenges in feature redundancy and dataset imbalance, offering a robust framework for future research in automated thermal image analysis, with promising applications in disease screening and early detection in clinical settings.

Chapter 4

Deep Learning-based Thermal Biomarker Analysis

This chapter proposes a light weight deep learning-based classification model that can be deployed on mobile devices for characterizing and detecting abnormality due to inflammation in human thermal images.

4.1 Introduction

This chapter proposes an automated and computational intelligence-aided diagnostic system that can be used for precise and timely detection of abnormality due to inflammation in human body. For the proposed statement, a lightweight model is presented that can be deployed on mobile devices for ease of human use. For the proposed statement, UnionFeature_Set, various hand-crafted and Deep Learning-based feature-sets are extracted from two thermal imaging based datasets and their performance is compared using four state-of-the-art classifiers and 10-fold cross validation sampling strategy. Also, light weight pre-trained Deep Learning models are proposed to characterize and classify abnormal patterns in medical thermal images.

This chapter describes the various Hand-crafted Features in section 4.2.1 and deep learning-based models for features extraction in section 4.2.2. The classifiers used for comparing the performance of UnionFeature_Set, hand-crafted, and deep learning-based feature-sets are discussed in section 4.2.3. The section 4.3 describes the experimental setup for the study, followed by results analysis in section 4.4. The chapter is summarized in section 4.5.

4.2 Methodology

Characteristics of a pattern in an image are extracted in the form of features. It is a crucial phase in a machine learning pipeline. Features may be manually extracted as Hand-crafted Features(section 4.2.1) or automatically using Deep Leaning Models (section 4.2.2). This section describes and contrasts various Hand-crafted and Deep Learning-based feature-sets extracted for classifying abnormal biomarkers in the medical thermal images. Also, the state-of-the-art classification methods used for evaluation in the study are stated in section 4.2.3.

4.2.1 Traditional Hand-crafted Feature-sets

The 12 hand-crafted feature-sets are extracted for the study (detailed in Table 4.1). They are categorized as Textural features (FOS, GLDS-based features, NGTDM-based features, GLRM-based features, SFM-based features, TEM, LBP, GLCM-based features), Multi-scale Features (WT-based features, features from FPS), SHAPE-based features, HOG-based features. The Table 4.1 briefly describes and compares the various texture based-hand-crafted feature sets. Also, the UnionFeature_Set obtained in Chapter3, section 3.4.3 are extracted for investigation. The features generated are normalized in the range [0,1] before applying the classifier.

4.2.2 Deep Learning-based Feature-sets

Deep Learning (DL) has redefined the task of image processing, wherein high-level features may be extracted using convolutional Neural Networks (CNN). Figure 4.1 illustrates the fundamental architecture of a CNN Model. A CNN model comprises multiple Convolutional layers, pooling layers and fully connected layers at the end. In convolutional layers, the filters convolve with the input thermal image, followed by activation functions, and intermediate feature maps are generated. The pooling layers scale down the feature map's dimensions, reducing the impact of overlapping receptive fields and improving the computational efficiency. The fully connected layers, along with the Soft-Max layer, operate as its classifier and finally generate the output. DL-based models require a vast amount of training data to learn the network parameters.

Table 4.1: Comparison of the hand-crafted feature-sets.

Feature Extraction Method	**Number of Features**	**Feature Names**	**Description**
First Order Statistics[FOS]	8	Mean, variance, median, mode, skewness, kurtosis, standard deviation, entropy	First Order Statistics are computed from the empirical probability density function denoted as image histogram.
Gray Level Co-Occurrence Matrix based features[GLCM] [110, 125, 126]	20	Contrast, Cluster Shade, Homogeneity, Sum Variance, Inverse Difference Normalized, Information Measure of Correlation 2, Angular Second Moment, Sum Entropy, Entropy, Difference Variance, Information Measure of Correlation 1, Sum Average, Variance, Correlation, Auto-correlation, Dissimilarity, Cluster, Prominence, Difference Entropy, Maximum Probability, Inverse Difference Moment Normalized	Gray Level Co-Occurrence Matrix based features are computed from second-order joint conditional probability density functions defining the co-occurrences of the pixel in given direction in the image.
Uniform Local Binary Patterns[LBP][127]	59	-	Uniform Local Binary Patterns based features encode the information in the equidistant neighbourhood around a pixel as local texture information as a binary Pattern. In uniform LBP, a centre pixel is labelled as uniform if the number of bit transitions in the circular bit-stream is less than or equal to 2.
Gray Level Run-length Matrix based features[GLRM][128]	11	Gray-Level and Run-Length Non-Uniformity, Non-Uniformity, Run Percentage, Low and High Gray-Level Run Emphasis, Short and Long Run Emphasis, Short Low Gray-Level Emphasis, Short Run High Gray-Level and Long Run Low Gray-Level emphasis, Long Run High-Level emphasis.	Gray-Level Run-length Matrix-based features are computed from the matrix indicating the set of consecutive runs of a pixel. Run Length denotes the pixel count with same gray-level in the run.
Histogram of Oriented Gradients based features[HOG][129]	5	-	Histogram of Oriented Gradients based features computes the frequency of gradient orientation occurrences in localized portions of an image. It returns the shape information of the region.
Wavelet Transform based features[WT][130]	120	Mean, Variance, Skewness, Kurtosis, Entropy are calculated from Wavelet Transformed component of images using wavelets - Daubechies- 3, Daubechies-10, Coiflet-1, Coiflet-5, Symlet-2, and Symlet-8.	Discrete Wavelet Transform-based features of an image include Mean, Variance, Skewness, Kurtosis, and Entropy calculated over four sub-images obtained by applying a family of wavelet functions on the input image.
Shape-Based features [SHAPE]	7	Area, Euler number, perimeter, convexity, eccentricity, orientation, solidity	Shape-based features highlight the region covered by the region in an image.
Gray-Level Difference Statistics based features[GLDS][131]	5	Homogeneity, contrast, energy, entropy, mean	Gray-Level Difference Statistics based features are computed from the first order statistics of local attributes based on absolute differences between pairs of gray-levels or of average gray-levels.
Neighborhood Gray-Tone Difference Matrix based features[NGTDM][132]	5	Contrast, Coarseness, Busyness, Texture Strength, Complexity	Neighborhood Gray-Tone Difference Matrix based features indicates the visual properties of texture in the image
Statistical Feature Matrix-based features[SFM][133]	4	Coarseness, contrast, periodicity, and regularity/roughness	Statistical Feature Matrix-based features are computed as the statistical properties of pixel pairs occurring at multiple distances within an image
Texture Energy Measure[TE][134]	6	Texture energy from LL (Level-Level Mask), EE (Edge-Edge Mask), and SS (Spot-Spot Mask) kernels and Average Texture Energy from LE (Level-Edge) and EL(Edge-Level), ES (Edge-Spot) and SE(Spot-Edge), and LS (Level-Spot) and SL (Spot-Level) kernels.	Law's texture Energy Measures are computed as statistics obtained from convoluted images of masks of length $L \times L$ and the image. Masks are obtained by self-convolution of vectors followed by multiplication of same-length row vectors
Fourier Power Spectrum-based features[FPS]	2	Radial sum and Angular sum	Fourier Power Spectrum-based features are extracted from Discrete Fourier transformed images.

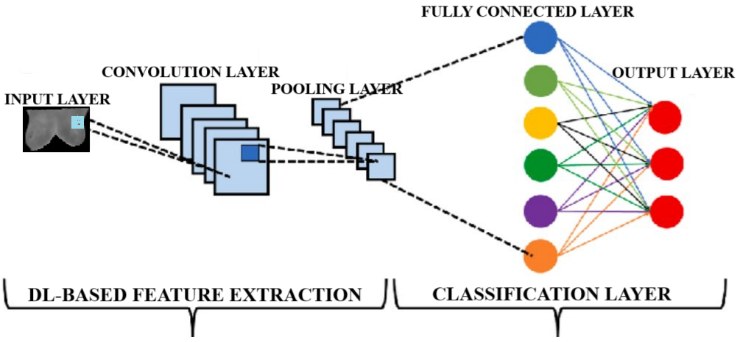

Fig. 4.1: A basic architecture of CNN Model.

Due to the paucity of large medical thermal imaging datasets to train a DL model from scratch, pre-trained CNN models are used as a feature extractor by preserving their initial architecture and network weights. The features from ten state-of-the-art CNN models - VGG16, Alexnet, GoogleNet, Resnet-18, EfficientNet-b0, Inception-Resnetv2, Mobilenet-V2, Nasnet-Mobile, Shufflenet, and Squeezenet, are extracted and investigated. The Table 4.2 briefly presents a comparison the stated CNN architectures.

4.2.3 Classifiers

The 12 hand-crafted, UnionFeature_Set and 10 DL-based feature-sets obtained are fed to the four state-of-the-art classifiers - DTC[118], RFC, SVM[117], and k-NN[116] along with 10fold cross validation sampling strategy..

DTC is a powerful classifier that presents the data in a decision tree form. DTC is greedy in nature while choosing attributes for splitting. It can handle datasets with categorical attributes only. To apply DTC on the numeric data, it has to be discretized. DTC provides a transparent model for a given dataset. A little addition or removal in the dataset may modify the tree entirely. Also, it may result in an over-fitted model for small datasets. In contrast, RFC uses an ensemble of two or more DTCs. An unlabeled instance is classified as a mode of the classes given by an individual DTC in the ensemble. It results in a reliable and precise ensemble of trees for problems with unbalanced datasets or datasets with large feature spaces. A slight modification in the dataset may change a tree, but the ensemble generated will be stable, comparatively. RFCs tend to generate less over-fitted ensembles. Computing an RFC-based model is a computationally expensive task.

k-NN is the most popular and straightforward instance-based method for classification, highly sensitive to the value of k (number of neighbors in k-NN)and

Table 4.2: Comparison of the most commonly used CNN Architectures.

Feature Extraction Method	Depth	Number of Parameters (Millions)	Layer Name	Number of Features Used	Network Details
Alexnet [ANET] [135]	8	61	’drop7’	4096	Alexnet is made up of 5 convolutional layers (with activation function as a Rectified linear unit (ReLU) and 3 connected layers. With the help of dropout layers, the over-fitting problem is handled, but the number of iterations required for convergence is huge. The number of parameters is also large in fully connected layers.
VGG16 [VGG16] [136]	16	138	’drop7’	4096	VGG-16 comprises of 13 convolutional layers with activation function as ReLU, 5 pooling layers, and 3 dense layers. Convolving and maxpool kernel sizes are 3×3 and 2×2 with a stride of two, respectively. The time complexity of VGGNet is high, and accuracy is reduced.
GoogleNet [GNET] [137]	22	7	’pool5-drop_7x7_s1’	1024	GoogleNet uses Network-in-network. It basically replaces convolution filters with an approximation function and uses global average pooling in place of dense layers. This increased the network’s width and depth without a huge computational complexity and performance.
Resnet-18 [RSN18] [138]	18	11.7	’pool5’	512	It comprises convolution layers with filters of size 3×3 with 2 pooling layers. It uses Residual blocks, repeated throughout the network, to solve the vanishing gradient problem. Residual blocks constitute skip-connections between convolutional and pooling layers. This model has fewer filters and lower complexity but suffers from over-fitting.
EfficientNet-b0 [EFF-b0] [139]	82	5.3	EfficientNet-b0|model|head|global_average_pooling2d|GlobAvgPool’	1280	EfficientNet, comparatively, has fewer parameters and FLOPs along with low time complexity and better performance for classification tasks. It uses compound dimension scaling to find the best combination of image resolution and network’s depth and width.
Inception-Resnetv2 [INRESV2] [140]	164	55.9	’avg_pool’	1536	Inception-ResNet-V2 has a total of 164 layers including 4 and 160 pooling and convolutional layers, respectively, with better better performance at shorter epochs. Its architecture uses a combination of Residual blocks with Inception’s architecture.
MobileNet-V2 [MOBNETV2] [141]	53	3.5	’global_average_pooling2d_1’	1280	MobileNet is a mobile suitable model, consisting of depthwise separable convolution -, separable into depth wise convolution and pointwise convolution. It comprises 19 inverted residual structures between thin bottleneck layers followed by a convolution layer with 32 filters.
Nasnet-Mobile [NAS-MOB] [142]	*	5.3	’global_average_pooling2d_1’	1056	NasNet architecture uses a regularization technique - Scheduled Drop Path to improve the generalization capability of the model. It uses a Neural Architecture search method to identify a network’s architectural building block on a small dataset and then use it for the larger dataset.
ShuffleNet [SHUF] [143]	50	1.4	’node_200’	544	ShuffleNet is designed for mobile devices requiring low computing power. ShuffleNet is made up of pointwise group convolution and channel shuffling.
SqueezeNet [SQZN] [144]	18	1.24	’pool10’	1000	SqueezeNet comprises of - Squeeze part and Expand part, wherein, Squeeze part has 1×1 filters channelling its output into expand layer, having a mix of filters of size 1×1 and 3×3.

choice of similarity function(for finding proximity with neighbors). It is considerably costly for computation and storage of classifying new instances. The lower values of k tend to incorrectly classify due to data inconsistencies, whereas the higher value minimizes the impact of noise but makes the experiments computationally expensive. Based on robust theory, SVM proposes to build an optimal hyperplane that separates two classes, with a maximum margin around the hyperplane. This approach does not cause the model to be over-fitted, even with the limited number of samples in the dataset. A fundamental limitation of SVM based model is its poor transparency and capability to interpret the model.

Also, five light weight pre-trained DL models(EfficientNet-b0[139], MobileNet-V2[141], Nasnet-Mobile[142], ShuffleNet[143], and SqueezeNet[144]) are used to characterize and classify abnormal patterns in medical thermal images.

4.3 Experimental Setup

The experiments are performed on a computer system having a Windows 10 operating system with an i7 (9^{th} generation) Processor and 32GB primary memory. The experiments are performed and analyzed using MATLAB 2024 (64-bit).The figure 4.2 elaborates the steps and experimental framework used for the study.

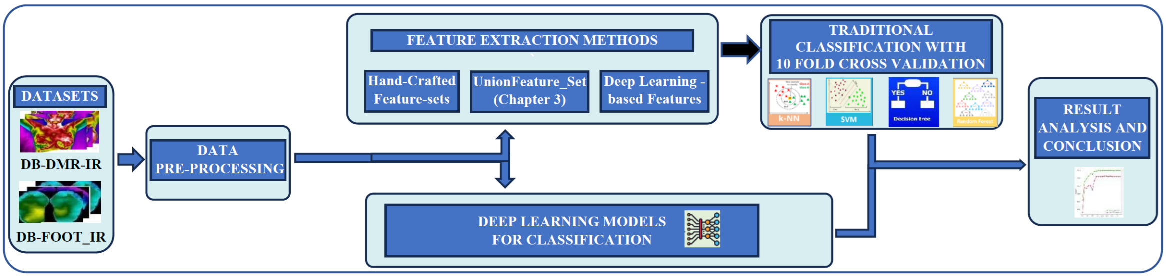

Fig. 4.2: The Experimental Framework used in the study.

In this study, two publicly available medical thermography-based datasets - **DB-DMR-IR**[20] and **DB-FOOT-IR**[21] are considered. DB-THY-IR is not used for the study as number of samples in the dataset is very less to be applied with a DL model. The pre-processing steps for the three datasets are described in Chapter 1, section 1.2.1. Table 4.3 states the number of patients/volunteers and the samples used in the study. DB-DMR-IR dataset is augmented with images acquired during the last 2 minutes of dynamic acquisition procedure to construct a larger dataset.

Altogether 23 various feature-sets are extracted from the transformed and segmented gray-scale thermal images(Table 4.3). All the feature-sets generated are

Table 4.3: Datasets size used for the analysis

DataSets	No. Of Participants	Normal Thermal Images	Abnormal Thermal Images	Total Thermal Images
DB-FOOT-IR	90	45	45	90
DB-DMR-IR	200	500	500	1000

Table 4.4: Parameters and their values used for model tuning.

Algorithm	Parameters	Parameters Values
k-NN	k	$[11 - 200]$
	Distance Metric	[Cosine, Euclidean, Jaccard, Hamming]
SVM	Cost	$[2^{-10} - 2^{10}]$
	Kernel Type	[Linear, RBF]
	Gamma	$[2^{-12} - 2^12]$
DTC	Splitting criteria	Gini's Diversity Index, Cross Entropy
	Pruning criteria	Enabled, Disabled
	Minimum leaf size	$[50 - 200]$.
RFC	Ensemble size	[3-50]

normalized.

The analysis with four promising classifiers - DTC, k-NN, SVM, and RFC is performed along with a grid search on the respective classifier's parameters (Table 4.4) to achieve the best results. LIBSVM[1] implementation of SVM is used in the study. The grid search for SVM is performed over the cost parameter, C, and two kernel functions. Various optimization parameters of DTC used are Minimum Leaf Size (minimum count of instances per leaf), Pruning Criteria (for pruning the tree to limit over-fitting of training data), and Splitting Criteria (for selecting an attribute for further splitting). The ensemble size (number of weak classifiers/trees in ensemble) used in RFC framework varies over the range [3 - 50]. A Random Forest is constructed using a Decision Tree template with parameters identical to those specified for the DTC. In addition, five light weight pre-trained DL models(EfficientNet-b0[139], Mobilenet-V2[141], Nasnet-Mobile[142], ShuffleNet[143], and SqueezeNet[144]) are used to characterize and classify abnormal patterns in medical thermal images.

Accuracy and F-measure are used as primary indicators to assess the performance of classification models. Also, K-fold cross validation (K = 10) is used as the sampling strategy. The values of Accuracy and F-Measure for a model are obtained by averaging them across each of its folds.

---

[1] https://www.csie.ntu.edu.tw/cjlin/libsvm/

4.4 Results and Discussion

This section discusses the performance of various hand-crafted and DL-based feature extraction methods on two datasets - DB-FOOT-IR and DB-DMR-IR using 4 classifiers - SVM, k-NN, DTC, and RFC. Also the performance light weight pre-trained DL Models is analyzed for both the datasets. The experiments conducted on both the datasets are independent and not related to each other in any respect. Accuracy and F-Measure are used as performance measures. The model parameters are considered to be optimal if the corresponding performance obtained is best for a classifier. Table 4.5 states classification performance of hand-crafted, UnionFeature_Set, and DL-based state-of-the-art feature extraction methods on two datasets - DB-FOOT-IR and DB-DMR-IR using SVM, k-NN, DTC, and RFC and 10-fold cross validation sampling Strategy. The Table 4.7 states the classification accuracy obtained from light-weight pre-trained DL models for DB-DMR-IR and DB-FOOT-IR datasets. Following observations are made from the tables 4.5 and 4.7 and figures 4.3 and 4.4-

- As classifiers, the DL models ShuffleNet and SqueezeNet performed well with an accuracy of 93.67% on DB-DMR-IR and 91.33% on DB-FOOT-IR, respectively (Table 4.7).

- The performance of DL-based feature-sets is considerably better than that of all the hand-crafted feature-sets for both the datasets, except for than that of UnionFeature_Set, for both the datasets.

- The best performance is obtained with accuracy as 99.3% with SVM and Nasnet-Mobile-based features for DB-DMR-IR. A comparable performance (accuracy = 99.2%) is achieved with ShuffleNet and SqueezeNet based features and SVM. Also, the number of parameters to be learned is 5.3 Millions in Nasnet-Mobile architecture which is significantly greater than that of ShuffleNet and SqueezeNet (Table 4.2).

- For DB-FOOT-IR, the best performance of accuracy score as 93.46% is obtained with k-NN and ShuffleNet-based features. Also, similar performance with accuracy = 93.4% is achieved with EfficientNet-b0 and SVM.

- On an average across the classifiers, the performance of features extracted from ShuffleNet and Nasnet-Mobile architectures is better than that of other DL-based models for both the datasets.

Table 4.5: Classification performance of various Hand-Crafted and DL-based feature extraction methods on two datasets - DB-FOOT-IR and DB-DMR-IR using SVM, k-NN, DTC, and RFC and 10-fold cross validation sampling Strategy.

Hand-Crafted Feature Extraction Methods

	DB-FOOT-IR								**DB-DMR-IR**							
	Accuracy				**F-Measure**				**Accuracy**				**F-Measure**			
Feature Extraction Method	**DTC**	**k-NN**	**SVM**	**RFC**	**DTC**	**k-NN**	**SVM**	**RFC**	**DTC**	**k-NN**	**SVM**	**RFC**	**DTC**	**k-NN**	**SVM**	**RFC**
FOS	70.13	75.5	58.4	81.23	81.8	77.73	58.07	86.2	83.8	80.5	63.4	86.7	81.8	83.6	63.54	86.2
GLCM	74.5	76.37	58.33	77.8	78.6	74.73	58.14	86.6	80.1	81.5	63.4	83.2	78.6	80.4	63.54	86.6
LBP	63.53	79.3	81.53	71.93	63	77.4	79.33	79	69.2	95.5	95.8	77.2	63	93.2	95.2	79
GLRM	70.73	83	57.6	77.67	69.4	82.67	60.5	86.4	81.4	88.8	63.4	83.2	81.4	88.4	66.1	86.4
HOG	65.3	63.33	57.43	67.27	74.2	60.6	63.67	71.6	70.9	69.4	63.5	73.2	74.2	66.4	69.6	71.6
WT	70.87	85.1	57.4	77.17	73.4	84.13	57.6	82.8	76.8	91.1	63.4	83.1	73.4	90	63.54	82.8
SHAPE	62.2	82.67	76.77	68.97	69.8	81.93	87.47	81.2	69.2	88.8	82.9	75.1	69.8	88	93.6	81.2
GLDS	52.73	80.56	58.76	53.67	58.6	79.13	60.52	63.8	58.8	87.3	65.5	59.8	58.6	85.2	66.52	63.8
NGTDM	49.57	65.47	54.57	49.23	54.6	65.41	54.31	54.19	55.3	72.4	61.5	55.3	54.6	71.28	60.38	54.19
SFM	55.2	60.87	59.97	66.03	49	51	70.33	70.95	61	66.8	65.9	72.1	49	57.2	76.4	70.95
TE	53.62	63.32	57.42	49.99	61	62.32	56.42	54.65	59.7	69.4	63.5	55.8	61	68.14	62.24	54.65
FPS	60	75.2	72.7	56.1	63	73.9	71.4	54.96	60	75.2	72.7	56.1	63	73.9	71.4	54.96
UnionFeature_Set	85.2	83.33	**88.25**	86.72	84.75	82.5	**87.5**	85	89.5	92.27	**96.33**	93.5	88.5	92.5	**95.45**	92.50

Deep Learning Feature Extraction Methods

	DB-FOOT-IR								**DB-DMR-IR**							
	Accuracy				**F-Measure**				**Accuracy**				**F-Measure**			
Feature Extraction Method	**DTC**	**k-NN**	**SVM**	**RFC**	**DTC**	**k-NN**	**SVM**	**RFC**	**DTC**	**k-NN**	**SVM**	**RFC**	**DTC**	**k-NN**	**SVM**	**RFC**
VGG16	75.6	90.69	90.99	84	75.51	91.17	92.46	83.01	83.2	98.1	98.4	90.5	82.82	98.05	98.36	90.4
ANET	75.66	92.44	90.16	82.39	74.88	84.89	90.06	81.64	82.2	96.2	98.3	88.6	81.71	96.16	98.26	88.39
GNET	81.86	90.6	91.21	84.92	78.37	91.12	93.15	84.14	85.6	97.7	99	91.1	85.39	97.68	98.99	91.01
RSN18	73.68	91.04	92.74	81.35	72.76	91.33	92.01	81.59	84.2	98.1	98.5	89.4	84.5	98.08	98.46	89.29
EFF-b0	73.84	87	**93.4**	82.79	75	92.2	92.95	84.61	82.6	97.1	99.09	92.4	82.25	97.03	99.4	92.3
INRESV2	76.58	87.08	92.73	81.36	74.8	92.77	91.62	84.52	84.7	97.4	98.1	91.3	84.27	97.34	98.07	91.2
MOBNETV2	77.21	90.45	93.36	85.41	75.91	91.22	92.14	86.26	84.1	98.3	98.8	92.7	83.53	98.27	98.79	92.64
NAS-MOB	81.44	90.36	91.36	86.83	77.14	92.31	93.84	88.65	85.2	98.5	**99.3**	92.53	84.29	98.48	99.29	95.6
SHUF	79.73	**93.46**	92.1	85.02	79.49	89.64	92.54	82.39	86.8	97.2	99.2	90.9	86.72	97.12	99.18	90.76
SQZN	74.79	91.88	92.04	83.64	75.59	90.93	90.97	81.04	84.4	98.4	99.1	91.6	84.12	98.39	99.08	91.36

- On an average across the classifiers, the performance of UnionFeature_Set is better than that of 12 hand-crafted feature-sets for the augmented DB-DMR-IR dataset.

- On an average across the performance of DL-based feature-sets and hand-crafted feature-sets, SVM have performed best with DL-based feature-sets for both the datasets.

- The performance of all the feature-sets from DB-FOOT-IR is lesser than that of DB-DMR-IR due the scarcity of samples in the available datasets.

- Among 12 Hand-crafted feature-sets, LBP-based features have performed better than that of any other feature-set with SVM for both the datasets.

The Table 4.6 states the inference time and memory requirements for predicting the class for a given thermal image of DB-DMR-IR dataset using the model. The analysis is performed for the best performing models only.

Table 4.6: The inference time and memory requirements on mobile device for best performing Light Weight Pre-trained DL features-based models for DB-DMR-IR dataset

Feature Extractor	**Classifier**	**Inference time (in ms)**	**Memory requirements (RAM) in MB**
NAS-MOB	SVM	93	25.8
SQZN	SVM	37	7.1
SHUF	SVM	23	11.3

Table 4.7: Classification accuracy obtained from Light Weight Pre-trained DL Models for DB-DMR-IR and DB-FOOT-IR datasets

Pre-Trained DL Models	**DB-DMR-IR**	**DB-FOOT-IR**
EFF-b0	85.39	85.41
MOBNETV2	82.82	91.1
NAS-MOB	92.53	82.82
SHUF	92.7	**91.33**
SQZN	**93.67**	81.36

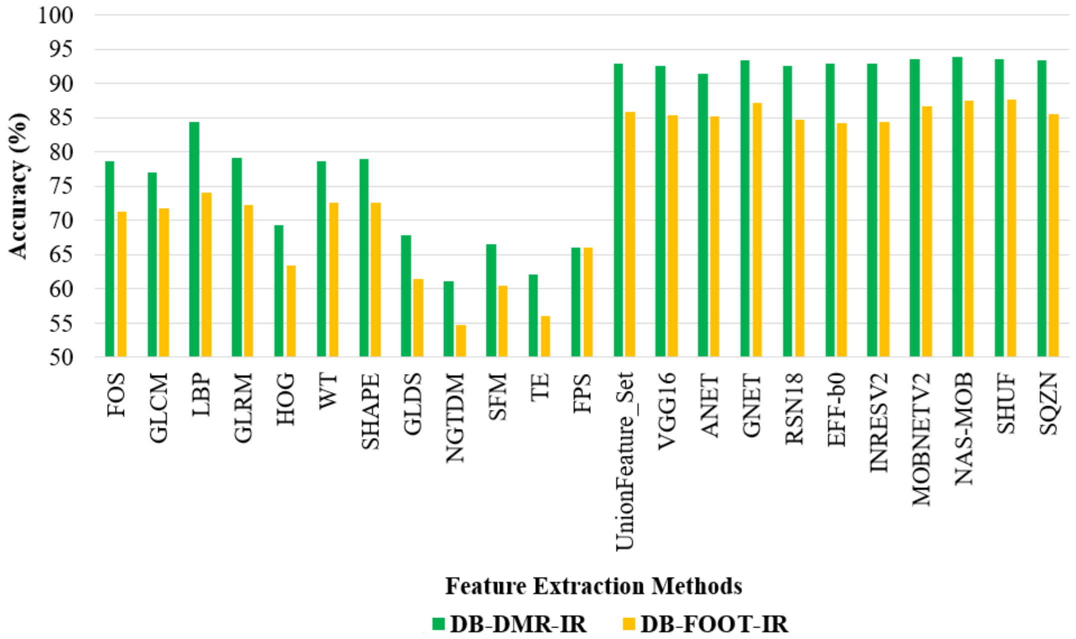

Fig. 4.3: Performance comparison of the average classification accuracy values(%) for the various Feature-sets and datasets - DB-DMR-IR and DB-FOOT-IR

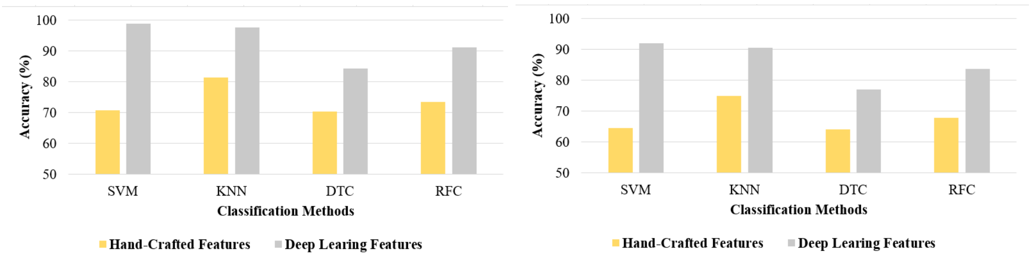

(a) (b)

Fig. 4.4: Performance comparison for the various classifiers, averaged over Hand-Crafted and DL-Based Feature-sets in terms of classification accuracy values(%), for DB-DMR-IR (a) and DB-FOOT-IR (b) datasets.

4.5 Chapter Summary

This chapter presents a lightweight deep learning-based classification model designed for mobile deployment to detect and characterize abnormalities caused by inflammation in human thermal images. Various hand-crafted and DL-based feature sets are extracted from two publicly available thermal imaging datasets, DB-DMR-IR and DB-FOOT-IR, and their classification performance is compared using four state-of-the-art classifiers — DTC, RFC, SVM, and k-NN, along with a 10-fold cross validation sampling strategy. Additionally, lightweight pre-trained deep learning models are investigated to improve characterization and classification accuracy. The UnionFeature_Set from the previous chapter is also utilized for comparison. DL-based features are extracted using ten pre-trained CNNs, including VGG16, AlexNet, GoogleNet, ResNet-18, EfficientNet-b0, Inception-ResNet-v2, MobileNet-V2, NASNet-Mobile, ShuffleNet, and SqueezeNet. Five of these lightweight models are optimized for mobile devices to facilitate real-time application.

The results indicate that DL-based feature extraction methods outperform traditional hand-crafted approaches and classification using UnionFeature_Set. Among the classifiers, SVM achieved the highest accuracy for deep learning-based features across both datasets. ShuffleNet and SqueezeNet demonstrated the best classification performance, achieving 93.67% accuracy on DB-DMR-IR and 91.33% on DB-FOOT-IR, respectively. The NASNet-Mobile-based feature set, when combined with SVM, yielded the highest accuracy of 99.3% for DB-DMR-IR, whereas ShuffleNet with *k*-NN provided the best accuracy of 93.46% for DB-FOOT-IR. The results also highlight that the UnionFeature_Set outperforms individual hand-crafted feature sets for the augmented DB-DMR-IR dataset. However, the overall performance on DB-FOOT-IR was lower due to the limited number of available samples.

The ShuffleNet + SVM pipeline is highly efficient, achieving inference in <30 ms with <12 MB memory use, and is therefore scalable for screening large population. The urban and rural environments would benefit from high-throughput batch processing using GPUs and low-power CPUs, respectively. This pipeline is well-suited for real-time screening in constrained environments, offering a strong balance between speed, accuracy, and scalability.

In conclusion, this study demonstrates that deep learning-based feature extraction, particularly using lightweight CNN architectures, significantly improves the accuracy and reliability of thermal biomarker classification. The findings establish the feasibility of deploying mobile-friendly deep learning models for real-time detection of inflammation-related abnormalities, bridging the gap between medical diagnostics and accessible AI-driven healthcare solutions.

Chapter 5

Framework for Inflamed Region Segmentation

This chapter presents two enhanced density-based modified Picture Fuzzy Clustering techniques for identifying and segmenting affected regions in abnormal thermal images. The optimization problem is formulated and solved to determine cluster prototypes. The proposed methods are evaluated using three publicly available medical thermal imaging datasets. Additionally, the chapter presents experimental results, analysis, and statistical validation for both the methods.

5.1 Introduction

Image segmentation is a prominent step in error-free medical image analysis in modern medicine. To our knowledge, limited work is done towards segmentation of affected regions in the diseased human body's thermal images ([15, 29, 30, 31, 32, 33, 34, 35, 36]). Also, most of the segmentation models proposed are evaluated on private datasets having fewer samples which is not available for further consideration and analysis by the research community. Hence, the performances obtained are not reputable.

Also, only a few research works [30, 32, 33, 98, 97] have evaluated their method on a publicly available dataset, wherein the in house-created ground truth is not available to the community for further analysis and thus makes the results highly subjective. Therefore, due to the inconsistency and variability in the evaluation procedures used in existing studies, selecting a suitable segmentation model, to identify inflammation/abnormality in the human body using thermography in practical-use, is not appropriate. Additionally, only a limited number of studies have experimented with their segmentation models on thermal imaging datasets involving multiple diseases [32, 33, 36]. The performance obtained is not satisfactory, suggesting a potential for improvement (Table 2.3). Also, the approaches proposed in literature are sensitive (Table 2.3), primarily due to manual selection of seed points and other hyper-parameters [32, 33, 100].

This chapter introduces two novel and robust Density-based modified Picture Fuzzy Clustering methods to identify and segment affected regions in abnormal thermal images. Picture Fuzzy sets are utilized for their enhanced representational capability, incorporating [Membership, Non-Membership, and Neutrality] matrices, which effectively manage uncertainty in complex real-world structures.

Based on Picture Fuzzy Sets, the Picture Fuzzy C-Means clustering method (FC-P_cFS) is proposed[90]. It is sensitive to the initialization of initial cluster centers, fuzzifier, membership partition matrix, and neutrality matrix. Moreover, this initialization may result in undesirable outcomes and affect the time taken for the results to converge.

To overcome this problem, the notion of density is used to automatically initialize the number of clusters, initial cluster centers, and positive membership matrix. To handle the noise and other imaging artifacts present in thermal images, the spatial information in the neighborhood of a data point is incorporated in the model. Also, the robustness of the proposed framework is investigated in contrast to other related methods on three publicly available thermal imaging datasets having different diseases, with and without artificial noise incorporated in them. The critical contributions of the chapter includes following-

1. Two robust Density-based Picture Fuzzy clustering models with spatial information, are proposed, to segment the affected regions/hotspots from abnormal thermal images. Hyper-parameters are automatically initialized using a density-based heuristic, requiring minimum hyper-parameter tuning. Incorporating Spatial information in the model has eliminated the requisite of smoothing the thermal image and retained fine image structures.

2. The optimization problem is formulated by combining Density-based P_cFS method with regularized and modified Renyi's Entropy to obtain a good partition matrix and appropriate number of clusters. The complete optimization problem is solved using Lagrangian method of multiplier [37] and obtained their cluster prototypes.

3. The robustness of the proposed segmentation methods is validated statisti-

cally over other methods using the Friedman Test. Also, the time complexity is investigated in comparison to other related methods.

4. To the best of our knowledge, research has yet to give a course to develop a robust segmentation method for analyzing and segmenting noisy and low-resolution human thermal images. To address this research gap, a separate dataset - DB-NOISE-IR, is created, wherein three types of artificial noise - Salt and Pepper Noise, Gaussian Noise, and Mixed Noise are introduced. We thoroughly performed the comparative performance analysis of our method with that of other methods. We found that the our methods have performed significantly better particularly for the noisy dataset.

This chapter is organized as follows. The section 5.2 describes the notations and preliminary concepts based on picture fuzzy sets used in our work. The section 5.3 describes the proposed density-based Picture Fuzzy Clustering methods for segmentation. The experimental setup for the proposed framework is described in section 5.4. The results are discussed in sections 5.5 and concluded in section 5.6.

5.2 Preliminaries and Notations

The research work [88] proposed and built theory on Picture Fuzzy Sets (P_cFS). A P_cFS *S* on a universe *Z* is defined as $S = \{(z, \mu_S(z), \eta_S(z), \nu_S(z)) : \mu_S(z) \in [0,1], \eta_S(z) \in [0,1]$ and $\mu_S(z) + \eta_S(z) + \nu_S(z) \leq 1, \forall z \in Z\}$, Where $\mu_S(z)$, $\eta_S(z)$, and $\nu_S(z)$ are the degree of positive, neutrality, and negative membership for a $z \in Z$, respectively. Also, $\xi_S(z) = 1 - (\mu_S(z) + \eta_S(z) + \nu_S(z))$ is defined as the degree of refusal membership of the $z \in Z$. Using Yager generalized Negation function([145, 146]), $\nu_S(z)$ can be expressed as $(1 - (\mu_S(z) + \eta_S(z))^{\omega})^{\frac{1}{\omega}}$ $\forall z \in Z$. Here, the uncertainty of a sample is defined using three parameters - its positive, neutral, and refusal degree.

A P_cFS is the direct generalization of Intuitionistic Fuzzy Sets (IFS) [147] and Fuzzy Sets (FS) [85]. A P_cFS *S* reduces to an IFS *S* when $\xi_S(z) = 0$ $\forall z \in Z$. Further, a P_cFS *S* reduces to a FS *S* when $\xi_S(z) = 0$ and $\eta_S(z) = 0$ $\forall z \in Z$. For the sake of simplicity $\mu_S(z_j)$, $\eta_S(z_j)$, $\nu_S(z_j)$, and $\xi_S(z_j)$ is denoted as μ_{Sj}, η_{Sj}, ν_{Sj} and ξ_{Sj}, respectively, in rest of the chapter.

5.2.1 Picture Fuzzy Clustering Method (FC-P_cFS)

The K-Means[84] clustering allows a data point (z_j), $j = 1, 2, 3...N$, to belong to only one cluster (C_p), $p = 1, 2, 3...C$, with the objective to minimize the average distance from the points to the closest cluster center. Whereas, Fuzzy clustering methods allows each instance z_j, $j = 1, 2, 3...N$, to belong to all the C clusters [C_1, C_2, C_3...C_C] with membership value as [μ_{1j}, μ_{2j}, μ_{3j},... μ_{Cj}] respectively, and $\sum_{p=1}^{C} \mu_{pj} = 1$. The item C_p is a cluster with center v_p, $p = 1, 2, 3...C$ and C is the number of clusters.

The matrix M denotes the fuzzy partition matrix of size $N \times C$ with the positive membership values for each z_j, $j = 1, 2, 3...N$, to belong to all C clusters i.e. $M = [\mu_{pj}]_{N \times C}$, $p = 1, 2, 3...C$ and $j = 1, 2, 3...N$.

The research work [90] proposed a generalized model of the Fuzzy clustering method based on P_cFS and called it FC-P_cFS. For this, matrices H and Ξ are defined, each of size $N \times C$, as Neutrality and Refusal degree matrices, respectively. The optimization problem for FC-P_cFS is given as equation 5.1.

Minimize:

$$J_{m,\omega}(M, H, V, \Xi : Z) = \sum_{p=1}^{C}\sum_{j=1}^{N}(\mu_{pj}(2 - \xi_{pj}))^m \|z_j - v_p\|^2 + \sum_{p=1}^{C}\sum_{j=1}^{N}\eta_{pj}(\log \eta_{pj} + \xi_{pj})$$

subject to

$$\begin{array}{ll} (1) & 0 \leq \mu_{pj}, \eta_{pj}, \xi_{pj} \leq 1, \quad p = 1, 2, 3...C \text{ and } j = 1, 2, 3...N \\ (2) & 0 \leq \mu_{pj} + \eta_{pj} + \xi_{pj} \leq 1, \quad p = 1, 2, 3...C \text{ and } j = 1, 2, 3...N \\ (3) & \displaystyle\sum_{p=1}^{C} \mu_{pj}(2 - \xi_{pj}) = 1, \quad j = 1, 2, 3...N \\ (4) & \displaystyle\sum_{p=1}^{C} (\eta_{pj} + \frac{\xi_{pj}}{C}) = 1, \quad j = 1, 2, 3...N \end{array} \tag{5.1}$$

The constraints 1 and 2 in equation 5.1 are obtained from the definition of P_cFS, and constraint 3 satisfies the sum-row constraint in the traditional FCM model with $[\mu_{pj}(2 - \xi_{pj})]$ as the true membership of z_j for cluster C_p with center v_p. The model is guaranteed to work when at least one of the neutral or refusal degree exist in the model. Constraint 4 in equation 5.1 takes care of this. Also, the FC-P_cFS clustering model [90] generalizes IFCM clustering model[87] when $\xi_{pj} = 0\ \forall z_j \in Z, j = 1, 2, 3...N$ and constraint 4 of equation 5.1 is removed. In addition, this model generalizes FCM[86] when $\eta_{pj} = 0\ \forall z_j \in Z, j = 1, 2, 3...N$.

The authors [90] solved the optimization problem using the Lagrangian method of multiplier [37] to determine the model's cluster prototype at every iteration (equations 5.2-5.5) for $p = 1, 2, 3...C$ and $j = 1, 2, 3...N$.

$$\xi_{pj} = 1 - (\mu_{pj} + \eta_{pj}) - (1 - (\mu_{pj} + \eta_{pj})^{\omega})^{\frac{1}{\omega}} \tag{5.2}$$

$$\mu_{pj} = \frac{1}{\sum\limits_{i=1}^{C}(2 - \xi_{pj})(\frac{\|z_j - v_p\|}{\|z_j - v_i\|})^{\frac{2}{m-1}}} \tag{5.3}$$

$$\eta_{pj} = \frac{e^{-\xi_{pj}}}{\sum\limits_{i=1}^{C} e^{-\xi_{ij}}}\left[1 - \frac{1}{C}\sum_{i=1}^{C}\xi_{ij}\right] \tag{5.4}$$

$$v_p = \frac{\sum\limits_{j=1}^{N}(\mu_{pj}(2 - \xi_{pj}))^m z_j}{\sum\limits_{j=1}^{N}(\mu_{pj}(2 - \xi_{pj}))^m}, p = 1, 2, 3...C \tag{5.5}$$

The above model is expressed as FC-P_cFS algorithm (Algorithm 1).

5.2.2 Kernel-based distance function

Transforming the data from a lower-dimensional space to a higher-dimensional space using a kernel function, ϕ, makes the samples linearly separable in the higher-dimensional space that is kernel space [148]. The benefit of the transformation is that the dot product in kernel space can be rewritten using Mercer Equation as $K(x_i, x_j) = \langle\phi(x_i)^T\phi(x_j)\rangle$, where x_i and x_j are the data points and $\phi(x_i)$ and $\phi(x_j)$ represents the data points in the higher dimensional space or kernel space.

$$\begin{aligned}\kappa_{ij} = \|\phi(x_i) - \phi(x_j)\|^2 =& \|\phi(x_i) - \phi(x_j)\|^T\|\phi(x_i) - \phi(x_j)\| \\ =& \phi(x_i)^T\phi(x_i) + \phi(x_j)^T\phi(x_j) - 2\phi(x_i)^T\phi(x_j) \\ =& K(x_i, x_i) + K(x_j, x_j) - 2K(x_i, x_j) \\ =& 2(1 - K(x_i, x_j)) \\ =& 2\tanh(\frac{-\|x_i - x_j\|^2}{\sigma^2})\end{aligned} \tag{5.6}$$

This work uses Hyper Tangent Kernel Function ($K(x_i, x_j) = 1 - \tanh(\frac{-\|x_i - x_j\|^2}{\sigma^2})$

Algorithm 1 FC-P_cFS algorithm [90]

```
Input: Image I of size $P \times Q$, C: Number of clusters, $\epsilon$: Threshold, m: fuzzifier,
    $\omega$: exponent, maxSteps: Maximal number of iterations.
Output: Matrices $M, H, \Xi, V$
procedure FC-$P_c$FS
    $i \leftarrow 0$
    $Z \leftarrow vectorize(I)$        //size of Z is N$(= P \times Q)$
    $[M^{(0)}, H^{(0)}] \leftarrow$ Random Values in the range [0, 1]
    Calculate $\Xi^{(0)}$ using equation 5.2
    repeat
        $i \leftarrow i + 1$
        Calculate $V^{(i)}$ using equation 5.5
        Calculate $M^{(i)}$ using equation 5.3
        Calculate $H^{(i)}$ using equation 5.4
        Calculate $\Xi^{(i)}$ using equation 5.2
    until $(\|M^{(i)} - M^{(i-1)}\| + \|H^{(i)} - H^{(i-1)}\| + \|\Xi^{(i)} - \Xi^{(i-1)}\|) < \epsilon$ or (i $\geq$ $maxSteps)$
    return Matrices $M, H, \Xi, V$
end procedure
```

where σ is the width controlling parameter; $\sigma > 0$). The choice of this kernel is due to the robustness of the kernel towards noise and nonlinear structures present in data. The distance function based on kernel between data points x_i and x_j, [$\kappa_{ij} = \|\phi(x_i) - \phi(x_j)\|^2$], is expressed as equation 5.6.

5.3 Methodology

This section describes the proposed approaches for segmenting the affected ROIs from abnormal thermograms - Density-based FC-P_cFS with Spatial Information (DSIFC-P_cFS) and Density-based Modified FC-P_cFS with Spatial Information (DSIMFC-P_cFS).

An image I, of size $P \times Q$, is transformed to a matrix of local energy levels using the equation 5.7. Further, this matrix normalized in the range [0, 1] is called Entropy Image (I^*).

$$\hat{I}(u, v) = -\sum_{k=-1}^{1}\sum_{l=-1}^{1} I(u+k, v+l)log(I(u+k, v+l)) \tag{5.7}$$

Finally, the vector Z is defined, on matrix I^*, as the vector of normalized Local Energy values, with element z_j, where $j = 1, 2, 3...N, N = P \times Q$. The proposed

DSIFC-P_cFS and DSIMFC-P_cFS methods are defined as follows.

5.3.1 Density-based FC-P_cFS with Spatial Information Method

The research works [91, 92] have proposed density-based FCM and IFCM methods, - DFCM and DIFCM, respectively. They initialized the initial cluster centers and partition matrix based on density information. However, the number of parameters - cutoff density, cutoff distance, and distance rate to be tuned is high[91, 92]. Also, they did not consider intra- and inter-cluster similarity simultaneously in their model.

In the Density-based FC-P_cFS with Spatial Information method (DSIFC-P_cFS) for segmenting the inflamed ROI, the density decision parameter γ_j for each local energy sample $z_j,\ z_j \in Z$ is defined as $\rho_j \times \delta_j$, where ρ_j and δ_j are the density and minimum distance parameters of sample z_j, respectively. The parameter γ_j indicates the importance of a sample z_j as a potential cluster center. It takes care of both intra-cluster and inter-cluster similarity with the help of parameters ρ_j and δ_j, respectively. The parameters ρ_j and δ_j segment the image into dense regions with their central points at large distances. The density parameter, ρ_j, for each local energy sample $z_j,\ z_j \in Z$ is defined as

$$\rho_j = \frac{\sum_{i=1, i\neq j}^{N} e^{-\frac{d_{ji}^2}{\varsigma^2}}}{N-1} \tag{5.8}$$

where N is the number of samples in $Z(= P \times Q)$, d_{ji} represents the Euclidean distance between z_i and z_j, and ς^2 is the measure of scatteredness of energy levels in I^* and is computed as $\varsigma^2 = \frac{1}{N}\sum_{i=1}^{N} \|z_i - \bar{z}\|^2$ and $\bar{z} = \frac{1}{N}\sum_{k=1}^{N} z_k$. The minimum distance parameter, δ_j, for each local energy sample z_j, $z_j \in Z$ is calculated as

$$\delta_j = \begin{cases} \min\,\{d_{ji}\},\ \forall i \text{ where } \rho_i > \rho_j \\ \max\,\{d_{ji}\},\ \nexists i \text{ where } \rho_i > \rho_j \end{cases} \tag{5.9}$$

A sample z_j with a higher value of ρ_j indicates that z_j is concentrated with a large number of similar samples. A higher value of δ_j signifies the degree of dissimilarity for z_j with a sample z_i having the next higher density. So, samples with lower ρ_j but higher δ_j will be considered outliers. Removing such points can improve the performance and enhance the method's stability.

The density decision parameter values γ_j obtained are sorted in descending order to define the potential initial clusters. To choose the potential cluster centers, a Decision cutoff parameter, d_c, is computed as $d_c = (\sum_{j=1}^{N} \gamma_j) \times \tau$, where $\tau \in (0, 1)$, is a cutoff parameter and is adjustable. The set of C potential cluster centers is defined as the data points having larger values of γ_j as

$$\mathbb{C} = \{z_i | \sum_{i=1}^{C-1} \gamma_i < d_c \text{ and } \sum_{i=1}^{C} \gamma_i > d_c\}, \qquad 1 \le i \le C \tag{5.10}$$

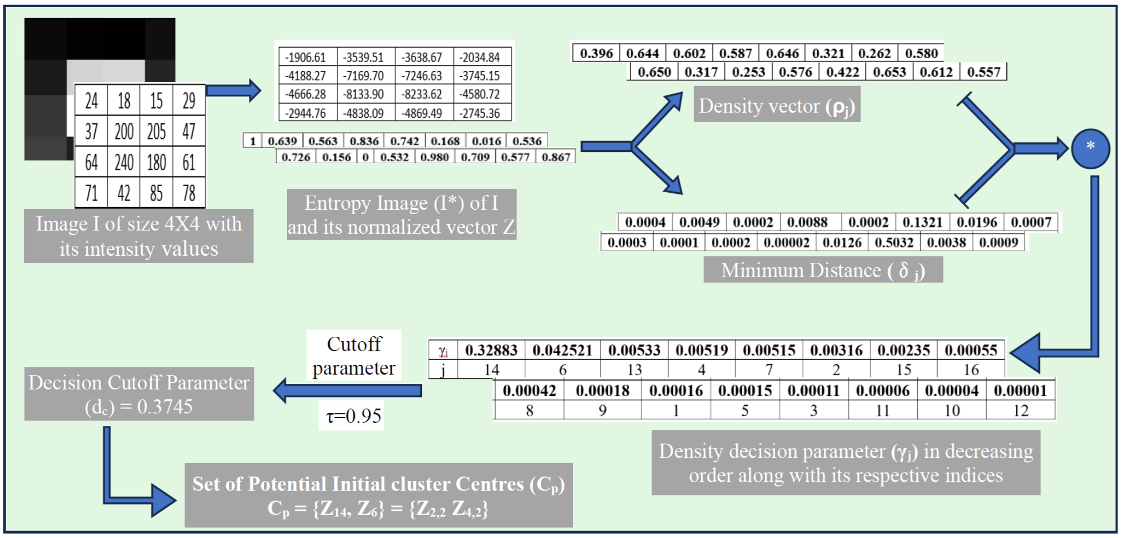

24	18	15	29
37	200	205	47
64	240	180	61
71	42	85	78

-1906.61	-3539.51	-3638.67	-2034.84
-4188.27	-7169.70	-7246.63	-3745.15
-4666.28	-8133.90	-8233.62	-4580.72
-2944.76	-4838.09	-4869.49	-2745.36

1	0.639	0.563	0.836	0.742	0.168	0.016	0.536
0.726	0.156	0	0.532	0.980	0.709	0.577	0.867

0.396	0.644	0.602	0.587	0.646	0.321	0.262	0.580
0.650	0.317	0.253	0.576	0.422	0.653	0.612	0.557

0.0004	0.0049	0.0002	0.0088	0.0002	0.1321	0.0196	0.0007
0.0003	0.0001	0.0002	0.00002	0.0126	0.5032	0.0038	0.0009

γ_i	0.32883	0.042521	0.00533	0.00519	0.00515	0.00316	0.00235	0.00055
j	14	6	13	4	7	2	15	16
	0.00042	0.00018	0.00016	0.00015	0.00011	0.00006	0.00004	0.00001
	8	9	1	5	3	11	10	12

Fig. 5.1: An example to illustrate that how potential initial cluster centers are selected heuristically.

This set of potential cluster centers forms the set of initial cluster center points in FC-P_cFS. The figure 5.1 illustrates an example that may be heuristically selected as potential initial cluster centers. The random approach to selecting initial cluster centers may result in corner points as initial cluster centers. Also, leveraging the knowledge of density decision parameters obtained for each sample z_j, the membership and neutrality matrices (M and H) are not assigned randomly. The membership values μ_{pj} is initialized using γ_j for sample z_j as:

$$\mu_{pj} = \begin{cases} 0.5, & z_j \in \mathbb{C} \text{ and } p = k \\ 0, & z_j \in \mathbb{C} \text{ and } p \neq k \\ \frac{\gamma_j/\gamma_1}{2k}, & z_j \notin \mathbb{C}, \rho_{v_{k+1}} \le \rho_j \le \rho_{v_k} \text{ and } p \le k \\ \frac{1-(\gamma_j/\gamma_1)}{2(C-k)}, & z_j \notin \mathbb{C}, \rho_{v_{k+1}} \le \rho_j \le \rho_{v_k} \text{ and } p > k \end{cases} \tag{5.11}$$

where $k = 1, 2, 3...C$. The values η_{pj} is calculated for sample z_j as:

$$\eta_{pj} = \begin{cases} 0.5, & z_j \in \mathbb{C} \text{ and } p = k \\ 0, & z_j \in \mathbb{C} \text{ and } p \neq k \\ \frac{1-|z_j - z_p|}{2}, & z_j \notin \mathbb{C} \text{ and } z_p \in \mathbb{C} \end{cases} \tag{5.12}$$

where $k = 1, 2, 3...C$.

The optimization problem for DSIFC-P_cFS is defined below:

Minimize:

$$J1_\omega(M, H, V, \Xi : Z) = \underbrace{\sum_{p=1}^{C}\sum_{j=1}^{N} [\mu_{pj}(2 - \xi_{pj})]^2 \, Dpj}_{\text{I}} + \underbrace{\sum_{p=1}^{C}\sum_{j=1}^{N} [\eta_{pj}(\log \eta_{pj} + \xi_{pj})]}_{\text{II}}$$

subject to

$$\begin{aligned} &(1) \quad 0 \leq \mu_{pj}, \eta_{pj}, \xi_{pj} \leq 1, \quad p = 1, 2, 3...C \text{ and } j = 1, 2, 3...N \\ &(2) \quad 0 \leq \mu_{pj} + \eta_{pj} + \xi_{pj} \leq 1, \quad p = 1, 2, 3...C \text{ and } j = 1, 2, 3...N \\ &(3) \quad \sum_{p=1}^{C} [\mu_{pj}(2 - \xi_{pj})] = 1, \quad j = 1, 2, 3...N \\ &(4) \quad \sum_{p=1}^{C} (\eta_{pj} + \frac{\xi_{pj}}{C}) = 1, \quad j = 1, 2, 3...N \end{aligned} \tag{5.13}$$

Where $Dpj = \kappa_{pj} + \zeta_{pj}$ and $\zeta_{pj} = \sum_{z_k \in N_{z_j}} \frac{[\mu_{pk}(2-\xi_{pk})]\kappa_{pk}}{\sum_{z_l \in N_{z_j}} [\mu_{pl}(2-\xi_{pl})]}$, is the Spatial Information in the neighborhood of z_j towards cluster center v_p. N_{z_j} is the immediate $w \times w$ neighborhood of the z_j. The term κ_{pj} is defined in equation 5.6. The parameter σ^2 in Hyper Tangent Kernel Function is defined as the dataset's degree of separation and computed as $\sigma^2 = \frac{1}{N}\sum_{i=1}^{N} \|z_i - \bar{z}\|^2$ and $\bar{z} = \frac{1}{N}\sum_{k=1}^{N} z_k$. The term $[\mu_{pj}(2 - \xi_{pj})]$ denotes the true membership of a data point z_j for cluster C_p as in FC-P_cFS and constraint 3 in equation 5.13 maintains the sum of z_j's true membership values for all the clusters(C_p, $p = 1 \cdots C$) to 1. Constraint 4 in equation 5.13 guarantees the existence of at least one of neutral or refusal degree.

The optimization problem *J1* (equation 5.13) is composed of two terms.

- The first term represents the aggregate value of within-cluster scatteredness for transformed data points. The objective is to minimize this within-cluster error by assigning high membership values to pixels close to the cluster center and vice-versa. With the help of nonlinear transformation and without increasing the computational complexity, the kernel-based mapping of data points will enhance their representational capability and tackle the problem of their nonlinear structures.

- Also, the first term consists of spatial information from the neighborhood of data point z_j, $j = 1, 2, 3...N$. This term indicates the weighted sum of the kernel-based distance between the pixels in the neighborhood of z_j and p^{th} cluster center, weighted by their normalized factual memberships towards p^{th} cluster. To obtain the optimal solution, the average weighted distance of the neighboring pixels k^{th} with the cluster center v_p is also required to be minimum. The spatial information of the neighborhood moderates the effect of noise. Incorporating this term will eliminate the requisite of smoothing and, therefore, retain fine image structures.
- The second term is the asymmetric logarithmic term. It is a monotonically decreasing function in η_{pj}; therefore, minimizing this term reduces the entropy of a P_cFS. Thus, it reduces a data point's neutrality and refusal degree to become a cluster member and increases the chance of getting a nontrivial solution.
- Also, the optimization problem J1 generalizes IFCM clustering model with Spatial information [93] when $\xi_{pj} = 0 \, \forall z_j \in Z, j = 1, 2, 3...N$ and constraint 4 of equation 5.13 is removed.

The optimization problem *J1* is solved for the cluster prototype and membership values using Lagrangian method of multiplier [37].

5.3.1.1 Derivation of Cluster Prototype for *J1*

The Lagrangian function $L1(\mu_{pj}, \eta_{pj}, v_p, \alpha_j, \beta_j)$, (equation 5.14), for the optimization problem *J1* (equation 5.13) is represented as

$$\begin{aligned} L1 = \sum_{p=1}^{C}\sum_{j=1}^{N} \left[\mu_{pj}(2-\xi_{pj})\right]^2 Dpj + \sum_{p=1}^{C}\sum_{j=1}^{N} \left[\eta_{pj}(\log \eta_{pj} + \xi_{pj})\right] \\ + \sum_{j=1}^{N} \alpha_j \left[1 - \sum_{p=1}^{C} \left[\mu_{pj}(2-\xi_{pj})\right]\right] + \sum_{j=1}^{N} \beta_j \left[1 - \sum_{p=1}^{C} \left[\eta_{pj} + \frac{\xi_{pj}}{C}\right]\right] \end{aligned} \tag{5.14}$$

where α_j and β_j are the Lagrange's Multipliers for $j = 1, 2, 3...N$. Now, equating the partial differential of *L1* w.r.t μ_{pj} to 0 i.e. $\frac{\partial L1}{\partial \mu_{pj}} = 0$ to derive the value of μ_{pj},

$$(2-\xi_{pj})\left[2\mu_{pj}(2-\xi_{pj})Dpj - \alpha_j\right] = 0 \tag{5.15}$$

In equation 5.15, $(2 - \xi_{pj}) \neq 0$ because $\xi_{pj} \in [0, 1]$,

$$\mu_{pj}(2 - \xi_{pj}) = \frac{\alpha_j}{2D_{pj}} \tag{5.16}$$

Applying the summation $\sum_{k=1}^{C}$, and then using constraint 3 of optimization problem (equation 5.13) in above equation, the value of $\frac{\alpha_j}{2}$ is obtained as $\frac{\alpha_j}{2} = \frac{1}{\sum_{k=1}^{C}(1/D_{kj})}$. Substituting this value of $\frac{\alpha_j}{2}$ back in equation 5.16 and solving further for μ_{pj},

$$\mu_{pj} = \frac{1}{(2 - \xi_{pj})}\left[\frac{(1/D_{pj})}{\sum_{k=1}^{C}(1/D_{kj})}\right] \tag{5.17}$$

Similarly, equating the partial differential of *L1* w.r.t η_{pj} to 0 i.e. $\frac{\partial L1}{\partial \eta_{pj}} = 0$,

$$\begin{aligned} &\Rightarrow 1 + \xi_{pj} + \log \eta_{pj} - \beta_j = 0 \\ &\Rightarrow \eta_{pj} = \exp\left(\beta_j - 1 - \xi_{pj}\right) \end{aligned} \tag{5.18}$$

Applying the summation $\sum_{k=1}^{C}$ to the above equation and then using constraint 4 of the optimization problem J1 (equation 5.13) in the above equation,

$$\begin{aligned} 1 - \sum_{k=1}^{C} \frac{\xi_{kj}}{C} &= \exp\left(\beta_j - 1\right) \sum_{k=1}^{C} \exp\left(-\xi_{kj}\right) \\ \Rightarrow \exp\left(\beta_j - 1\right) &= \frac{1 - \sum_{k=1}^{C} \frac{\xi_{kj}}{C}}{\sum_{k=1}^{C} \exp\left(-\xi_{kj}\right)} \end{aligned} \tag{5.19}$$

Substituting the value of $\exp\left(\beta_j - 1\right)$, the value of η_{pj} is finally obtained as

$$\eta_{pj} = \frac{\exp\left(-\xi_{pj}\right)}{\sum_{k=1}^{C} \exp\left(-\xi_{kj}\right)}\left[1 - \sum_{k=1}^{C} \frac{\xi_{kj}}{C}\right] \tag{5.20}$$

Now, substituting the value of D_{pj} in equation 5.14 and then equating its partial differential w.r.t v_p to 0 i.e. $\frac{\partial L1}{\partial v_p} = 0$,

$$\sum_{j=1}^{N} \frac{-4[\mu_{pj}(2 - \xi_{pj})]^2}{\sigma^2}\left[(K'_{pj}\|z_j - v_p\|) + \sum_{z_k \in N_{z_j}} \frac{[\mu_{pk}(2 - \xi_{pk})]}{\sum\limits_{z_l \in N_{z_j}} [\mu_{pl}(2 - \xi_{pl})]} K'_{pk}(\|z_k - v_p\|)\right] = 0 \tag{5.21}$$

where $K'_{pj} = 1 - \tanh^2\left[-\frac{\|z_j - v_p\|^2}{\sigma^2}\right]$. The term K'_{pj} can be simplified as $K'_{pj} = \left[1 + \tanh\left[-\frac{\|z_j - v_p\|^2}{\sigma^2}\right]\right] K(z_j, v_p)$. The final value of v_p for iteration by simplifying equation 5.21 is obtained as

$$v_p = \frac{\sum\limits_{j=1}^{N} [\mu_{pj}(2-\xi_{pj})]^2 \left[K'_{pj} z_j + \sum\limits_{z_k \in N_{z_j}} \frac{\left[\mu_{pk}(2-\xi_{pk})\right]}{\sum\limits_{z_l \in N_{z_j}} \left[\mu_{pl}(2-\xi_{pl})\right]} K'_{pk} z_k \right]}{\sum\limits_{j=1}^{N} [\mu_{pj}(2-\xi_{pj})]^2 \left[K'_{pj} + \sum\limits_{z_k \in N_{z_j}} \frac{\left[\mu_{pk}(2-\xi_{pk})\right]}{\sum\limits_{z_l \in N_{z_j}} \left[\mu_{pl}(2-\xi_{pl})\right]} K'_{pk} \right]} \tag{5.22}$$

The equations 5.17, 5.20, and 5.22 shows the derived prototype for J1 (equation 5.13). The value of refusal degree ξ_{pj} is computed using equation 5.2. The above-proposed methodology - DSIFC-P_cFS, is outlined as Algorithm 2.

Algorithm 2 Density-based FC-P_cFS (DSIFC-P_cFS) with Spatial Information Algorithm

```
Input: Image I of size $P \times Q$, $\epsilon$: Threshold, $\omega$: Exponent, maxSteps: Maximal
    number of iterations, $\tau$: Adjustable cutoff parameter.
Output: Matrices $M, H, \Xi, V$
procedure DSIFC-$P_c$FS
    Calculate the local energy matrix $\hat{I}$ from I using equation 5.7.
    $I^* \leftarrow$ Normalize the matrix $\hat{I}$ in the range [0,1].
    $Z \leftarrow$ vectorize($I^*$)        //size of Z is N($= P \times Q$)
    for each $z_j \in Z$ do
        Calculate $\rho_j$ using using equation 5.8
        Calculate $\delta_j$ using using equation 5.9
        $\gamma_j \leftarrow \rho_j \times \delta_j$
    end for
    Arrange the $\gamma_j$ values in descending order
    $d_c \leftarrow (\sum_{j=1}^{N} \gamma_j) \times \tau$
    Initialize the cluster centers using equation 5.10
    $i \leftarrow 0$
    Initialize the matrix $M^{(0)}$ using equation 5.11
    Initialize the matrix $H^{(0)}$ using equation 5.12
    Calculate $\Xi^{(0)}$ using equation 5.2
    repeat
        $i \leftarrow i + 1$
        Calculate $V^{(i)}$ using equation 5.22
        Calculate $M^{(i)}$ using equation 5.17
        Calculate $H^{(i)}$ using equation 5.20
        Calculate $\Xi^{(i)}$ using equation 5.2
    until ($\|M^{(i)} - M^{(i-1)}\| + |H^{(i)} - H^{(i-1)}\| + \|\Xi^{(i)} - \Xi^{(i-1)}\|) < \epsilon$ or (i $\geq$ $maxSteps$)
    return Matrices $M, H, \Xi, V$
end procedure
```

5.3.2 Density-based Modified FC-P_cFS with Spatial Information method (DSIMFC-P_cFS)

This subsection presents the optimization problem and its prototype derivation for Density-based Modified FC-P_cFS with Spatial Information (DSIMFC-P_cFS). The proposed optimization problem for DSIMFC-P_cFS is given as:

Minimize:

$$J2_{\omega,t,\lambda}(M,H,V,\Xi:Z)=\underbrace{\sum_{p=1}^{C}\sum_{j=1}^{N}[\mu_{pj}(2-\xi_{pj})]^2\,Dpj}_{\text{I}}+\underbrace{\sum_{p=1}^{C}\sum_{j=1}^{N}[\eta_{pj}(\log\eta_{pj}+\xi_{pj})]}_{\text{II}}$$
$$+\underbrace{\frac{\lambda}{1-t}\log\left[\sum_{p=1}^{C}(G_p^{'}+1)^t\right]}_{\text{III}}$$

subject to

$$(1)\quad 0\le\mu_{pj},\eta_{pj},\xi_{pj}\le 1,\quad p=1,2,3...C \text{ and } j=1,2,3...N$$
$$(2)\quad 0\le\mu_{pj}+\eta_{pj}+\xi_{pj}\le 1,\quad p=1,2,3...C \text{ and } j=1,2,3...N$$
$$(3)\quad \sum_{p=1}^{C}[\mu_{pj}(2-\xi_{pj})]=1,\quad j=1,2,3...N$$
$$(4)\quad \sum_{p=1}^{C}(\eta_{pj}+\frac{\xi_{pj}}{C})=1,\quad j=1,2,3...N \tag{5.23}$$

Where Dpj, $[\mu_{pj}(2-\xi_{pj})]$ and the constraints represent the same information as in optimization problem *J1* (equation 5.13). The term $G_p^{'}=\frac{1}{N}\sum_{j=1}^{N}\frac{[\mu_{pj}(2-\xi_{pj})]}{\bar{\mu}_{pj}}$, $\bar{\mu}_{pj}=\frac{1}{|N_{z_j}|}\sum_{z_k\in N_{z_j}}[\mu_{pk}(2-\xi_{pk})]$. The parameter *t* ($t>1$) is the order of modified Renyi's Entropy and λ is the regularization parameter. The optimization problem *J2* (equation 5.23) is composed of 3 terms.

- The first two terms are the same as in optimization problem *J1* (equation 5.13).

- The third term represents the t^{th} order modified Renyi's Entropy. The value of $G_p^{'}$ defines the expected value of normalized factual membership (true belongingness) vector for a cluster C_p, wherein the membership values of z_j, $j=1,2,3...N$ are normalized by the average factual membership of its neighborhood. The term $G_p^{'}$ denotes the probability of a data point, in a given neighborhood, belonging to cluster C_p. G_p approaching to 1 means that cluster p dominates the whole data set while the other clusters are nearly empty. To ensure $-\log\left[\sum_{p=1}^{C}(G_p^{'}+1)^t\right] > 0$, 1 is added to $G_p^{'}$. This term is included in the model to overcome the limitation of [90] and obtain a good partition matrix. Minimizing the term will result in fewer number of clusters.

- Minimizing the first term intends to make a large number of clusters, whereas minimizing the third term targets fewer clusters. The suitable value of the regularization parameter λ controls the balance between the first and last term and regulates the degree of fuzziness for overlapping clusters.

The optimization problem *J2* (equation 5.23) is solved for the cluster prototype and membership values, $(\mu_{pj}, \eta_{pj}, v_p, \alpha_j, \beta_j)$, using Lagrangian method of multiplier [37]. Also, the matrices M and H are initialized using equations 5.11 and 5.12, respectively, and the cluster centers are initialized using equation 5.10.

5.3.2.1 Derivation of Cluster Prototype for *J2*

The Lagrangian function $L2(\mu_{pj}, \eta_{pj}, v_p, \alpha_j, \beta_j)$ (equation 5.24), for the optimization problem *J2* (equation 5.23) is represented as

$$\begin{aligned} L2 = {} & \sum_{p=1}^{C}\sum_{j=1}^{N}\left[\mu_{pj}(2-\xi_{pj})\right]^2 Dpj + \sum_{p=1}^{C}\sum_{j=1}^{N}\left[\eta_{pj}(\log\eta_{pj}+\xi_{pj})\right] + \frac{\lambda}{1-t}\log\left[\sum_{p=1}^{C}(G_p^{'}+1)^t\right] \\ & + \sum_{j=1}^{N}\alpha_j\left[1-\sum_{p=1}^{C}\left[\mu_{pj}(2-\xi_{pj})\right]\right] + \sum_{j=1}^{N}\beta_j\left[1-\sum_{p=1}^{C}\left[\eta_{pj}+\frac{\xi_{pj}}{C}\right]\right] \end{aligned} \tag{5.24}$$

where α_j and β_j are the Lagrange's Multipliers for $j = 1, 2, 3...N$.

Now, equating the partial differential of *L2* w.r.t μ_{pj} to 0 i.e. $\frac{\partial L2}{\partial \mu_{pj}} = 0$ to derive the value of μ_{pj},

$$(2-\xi_{pj})\left[2\mu_{pj}(2-\xi_{pj})Dpj + \frac{\lambda t}{N(1-t)\bar{\mu}_{pj}}\frac{(G_p^{'}+1)^{t-1}}{\sum_{p=1}^{C}(G_p^{'}+1)^t} - \alpha_j\right] = 0 \tag{5.25}$$

In equation 5.25, $(2-\xi_{pj}) \neq 0$ because $\xi_{pj} \in [0, 1]$,

$$\mu_{pj}(2-\xi_{pj}) = \frac{1}{2D_{pj}}\left[\alpha_j - \frac{\lambda t}{N(1-t)\bar{\mu}_{pj}}\frac{(G_p^{'}+1)^{t-1}}{\sum_{p=1}^{C}(G_p^{'}+1)^t} + \right] \tag{5.26}$$

Applying the summation $\sum_{k=1}^{C}$, and then using constraint 3 of optimization problem (equation 5.23) in above equation,

$$1 = \frac{\alpha_j}{2}\sum_{k=1}^{C}\frac{1}{D_{kj}} - \frac{\lambda t}{2N(1-t)\sum_{p=1}^{C}(G'_p+1)^t}\sum_{k=1}^{C}\left[\frac{(G'_k+1)^{t-1}}{\bar{\mu}_{kj}D_{kj}}\right] \tag{5.27}$$

Solving the above equation for $\frac{\alpha_j}{2}$,

$$\frac{\alpha_j}{2} = \frac{1}{\sum_{k=1}^{C}(1/D_{kj})} + \frac{\lambda t}{2N(1-t)\sum_{p=1}^{C}(G'_p+1)^t}\frac{\sum_{k=1}^{C}\frac{(G'_k+1)^{t-1}}{D_{kj}\bar{\mu}_{kj}}}{\sum_{k=1}^{C}(1/D_{kj})} \tag{5.28}$$

Now substituting the value of $\frac{\alpha_j}{2}$ back in equation 5.26 and solving further for μ_{pj}

$$\begin{aligned}\mu_{pj} = \frac{(1/D_{pj})}{(2-\xi_{pj})}\Bigg[&\frac{1}{\sum_{k=1}^{C}(1/D_{kj})} - \frac{\lambda t}{2N(1-t)}\frac{1}{\bar{\mu}_{pj}}\frac{(G'_p+1)^{t-1}}{\sum_{p=1}^{C}(G'_p+1)^t}\\ &+\frac{\lambda t}{2N(1-t)\sum_{p=1}^{C}(G'_p+1)^t}\frac{\sum_{k=1}^{C}\frac{(G'_k+1)^{t-1}}{D_{kj}\bar{\mu}_{kj}}}{\sum_{k=1}^{C}(1/D_{kj})}\Bigg]\end{aligned} \tag{5.29}$$

The Equation 5.29 is further simplified to

$$\mu_{pj} = \frac{(1/D_{pj})}{(2-\xi_{pj})}\left[\frac{1}{\sum_{k=1}^{C}(1/D_{kj})} + \frac{\lambda t}{2N(1-t)\sum_{p=1}^{C}(G'_p+1)^t}\left[\frac{\sum_{k=1}^{C}\frac{(G'_k+1)^{t-1}}{D_{kj}\bar{\mu}_{kj}}}{\sum_{k=1}^{C}(1/D_{kj})} - \frac{(G'_p+1)^{t-1}}{\bar{\mu}_{pj}}\right]\right] \tag{5.30}$$

Using Taylor's Expansion for $(1+G'_p)^{t-1} = 1+(t-1)G'_p + \frac{(t-2)(t-1)G'^2_p}{2!} + ...$ and $0 < G'_p < 1$. So, the higher powers of $G'_p \simeq 0$ and can be neglected. Therefore $(1+G'_p)^{t-1} \simeq 1+(t-1)G'_p$. Using this, the value of μ_{pj} is finally obtained as

$$\mu_{pj} = \frac{(1/D_{pj})}{(2-\xi_{pj})}\left[\underbrace{\frac{1}{\sum_{k=1}^{C}(1/D_{kj})}}_{\text{I}} + \underbrace{\frac{\lambda t}{2N(1-t)\sum\limits_{p=1}^{C}(1+G'_p)^t}\left[\frac{\sum\limits_{k=1}^{C}\frac{1+(t-1)G'_k}{D_{kj}\bar{\mu}_{kj}}}{\sum\limits_{k=1}^{C}(1/D_{kj})} - \frac{1+(t-1)G'_p}{\bar{\mu}_{pj}}\right]}_{\text{II}}\right] \tag{5.31}$$

The value of μ_{pj} obtained comprises two terms. The first term is the same as the μ_{pj} value in DSIFC-P_cFS optimization problem. The second term represents the bias/partiality in the value of membership μ_{pj} for the boundary edges. For Second order modified Renyi's Entropy, t=2, μ_{pj} is obtained as

$$\mu_{pj} = \frac{(1/D_{pj})}{(2-\xi_{pj})}\left[\frac{1}{\sum_{k=1}^{C}(1/D_{kj})} - \frac{\lambda}{N\sum_{p=1}^{C}(1+G_p^{'})^2}\left[\frac{\sum_{k=1}^{C}\frac{1+G_k^{'}}{D_{kj}\bar{\mu}_{kj}}}{\sum_{k=1}^{C}(1/D_{kj})} - \frac{1+G_p^{'}}{\bar{\mu}_{pj}}\right]\right] \tag{5.32}$$

Similarly, solving the equation of partial differential of *L2* w.r.t η_{pj} to 0 i.e. $\frac{\partial L2}{\partial \eta_{pj}} = 0$, the value of η_{pj} is finally obtained as

$$\eta_{pj} = \frac{\exp\left(-\xi_{pj}\right)}{\sum_{k=1}^{C}\exp\left(-\xi_{kj}\right)}\left[1 - \sum_{k=1}^{C}\frac{\xi_{kj}}{C}\right] \tag{5.33}$$

Now, substituting the value D_{pj} in equation 5.24 and then solving the equation of partial differential w.r.t v_p to 0 i.e. $\frac{\partial L2}{\partial v_p} = 0$, the final value of v_p for iteration is computed as

$$v_p = \frac{\sum\limits_{j=1}^{N}[\mu_{pj}(2-\xi_{pj})]^2\left[K_{pj}^{'}z_j + \sum\limits_{z_k \in N_{z_j}}\frac{\left[\mu_{pk}(2-\xi_{pk})\right]}{\sum\limits_{z_l \in N_{z_j}}\left[\mu_{pl}(2-\xi_{pl})\right]}K_{pk}^{'}z_k\right]}{\sum\limits_{j=1}^{N}[\mu_{pj}(2-\xi_{pj})]^2\left[K_{pj}^{'} + \sum\limits_{z_k \in N_{z_j}}\frac{\left[\mu_{pk}(2-\xi_{pk})\right]}{\sum\limits_{z_l \in N_{z_j}}\left[\mu_{pl}(2-\xi_{pl})\right]}K_{pk}^{'}\right]} \tag{5.34}$$

where $K_{pj}^{'} = \left[1 + \tanh\left[-\frac{\|z_j - v_p\|^2}{\sigma^2}\right]\right]K(z_j, v_p)$.

The equations 5.31, 5.33, and 5.34 shows the derived prototype for *J2* (equation 5.23). The value of refusal degree ξ_{pj} is computed using equation 5.2. The above optimization model, combined with the density concept used in this work, is outlined as Algorithm 3.

5.4 Experimental Setup

The experiments are conducted on a computer system having a Windows 10 operating system with an i7 (9^{th} generation) Processor and 16GB primary memory. The experiments are performed and statistical analyzed for the proposed framework using MATLAB 2020(64-bit). Figure 5.2 displays the graphical abstract for conducting the experiments. Figure 5.3 elaborates the mechanism and difference between the two proposed methods.

Algorithm 3 Density-based Modified FC-P_cFS with Spatial Information method (DSIMFC-P_cFS)

Input: Image I of size $P \times Q$, ϵ: Threshold, λ: Regularization Parameter, ω: Exponent, *maxSteps*: Maximal number of iterations, τ: Adjustable cutoff parameter.

Output: Matrices M, H, Ξ, V

```
procedure DSIMFC-$P_c$FS
    Calculate the local energy matrix $I^*$from I using equation 5.7.
    Normalize the matrix $I^*$in the range [0,1].
    $Z \leftarrow$ vectorize($I^*$)          $//$size of Z is N($= P \times Q$)
    for each $z_j \in Z$ do
        Calculate $\rho_j$ using using equation 5.8
        Calculate $\delta_j$ using using equation 5.9
        $\gamma_j \leftarrow \rho_j \times \delta_j$
    end for
    Arrange the $\gamma_j$ values in descending order
    $d_c \leftarrow (\sum_{j=1}^{N} \gamma_j) \times \tau$
    Initialize the cluster centers using equation 5.10
    $i \leftarrow 0$
    Initialize the matrix $M^{(0)}$ using equation 5.11
    Initialize the matrix $H^{(0)}$ using equation 5.12
    Calculate $\Xi^{(0)}$ using equation 5.2
    repeat
        $i \leftarrow i + 1$
        Calculate $V^{(i)}$ using equation 5.34
        Calculate $M^{(i)}$ using equation 5.32
        Calculate $H^{(i)}$ using equation 5.33
        Calculate $\Xi^{(i)}$ using equation 5.2
    until $(\|M^{(i)} - M^{(i-1)}\| + |H^{(i)} - H^{(i-1)}\| + \|\Xi^{(i)} - \Xi^{(t-1)}\|) < \epsilon$ or $(i \geq maxSteps)$
    return Matrices $M, H, \Xi, V$
end procedure
```

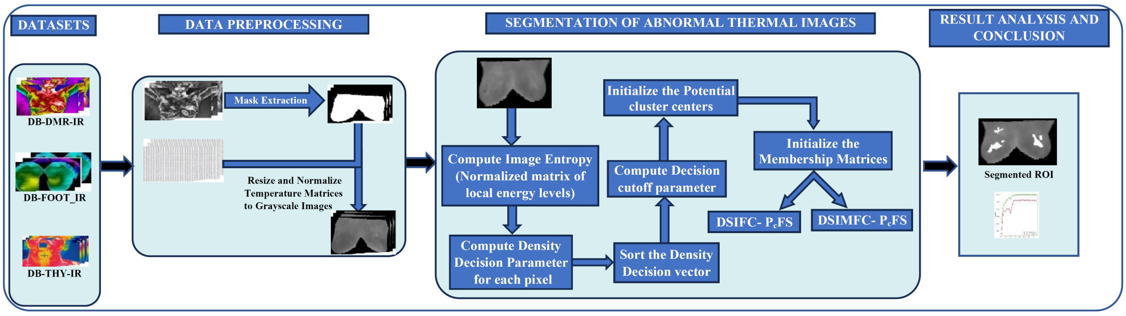

Fig. 5.2: The framework of the proposed work (Graphical abstract).

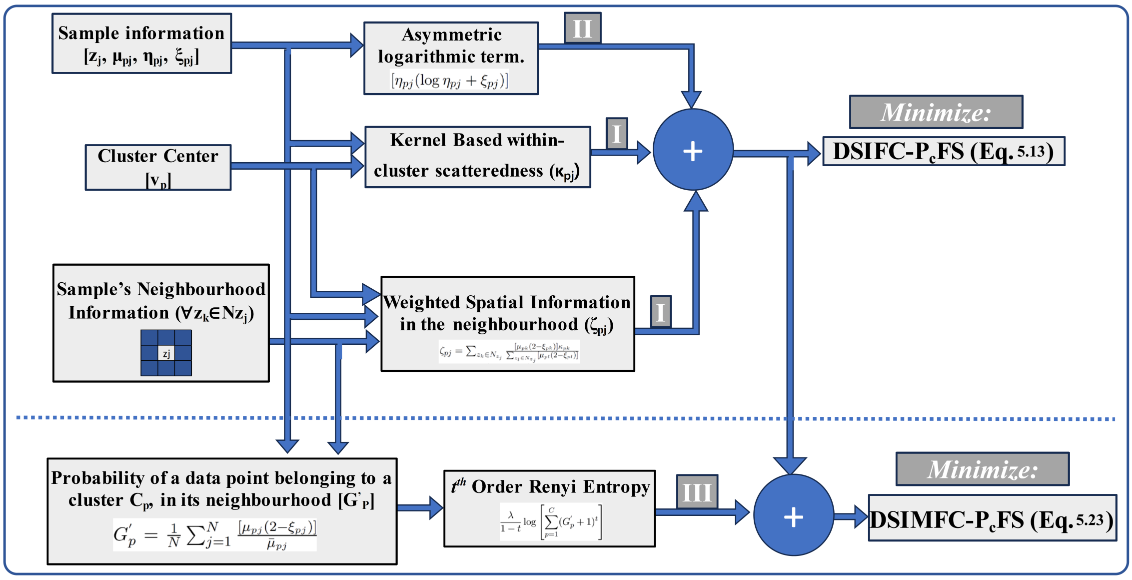

Fig. 5.3: Mechanism and difference between the two proposed methods - DSIFC-P_cFS and DSIMFC-P_cFS. (Roman values written on arrows denotes the parts in equations 5.13 and 5.23, respectively.)

Three medical thermography-based public datasets (DB-THY-IR, DB-DMR-IR, and DB-FOOT-IR) and an artificially-created noisy dataset (DB-NOISE-IR) are considered in the experiments. This work uses only abnormal thermal images, with and without noise, to segment the hotspots in them. The pre-processing steps for the three datasets are described in Chapter 1, section 1.2.1. The Table 5.1 states the number of abnormal samples in each dataset.

Table 5.1: Size of the datasets used in the study

DataSets	DB-FOOT-IR	DB-THY-IR	DB-DMR-IR
Number of Abnormal Samples	45	18	40

The dataset - DB-NOISE-IR, consists of 15 subsets of five images each. The five thermal images are randomly picked from each of the three above-stated datasets. These images are then corrupted with three types of artificial noise - Salt and Pepper noise (SP Noise) of 1% and 5% intensities, Gaussian Noise with $\sigma = 1\%$ and 0.5%, and Mixed Noise. A thermal image is corrupted with mixed noise by first adding the Gaussian Noise ($\sigma = 0.5\%$) followed by SP noise of 1% intensity. Table 5.2 details the 15 subsets of DB-NOISE-IR dataset. Figure 5.4 demonstrates the sample original and corrupted thermal images from the three datasets.

Table 5.2: Details of subsets of DB-NOISE-IR dataset.

Subset Name**	**Details**
XXX-N1	Corrupted with Gaussian Noise ($\sigma = 0.5\%$)
XXX-N2	Corrupted with Gaussian Noise ($\sigma = 1\%$)
XXX-N3	Corrupted with SP Noise (1% Intensity)
XXX-N4	Corrupted with SP Noise (5% Intensity)
XXX-N5	Corrupted with Mixed Noise

*XXX - DMR, FOOT, and THY datasets

The approaches proposed - DSIFC-P_cFS and DSIMFC-P_cFS, for segmenting thermal images are compared with 10 State-of-the-art methods- EnMRG[32], LSNAP[36], FC-P_cFS[90], ColK-Means[102], DFCM [91], DIFCM[92], FLICM[94], and KFCM_S[95], IFCMSNI[93], KPFCMSNI[96]. We implemented the methods with exact lines of detail in MATLAB 2020 (64-bit) for a fair comparison.

The table 5.3 describes all the notations and symbols used in this work. The table 5.4 lists the various parameters and their values used in State-of-the-art approaches and proposed approaches for the investigation purpose.

The manually-segmented reference image does not exist for the datasets under consideration. Therefore, the effectiveness of proposed approaches and related methods is analyzed using unsupervised objective evaluation performance metrics. These measures do not require a human visual comparison or comparison with the ground-truth reference image.

For the publicly available dataset DB-DMR-IR, the research works [32, 33, 98, 97] created reference images themselves, which is intrinsically subjective. To eliminate the subjectivity, following performance metrics are used for evaluating the segmentation results -

1. **Modified Partition Coefficient (MPC)** [149]- Modified Partition Coefficient (MPC) is the modification of Partition Coefficient and retards its monotonic trend with an increase in the number of clusters. An optimal value of MPC is obtained by solving $\max_{2 \leq C \leq N-1} MPC$ for possible values of *C*. The value of $MPC \in [0, 1]$ and is computed using equation -

$$MPC = 1 - \frac{C}{C-1}\left[\frac{1}{N}\sum_{p=1}^{C}\sum_{j=1}^{N} U_{pj}^{2}\right] \tag{5.35}$$

2. **Bensaid Validity index (BVI)** [150] - BVI is computed as a ratio of intra-

region compactness and inter-region separation using equation -

$$BVI = \sum_{p=1}^{C} \frac{\sum_{j=1}^{N} U_{pj}^2 (z_j - v_p)^2}{n_p \sum_{k=1}^{C} (v_k - v_p)^2} \tag{5.36}$$

where $n_p = \sum_{j=1}^{N} U_{pj}$. It normalizes the compactness to separation ratio with the weights $1/n_p$. A well-defined segmentation will have a minimal value of BVI.

3. **Uniformity Index (UI)** [151] - Uniformity of a region is inversely proportional to variance in intensity of its pixels. The Uniformity Index (UI) quantifies the intra-region uniformity based on its variance. It provides global texture uniformity and is computed as a measure within each region, independent of its neighboring regions. The value of $UI \in [0, 1]$. A well-segmented region would maximize the value of this criteria. Mathematically, UI is calculated as

$$UI = 1 - \frac{2}{N} \sum_{p=1}^{C} \frac{\sum_{z_j \in C_p} [z_j - \overline{z_p}]^2}{\left[\max\limits_{z_j \in C_p}(z_j) - \min\limits_{z_j \in C_p}(z_j) \right]^2} \tag{5.37}$$

   where $\overline{z_p}$ is the average of sample points in cluster/region C_p.

4. **Inter-Region Contrast Measure (IRCM)** [151] - Inter-Region Contrast Measure (IRCM) is the weighted sum of per-region contrast and is computed as

$$IRCM = \frac{\sum_{p=1}^{C} y_p c_p}{\sum_{p=1}^{C} y_p} \tag{5.38}$$

   where the weights y_p are defined as per human contrast sensitivity curve[151], $y_p = \frac{1}{\sqrt{2\pi A_\sigma^2}} \exp - \frac{(A_p - A_\mu)^2}{A_\sigma^2}$. The terms A_p, A_μ, and A_σ denote the size of p^{th} cluster, average of clusters' sizes, and variation in sizes of clusters, respectively. The per-region contrast, (c_p), is computed for a region/cluster C_p in relation with all its neighboring regions, as $c_p = \sum\limits_{C_q \in Nbd(C_p)} d_{pq} \frac{|\overline{z_p} - \overline{z_q}|}{\overline{z_p} + \overline{z_q}}$. The weight d_{pq} is the ratio of perimeter common to C_p and C_q to the perimeter of C_p. $Nbd(C_p)$ is the set of regions in the immediate neighborhood of C_p. Note that $\sum\limits_{C_q \in Nbd(C_p)} d_{pq} = 1$. The value of $IRCM \in [0, 1]$. A higher value of IRCM denotes a good segmentation.

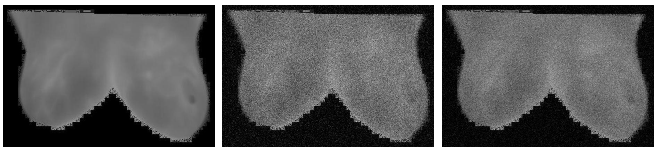

(a) DB-DMR-IR - Original Image

(b) Gaussian Noise ($\sigma = 1\%$)

(c) Gaussian Noise ($\sigma = 0.5\%$)

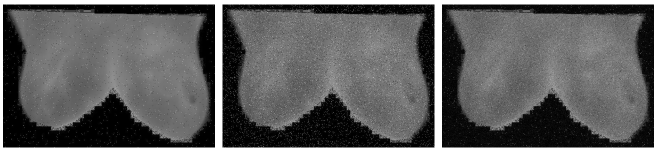

(d) SP Noise (1% Intensity)

(e) SP Noise (5% Intensity)

(f) Mixed Noise

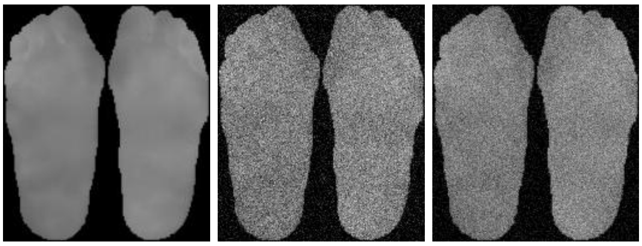

(g) DB-FOOT-IR - Original Image

(h) Gaussian Noise ($\sigma = 1\%$)

(i) Gaussian Noise ($\sigma = 0.5\%$)

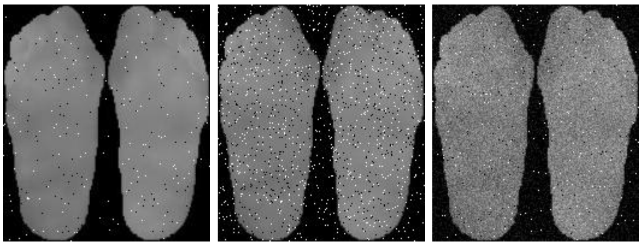

(j) SP Noise (1% Intensity)

(k) SP Noise (5% Intensity)

(l) Mixed Noise

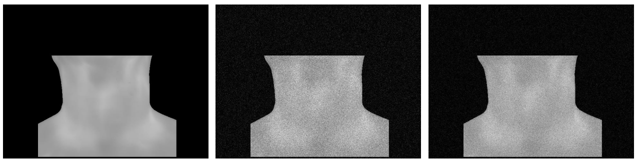

(m) DB-THY-IR - Original Image

(n) Gaussian Noise ($\sigma = 1\%$)

(o) Gaussian Noise ($\sigma = 0.5\%$)

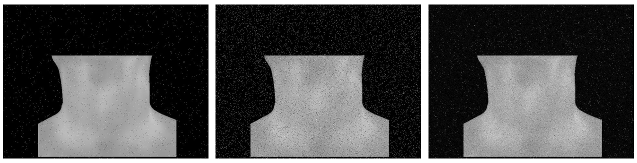

(p) SP Noise (1% Intensity)

(q) SP Noise (5% Intensity)

(r) Mixed Noise

Fig. 5.4: The sample of original thermal image and corresponding corrupted images from the three datasets.

Table 5.3: Notations used in the proposed work.

Notation	Description	Notation	Description
I	An image, of size $N = P \times Q$.	d_c	Decision cutoff parameter
I^*	An image I transformed to a normalized matrix of local energy levels (Entropy Image).	ζ_{pj}	Spatial Information in the neighborhood of data point z_j towards cluster center v_p.
Z	A vector of data points/items formed from I^*.	ϵ	Threshold Value
z_j	A data point/element in Z, $j = 1, 2, 3...N$	λ	Regularization parameter
S	A P_cFS defined over Z with element s_j as $\langle z_j,\ \mu_S(z_j),\ \eta_S(z_j),\ \nu_S(z_j)\rangle$ corresponding to $z_j \in Z$, $j = 1, 2, 3...N$.	M	Fuzzy partition matrix of size $N \times C$ with the positive membership values for each $z_j \in Z$ to belong to all C clusters.
H	Matrix of neutrality of size $N \times C$ with the values for each $z_j \in Z$ to be neutral to C clusters.	Ξ	Matrix of refusal degree, of size $N \times C$ with the refusal of each $z_j \in Z$ to C clusters.
$\alpha_j \& \beta_j$	Lagrangian Multiplier of data point $z_j \in Z$, j = 1,2,3...N	N_{z_j}	Set of data points in the w× w neighborhood of data point z_j.
$K(x_i, x_j)$	Kernel Function	$\phi(z_j)$	A data point z_j in kernel space
t	Order of modified Renyi's Entropy	ρ_j	Density parameter of $z_j \in Z$, j = 1,2,3...N
μ_{pj}	Positive membership of $z_j \in Z$ to cluster C_p, $p = 1, 2, 3...C$ and $j = 1, 2, 3...N$	κ_{ij}	Kernel-based distance between data points z_i and z_j.
η_{pj}	Degree of neutrality of $z_j \in Z$ to cluster C_p, $p = 1, 2, 3...C$ and $j = 1, 2, 3...N$	$G_p^{'}$	probability of a data point, in a given neighborhood, belonging to cluster C_p
ν_{pj}	Negative membership of $z_j \in Z$ to cluster C_p, $p = 1, 2, 3...C$ and $j = 1, 2, 3...N$	$\bar{\mu}_{pj}$	Average factual membership of neighborhood of data point z_j towards cluster center v_p.
ξ_{pj}	Degree of refusal of $z_j \in Z$ to cluster C_p, $p = 1, 2, 3...C$ and $j = 1, 2, 3...N$	δ_j	Minimum distance parameters of $z_j \in Z$, j = 1,2,3...N
γ_j	Density decision parameter of $z_j \in Z$, j = 1,2,3...N	d_{ji}	Euclidean distance between samples z_i and z_j
$maxSteps$ or T	Maximal number of iterations.	ς	Measure of scatter of energy levels in I^*
ω	Negation Exponent	m	Fuzzifier
C	Number of clusters.	τ	Adjustable cutoff parameter
C_p	p^{th} Cluster with center v_p, $p = 1, 2, 3...C$	$\mathbb{C}$	Set of potential initial cluster centers

5. **Zeboudj's Criterion (ZC) [152]** - Zeboudj's Criterion (ZC) is a composite of maximal inter-region and minimal intra-region disparity and is a suitable metric for a noisy image. The intra-region disparity and inter-region disparity for a region C_p are defined as $CI(C_p) = \frac{1}{A_p} \sum\limits_{z_j \in C_p} \max\{(z_j - z_t), z_t \in N_{z_j} \cup C_p\}$ and $CE(C_p) = \frac{1}{P_p} \sum\limits_{z_j \in B_p} \max\{(z_j - z_t), z_t \in N_{z_j} - C_p\}$, respectively. The term P_p is the perimeter of Boundary B_p of cluster C_p. Then, ZC

is computed as $ZC = \frac{1}{N}\sum_{p=1}^{C} A_p Z_p$, where

$$Z_p = \begin{cases} 1 - \frac{CI(C_p)}{CE(C_p)}, & \text{if } 0 < CI(C_p) < CE(C_p) \\ CE(C_p), & \text{if } CI(C_p) = 0 \\ 0, & otherwise. \end{cases} \tag{5.39}$$

The value of $ZC \in [0,1]$. A higher value of ZC denotes a good segmentation.

Table 5.4: Parameters and their Values for various State-of-the-art and proposed approaches for segmenting medical thermal images

S. No.	Segmentation Methods	Parameters and their Values
1.	EnMRG[32]	Parameter η = [0,1] with a step size of 0.1, *Image Threshold* = [0, 0.1] with a step size of 0.01, *Entropy Image Threshold* = [0, 0.1] with a step size of 0.01
2.	LSNAP[36]	-
3.	ColK-Means[102]	C=5
4.	FLICM[94]	m = 2, *maxSteps* = 1000, ϵ = 0.0001, C = [3, 4, 5, 6, 7]
5.	KFCM_S[95]	m = 2, Spatial Penalty Parameter = [0-4] with a step size of 0.2 *maxSteps* = 1000, ϵ = 0.0001, C = [3, 4, 5, 6, 7]
6.	DFCM[91]	m = 2, *Density Rate* = 0.25, ϵ = 0.0001, *maxSteps* = 1000, *Distance Rate* = 1.0, and *Cutoff Distance* = 0.45
7.	DIFCM[92]	m=2, *Density Rate* = 0.25, ϵ = 0.0001, *maxSteps* = 1000, *Distance Rate* = 1.0, and ω = [0-2] with a step size of 0.15
8.	IFCMSNI[93]	ω = [0-2] with a step size of 0.15m = 2, Spatial Regularization Parameter = [0-4] with a step size of 0.2, *maxSteps* = 1000, ϵ = 0.0001, C = [3, 4, 5, 6, 7]
9.	FC-P_cFS[90]	m = 2, ω = [0-2] with a step size of 0.15, ϵ = 0.0001, *maxSteps* = 1000, C = [3, 4, 5, 6, 7]
10.	KPFCMSNI[96]	ω = [0-2] with a step size of 0.15, m = 2, Spatial Regularization Parameter = [0-4] with a step size of 0.2, *maxSteps* = 1000, ϵ = 0.0001, C = [3, 4, 5, 6, 7]
11.	DSIFC-P_cFS	ω = [0-2] with a step size of 0.15, m = 2, *maxSteps* = 1000, ϵ = 0.0001, τ = 0.25
12.	DSIMFC-P_cFS	ω = [0-2] with a step size of 0.15, *maxSteps* = 1000, ϵ = 0.0001, τ = 0.25, $\lambda = [2^{10}, 2^{11}, 2^{12}, 2^{13}, 2^{14}]$, and t = 2

All the performance metrics values corresponding to each hyper-parameter value are recorded for the grid search. The performance obtained corresponding to the ZC's optimal value (among all the hyper-parameters) is considered for analysis(Table 5.5). The value of a metric for a segmentation method is obtained by averaging its value over all the images in a dataset.

5.5 Results and Discussion

This section demonstrates the effectiveness and robustness of the proposed segmentation methods on three publicly available thermal medical imaging datasets - DB-FOOT-IR, DB-THY-IR, and DB-DMR-IR and an artificially created noisy dataset - DB-NOISE-IR. The experiments conducted on all the datasets and images are independent and not related to each other in any respect. Metrics - MPC, BVI, UI, IRCM, and ZC are used to compare the performance of two proposed segmentation techniques - DSIFC-P_cFS and DSIMFC-P_cFS, with 10 State-of-the-art methods- EnMRG[32], LSNAP[36], ColK-Means[102], KFCM_S[95], FLICM[94], DFCM [91], DIFCM[92], IFCMSNI[93], FC-P_cFS[90], and KPFCMSNI[96].

We analyze the results quantitatively and statistically in subsections 5.5.1 and 5.5.2, respectively. The computational complexity of the methods is compared in section 5.5.3.

5.5.1 Result Analysis

The table 5.5 states the results obtained for all the metrics and methods used in this work. Figure 5.5 illustrates the visual comparison of values of ZC values for thermal images with and without noise. To plot the graph (Figure 5.5), the ZC score is averaged over all the different types and levels of noise (XXX-N1, XXX-N2, XXX-N3, XXX-N4, and XXX-N5) for each dataset (XXX - DMR, FOOT, and THY). Following observations are made from the table 5.5 and figures 5.5-

- The proposed methods DSIMFC-P_cFS and DSIFC-P_cFS performed better in comparison with the related methods for all three datasets without noise for the metrics - MPC, BVI, UI, IRCM, and ZC. Also, the proposed methods outperformed other related methods in the presence of Gaussian, SP, and Mixed noise at different levels (Table 5.5).

- The proposed methods -DSIMFC-P_cFS and DSIFC-P_cFS, are found to be robust and effective for images corrupted with high levels of noise. It is observed that the performance of all the stated methods has decreased with the increase in levels of noise. However, the reduction in the performance of the DSIMFC-P_cFS and DSIFC-P_cFS is significantly lesser than that of related methods. This is due to the incorporation of combination of density-based heuristic and spatial information with the minimization of modified

Renyi's Entropy. This shows the robustness of our proposed method for noisy images (Table 5.5).

- Segmentation Methods like EnMRG[32], LSNAP[36], ColK-Means[102], and FC-P_cFS[90] do not utilize spatial information, and therefore their performance decay remarkably with increase in levels of noise (Table 5.5).
- P_cFS based clustering methods like DSIMFC-P_cFS, DSIFC-P_cFS, KPFCMSNI[96], and FC-P_cFS[90] have performed better for all the datasets, without noise and corrupted with noise than that of other stated methods. This is due to the robust representational structure of P_cFS (Figure 5.5).
- No significant difference is observed in the performance of DIFCM[92], IFCMSNI[93], and FC-P_cFS[90] for DB-DMR-IR dataset. For DB-THY-IR and DB-FOOT-IR datasets, DIFCM[92] has performed better for images with and without noise (Figure 5.5).
- Density-based methods - DFCM [91], DIFCM[92], and our proposed methods have performed better than their corresponding variants in FCM, IFCM, and FC-P_cFS, respectively, for the images corrupted with noise. This is due to meticulously assigning the initial cluster centers and membership matrices (Figure 5.5).

The qualitative results on the images corrupted with Gaussian noise (σ =1%) from three datasets - DB-DMR-IR, DB-FOOT-IR, and DB-THY-IR are demonstrated in figures 5.6, 5.7, and 5.8, respectively. Among all, DSIMFC-P_cFS and DSIFC-P_cFS performed better than other methods, capturing all the hotspots/suspicious regions in the thermal images. Through the quantitative and qualitative analysis, it can be inferred that the proposed methods - DSIMFC-P_cFS and DSIFC-P_cFS- are effective and can accurately identify the hotspots, especially in the presence of noise. As the noise level increases, the proposed DSIMFC-P_cFS method outperforms other related methods in terms of MPC, BVI, UI, IRCM, and ZC, thereby suppressing the effect of noise. The proposed method is robust due to the incorporation of spatial information along with density information and modified Renyi's Entropy.

Table 5.5: Performance comparison of various Segmentation methods for three datasets with and without noise.

Segmentation Results for DB-DMR-IR(with and without noise)

	Without Noise					**Gaussian Noise** ($\sigma = 0.5\%$) **(DMR-N1)**					**Gaussian Noise** ($\sigma = 1\%$) **(DMR-N2)**					**SP Noise (1% Intensity) (DMR-N3)**					**SP Noise (5% Intensity) (DMR-N4)**					**Mixed Noise (DMR-N5)**				
Segmentation Methods	**MPC**	**BVI**	**UI**	**IRCM**	**ZC**	**MPC**	**BVI**	**UI**	**IRCM**	**ZC**	**MPC**	**BVI**	**UI**	**IRCM**	**ZC**	**MPC**	**BVI**	**UI**	**IRCM**	**ZC**	**MPC**	**BVI**	**UI**	**IRCM**	**ZC**	**MPC**	**BVI**	**UI**	**IRCM**	**ZC**
LSNAP[36]	0.67	0.126	0.61	0.697	0.7	0.606	0.242	0.567	0.611	0.584	0.561	0.31	0.411	0.442	0.447	0.574	0.146	0.6	0.59	0.676	0.41	0.179	0.595	0.55	0.525	0.453	0.326	0.407	0.515	0.538
EnMRG[32]	0.565	0.218	0.596	0.601	0.632	0.499	0.292	0.561	0.57	0.556	0.461	0.333	0.408	0.399	0.425	0.469	0.229	0.596	0.55	0.59	0.43	0.261	0.58	0.533	0.453	0.429	0.357	0.404	0.474	0.478
ColK-Means[102]	0.727	0.121	0.684	0.75	0.707	0.661	0.219	0.646	0.616	0.665	0.621	0.265	0.478	0.488	0.499	0.66	0.135	0.67	0.6	0.701	0.506	0.164	0.65	0.57	0.527	0.495	0.258	0.475	0.583	0.57
KFCM_S[95]	0.731	0.102	0.759	0.764	0.844	0.669	0.18	0.73	0.682	0.754	0.627	0.215	0.592	0.563	0.712	0.681	0.123	0.67	0.622	0.702	0.525	0.14	0.65	0.587	0.586	0.616	0.21	0.589	0.6	0.695
FLICM[94]	0.776	0.098	0.767	0.775	0.865	0.717	0.137	0.743	0.772	0.814	0.708	0.178	0.641	0.622	0.731	0.755	0.117	0.71	0.749	0.804	0.649	0.139	0.67	0.73	0.651	0.686	0.209	0.638	0.701	0.736
DFCM **[91]**	0.797	0.076	0.811	0.803	0.865	0.754	0.137	0.776	0.788	0.816	0.733	0.144	0.68	0.73	0.811	0.763	0.107	0.73	0.76	0.816	0.667	0.131	0.67	0.746	0.657	0.723	0.206	0.678	0.728	0.812
DIFCM[92]	0.923	0.068	0.874	0.854	0.894	0.894	0.098	0.844	0.833	0.888	0.873	0.101	0.755	0.82	0.869	0.902	0.098	0.77	0.831	0.892	0.831	0.122	0.75	0.82	0.838	0.837	0.205	0.752	0.815	0.838
IFCMSNI[93]	0.806	0.07	0.817	0.804	0.884	0.78	0.124	0.786	0.8	0.818	0.761	0.141	0.701	0.773	0.813	0.786	0.106	0.75	0.793	0.846	0.693	0.127	0.71	0.789	0.693	0.729	0.205	0.698	0.786	0.815
FC-P_c**FS[90]**	0.818	0.069	0.851	0.833	0.893	0.8	0.105	0.822	0.8	0.823	0.769	0.133	0.751	0.8	0.819	0.814	0.101	0.76	0.796	0.857	0.772	0.124	0.73	0.79	0.715	0.74	0.2	0.748	0.794	0.82
KPFCMSNI[96]	0.925	0.058	0.887	0.882	0.9	0.9	0.097	0.865	0.856	0.893	0.878	0.099	0.808	0.852	0.879	0.904	0.086	0.78	0.869	0.9	0.852	0.115	0.75	0.85	0.892	0.842	0.2	0.775	0.833	0.885
DSIFC-P_c**FS**	0.933	0.038	0.917	0.911	0.923	0.91	0.088	0.884	0.889	0.91	0.88	0.091	0.812	0.866	0.901	0.92	0.065	0.852	0.9	0.923	0.871	0.09	0.815	0.882	0.912	0.847	0.168	0.792	0.842	0.9
DSIMFC-P_c**FS**	**0.953**	**0.021**	**0.926**	**0.918**	**0.938**	**0.933**	**0.052**	**0.894**	**0.9**	**0.924**	**0.882**	**0.055**	**0.815**	**0.88**	**0.92**	**0.935**	**0.037**	**0.875**	**0.913**	**0.934**	**0.925**	**0.07**	**0.822**	**0.893**	**0.933**	**0.861**	**0.139**	**0.811**	**0.89**	**0.913**

Segmentation Results for DB-FOOT-IR(with and without noise)

	Without Noise					**Gaussian Noise** ($\sigma = 0.5\%$) **(FOOT-N1)**					**Gaussian Noise** ($\sigma = 1\%$) **(FOOT-N2)**					**SP Noise (1% Intensity) (FOOT-N3)**					**SP Noise (5% Intensity) (FOOT-N4)**					**Mixed Noise (FOOT-N5)**				
Segmentation Methods	**MPC**	**BVI**	**UI**	**IRCM**	**ZC**	**MPC**	**BVI**	**UI**	**IRCM**	**ZC**	**MPC**	**BVI**	**UI**	**IRCM**	**ZC**	**MPC**	**BVI**	**UI**	**IRCM**	**ZC**	**MPC**	**BVI**	**UI**	**IRCM**	**ZC**	**MPC**	**BVI**	**UI**	**IRCM**	**ZC**
LSNAP[36]	0.697	0.156	0.719	0.597	0.55	0.639	0.238	0.637	0.597	0.522	0.639	0.295	0.605	0.475	0.491	0.64	0.214	0.679	0.552	0.473	0.623	0.29	0.636	0.531	0.407	0.578	0.317	0.548	0.523	0.459
EnMRG[32]	0.667	0.187	0.705	0.55	0.525	0.606	0.274	0.578	0.55	0.503	0.606	0.299	0.52	0.409	0.449	0.567	0.263	0.66	0.506	0.446	0.549	0.316	0.613	0.483	0.387	0.563	0.338	0.536	0.487	0.361
ColK-Means[102]	0.721	0.154	0.72	0.686	0.62	0.664	0.236	0.643	0.686	0.555	0.664	0.287	0.612	0.528	0.496	0.642	0.206	0.684	0.649	0.615	0.627	0.276	0.639	0.627	0.532	0.614	0.296	0.567	0.648	0.492
KFCM_S[95]	0.737	0.097	0.729	0.778	0.753	0.672	0.22	0.68	0.778	0.585	0.672	0.224	0.653	0.599	0.517	0.654	0.17	0.695	0.741	0.633	0.632	0.23	0.649	0.718	0.545	0.629	0.292	0.587	0.734	0.522
FLICM[94]	0.741	0.091	0.747	0.808	0.776	0.688	0.208	0.699	0.808	0.645	0.688	0.221	0.692	0.634	0.531	0.655	0.164	0.712	0.779	0.653	0.637	0.222	0.668	0.756	0.596	0.64	0.261	0.646	0.775	0.583
DFCM[91]	0.825	0.089	0.764	0.831	0.803	0.735	0.201	0.701	0.831	0.665	0.735	0.213	0.695	0.745	0.625	0.765	0.148	0.725	0.801	0.672	0.751	0.218	0.683	0.777	0.611	0.67	0.258	0.646	0.795	0.602
DIFCM[92]	0.867	0.078	0.833	0.901	0.867	0.816	0.146	0.797	0.901	0.796	0.788	0.171	0.782	0.803	0.729	0.794	0.13	0.796	0.867	0.779	0.764	0.185	0.747	0.844	0.708	0.722	0.226	0.7	0.827	0.733
IFCMSNI[93]	0.833	0.08	0.775	0.875	0.832	0.757	0.178	0.733	0.875	0.732	0.757	0.203	0.718	0.766	0.629	0.771	0.142	0.735	0.818	0.681	0.758	0.202	0.689	0.792	0.614	0.706	0.252	0.667	0.814	0.669
FC-P_c**FS[90]**	0.851	0.079	0.804	0.897	0.855	0.774	0.154	0.752	0.897	0.775	0.774	0.179	0.743	0.785	0.645	0.775	0.141	0.76	0.855	0.685	0.76	0.187	0.713	0.839	0.62	0.718	0.238	0.667	0.825	0.673
KPFCMSNI[96]	0.894	0.061	0.882	0.92	0.91	0.815	0.131	0.807	0.92	0.883	0.815	0.135	0.803	0.83	0.789	0.832	0.113	0.835	0.867	0.789	0.815	0.182	0.793	0.844	0.732	0.741	0.226	0.713	0.858	0.775
DSIFC-P_c**FS**	0.903	0.047	0.911	0.944	0.925	0.826	0.121	0.885	0.944	0.912	0.826	0.126	0.862	0.9	0.799	0.833	0.107	0.879	0.901	0.885	0.815	0.18	0.833	0.877	0.813	0.771	0.169	0.744	0.898	0.849
DSIMFC-P_c**FS**	**0.943**	**0.041**	**0.918**	**0.956**	**0.947**	**0.853**	**0.104**	**0.91**	**0.956**	**0.928**	**0.846**	**0.114**	**0.896**	**0.908**	**0.814**	**0.843**	**0.104**	**0.905**	**0.945**	**0.916**	**0.823**	**0.159**	**0.865**	**0.928**	**0.856**	**0.803**	**0.165**	**0.767**	**0.928**	**0.866**

Segmentation Results for DB-THY-IR(with and without noise)

	Without Noise (DB-THY-IR)					**Gaussian Noise** ($\sigma = 0.5\%$) **(THY-N1)**					**Gaussian Noise** ($\sigma = 1\%$) **(THY-N2)**					**SP Noise (1% Intensity) (THY-N3)**					**SP Noise (5% Intensity) (THY-N4)**					**Mixed Noise (THY-N5)**				
Segmentation Methods	**MPC**	**BVI**	**UI**	**IRCM**	**ZC**	**MPC**	**BVI**	**UI**	**IRCM**	**ZC**	**MPC**	**BVI**	**UI**	**IRCM**	**ZC**	**MPC**	**BVI**	**UI**	**IRCM**	**ZC**	**MPC**	**BVI**	**UI**	**IRCM**	**ZC**	**MPC**	**BVI**	**UI**	**IRCM**	**ZC**
LSNAP[36]	0.645	0.236	0.678	0.608	0.674	0.634	0.289	0.619	0.604	0.535	0.54	0.357	0.532	0.502	0.435	0.581	0.247	0.603	0.558	0.563	0.49	0.334	0.542	0.487	0.433	0.512	0.361	0.414	0.474	0.49
EnMRG[32]	0.55	0.263	0.658	0.589	0.643	0.49	0.327	0.57	0.565	0.479	0.452	0.449	0.424	0.48	0.326	0.498	0.313	0.595	0.486	0.55	0.439	0.373	0.536	0.456	0.396	0.443	0.368	0.374	0.451	0.391
ColK-Means[102]	0.718	0.201	0.681	0.667	0.692	0.689	0.21	0.625	0.642	0.581	0.665	0.303	0.561	0.504	0.445	0.692	0.224	0.623	0.615	0.628	0.522	0.265	0.554	0.532	0.44	0.537	0.339	0.457	0.559	0.535
KFCM_S[95]	0.731	0.177	0.69	0.792	0.709	0.693	0.189	0.657	0.738	0.641	0.676	0.243	0.593	0.535	0.592	0.71	0.182	0.639	0.624	0.659	0.595	0.222	0.556	0.572	0.572	0.599	0.33	0.618	0.601	0.578
FLICM[94]	0.764	0.153	0.723	0.82	0.777	0.705	0.179	0.68	0.763	0.659	0.703	0.198	0.634	0.593	0.643	0.735	0.17	0.676	0.752	0.684	0.607	0.215	0.67	0.684	0.618	0.668	0.294	0.638	0.714	0.637
DFCM[91]	0.79	0.141	0.783	0.825	0.841	0.758	0.161	0.703	0.782	0.721	0.727	0.188	0.684	0.641	0.646	0.737	0.152	0.763	0.788	0.738	0.665	0.168	0.718	0.715	0.641	0.674	0.294	0.655	0.774	0.648
DIFCM[92]	0.873	0.102	0.843	0.888	0.882	0.859	0.114	0.837	0.854	0.827	0.857	0.122	0.786	0.83	0.815	0.824	0.109	0.791	0.862	0.868	0.786	0.143	0.739	0.804	0.775	0.748	0.21	0.762	0.805	0.728
IFCMSNI[93]	0.791	0.116	0.803	0.852	0.845	0.77	0.138	0.735	0.799	0.755	0.741	0.154	0.73	0.689	0.739	0.767	0.124	0.768	0.797	0.831	0.673	0.147	0.732	0.759	0.654	0.699	0.283	0.719	0.795	0.679
FC-P_c**FS[90]**	0.824	0.102	0.809	0.868	0.852	0.811	0.126	0.796	0.834	0.767	0.757	0.131	0.772	0.815	0.754	0.816	0.114	0.777	0.852	0.837	0.714	0.144	0.732	0.792	0.693	0.703	0.221	0.73	0.797	0.697
KPFCMSNI[96]	0.894	0.083	0.891	0.901	0.877	0.878	0.087	0.872	0.866	0.868	0.878	0.104	0.844	0.841	0.858	0.85	0.091	0.817	0.873	0.868	0.789	0.123	0.759	0.838	0.785	0.808	0.205	0.801	0.815	0.808
DSIFC-P_c**FS**	0.914	0.056	0.917	0.929	0.923	0.886	0.068	0.889	0.892	0.908	0.877	0.078	0.859	0.869	0.877	0.914	0.09	0.883	0.888	0.88	0.844	0.096	0.865	0.872	0.876	0.822	0.188	0.839	0.858	0.864
DSIMFC-P_c**FS**	**0.936**	**0.025**	**0.944**	**0.936**	**0.933**	**0.933**	**0.047**	**0.925**	**0.92**	**0.895**	**0.913**	**0.076**	**0.921**	**0.892**	**0.885**	**0.911**	**0.041**	**0.897**	**0.894**	**0.901**	**0.893**	**0.063**	**0.903**	**0.887**	**0.879**	**0.88**	**0.157**	**0.863**	**0.887**	**0.887**

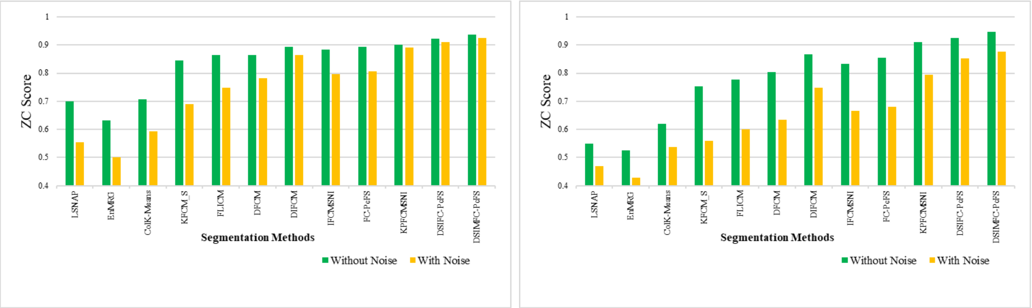

(a) DB-DMR-IR (b) DB-FOOT-IR

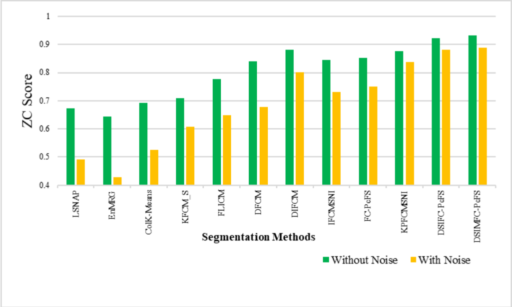

(c) DB-THY-IR

Fig. 5.5: Visual comparison of values of ZC values for images without noise and with noise (averaged over all the noise types and levels).

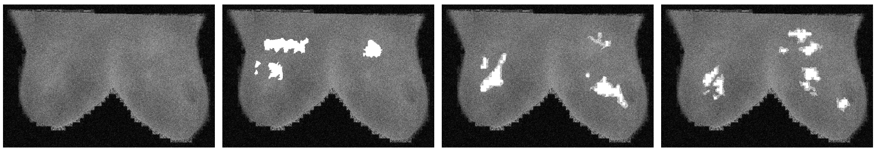

(a) Original Image (b) ColK-Means[102] (c) LSNAP[36] (d) KFCM_S[95]

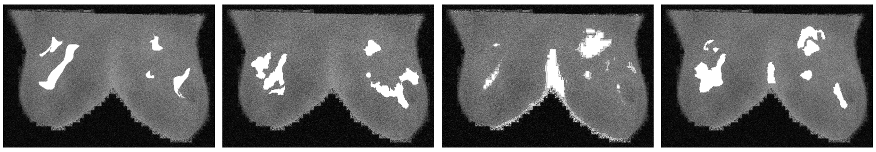

(e) FLICM[94] (f) DFCM [91] (g) DIFCM[92] (h) IFCMSNI[93]

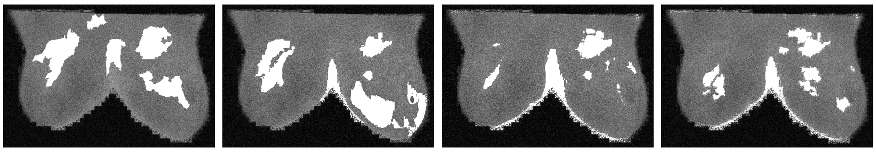

(i) FC-P_cFS[90] (j) KPFCMSNI[96] (k) DSIFC-P_cFS (l) DSIMFC-P_cFS

Fig. 5.6: Qualitative comparison of segmentation methods on abnormal thermal image corrupted with Gaussian noise (σ =1%) from DB-NOISE-IR (DMR-N2).

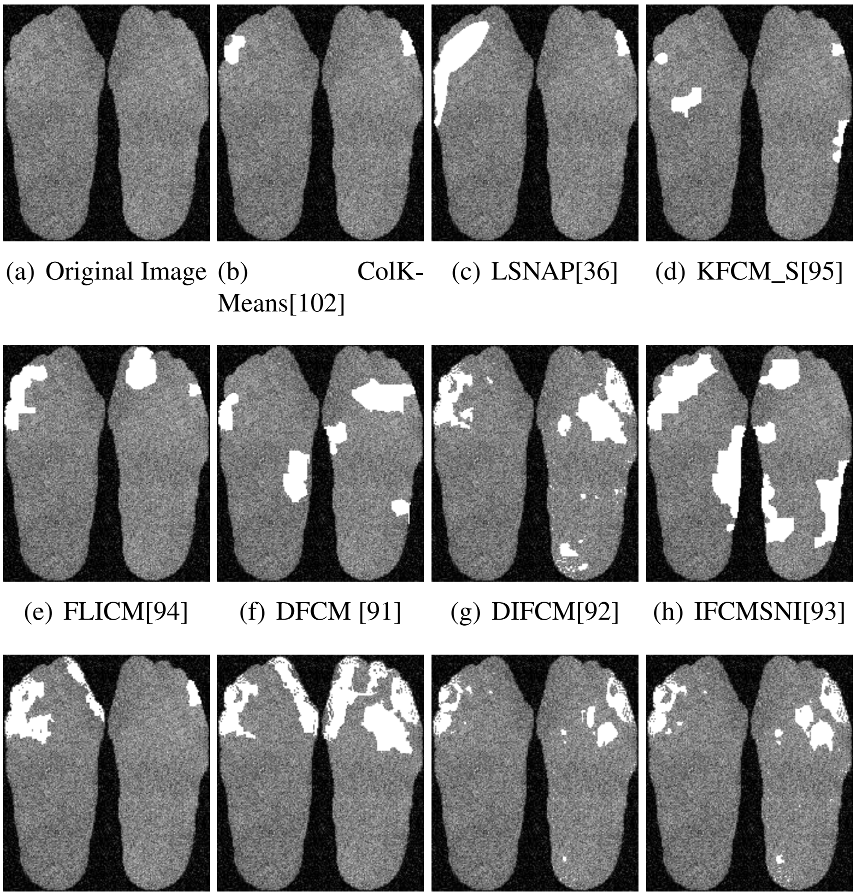

(a) Original Image (b) ColK-Means[102] (c) LSNAP[36] (d) KFCM_S[95]

(e) FLICM[94] (f) DFCM [91] (g) DIFCM[92] (h) IFCMSNI[93]

(i) FC-P_cFS[90] (j) KPFCMSNI[96] (k) DSIFC-P_cFS (l) DSIMFC-P_cFS

Fig. 5.7: Qualitative comparison of segmentation methods on abnormal thermal image corrupted with Gaussian noise (σ =1%) from DB-NOISE-IR(FOOT-N2).

Also, the relative increase in the performance (in terms of IRCM) of the proposed and related segmentation methods is analyzed for images without noise and corrupted with mixed noise. The relative increase in the performance is calculated with respect to the lowest performing method for all the datasets, that is, EnMRG[32], respectively, for without noise and with mixed noise.

Table 5.6 shows the net increment in IRCM values (in %) of images without noise and with mixed noise for all the stated segmentation methods and datasets. Figure 5.9 illustrates the ranking of the segmentation methods in terms of % increment in IRCM values (in descending order) for images without noise and with Mixed Noise. Following are observed from Table 5.6 and Figure 5.9:

- The relative improvement (in %) is maximum in the proposed approaches for segmenting thermal images without noise and with mixed noise in terms of IRCM scores.

- Though the ZC score of proposed methods over noisy images is lower than that of images without noise, but the relative increment in the ZC (in %) score (with respect to the control method) is better and more significant, especially for images corrupted with mixed noise. This significant improvement is due to the incorporation of spatial information along with modified Renyi's Entropy.

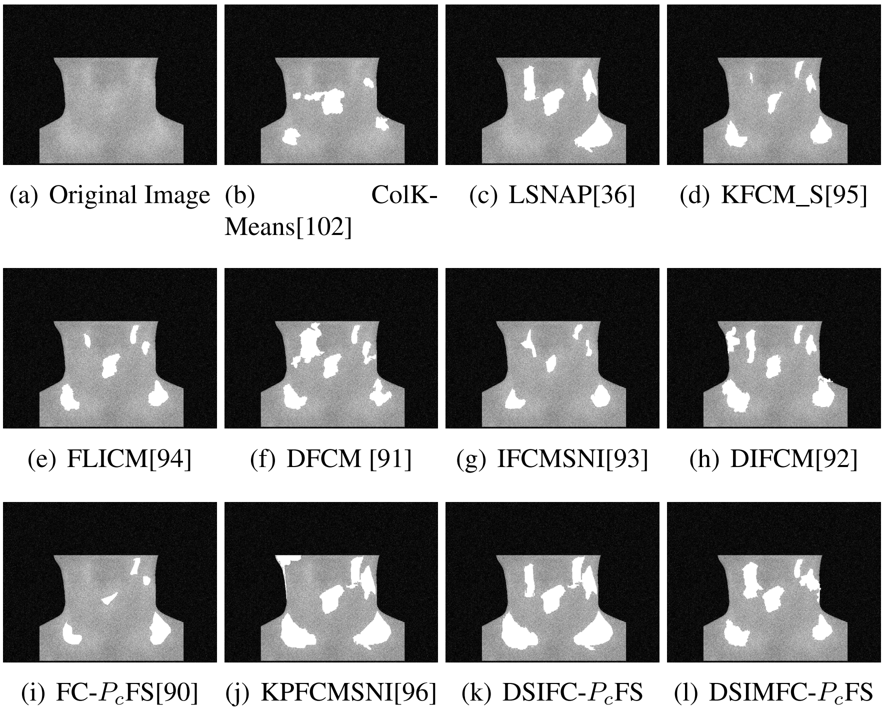
(a) Original Image (b) ColK-Means[102] (c) LSNAP[36] (d) KFCM_S[95]

(e) FLICM[94] (f) DFCM [91] (g) IFCMSNI[93] (h) DIFCM[92]

(i) FC-P_cFS[90] (j) KPFCMSNI[96] (k) DSIFC-P_cFS (l) DSIMFC-P_cFS

Fig. 5.8: Qualitative comparison of segmentation methods on abnormal thermal image corrupted with Gaussian noise (σ =1%) from DB-NOISE-IR(THY-N2).

- Density-based methods - DFCM [91], DIFCM[92], and our proposed methods have better relative percentage increments than their corresponding variants in FCM, IFCM, and FC-P_cFS, respectively, for the images corrupted with mixed noise. Also, the gain in performance of DIFCM[92] is better than that of FC-P_cFS. This shows that density-based methods are more robust than their corresponding variants.

- The relative increment in IRCM scores of LSNAP[36] and ColK-Means[102] is minimum for images with and without noise.

Table 5.6: Net increment in IRCM values(in %) of images without noise and with Mixed Noise (XXX-N5, XXX-DMR, FOOT, THY) for all the segmentation methods and all the datasets.

Segmentation Methods	**DB-DMR-IR**		**DB-FOOT-IR**		**DB-THY-IR**	
	Without Noise	**Mixed Noise (DMR-N5)**	**Without Noise**	**Mixed Noise (FOOT-N5)**	**Without Noise**	**Mixed Noise (THY-N5)**
DSIMFC-P_cFS	**52.745**	**87.764**	**73.818**	**90.554**	**58.913**	**96.674**
DSIFC-P_cFS	51.581	77.637	71.636	84.394	57.725	90.244
KPFCMSNI[96]	46.755	75.738	67.273	76.181	52.971	80.71
DIFCM[92]	42.097	71.941	63.818	69.815	50.764	78.492
FC-P_cFS[90]	38.602	67.511	63.091	69.405	47.368	76.718
IFCMSNI[93]	33.777	65.823	59.091	67.146	44.652	76.275
DFCM[91]	33.611	53.586	51.091	63.244	40.068	71.619
FLICM[94]	28.952	47.89	46.909	59.138	39.219	58.315
KFCM_S[95]	27.121	26.582	41.455	50.719	34.465	33.259
ColK-Means[102]	24.792	22.996	24.727	33.06	13.243	23.947
LSNAP[36]	15.973	8.65	8.545	7.392	3.226	5.1

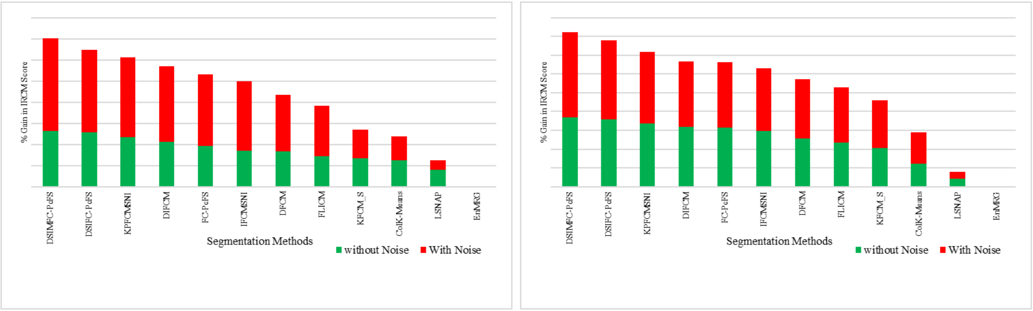

(a) DB-DMR-IR (b) DB-FOOT-IR

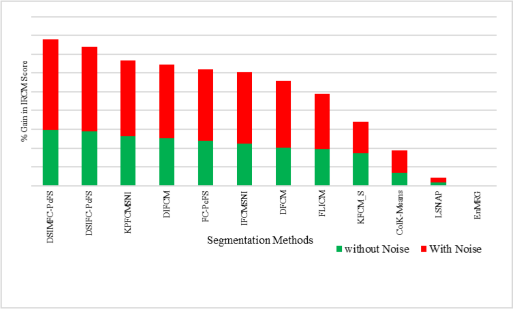

(c) DB-THY-IR

Fig. 5.9: The ranking of segmentation methods in terms of % increment in IRCM values(in descending order) for images without noise and with Mixed Noise (XXX-N5, XXX-DMR, FOOT, THY).

5.5.2 Statistical Analysis

This section introspects the performance of the framework statistically. Statistical analysis is performed using Friedman test [153], a 2-way non-parametric test, to evaluate the significant difference between the performance of proposed and related methods. The test is evaluated on the optimal value of ZC measure (among all the hyper-parameters) obtained on two randomly chosen images from fifteen subsets (XXX-Ni where XXX-DMR, FOOT, THY and i = 1...5) of DB-NOISE-IR dataset. The Null and Alternate Hypothesis, H_0 and H_1 respectively, are formulated as follows-

$$\begin{aligned} H_0: \quad & ZC_{DSIFC-P_cFS} = ZC_{DSIMFC-P_cFS} = ZC_{EnMRG} = ZC_{LSNAP} \\ & = ZC_{ColK-Means} = ZC_{KFCM\_S} = ZC_{FLICM} = ZC_{DFCM} = ZC_{DIFCM} \\ & = ZC_{IFCMSNI} = ZC_{FC-P_cFS} = ZC_{KPFCMSNI} \end{aligned} \tag{5.40}$$

$$\begin{aligned} H_1: \quad & ZC_{DSIFC-P_cFS} \neq ZC_{DSIMFC-P_cFS} \neq ZC_{EnMRG} \neq ZC_{LSNAP} \\ & \neq ZC_{ColK-Means} \neq ZC_{KFCM\_S} \neq ZC_{FLICM} \neq ZC_{DFCM} \neq ZC_{DIFCM} \\ & \neq ZC_{IFCMSNI} \neq ZC_{FC-P_cFS} \neq ZC_{KPFCMSNI} \end{aligned} \tag{5.41}$$

where H_0 indicates no significant difference between the performance of 10 methods under investigation, whereas H_1 indicates that a significant difference exists between their performances. The methods are ranked using Friedman ranking method. The average rank R_i of the i^{th} segmentation method is computed as $R_i = \frac{1}{S}\sum_{j=1}^{S} r_j^i$, $i = 1, 2, 3...T$, where r_j^i denotes rank of the i^{th} method on j^{th} thermal image in terms of ZC metric, S = 30 represents the number of images used for statistical analysis, and T=12 is the number of treatments/segmentation methods under investigation. The average Friedman ranking of all the segmentation methods is mentioned in table 5.7. Lower is the rank value, better is the segmentation method. Table 5.7 shows that the proposed methods DSIMFC-P_cFS and DSIFC-P_cFS achieve the best segmentation performance.

The Friedman statistic F is calculated using average ranking R_i (equation 5.42). With 11 degrees of freedom, *p*-value computed is 1.427E-10. This *p*-value supports the rejection of H_0 at *0.05* level of significance.

$$F = \frac{12S}{T(T+1)}\left[\sum_{i=1}^{T} R_i^2 - \frac{T(T+1)^2}{4}\right] \text{ and } F_{ID} = \frac{(S-1)F}{S(T-1)-F} \tag{5.42}$$

Table 5.7: Average ranking of the methods using Friedman method.

Segmentation Method	Ranking	Segmentation Method	Ranking
DSIMFC-P_cFS	**1.06**	**DFCM[91]**	7.01
DSIFC-P_cFS	**1.93**	**FLICM[94]**	8.01
KPFCMSNI[96]	3.02	**KFCM_S[95]**	9.0
DIFCM[92]	3.98	**ColK-Means[102]**	10.32
FC-P_cFS[90]	5.07	**LSNAP[36]**	11.03
IFCMSNI[93]	6.03	**EnMRG[32]**	12.00

The research work [154] adjusted the Friedman statistic F by proposing a new statistic - F_{ID} which is computed using equation5.42. F_{ID} is distributed according to F-distribution with 11 and 319 degrees of freedom. The p-value computed according to F-distribution is 2.61E-97. This p-value also supports the rejection of H_0 at 0.05 level of significance.

5.5.3 Computational Complexity

This subsection analyzes the time complexity of state-of-the-art and proposed segmentation methods. The time complexity for computing the Entropy Image is $O(Nw^2)$ (equation 5.7). The cost of computing density decision information is $O(N^2)$ (lines 5-9, Algorithms 2 and 3). Sorting density decision information costs $O(N \log N)$ (line 10, Algorithms 2 and 3).

Most of the computational time is spent computing the membership values μ_{pj}. In DSIFC-P_cFS (lines 17-23, Algorithm 2), the computational cost of computing matrices M, H and Ξ are $O(NCw^2)$, $O(NC)$ and $O(NC)$ and vector of cluster centers v_p, $p = 1, 2, 3...C$ is $O(NCw^2)$, respectively. Hence, the overall computational cost[1] of DSIFC-P_cFS is $O(N^2 + NCw^2T)$.

In every iteration (lines 17-23, Algorithms 3), to reduce the computational cost, we stored the vector G_p (as $C <<< N$). Then, the cost for computing a μ_{pj} is $O(Cw^2)$. Hence, the time to compute matrix M is $O(NC^2w^2)$. The computational cost of calculating the matrices H and Ξ and vector of cluster centers v_p, $p = 1, 2, 3...C$ are $O(NC)$ and $O(NCw^2)$, respectively. Thus, the overall time complexity of DSIMFC-P_cFS is $O(N^2 + NC^2w^2T)$.

Additionally, the state-of-the-art and proposed segmentation method's computational time is stated in table 5.8 for comparison in terms of an average number of

---

[1] Notations used here are same as mentioned in table 5.3

Table 5.8: Comparison of computational time of state-of-the-art and proposed segmentation methods.

Segmentation Method	Time Complexity	Average No of Iterations	Average Execution Time (with variance) (in Seconds)
EnMRG[32]	$O(Nw^2 + N^2T)$	47.23	4.17 (0.22)
LSNAP[36]	$O(N^2T)$	76.34	6.66 (0.31)
ColK-Means[102]	$O(NCT)$	91.53	3.86 (0.15)
KFCM_S[95]	$O(NCw^2T)$	53.48	5.67 (0.32)
FLICM[94]	$O(NCw^2T)$	51.42	8.61 (0.48)
DFCM [91]	$O(N^2 + NCT)$	43.69	3.97 (0.31)
DIFCM[92]	$O(N^2 + NCT)$	38.71	8.27 (0.42)
IFCMSNI[93]	$O(NCw^2T)$	68.51	13.45 (0.64)
FC-P_cFS[90]	$O(NCT)$	82.55	21.25 (0.28)
KPFCMSNI[96]	$O(NCw^2T)$	36.82	24.83 (0.66)
DSIFC-P_cFS	$O(N^2 + NCw^2T)$	**24.47**	22.79 (0.26)
DSIMFC-P_cFS	$O(N^2 + NC^2w^2T)$	**21.32**	32.64 (0.27)

iterations and execution time for the thermal images without noise for DB-DMR-IR dataset. The number of iterations and execution time are averaged over all the abnormal images in the dataset. It can be observed from the table 5.8 that the proposed methods DSIFC-P_cFS and DSIMFC-P_cFS take significantly lesser number of iterations than other state-of-the-art approaches and hence converge faster. Comparatively, the execution time is higher due to the complex computation of membership values using equations 5.32, 5.33, and 5.34.

5.6 Chapter Summary

This chapter introduces two novel density-based modified P_CFS techniques, - DSIFC-P_cFS and DSIMFC-P_cFS, for segmenting inflamed regions in abnormal thermal images. Recognizing the limitations of existing segmentation models—such as reliance on private datasets with limited samples, subjectivity in ground truth generation, and sensitivity to parameter selection—the proposed methods aim to improve robustness, accuracy, and reliability in medical thermal image analysis with regard to their segmentation. These methods are evaluated using three publicly available thermal imaging datasets, and an additional dataset with artificially introduced noise is created to assess the robustness of the models. The first model (DSIFC-P_CFS) uses a density-based heuristic to automatically determine cluster centers and membership values. Furthermore, spatial information is integrated into the model to reduce sensitivity to noise and preserve fine image structures without requiring prior smoothing. While the second model (DSIMFC-P_CFS) further refines clustering by incorporating modified Renyi's entropy to improve segmentation accuracy and optimize cluster partitions. The models are optimized using Lagrangian methods and validated on thermal imaging datasets covering diabetic foot, breast cancer, and thyroid disorders, with and without artificial noise (Gaussian, Salt & Pepper, and Mixed Noise).

The proposed segmentation frameworks are compared with ten state-of-the-art segmentation methods using MPC, BVI, UI, IRCM, and ZC. The proposed methods significantly outperformed existing techniques across all datasets, demonstrating improved segmentation of inflamed regions in medical thermal images. Also, unlike traditional approaches, which degrade in performance under noisy conditions, DSIFC-P_CFS and DSIMFC-P_CFS maintained high segmentation accuracy across all types of artificial noise. The introduction of modified Renyi's entropy in DSIMFC-P_CFS enhanced clustering stability, leading to better differentiation between normal and inflamed regions. The models demonstrated lower computational complexity and early convergence compared to existing approaches, making them feasible for real-world medical applications. Overall the findings establish a strong foundation for future research in automated thermography-based diagnostic systems, particularly for early disease detection in real-world clinical settings.

Chapter 6

Conclusion, Future Scope and Social Impact

In this thesis, we attempted classification and segmentation of medical thermal images. The following sections presents the important conclusions drawn from the proposed work. Additionally it presents the details of future works and impact of the study in society.

6.1 Conclusion

In summary, The outcomes of this study are divided in two parts. The first part addresses proposing a refined feature set comprising relevant and non-redundant features for distinguishing thermal patterns as normal/abnormal. We obtained a feature-subset of 45, 57, and 39 features (from UnionFeature_Set) for DB-DMR-IR and DB-FOOT-IR, and DB-THY-IR, that are relevant, non-redundant, and distinguishes normal and abnormal thermal patterns with an accuracy of 94.75%, 93.14%, and 92.06%, respectively. The findings establish a uniform platform-based approach for thermal pattern differentiation using machine learning, highlighting the potential of thermography as a diagnostic tool. The study addresses critical challenges in feature redundancy and dataset imbalance, offering a robust framework for future research in automated thermal image analysis, with promising applications in disease screening and early detection in clinical settings. Additionally, we developed lightweight DL-based features capable of differentiating abnormal thermal patterns from normal ones, making them suitable for deployment on mobile devices. The results indicate that DL-based feature extraction methods outperform traditional hand-crafted approaches and classification using UnionFeature_Set. The NASNet-Mobile-based feature set, when combined with SVM, yielded the highest accuracy of 99.3% for DB-DMR-IR, whereas ShuffleNet with k-NN provided the best accuracy of 93.46% for DB-FOOT-IR. However, the overall performance on DB-FOOT-IR was lower due to the limited number of available samples. The findings establish the feasibility of deploying mobile-friendly deep learning models for real-time detection of inflammation-related abnormalities, bridging the gap between medical diagnostics and accessible AI-driven healthcare solutions.

Furthermore, the second part designed a pre-processing framework and introduced two robust picture fuzzy clustering-based methods for segmenting inflamed regions from thermal images. Recognizing the limitations of existing segmentation models—such as reliance on private datasets with limited samples, subjectivity in ground truth generation, and sensitivity to parameter selection—the proposed methods aim to improve robustness, accuracy, and reliability in medical thermal image analysis. The proposed methods significantly outperformed existing techniques across all datasets, demonstrating improved segmentation of inflamed regions in medical thermal images. Also, unlike traditional approaches, which degrade in performance under noisy conditions, DSIFC-P_CFS and DSIMFC-P_CFS maintained high segmentation performance across various types of artificial noise. Also, the introduction of modified Renyi's entropy in DSIMFC-P_CFS enhanced clustering stability, leading to better differentiation between normal and inflamed regions. The models demonstrated lower computational complexity and early convergence compared to existing approaches, making them feasible for real-world medical applications. Overall the findings establish a strong foundation for future research in automated thermography-based diagnostic systems, particularly for early disease detection in real-world clinical settings.

6.2 Social Impact

The social impact of developing a framework for thermal patterns analysis for disease diagnosis is both significant and far-reaching. Thermal Imaging combined with a Computer-Integrated AI Diagnosis system bears the capability of strengthening the human health by timely cautioning about their body's physical conditions. Thermal imaging is a non-invasive, cost-effective, and contact-free diagnostic tool, making it particularly valuable in resource-limited settings. By detecting abnormalities in thermal patterns, this framework enables early diagnosis of conditions such as cancer, diabetic neuropathy, and other inflammatory diseases, ultimately reducing mortality rates and improving patient outcomes. The non-contact nature of thermal imaging also ensures better hygiene, preventing cross-contamination, especially during pandemic outbreaks.

The development of an AI-driven thermal pattern analysis framework in medicine directly and indirectly contributes to multiple United Nations SDGs by enhancing early diagnosis, healthcare accessibility, cost efficiency, and sustainability, ultimately leading to a more equitable and effective healthcare system as follows:

- **SDG 3** (***Ensure healthy lives and promote well-being for all at all ages.***) - The proposed framework directly supports SDG 3 by enabling timely interventions for diseases such as cancer, diabetes complications, and infections. Its accessibility and affordability make AI-driven thermal imaging a viable solution for improving global healthcare. Additionally, its non-invasive nature ensures patient comfort and safety.
- **SDG 9** (***Build resilient infrastructure, promote sustainable industrialization, and foster innovation.***) - Integrating AI with thermal imaging reduces reliance on manual interpretations, enhancing efficiency, accuracy, and scalability in disease diagnosis.
- **SDG 10** (***Reduce inequality within and among countries.***) - ML-powered thermal analysis provides a cost-effective diagnostic solution, reducing the financial burden on low-income individuals and ensuring healthcare accessibility in under-served communities.
- **SDG 11** (***Make cities and human settlements inclusive, safe, resilient, and sustainable.***) - AI-powered thermal screening can be deployed in public spaces to facilitate early disease detection and enhance pandemic preparedness, contributing to public health safety.
- **SDG 12** (***Ensure sustainable consumption and production patterns.***) - The framework serves as an eco-friendly alternative to traditional diagnostic methods by reducing reliance on radiation-based imaging, thus minimizing medical waste and lowering environmental hazards.

In a medical setup the proposed framework can be deployed and used in a clinical setting through:

- Usability Testing with Medical Staff: Radiologists or clinicians can assess how intuitive and efficient the system is for identifying abnormal thermal patterns. Metrics might include diagnostic accuracy, time to decision, and ease of interpreting results.
- Clinical Workflow Integration: Evaluation can involve observing how the tool fits into real diagnostic workflows—e.g., during breast cancer screening or diabetic foot monitoring—assessing whether it supports or disrupts routine practice.
- Feedback from End Users: Structured interviews or surveys can capture feedback from both clinicians and, where appropriate, patients, regarding trust in the system, perceived usefulness, and ease of understanding outputs.
- Clinical Validation Studies: Comparative studies where thermal imaging results are evaluated against gold standards (e.g., biopsy or MRI) in real patient cases, with clinician involvement, can validate both accuracy and practical relevance.

The Computer-Integrated AI Diagnosis system with DITI makes a lasting contribution to public health and well-being by promoting innovation, reducing environmental impact, and supporting global health infrastructure.

6.3 Future Scope

The methods developed in this thesis represent a significant advancement in the field of Computer-Integrated AI Diagnosis system using Thermography. However, as with any research endeavor, there are numerous opportunities for further exploration, enhancement, and deployment. Below are several key directions for future work:

- A standardized, large-scale dataset with ground truth for segmentation is currently unavailable. Future work will focus on developing such a dataset, encompassing diverse abnormalities, to facilitate bench-marking and improve classification and segmentation models using deep learning.
- While the current methods perform robustly, further enhancements are needed to improve computational speed and efficiency without sacrificing accuracy. Research will explore hardware acceleration, algorithmic refinements, and parallel processing techniques.

- In view of the societal impact, efforts will focus on integrating the developed models into a single framework for deployment in public spaces. Testing in areas such as urban planning, environmental monitoring, and public health will help quantify benefits and identify areas for improvement.
- Future research will investigate advanced methodologies, including quantum computing, Generative Adversarial Networks (GANs), and novel machine learning paradigms. These approaches could lead to breakthroughs in handling complex, noisy environments and enhancing AI-driven thermographic diagnosis.
- In future, the work may be expanded upon building the concept of multimodal analysis, beyond the initial framework to create an even more robust and comprehensive diagnostic system. The integration of visual and depth images will be a key step, providing a richer visual and spatial understanding of the subject. This visual data, USG images, MRI images, etc. will be fused with thermal data to move beyond isolated findings and build a holistic, patient-centric view.

By tackling these challenges, future research will not only improve existing methods for the Computer-Integrated AI Diagnosis system using Thermography but also drive groundbreaking innovations in thermal imaging. This will lead to safer, smarter, and more efficient technologies across various thermography applications.

References

[1] S. P. Power, F. Moloney, M. Twomey, K. James, O. J. O'Connor, and M. M. Maher, "Computed Tomography and Patient Risk: Facts, Perceptions and Uncertainties," *World Journal of Radiology*, Vol. 8, No. 12, pp. 902, 2016.

[2] U. R. Acharya, E. Y. K. Ng, J. H. Tan, and S. V. Sree, "Thermography Based Breast Cancer Detection Using Texture Features and Support Vector Machine," *Journal of Medical Systems*, Vol. 36, No. 3, pp. 1503– 1510, 2012.

[3] K. Khaksari, T. Nguyen, B. Y. Hill, T. Quang, J. Perrault, V. Gorti, R. Malpani, E. Blick, T. G. Cano, and B. Shadgan, "Review of the Efficacy of Infrared Thermography for Screening Infectious Diseases with Applications to Covid-19," *Journal of Medical Imaging*, Vol. 8, No. S1, pp. 010901, 2021.

[4] V. O. Silvino, R. B. B. Gomes, S. L. G. Ribeiro, D. De Lima Moreira, and M. A. P. Dos Santos, "Identifying Febrile Humans Using Infrared Thermography Screening: Possible Applications During Covid-19 Outbreak," *Revista Contexto & Saúde*, Vol. 20, No. 38, pp. 5–9, 2020.

[5] M. R. Canales-Fiscal, R. O. López, R. Barzilay, V. Treviño, S. Cardona-Huerta, L. J. Ramírez-Treviño, A. Yala, and J. Tamez-Peña, "Covid-19lassification Using Thermal Images: Thermal Images Capability for Identifying Covid-19 Using Traditional Machine Learning Classifiers," in *Proceedings of the 12th ACM Conference on Bioinformatics, Computational Biology, and Health Informatics,* Florida, August 1 - 4, 2021, pp. 1–5.

[6] R. Y. Brzezinski, N. Rabin, N. Lewis, R. Peled, A. Kerpel, A. M. Tsur, O. Gendelman, N. Naftali-Shani, I. Gringauz, and H. Amital, “Automated Processing of Thermal Imaging to Detect Covid-19,” *Scientific Reports*, Vol. 11, No. 1, pp. 17489, 2021.

[7] J. Stefan and K.-K. H. Und Staatsdruckerie, Über Die Beziehung Zwischen Der Wärmestrahlung Und Der Temperatur. *Aus Der Kk Hof-Und Staatsdruckerei*, 1879.

[8] L. Boltzmann, Ableitung Des Stefanschen Gesetzes, 1) Betreffend Die Abhängigkeit Der Wärmestrahlung Von Der Temperatur, *Aus Der Elektromagnetischen Lichttheorie*, Springer, 1978.

[9] H. Usuki, T. Ikeda, Y. Igarashi, I. Takahashi, A. Fukami, T. Yokoe, H. Sonoo, and K. Asaishi, “What Kinds of Non-Palpable Breast Cancer can be Detected by Thermography?”, *Biomedical Thermology*, Vol. 4, No. 18, pp. 8–12, 1998.

[10] E. Ingelsson, J. Årnlöv, J. Sundström, and L. Lind, “Inflammation, as Measured by the Erythrocyte Sedimentation Rate, is an Independent Predictor for the Development of Heart Failure,” *Journal of the American College of Cardiology*, Vol. 45, No. 11, pp. 1802–1806, 2005.

[11] V. A. Van Atteveld, J. M. Van Ancum, E. M. Reijnierse, M. C. Trappenburg, C. G. Meskers, and A. B. Maier, “Erythrocyte Sedimentation Rate and Albumin as Markers of Inflammation are Associated with Measures of Sarcopenia: A Cross-Sectional Study,” *BMC Geriatrics*, Vol. 19, No. 1, pp. 1–8, 2019.

[12] B. Can, O. Kara, M. C. Kizilarslanoglu, G. Arik, G. S. Aycicek, F. Sumer, R. Civelek, C. Demirtas, and Z. Ulger, “Serum Markers of Inflammation and Oxidative Stress in Sarcopenia,” *Aging Clinical and Experimental Research*, Vol. 2 9, No. 4, pp. 745–752, 2017.

[13] S. Bardhan, M. K. Bhowmik, S. Nath, and D. Bhattacharjee, “A Review on Inflammatory Pain Detection in Human Body Through Infrared Image Analysis,” in *2015 International Symposium on Advanced Computing and Communication (ISACC)*, 2015, pp. 251–257.

[14] L. N. Ko, A. B. Raff, A. C. Garza-Mayers, A. S. Dobry, A. Ortega-Martinez, R. R. Anderson, and D. Kroshinsky, “Skin Surface Temperatures Measured

by Thermal Imaging Aid in the Diagnosis of Cellulitis," *Journal of Investigative Dermatology*, Vol. 138, No. 3, pp. 520–526, 2018.

[15] S. Bardhan and M. K. Bhowmik, "2-Stage Classification of Knee Joint Thermograms for Rheumatoid Arthritis Prediction in Subclinical Inflammation," *Australasian Physical & Engineering Sciences in Medicine*, Vol. 42, No. 1, pp. 259– 277, 2019.

[16] N. A. Diakides and J. D. Bronzino, Medical Infrared Imaging. *CRC Press*, 2007.

[17] L. N. Ko, A. B. Raff, A. C. Garza-Mayers, A. S. Dobry, A. Ortega-Martinez, R. R. Anderson, and D. Kroshinsky, "Skin Surface Temperatures Measured by Thermal Imaging Aid in the Diagnosis of Cellulitis," *Journal of Investigative Dermatology*, Vol. 138, No. 3, pp. 520–526, 2018.

[18] O. Faust, U. R. Acharya, E. Ng, T. J. Hong, and W. Yu, "Application of Infrared Thermography in Computer Aided Diagnosis," *Infrared Physics & Technology*, Vol. 66, pp. 160–175, 2014.

[19] J. I. Priego Quesada, M. R. Kunzler, and F. P. Carpes, "Methodological Aspects of Infrared Thermography in Human Assessment," in *Application of Infrared Thermography in Sports Science*, Springer, 2017, pp. 49–79.

[20] L. Silva, D. Saade, G. Sequeiros, A. Silva, A. Paiva, R. Bravo, and A. Conci, "A New Database for Breast Research with Infrared Image," *Journal of Medical Imaging and Health Informatics*, Vol. 4, No. 1, pp. 92–100, 2014.

[21] D. A. H. Contreras, H. Peregrina-Barreto, J. Rangel-Magdaleno, and F. J. Renero Carrillo, "Plantar Thermogram Database for the Study of Diabetic Foot Complications,", *IEEE Access*, Vol. *7*, pp. 161296-161307, 2019.

[22] J. R. González, C. Damião, and A. Conci, "An Infrared Thermal Images Database and a New Technique for Thyroid Nodules Analysis," *Studies in Health Technology and Informatics*, Vol. 245, pp. 384—387, 2017.

[23] G. Schaefer, M. Závišek, and T. Nakashima, "Thermography Based Breast Cancer Analysis Using Statistical Features and Fuzzy Classification," *Pattern Recognition*, Vol. 42, No. 6, pp. 1133–1137, 2009.

[24] R. Rastghalam and H. Pourghassem, "Breast Cancer Detection Using MRF-

Based Probable Texture Feature and Decision-Level Fusion-Based Classification Using HMM on Thermography Images," *Pattern Recognition*, Vol. 51, No. 1, pp. 176–186, 2016.

[25] D. Sathish, S. Kamath, K. Prasad, and R. Kadavigere, "Role of Normalization of Breast Thermogram Images and Automatic Classification of Breast Cancer," *The Visual Computer*, Vol. 35, No. 1, pp. 57–70, 2019.

[26] I. Cruz-Vega, H. Peregrina-Barreto, J. De Jesus Rangel-Magdaleno, and J. M. Ramirez-Cortes, "A Comparison of Intelligent Classifiers of Thermal Patterns in Diabetic Foot," in *2019 IEEE International Instrumentation and Measurement Technology Conference (I2MTC)*. Auckland, New Zealand: IEEE, 20-23 May 2019, pp. 1–6.

[27] J. Saminathan, M. Sasikala, V. Narayanamurthy, K. Rajesh, and R. Arvind, "Computer Aided Detection of Diabetic Foot Ulcer Using Asymmetry Analysis of Texture and Temperature Features," *Infrared Physics & Technology*, Vol. 105, pp. 103219, 2020.

[28] R. Karthiga and K. Narasimhan, "Medical Imaging Technique Using Curvelet Transform and Machine Learning for the Automated Diagnosis of Breast Cancer from Thermal Image," *Pattern Analysis and Applications*, Vol. 24, pp. 981—-991, 2021.

[29] U. Snekhalatha, M. Anburajan, T. Teena, B. Venkatraman, M. Menaka, and B. Raj, "Thermal Image Analysis and Segmentation of Hand in Evaluation of Rheumatoid Arthritis," in *2012 International Conference on Computer Communication and Informatics*. Coimbatore, India: IEEE, 10-12 January 2012, pp. 1–6.

[30] S. Pramanik, D. Banik, D. Bhattacharjee, M. Nasipuri, M. K. Bhowmik, and G. Majumdar, "Suspicious-Region Segmentation from Breast Thermogram Using DLPE-Based Level Set Method," *IEEE Transactions on Medical Imaging*, Vol. 38, No. 2, pp. 572–584, 2018.

[31] K. Das, M. K. Bhowmik, and D. P. Mukherjee, "Segmentation of Knee Thermograms for Detecting Inflammation," in *2019 IEEE International Conference on Image Processing (ICIP)*. Taipei, Taiwan: IEEE, 22-25 September 2019, pp. 1550–1554.

[32] M. K. Bhowmik, K. Das, and D. Bhattacharjee, "Temperature Profile Guided Segmentation for Detection of Early Subclinical Inflammation in Arthritis

Knee Joints from Thermal Images," *Infrared Physics & Technology*, Vol. 99, pp. 102–112, 2019.

[33] S. Bardhan, M. K. Bhowmik, T. Debnath, and D. Bhattacharjee, "RASIT: Region Shrinking Based Accurate Segmentation of Inflammatory Areas from Thermograms," *Biocybernetics and Biomedical Engineering*, Vol. 38, No. 4, pp. 903–917, 2018.

[34] F. Bahramian and A. Mojra, "Thyroid Cancer Estimation Using Infrared Thermography Data," *Infrared Physics & Technology*, Vol. 104, pp. 103126, 2020.

[35] R. M. Prakash, K. Bhuvaneshwari, M. Divya, K. J. Sri, and A. S. Begum, "Segmentation of Thermal Infrared Breast Images Using K-Means, and EM Algorithms for Breast Cancer Detection," in *2017 International Conference on Innovations in Information, Embedded and Communication Systems (ICIIECS)*. Coimbatore, India: IEEE, 17-18 March 2017, pp. 1–4.

[36] M. Etehadtavakol, Z. Emrani, and E. Y. K. Ng, "Rapid Extraction of the Hottest or Coldest Regions of Medical Thermographic Images," *Medical & Biological Engineering & Computing*, Vol. 57, No. 2, pp. 379–388, 2019.

[37] H. W. Kuhn and A. W. Tucker, "Nonlinear Programming," in *Proceedings of the Second Berkeley Symposium on Mathematical Statistics and Probability*, 1950. Berkeley and Los Angeles: University of California Press, 1951, pp. 481–492.

[38] T. Gupta, R. Agrawal, R. Sangal, and S. A. Rao, "Performance Evaluation of Thermography-Based Computer-Aided Diagnostic Systems for Detecting Breast Cancer: an Empirical Study," *ACM Transactions on Computing for Healthcare*, Vol. 5, No. 4, pp. 1–30, 2024.

[39] E. Y. Ng and M. Etehadtavakol, Application of Infrared to Biomedical Sciences. *Springer*, 2017.

[40] T. B. Borchartt, A. Conci, R. C. Lima, R. Resmini, and A. Sanchez, "Breast Thermography from an Image Processing Viewpoint: a Survey," *Signal Processing*, Vol. 93, No. 10, pp. 2785 – 2803, 2013,

[41] S. Bagavathiappan, J. Philip, T. Jayakumar, B. Raj, P. Rao, M. Varalakshmi, and V. V. Mohan, "Correlation Between Plantar Foot Temperature and Diabetic Neuropathy: a Case Study by Using an Infrared Thermal Imaging

Technique," *Journal of Diabetes Science Technology*, pp. 1386–1392, 2010.

[42] R. Vardasca, C. Magalhaes, and J. Mendes, "Biomedical Applications of Infrared Thermal Imaging: Current State of Machine Learning Classification," in *Multidisciplinary Digital Publishing Institute Proceedings*, Vol. 27, No. 1. Firenze, Italy: MDPI, 17-19 September 2019, pp. 46.

[43] M. A. Saleh, "Enhancing Musculoskeletal Healthcare Through Mobile Application-Integrated Infrared Thermography: A Promising Approach for Diagnosis and Monitoring,", *TRIDHA: Journal of Clinical Cases & Reports*, Vol. 2024, No. 3, pp. 117-128, 2024.

[44] R. Lawson, "Implications of Surface Temperatures in the Diagnosis of Breast Cancer." *Canadian Medical Association Journal,* Vol. 75, No. 4, pp. 309–310, 1956.

[45] O. Beahrs, "Report to the Working Group to Review the National Cancer Institute American Cancer Society Breast Cancer Demonstration Projects," *Journal of National Cancer Institute*, Vol. 62, pp. 639–709, 1979.

[46] M. Gautherie, "Thermo-Biological Assessment of Benign and Malignant Breast Diseases," *American Journal of Obstetrics and Gynecology*, Vol. 147, No. 8, pp. 861– 869, 1983.

[47] M. Etehadtavakol, E. Y. Ng, and M. H. Emami, "Potential of Infrared Imaging in Assessing Digestive Disorders," *Application of Infrared to Biomedical Sciences*, Springer, 2017, pp. 1–18.

[48] M. Etehadtavakol and E. Y. Ng, "Potential of Thermography in Pain Diagnosing and Treatment Monitoring," *Application of Infrared to Biomedical Sciences*, Springer, 2017, pp. 19–32.

[49] V. A. S. Vaz, "Diagnosis of Hypo and Hyperthyroid Using MLPN Network," I*nternational Journal of Innovative Research in Science, Engineering and Technology*, Vol. 3, No. 7, pp. 14 314–14 323, 2014.

[50] P. Mahajan and S. Madhe, "Hypo and Hyperthyroid Disorder Detection from Thermal Images Using Bayesian Classifier," *2014 International Conference on Advances in Communication and Computing Technologies (ICACACT 2014)*. Mumbai, India: IEEE, 10-11 August 2014, pp. 1–4.

[51] P. C. Sun, H.-D. Lin, S.-H. E. Jao, Y.-C. Ku, R.-C. Chan, and C.-K. Cheng,

"Relationship of Skin Temperature to Sympathetic Dysfunction in Diabetic At-Risk Feet," *Diabetes Research and Clinical Practice*, Vol. 73, No. 1, pp. 41–46, 2006.

[52] R. M. Stess, P. C. Sisney, K. M. Moss, P. M. Graf, K. S. Louie, G. A. Gooding, and C. Grunfeld, "Use of Liquid Crystal Thermography in the Evaluation of the Diabetic Foot," *Diabetes Care*, Vol. 9, No. 3, pp. 267– 272, 1986.

[53] D. G. Armstrong, K. Holtz-Neiderer, C. Wendel, M. J. Mohler, H. R. Kimbriel, and L. A. Lavery, "Skin Temperature Monitoring Reduces the Risk for Diabetic Foot Ulceration in High-Risk Patients*," The American Journal of Medicine*, Vol. 120, No. 12, pp. 1042–1046, 2007.

[54] L. A. Lavery, K. R. Higgins, D. R. Lanctot, G. P. Constantinides, R. G. Zamorano, K. A. Athanasiou, D. G. Armstrong, and C. M. Agrawal, "Preventing Diabetic Foot Ulcer Recurrence in High-Risk Patients: Use of Temperature Monitoring as a Self-Assessment Tool," *Diabetes Care*, Vol. 30, No. 1, pp. 14–20, 2007.

[55] H. Qi, P. T. Kuruganti, and W. E. Snyder, "Detecting Breast Cancer from Thermal Infrared Images by Asymmetry Analysis," *Medical Infrared Imaging*, Vol. 38, 2007.

[56] U. R. Gogoi, M. K. Bhowmik, A. K. Ghosh, D. Bhattacharjee, and G. Majumdar, "Discriminative Feature Selection for Breast Abnormality Detection and Accurate Classification of Thermograms," in *2017 International Conference on Innovations in Electronics, Signal Processing and Communication (IESC)*. Shillong, India: IEEE, 06-07 April 2017, pp. 39–44.

[57] S. V. Francis, M. Sasikala, and S. Saranya, "Detection of Breast Abnormality from Thermograms Using Curvelet Transform Based Feature Extraction," *Journal of Medical Systems*, Vol. 38, No. 4, pp. 23, 2014.

[58] M. Aweda, A. Adeyomoye, and G. Abe, "Thermographic Analysis of Thyroid Diseases," *Adv. Appl. Sci. Res*, Vol. 3, No. 4, pp. 2027–2032, 2012.

[59] G. Serbu, "Infrared Imaging of the Diabetic Foot," Proceedings on Information, *Romanian Society of Thermography*, 2009, pp. 5–20.

[60] M. Adam, E. Y. Ng, S. L. Oh, M. L. Heng, Y. Hagiwara, J. H. Tan, J. W.

Tong, and U. R. Acharya, “Automated Detection of Diabetic Foot with and Without Neuropathy Using Double Density-Dual Tree-Complex Wavelet Transform on Foot Thermograms,” *Infrared Physics & Technology*, Vol. 92, pp. 270–279, 2018.

[61] K. Pafili and N. Papanas, “Thermography in the Follow Up of the Diabetic Foot: Best to Weigh the Enemy More Mighty Than He Seems,” 2015. *Expert Review of Medical Devices*, Vol. 12, No. 2, pp. 131-133.

[62] G. Machin, A. Whittam, S. Ainarkar, J. Allen, J. Bevans, M. Edmonds, B. Kluwe, A. Macdonald, N. Petrova and P. Plassmann, “A Medical Thermal Imaging Device for the Prevention of Diabetic Foot Ulceration,” *Physiological Measurement*, Vol. 38, No. 3, pp. 420, 2017.

[63] J. Singh, B. Pandey, S. Karna, A. S. Arora, and A. Kumar, “Enhancing the Thermographic Diagnosis of Maxillary Sinusitis Using Deep Learning Approach,” *Quantitative Infrared Thermography Journal*, pp. 1–15, 2024.

[64] E. A. Mohamed, E. A. Rashed, T. Gaber, and O. Karam, “Deep Learning Model for Fully Automated Breast Cancer Detection System from Thermograms,” *PLOS One*, Vol. 17, No. 1, pp. E0262349, 2022.

[65] N. Dharani, I. Govardhini Immadi, and M. V. Narayana, “Enhanced Deep Learning Model for Diagnosing Breast Cancer Using Thermal Images,” *Soft Computing*, Vol. 28, No. 13, pp. 8423–8434, 2024.

[66] A. Özdil and B. Yilmaz, “Medical Infrared Thermal Image Based Fatty Liver Classification Using Machine and Deep Learning,” *Quantitative Infrared Thermography Journal*, Vol. 21, No. 2, pp. 102–119, 2024.

[67] R. K. Ahalya and U. Snekhalatha, “CNN Transformer for the Automated Detection of Rheumatoid Arthritis in Hand Thermal Images,” in *Artificial Intelligence over Infrared Images for Medical Applications*, Springer Nature Switzerland, November 9, 2024, pp. 23–32.

[68] R. Basiri, K. Manji, P. M. Lelievre, J. Toole, F. Kim, S. S. Khan, and M. R. Popovic, “Protocol for Metadata and Image Collection at Diabetic Foot Ulcer Clinics: Enabling Research in Wound Analytics and Deep Learning,” *Biomedical Engineering*, Vol. 23, No. 1, pp. 12, 2024.

[69] S. Civilibal, K. K. Cevik, and A. Bozkurt, “A Deep Learning Approach for Automatic Detection, Segmentation and Classification of Breast Lesions from

Thermal Images," *Expert Systems with Applications*, Vol. 212, pp. 118774, 2023.

[70] H. Ghayoumi Zadeh, A. Fayazi, B. Binazir, and M. Yargholi, "Breast Cancer Diagnosis Based on Feature Extraction Using Dynamic Models of Thermal Imaging and Deep Autoencoder Neural Networks," *Journal of Testing and Evaluation*, Vol. 49, No. 3, pp. 1516–1532, 2021.

[71] M. Ensafi, M. R. Keyvanpour, and S. V. Shojaedini, "A New Method for Promote the Performance of Deep Learning Paradigm in Diagnosing Breast Cancer: Improving Role of Fusing Multiple Views of Thermography Images," *Health and Technology*, Vol. 12, No. 6, pp. 1097–1107, 2022.

[72] S. Chatterjee, S. Biswas, A. Majee, S. Sen, D. Oliva, and R. Sarkar, "Breast Cancer Detection from Thermal Images Using a Grunwald-Letnikov-Aided Dragon-Fly Algorithm-Based Deep Feature Selection Method," *Computers in Biology and Medicine*, Vol. 141, pp. 105027, 2022.

[73] E. H. Houssein, M. M. Emam, and A. A. Ali, "An Efficient Multilevel Thresholding Segmentation Method for Thermography Breast Cancer Imaging Based on Improved Chimp Optimization Algorithm," *Expert Systems with Applications*, Vol. 185, pp. 115651, 2021.

[74] S. Pare, A. Kumar, G. K. Singh, and V. Bajaj, "Image Segmentation Using Multi-Level Thresholding: a Research Review," *Iranian Journal of Science and Technology, Transactions of Electrical Engineering*, Vol. 44, No. 1.

[75] N. Shrivastava and J. Bharti, "Automatic Seeded Region Growing Image Segmentation for Medical Image Segmentation: A Brief Review," *International Journal of Image and Graphics*, Vol. 20, No. 03, pp. 2050018, 2020.

[76] P. Ge, Y. Chen, G. Wang, and G. Weng, "An Active Contour Model Driven by Adaptive Local Pre-Fitting Energy Function Based on Jeffreys Divergence for Image Segmentation," *Expert Systems with Applications*, Vol. 210, pp. 118493, 2022.

[77] N. Dhanachandra and Y. J. Chanu, "A Survey on Image Segmentation Methods Using Clustering Techniques," *European Journal of Engineering and Technology Research*, Vol. 2, No. 1, pp. 15–20, 2017.

[78] D. S. Manoharan, "Performance Analysis of Clustering Based Image

Segmentation Techniques," *Journal of Innovative Image Processing*, Vol. 2, No. 1, pp. 14–24, 2020.

[79] H. Mittal, A. C. Pandey, M. Saraswat, S. Kumar, R. Pal, and G. Modwel, "A Comprehensive Survey of Image Segmentation: Clustering Methods, Performance Parameters, and Benchmark Datasets," *Multimedia Tools and Applications*, Vol. 81, No. 24, pp. 1–26, 2021.

[80] A. Kumar and S. K. Jain, "Deformable Models for Image Segmentation: A Critical Review of Achievements and Future Challenges," *Computers & Mathematics with Applications*, Vol. 119, pp. 288–311, 2022.

[81] H. Yu, Z. Yang, L. Tan, Y. Wang, W. Sun, M. Sun, and Y. Tang, "Methods and Datasets on Semantic Segmentation: A Review," *Neurocomputing*, Vol. 304, pp. 82–103, 2018.

[82] S. Hao, Y. Zhou, and Y. Guo, "A Brief Survey on Semantic Segmentation with Deep Learning," *Neurocomputing*, Vol. 406, pp. 302– 321, 2020.

[83] H. Lohit and D. Kumar, "Modified Total Bregman Divergence Driven Picture Fuzzy Clustering with Local Information for Brain MRI Image Segmentation," *Applied Soft Computing*, Vol. 144, pp. 110460, 2023.

[84] J. A. Hartigan and M. A. Wong, "A K-Means Clustering Algorithm," *Applied Statistics*, Vol. 28, No. 1, pp. 100–108, 1979.

[85] L. Zadeh, "Fuzzy Sets," *Information and Control*, Vol. 8, No. 3, pp. 338–353, 1965.

[86] J. C. Bezdek, "Objective Function Clustering," *Pattern Recognition with Fuzzy Objective Function Algorithms*, pp. 43–93, 1981.

[87] Z. Xu and J. Wu, "Intuitionistic Fuzzy C-Means Clustering Algorithms," *Journal of Systems Engineering and Electronics*, Vol. 21, No. 4, pp. 580–590, 2010.

[88] B. C. Cuong and V. Kreinovich, "Picture Fuzzy Sets," *Journal of Computer Science and Cybernetics*, Vol. 30, No. 4, pp. 409–420, 2014.

[89] L. H. Son, "DPFCM: a Novel Distributed Picture Fuzzy Clustering Method on Picture Fuzzy Sets," *Expert Systems with Applications*, Vol. 42, No. 1, pp. 51–66, 2015.

[90] P. H. Thong and L. H. Son, “Picture Fuzzy Clustering: a New Computational Intelligence Method,” *Soft Computing*, Vol. 20, No. 9, pp. 3549–3562, 2016.

[91] H.-X. Pei, Z.-R. Zheng, C. Wang, C.-N. Li, and Y.-H. Shao, “D-FCM: Density Based Fuzzy C-Means Clustering Algorithm with Application in Medical Image Segmentation,” *Procedia Computer Science*, Vol. 122, No. 1, pp. 407–414, 2017.

[92] A. K. Varshney, P. K. Muhuri, and Q. D. Lohani, “Density-Based IFCM Along with Its Interval Valued and Probabilistic Extensions, and a Review of Intuitionistic Fuzzy Clustering Methods,” *Artificial Intelligence Review*, Vol. 56, No. 1, pp. 3755–3795, 2022.

[93] D. Kumar, R. K. Agrawal, and J. S. Kirar, “Intuitionistic Fuzzy Clustering Method with Spatial Information for MRI Image Segmentation,” in *2019 IEEE International Conference on Fuzzy Systems (FUZZ-IEEE)*. New Orleans, LA, USA: IEEE, 23- 26 June 2019, pp. 1–7.

[94] S. Krinidis and V. Chatzis, “A Robust Fuzzy Local Information C-Means Clustering Algorithm,” *IEEE Transactions on Image Processing*, Vol. 19, No. 5, pp. 1328– 1337, 2010.

[95] S. Chen and D. Zhang, “Robust Image Segmentation Using FCM with Spatial Constraints Based on New Kernel-Induced Distance Measure,” *IEEE Transactions on Systems, Man, and Cybernetics*, Part B (Cybernetics), Vol. 34, No. 4, pp. 1907– 1916, 2004.

[96] D. Kumar, I. Khatri, A. Gupta, and R. Gusain, “Kernel Picture Fuzzy Clustering with Spatial Neighborhood Information for MRI Image Segmentation.” *Soft Computing*, Vol. 26, No. 22, pp. 12717–12740, 2022.

[97] U. R. Gogoi, M. K. Bhowmik, and G. Majumdar, “MMSHRS: a Morphology Model of Suspicious Hyperthermic Regions for Degree of Severity Prediction from Breast Thermograms,” *Quantitative Infrared Thermography Journal*, Vol. 20, No. 4, pp. 1–25, 2022.

[98] K. Das, M. K. Bhowmik, O. Chowdhuary, D. Bhattacharjee, and B. K. De, “Accurate Segmentation of Inflammatory and Abnormal Regions Using Medical Thermal Imagery,” *Australasian Physical & Engineering Sciences in Medicine*, Vol. 42, pp. 647–657, 2019.

[99] M. Etehadtavakol, E. Y. Ng, and N. Kaabouch, “Automatic Segmentation of Thermal Images of Diabetic-At-Risk Feet Using the Snakes Algorithm,” *Infrared Physics & Technology*, Vol. 86, pp. 66–76, 2017.

[100] M. Etehadtavakol, S. Sadri, and E. Ng, “Application of K-And Fuzzy C-Means for Color Segmentation of Thermal Infrared Breast Images,” *Journal of Medical Systems*, Vol. 34, pp. 35–42, 2010.

[101] N. Mir, U. Snekhalatha, M. Khan, and Y. Choden, “Thermal Image Segmentation of Facial Thermograms Using K-Means Algorithm in Evaluation of Orofacial Pain,” in *Proceedings of the International Conference on ISMAC in Computational Vision and Bio-Engineering 2018 (ISMAC-CVB)*, Palladam, India: Springer, 16- 17 May, 2018 2019, pp. 565–572.

[102] R. Ahalya, U. Snekhalatha, and V. Dhanraj, “Automated Segmentation and Classification of Hand Thermal Images in Rheumatoid Arthritis Using Machine Learning Algorithms: A Comparison with Quantum Machine Learning Technique,” *Journal of Thermal Biology*, Vol. 111, pp. 103404, 2023.

[103] A. S. Hakim and R. Awale, “Extraction of Hottest Blood Vessels from Breast Thermograms Using State-Of-The-Art Image Segmentation Methods,” *Quantitative Infrared Thermography Journal*, Vol. 19, No. 5, pp. 347–365, 2022.

[104] T. Tirupal, B. C. Mohan, and S. S. Kumar, “Multimodal Medical Image Fusion Techniques – A Review,” *Current Signal Transduction Therapy*, Vol. 16, No. 2, pp. 142–163, 2021.

[105] C. H. Hsu, C. Pandeeswaran, E. Jesi, And R. Thilahar, “Multi-Modal Fusion in Thermal Imaging and MRI for Early Cancer Detection,” *Journal of Thermal Biology*, Vol. 129, pp. 104090, 2025.

[106] N. Zhang, J. Liu, Y. Jin, W. Duan, Z. Wu, Z. Cai, And M. Wu, “An Adaptive Multimodal Hybrid Model for Classifying Thyroid Nodules by Combining Ultrasound and Infrared Thermal Images,” BMC Bioinformatics, Vol. 24, No. 1, pp. 315, 2023.

[107] C. Li, P. Wang, M. Zheng, W. Li, J. Zhou, And L. Fu, “One-Stop Multi-Sensor Fusion and Multimodal Precise Quantified Traditional Chinese

Medicine Imaging Health Examination Technology," *Journal of Radiation Research and Applied Sciences*, Vol. 17, No. 4, pp. 101038, 2024.

[108] J. Ma, C. Chen, C. Li, And J. Huang, "Infrared and Visible Image Fusion Via Gradient Transfer and Total Variation Minimization," *Information Fusion*, Vol. 31, pp. 100–109, 2016.

[109] T. Gupta, R. Jindal, and S. Indu, "Empirical Analysis of Thermography Effectiveness for Health Diagnosis," in *2020 International Conference on Computational Science and Computational Intelligence (CSCI)*, Las Vegas, NV, USA: IEEE, 16-18 December 2020, pp. 830–835.

[110] R. M. Haralick, K. Shanmugam, and I. H. Dinstein, "Textural Features for Image Classification," *IEEE Transactions on Systems, Man, and Cybernetics*, Vol. 3, No. 6, pp. 610–621, 1973.

[111] K. Pearson, "Notes on the History of Correlation," *Biometrika*, Vol. 13, No. 1, pp. 25–45, 10 1920.

[112] H. Liu and R. Setiono, "Chi2: Feature Selection and Discretization of Numeric Attributes," in *Proceedings of 7th IEEE International Conference on Tools with Artificial Intelligence*, Herndon, VA, USA: IEEE, 05-08 November 1995, pp. 388–391.

[113] I. Kononenko, "Estimating Attributes: Analysis and Extensions of Relief," in *European Conference on Machine Learning*, Catania, Italy: Springer, April 6-8, 1994, pp. 171–182.

[114] K. Kira and L. A. Rendell, "The Feature Selection Problem: Traditional Methods and a New Algorithm," in *AAAI*, Vol. 2, No. 1992a, July 12– 16, 1992 1992, pp. 129– 134.

[115] H. Peng, F. Long, and C. Ding, "Feature Selection Based on Mutual Information: Criteria of Max-Dependency, Max-Relevance, and Min-Redundancy," *IEEE Transactions in Pattern Analysis and Machine Intelligence*, Vol. 27, No. 8, pp. 1226–1238, 2005.

[116] T. Cover and P. Hart, "Nearest Neighbor Pattern Classification," *IEEE Transactions on Information Theory*, Vol. 13, No. 1, pp. 21–27, 1967.

[117] C. Cortes and V. Vapnik, "Support-Vector Networks," *Machine Learning*, Vol. 20, pp. 273–297, 1995.

[118] L. Breiman, J. H. Friedman, R. A. Olshen, and C. J. Stone, Classification and Regression Trees, Ser. *Statistics/Probability Series*, Belmont, California, U.S.A.: Wadsworth Publishing Company, 1984.

[119] P. E. Hart, D. G. Stork, and R. O. Duda, Pattern Classification. *Wiley Hoboken*, 2000.

[120] C. M. Bishop, Pattern Recognition and Machine Learning. *Springer*, 2006.

[121] R. Adhikari and R. Agrawal, "Performance Evaluation of Weights Selection Schemes for Linear Combination of Multiple Forecasts," *Artificial Intelligence Review*, Vol. 42, No. 4, pp. 529–548, 2014.

[122] H. Liu, Y. Wang, W. Fan, X. Liu, Y. Li, S. Jain, Y. Liu, A. Jain, and J. Tang, "Trustworthy AI: A Computational Perspective," *ACM Transactions on Intelligent Systems and Technology*, Vol. 14, No. 1, pp. 1–59, 2022.

[123] S. M. Lundberg, G. Erion, H. Chen, A. Degrave, J. M. Prutkin, B. Nair, R. Katz, J. Himmelfarb, N. Bansal, and S. I. Lee, "From Local Explanations to Global Understanding with Explainable AI for Trees," *Nature Machine Intelligence*, Vol. 2, No. 1, pp. 2522–5839, 2020.

[124] S. M. Lundberg and S. I. Lee, "A Unified Approach to Interpreting Model Predictions," in *Advances in Neural Information Processing Systems 30*, I. Guyon, U. V. Luxburg, S. Bengio, H. Wallach, R. Fergus, S. Vishwanathan, and R. Garnett, Eds. Curran Associates, Inc., 2017, pp. 4765–4774.

[125] L.-K. Soh and C. Tsatsoulis, "Texture Analysis of SAR Sea Ice Imagery Using Gray Level Co-Occurrence Matrices," *IEEE Transactions on Geoscience and Remote Sensing*, Vol. 37, No. 2, pp. 780–795, 1999.

[126] D. A. Clausi, "An Analysis of Co-Occurrence Texture Statistics as a Function of Grey Level Quantization," *Canadian Journal of Remote Sensing*, Vol. 28, No. 1, pp. 45–62, 2002.

[127] T. Ojala, M. Pietikainen, and T. Maenpaa, "Multiresolution Gray-Scale and Rotation Invariant Texture Classification with Local Binary Patterns," *IEEE Transactions on Pattern Analysis and Machine Intelligence*, Vol. 24, No. 7, pp. 971–987, 2002.

[128] X. Tang, "Texture Information in Run-Length Matrices," *IEEE Transactions*

on Image Processing, Vol. 7, No. 11, pp. 1602–1609, 1998.

[129] N. Dalal and B. Triggs, “Histograms of Oriented Gradients for Human Detection,” in *2005 IEEE Computer Society Conference on Computer Vision and Pattern Recognition (CVPR’05)*, Vol. 1. San Diego, CA, USA: IEEE, 20-25 June 2005, pp. 886–893.

[130] S. G. Mallat, “A Theory for Multiresolution Signal Decomposition: The Wavelet Representation,” *IEEE Transactions on Pattern Analysis and Machine Intelligence*, Vol. 11, No. 7, pp. 674–693, 1989.

[131] J. S. Weszka, C. R. Dyer, and A. Rosenfeld, “A Comparative Study of Texture Measures for Terrain Classification,” *IEEE Transactions on Systems, Man, and Cybernetics*, Vol. 6, No. 4, pp. 269–285, 1976.

[132] C. Sun and W. G. Wee, “Neighboring Gray Level Dependence Matrix for Texture Classification,” *Computer Graphics and Image Processing*, Vol. 20, No. 3, pp. 297, 1982.

[133] C.-M. Wu and Y.-C. Chen, “Statistical Feature Matrix for Texture Analysis,” *CVGIP: Graphical Models and Image Processing*, Vol. 54, No. 5, pp. 407–419, 1992.

[134] K. I. Laws, “Texture Energy Measures,” in Proc. *Image Understanding Workshop*, 1979, pp. 47–51.

[135] A. Krizhevsky, I. Sutskever, and G. E. Hinton, “ImageNet Classification with Deep Convolutional Neural Networks,” *Communications of the ACM*, Vol. 60, No. 6, pp. 84–90, 2017.

[136] K. Simonyan, “Very Deep Convolutional Networks for Large-Scale Image Recognition,” *Arxiv Preprint,* Arxiv:1409.1556, 2014.

[137] C. Szegedy, W. Liu, Y. Jia, P. Sermanet, S. Reed, D. Anguelov, D. Erhan, V. Vanhoucke, and A. Rabinovich, “Going Deeper with Convolutions,” in *Proceedings of the IEEE Conference on Computer Vision and Pattern Recognition*. Boston, MA, USA: IEEE, June 7-12, 2015, pp. 1–9.

[138] K. He, X. Zhang, S. Ren, and J. Sun, “Deep Residual Learning for Image Recognition,” in *Proceedings of the IEEE Conference on Computer Vision and Pattern Recognition*, 2016, pp. 770–778.

[139] M. Tan and Q. Le, “EfficientNet: Rethinking Model Scaling for Convolutional Neural Networks,” in *International Conference on Machine Learning*. Long Beach, California: PMLR, Jun 10-15, 2019, pp. 6105–6114.

[140] C. Szegedy, S. Ioffe, V. Vanhoucke, and A. Alemi, “Inception-V4, Inception-Resnet and the Impact of Residual Connections on Learning,” in *Proceedings of the AAAI Conference on Artificial Intelligence*, Vol. 31, No. 1. San Francisco California USA: AAAI Press, February 4 - 9, 2017.

[141] M. Sandler, A. Howard, M. Zhu, A. Zhmoginov, and L.-C. Chen, “MobileNetv2: Inverted Residuals and Linear Bottlenecks,” in *Proceedings of the IEEE Conference on Computer Vision and Pattern Recognition*. Salt Lake City, UT, USA: IEEE, June 18-23, 2018, pp. 4510–4520.

[142] B. Zoph, V. Vasudevan, J. Shlens, and Q. V. Le, “Learning Transferable Architectures for Scalable Image Recognition,” in *Proceedings of the IEEE Conference on Computer Vision and Pattern Recognition*. Los Alamitos, CA, USA: IEEE Computer Society, June 18-23, 2018, pp. 8697–8710.

[143] X. Zhang, X. Zhou, M. Lin, and J. Sun, “ShuffleNet: an Extremely Efficient Convolutional Neural Network for Mobile Devices,” in *Proceedings of the IEEE Conference on Computer Vision and Pattern Recognition*. Los Alamitos, CA, USA: IEEE Computer Society, June 18- 23, 2018, pp. 6848–6856.

[144] F. N. Iandola, “SqueezeNet: AlexNet-Level Accuracy with 50 x Fewer Parameters and < 0.5 MB Model Size,” *Arxiv Preprint,* Arxiv:1602.07360, 2016.

[145] R. R. Yager, “On the Measure of Fuzziness and Negation Part I: Membership in the Unit Interval,” *International Journal of General Systems*, Vol. 5, No. 4, pp. 221–229, 1979.

[146] ——, “On the Measure of Fuzziness and Negation. II. Lattices,” *Information and Control*, Vol. 44, No. 3, pp. 236–260, 1980.

[147] K. T. Atanassov, “Intuitionistic Fuzzy Sets,” *Intuitionistic Fuzzy Sets: Theory and Applications*, pp. 1-137, Heidelberg: Physica-Verlag HD, 1999.

[148] T. M. Cover, “Geometrical and Statistical Properties of Systems of Linear Inequalities with Applications in Pattern Recognition,” *IEEE Transactions on Electronic Computers*, No. 3, pp. 326–334, 1965.

[149] R. N. Dave, "Validating Fuzzy Partitions Obtained Through C-Shells Clustering," *Pattern Recognition Letters*, Vol. 17, No. 6, pp. 613–623, 1996.

[150] A. M. Bensaid, L. O. Hall, J. C. Bezdek, L. P. Clarke, M. L. Silbiger, J. A. Arrington, and R. F. Murtagh, "Validity-Guided (Re) Clustering with Applications to Image Segmentation," *IEEE Transactions on Fuzzy Systems*, Vol. 4, No. 2, pp. 112–123, 1996.

[151] M. D. Levine and A. M. Nazif, "Dynamic Measurement of Computer-Generated Image Segmentations," *IEEE Transactions on Pattern Analysis and Machine Intelligence*, Vol. 7, No. 2, pp. 155–164, 1985.

[152] R. Zéboudj, "Filtrage, Seuillage Automatique, Contraste Et Contours: Du Pré-Traitement À L'analyse D'image," *Ph.D. Dissertation*, Saint- Etienne, 1988.

[153] M. Friedman, "The Use of Ranks to Avoid the Assumption of Normality Implicit in the Analysis of Variance," *Journal of the American Statistical Association*, Vol. 32, No. 200, pp. 675–701, 1937.

[154] R. L. Iman and J. M. Davenport, "Approximations of the Critical Region of the FBI-Ktkan Statistic," *Communications in Statistics Theory and Methods*, Vol. 9, No. 6, pp. 571–595, 1980.

PUBLICATIONS

SCI/SCIE-INDEXED JOURNALS (Published/ Accepted)

- **Trasha Gupta**, S. Indu, and Rajni Jindal,"Segmenting hotspots from medical thermal images using Density-based Modified FC-P_cFS with spatial information", **Quantitative InfraRed Thermography Journal**, pp. 1-37, October 2024, (Publisher: TAYLOR & FRANCIS LTD; ISSN / eISSN: 1768-6733 / 2116-7176). (*Published*). **Impact factor: 3.2**
  DOI: https://www.tandfonline.com/doi/abs/10.1080/17686733.2024.2408714.

- **Trasha Gupta**, Rajni Jindal, and S. Indu, "Empirical Review of Various Thermography - based Computer-aided Diagnostic Systems for Multiple Diseases", **ACM Transactions on Intelligent Systems and Technology**, Volume 14, Issue 3, Article No.: 56, Pages 1 - 33, 2023, (Publisher: ASSOC COMPUTING MACHINERY; ISSN / eISSN: 2157-6904 / 2157-6912) (*Published*). **Impact factor: 7.2**
  DOI: https://dl.acm.org/doi/abs/10.1145/3583778.

SCOPUS-INDEXED CONFERENCES (Published/ Accepted)

- **Trasha Gupta**, Rajni Jindal, and S. Indu, "Empirical Analysis of Thermography Effectiveness for Health Diagnosis", ***International Conference on Computational Science and Computational Intelligence (CSCI-2020)***, IEEE, Las Vegas, NV, USA, 2020, pp. 830-835, DOI: 10.1109/CSCI51800.2020.00155. **(Presented & Published).**

- **Trasha Gupta**, S. Indu, and Rajni Jindal, "2-Phase Framework of Suspicious Region Identification in Medical Thermal Images", ***International Conference on Sustainability and Technological Advancements in Engineering Domain (SUSTAINED 2024)***, IEEE, Manav Rachna International Institute of Research and Studies, New Delhi, India, 2024. (Accepted and Presented).

- **Trasha Gupta**, S. Indu, and Rajni Jindal, "Deep Thermal Biomarkers for Classification of Abnormality in Medical Thermal Images", ***International Conference On Computing Systems And Intelligent Applications (ComSia 2025)***, Springer, School Of Open Learning, University Of Delhi, 2025. (Accepted).

DELHI TECHNOLOGICAL UNIVERSITY
(Formerly Delhi College of Engineering)
Shahabad Daulatpur, Main Bawana Road, Delhi-110042, INDIA

PLAGIARISM VERIFICATION

Title of the Thesis - **Development of Framework for Thermal Patterns Analysis for Diagnosis of Diseases**
Total Pages - **132 pages (Abstract onward)**
Name of the Scholar - **Trasha Gupta**
Department - **Department of Computer Science & Engineering**
Supervisors-

1. **Prof. Rajni Jindal, Department of Computer Science & Engineering** (Supervisor)
2. **Prof. S. Indu, Department of Electronics and Communications Engineering** (Co-Supervisor)

This is to report that the above thesis was scanned for similarity detection. Process and outcome is given below: Software used: Turnitin Similarity Index: **5%(=20%-15%(Self-Plagiarism))**, Total Word Count: **63,806**

Candidate's Signature - Trasha Gupta

Prof. Rajni Jindal
(Supervisor)
Department of Computer
Science and Engineering

Prof. S. Indu
(Co-Supervisor)
Department of Electronics and
Communications Engineering

Date: 05/08/2025
Place: New Delhi

Author Biography

Trasha Gupta

Assistant Professor,
Department of Applied Mathematics
Delhi Technological University, Delhi, India
Email: trashagupta@gmail.com; trashagupta@dtu.ac.in

Trasha Gupta is an assistant Professor in the department of Applied Mathematics, DTU since 2018. Prior to this, she lent her expertise to Deen Dayal Upadhyaya College, Delhi University and Aricent Technologies. She completed her M. Tech. Computer Science and Engineering from IIIT Delhi, M. Sc Computer Science and B. Sc (Hons.) Computer Science from University of Delhi. She is pursuing his PhD from Delhi Technological University, New Delhi, India. Her interest lies in the fascinating realm of medical thermal image Processing.